

Inferring bifurcations between phenotypes

Grisha Szep

A dissertation submitted in fulfillment
of the requirements for the degree of

Doctor of Philosophy

at

King's College London

Randall Division of Cell & Molecular Biophysics



funded by **Microsoft Research Cambridge**



October 29, 2021

Abstract

The gene-expression history of an organism and its environment determine the organism's phenotype. The phenotype is an inherently qualitative state, deduced by relative biochemical concentration measurements collected by methods such as flow cytometry or fluorescence microscopy. The biochemical threshold concentrations that distinguish different phenotypes can be modelled by applying bifurcation analysis to differential equation models and the search for these boundaries in experimental data can be done using dimensionality reduction and clustering techniques. This establishes a relationship between bifurcations, phenotypes and machine learning techniques that are the subject of this thesis.

The first chapter presents an interactive tool for exploring phenotypes in flow cytometry data. In particular we explore a multi-tissue, high-dimensional, immune cell dataset. The tool bridges machine learning methods and the popular FlowJo, used to annotate cells with gating strategies. An assortment of dimensionality reduction techniques are applied to create two dimensional embeddings and confusion matrices are used to quantify annotation agreement between immunologists. By leveraging the geospatial mapping library OpenLayers to render, annotate and analyze cells, immunologists can now efficiently navigate the phenotype space of Human Cell Atlas datasets.

The next chapter focuses on a model-driven approach for exploring and designing phenotypes, where we demonstrate how model-guided design of synthetic E. Coli can elucidate pattern formation mechanisms in

multicellular development. We infer the parameters of a biochemically motivated system of differential equations against time course fluorescence data acquired from plate reader experiments. Our design goals however were not in the temporal domain, rather we wanted to control the shape and size of a cusp bifurcation in the space of experimentally controlled input concentrations.

To address these limitations, I define a differentiable semi-supervised cost function that uses bifurcation locations as targets. Bifurcations are encouraged by an unsupervised term that extremises the curvature of the determinant of the Jacobian. By exploring the cost landscape for minimal models that span the space of saddle-nodes and pitchforks, I show that the parameter space basins define regions of qualitatively equivalent differential equations. The differentiability of the cost function enables efficient optimisation using libraries such as Flux.jl that leverage automatic differentiation. The impact of this work would enable experimentalists to efficiently navigate design spaces of differential equation models.

Acknowledgements

Acknowledgements to people I love

Contents

1	Introduction & Motivation	15
1.1	Bottom-up and Top-down Biology	16
1.2	Design, Build, Test, Learn	18
1.3	State of the Art	19
1.3.1	Inference of Differential Equations	19
1.3.2	Model Reduction and Classification	20
1.4	Design–Learn Pipeline	20
1.4.1	Experimental Design Loop	21
1.4.2	Hypothesis Scoring and Model Refinement Loop . . .	22
1.4.3	System Design	23
2	Theoretical Background	24
2.1	Describing Phenotypes with Bifurcations	25
2.1.1	Differential Equation Models	28
2.1.2	Bifurcation Analysis	39
2.1.3	Spatially Extended Systems	43
2.2	Applications in Cell Biology	45
2.2.1	Genetic Switches & Phenotype Boundaries	45
2.2.2	Self-organised Patterns & Development	50
2.3	Phenotype Inference with Machine Learning	53
2.3.1	Phenotypes from Statistics in Homeostasis	55
2.3.2	Phenotypes from Machine Learning Models	58
2.4	Applications in Flow Cytometry	64

<i>Contents</i>	6
2.4.1 Immunophenotyping Panels	64
3 Interpretation of Morphogen Gradients by a Bistable Circuit	65
3.1 Preface	65
3.1.1 Problem Statement & Context	65
3.1.2 Contributions	66
3.2 Abstract	68
3.3 Introduction	69
3.4 Results	69
3.4.1 Engineering mutual exclusivity	69
3.4.2 Mutual inhibition results in bistability	70
3.4.3 Hysteresis produces stable boundaries	71
3.4.4 A secondary gradient creates self-organised domains .	71
3.5 Discussion	72
3.6 Methods	73
3.6.1 Plasmid construction	73
3.6.2 Plate fluorometer assay	73
3.6.3 Flow-cytometric analysis of hysteresis	73
3.6.4 Microfluidics	74
3.6.5 Microfluidics microscopy	74
3.6.6 Solid culture assays	74
3.7 Afterword	76
4 Parameter Inference with Bifurcation Diagrams	77
4.1 Preface	77
4.1.1 Problem Statement & Context	77
4.1.2 Contributions	78
4.2 Abstract	79
4.3 Introduction	79
4.3.1 Preliminaries	80
4.4 Proposed Method	82

4.4.1	Semi-supervised Cost Function	82
4.4.2	Differentiating the semi-supervised cost function . . .	83
4.5	Experiments & Results	84
4.5.1	Minimal Models	84
4.5.2	Genetic Toggle Switch	84
4.5.3	Complexity	85
4.6	Conclusion & Broader Impact	87
4.7	References	88
4.8	Afterword	90
5	Exploring Bifurcations between Phenotypes	91
5.1	Preface	91
5.1.1	Problem Statement & Context	91
5.1.2	Contributions	92
5.2	Abstract	93
5.3	Introduction	93
5.4	Proposed Method	95
5.4.1	Pre-processing	95
5.4.2	Annotation in FlowJo	96
5.4.3	Exploration in FlowAtlas.jl	98
5.5	Results	99
5.5.1	T-regulatory Sub-populations	99
5.5.2	T-helper cell populations	102
5.6	Discussion	102
5.7	Methods	103
5.7.1	Tissue Acquisition & Dissociation	103
5.7.2	Flow Cytometry	104
5.7.3	Imputation & Embedding	105
5.7.4	Data & Code Availability	105
5.8	Afterword	105

<i>Contents</i>	8
6 Conclusions	106
6.1 Limitations	106
6.2 Future work	106
Appendices	107
A Interpretation of Morphogen Gradients by a Bistable Circuit	107
A.1 Supplementary Figures	109
A.2 Supplementary Methods	125
A.2.1 Differential Equation Models & Parameter Inference .	126
A.2.2 Bistability Analysis	147
A.2.3 Boundary Experiments	149
A.2.4 Models of the Exclusive Receiver Relay Circuits	157
B Parameter Inference with Bifurcation Diagrams	159
B.1 Bifurcation Diagrams as Tangent Fields	160
B.2 Bifurcation Measure Properties	161
B.3 Leibniz Rule for Space Curves	162
B.4 Application to the Double Exclusive Model	164
B.5 Extension for Hopf Bifurcations	165
C Exploring Bifurcations between Phenotypes	166
C.1 Supplementary Tables	166
Bibliography	170

List of Figures

1.1	<i>Enigma I</i> reverse engineered by Marian Adam Rejewski	16
1.2	Top-down and bottom-up modelling methods	18
1.3	Design-Build-Test-Learn cycle from synthetic biology	19
1.4	Workflow loop for optimal experimental design, without mechanistic model	21
1.5	Overview of hypothesis scoring pipeline and model refinement loop	22
1.6	Overview of system design pipeline	23
2.1	a) The bifurcations (shown in gold) at critical voltage p^* above argon concentration θ^* give rise to sudden jumps in brightness (right-hand panels). θ^* separates two bulb phenotypes and p^* separates the <i>on</i> and <i>off</i> states.	25
2.2	Waddington landscapes representing the set of available behaviours for two phenotypes in response to a controlled condition p . Phenotypes are related by changes in landscape topology via changes in θ	27
2.3	Illustration of a trajectory between $u = u(t)$ and $u' = u(t')$ over finite time $t - t'$ following the field lines of F_θ . In this example field lines either point towards steady state u^* or a limit cycle $\omega(t)$. There are two unstable fixed points marked by crosses: a saddle point separating the basins of attraction and an unstable focus enclosed by the limit cycle.	29

2.4	Illustration how the Jacobian matrix $\frac{\partial F_\theta}{\partial u}$ transforms the basis vectors $\hat{u}(t)$ defining a small patch of initial conditions for a short period of time Δt . The eigenvalues λ and eigenvectors \hat{v}_λ define the deformation of the patch	30
2.5	Illustration how the time ordering operator $\mathcal{T} \left\{ e^{\int_{t'}^t J(s) ds} \right\}$ propagates the separation $\delta u(t)$ between adjacent trajectories u and $u + \delta u$ by repeated application of the exponentiated Jacobian $e^{J(t)\Delta t}$ evaluated along trajectory $u(t)$	32
2.6	Classification of stable and unstable fixed points for a general two dimensional systems in terms of trace $\text{Tr}[\frac{\partial F_\theta}{\partial u}]$ and determinant $ \frac{\partial F_\theta}{\partial u} $ of its Jacobian	34
2.7	Generic and robust bifurcations. A. <i>Saddle-node</i> bifurcations create or annihilate stable and unstable pairs of fixed points. B. In <i>Hopf</i> bifurcations a stable fixed point becomes an unstable focus that pushes trajectories towards a limit cycle.	40
2.8	Fragile bifurcations	41
2.9	Global Bifurcations	42
2.10	Homoclinic Bifurcation	43
2.11	Overview of the <i>lac operon</i>	46
2.12	Monostable and bistable behaviour in the lac operon	49
2.13	Top: <i>Hox</i> gene expression patterns in body segments of drosophila Bottom: Mutation where legs grow in-place of antenna []	51
2.14	Expression patterns of pair-rule <i>Gap</i> genes in Drosophila embryo []	52
2.15	Pigment patterns hypothesised to be generated by Turing mechanism	52

2.16 Bifurcation point extraction along the condition p via two possible routes: steady state inference (a,d→c) and fixed point inference (a,d→b,e→c). The fixed point inference route requires <i>universal function approximator</i> $F(u)$ at different values of the condition p and yields additional unstable fixed points.	53
2.17 Overview of the impute, reduce & cluster methods. A. Heatmap of $N \times \mathcal{U} $ data matrix revealing regions of missing data that are imputed. B. Dimensionality reduction yielding an embedding which can be coloured by any feature u_k to reveal differentials between regions. C. Clustering methods yield a segmentation of the dataset into populations that share features u	56
2.18 Protocols (a) for extracting limit points with respect to conditions p, p' . Steady state distributions (b). Similarity measure (c)	57
2.19 Gaussian process regressors estimating derivative of the trajectories \hat{f} from example trajectory datasets $\mathcal{D}_1 \dots \mathcal{D}_K$ with varying signal to noise ratios. Interpolation error E is shown as a heatmap; extrapolation fails	63
3.1 Geometry of opposing gradients experiment	65
3.2 Fig. 1 A synthetic gene circuit for morphogen interpretation.	69
3.3 Fig. 2 Mutual inhibition produces bistability.	70
3.4 Fig. 3 Formation of stable boundaries.	72
3.5 Fig. 4 Addition of a Relay circuit creates self-organised domains of gene expression.	73

- 4.1 *Fig. 1* Illustration of bifurcation diagrams for minimal models of bifurcations. A. Saddle-node bifurcations arise for $F_\theta(u, p) = p + \theta_1 u + \theta_2 u^3$ when $\theta = (\frac{5}{2}, -1)$. B. Pitchfork bifurcations arise for $F_\theta(u, p) = \theta_1 + pu + \theta_2 u^3$ when $\theta = (\frac{1}{2}, -1)$. Targets are illustrated by light yellow vertical lines. Bifurcation curves are shown as solid blue and red lines, with lighter shades indicating the determinant crossing zero at locations $\mathcal{P}(\theta)$ giving rise to unstable solutions. 81
- 4.2 *Fig. 2* Bifurcation measure $\varphi_\theta(s)$ and determinant $\left| \frac{\partial F_\theta}{\partial u} \right|$ along the arclength s of two different bifurcation curves demonstrating how maximising the measure along the curve maintains the existing bifurcation marked by a circle, while encouraging new bifurcations marked by stars. 82
- 4.3 *Fig. 3* Saddle-node $F_\theta(u, p) = p + \theta_1 u + \theta_2 u^3$ and pitchfork $F_\theta(u, p) = \theta_1 + up + \theta_2 u^3$ optimised with respect to θ so that predicted bifurcations $\mathcal{P}(\theta)$ match targets \mathcal{D} in control condition p . The right panel shows bifurcation diagrams for the three optimal θ^* marked by stars on the left panel. The optimisation trajectories in white follow the gradient of the cost, approaching the black lines of global minima in the left panel 84
- 4.4 *Fig. 4* Bifurcation inference for the two-state model (11). A. Optimal parameter estimates θ^* for the targets $\mathcal{D} = \{4, 5\}$ reveal two clusters of qualitatively different regimes: mutual activation ($a_1 < 1$; cluster 1) and mutual inhibition ($a_1 > 1$; cluster 2). B. Example bifurcation diagrams indicate positively and negatively correlated dependencies between the two model states, as a function of the control condition. 85

4.5 <i>Fig. 5</i> A. Execution time (time to calculate cost gradient) with respect to states N . B. Convergence times (the time it takes to find and match a bifurcation to within 1% of a specified target) with respect to the number of parameters M , comparing against a gradient-free approach: Nelder-Mead. Calculations were performed on an Intel Core i7-6700HQ CPU @ 2.60GHz x 8 without GPU acceleration.	86
5.1 Overview of FlowAtlas.jl workflow in tandem with FlowJo	94
5.2 Panel-specific gating strategies created in FlowJo.	97
5.3 Treg sub-population discovery with FlowAtlas.jl and verification with FlowJo	101
5.4 Exploration of Th1 T cell subpopulations.	102
A.1 <i>Supplementary Figure 1</i> Circuit variants	109
A.2 <i>Supplementary Figure 2</i> Raw timecourse fluorescence traces .	111
A.3 <i>Supplementary Figure 13</i> Hysteresis flow cytometry experiments	122
A.4 <i>Supplementary Figure 25</i> Bifurcation curves for uniform and protected degradation models	148
A.5 <i>Supplementary Figure 26</i> bifurcation curve insensitivity specific growth rate γ_0	148
B.1 <i>Supplementary Figure 1</i> Two implicit surfaces $f_\theta(z) = 0$ and $g_\theta(z) = 0$ in \mathbb{R}^3 intersecting to form a space curve which is tangent to field $T_\theta(z)$ and perpendicular to gradients $\partial_z f_\theta$ and $\partial_z g_\theta$	160
B.2 <i>Supplementary Figure 2</i> Left/Right : Determinant $\left \frac{\partial F_\theta}{\partial u} \right $ and tangent field $T_\theta(z)$ for the saddle-node/pitchfork models for some set values of θ revealing that $\left \frac{\partial F_\theta}{\partial u} \right = 0$ defines bifurcations	161

- B.3 *Supplementary Figure 3* Bifurcation inference for the *double exclusive reporter*. A. Optimal parameter estimates θ^* for the targets $\mathcal{D} = \{1,2\}$ (indicated by yellow lines in panel B) reveal four regions with two geometrically different regimes: mutual activation (region 1) and mutual inhibition (regions 2-4). B. Example bifurcation diagrams indicate that region 2 has swapped kinetics between L and T to region 3. Region 4 has models with non-zero imaginary parts to eigenvalues indicating damped oscillations (shown in light green). 164
- B.4 *Supplementary Figure 4* Bifurcation measure $\varphi_\theta(s)$ and eigenvalues $\lambda(s)$ along the arclength s for two different bifurcation curves demonstrating how the measure detects non-zero imaginary parts $\Im[\lambda]$ (onset of damped oscillations marked by circle) and sign changes in real parts $\Re[\lambda]$ (Hopf bifurcations marked by stars) 165

Chapter 1

Introduction & Motivation



one thing that won't change with time is the memories of younger years

Minuet of Forest — Ocarina of Time

The advent of the modern digital computer, as formalised by Alan Turing,[1] ignited the field of computational physics, aided by pre-existing theoretical formulations of algorithms. Starting from the first experiments with Monte Carlo (MC) simulations in the 1930s by Fermi and the formulation of the Markov-Chain Monte Carlo (MCMC) technique by Ulam in the 1940s, von Neumann programmed the 18,000 vacuum-tube Electronic Numerical Integrator and Computer (ENIAC) computer to investigate neutron diffusion in fissionable materials.[2] This success paved the way for the integration of Newton's equations of motion to compute the time evolution of a many-body system.

Consider being Marian Adam Rejewski, a Polish mathematician and cryptologist in 1932, almost seven years before the beginning of World War II. It was known at the time that the Germans were using a machine called *Enigma I* to send secret messages, but no one knew what the machine looked like nor how it worked. Based on a handful of intercepted en-

cripted messages and pictures of the operating instructions obtained by Polish intelligence, he derived a set of permutation equations that allowed him the reverse-engineer the machine [3]. The cryptologic achievements of Rejewski and colleagues Jerzy Różycki and Henryk Zygalski are considered the some of the greatest feats in reverse-engineering of the 20th century.



Figure 1.1: *Enigma I* reverse engineered by Marian Adam Rejewski

Today we are getting ever closer to reverse-engineering the cell. The fields of synthetic and systems biology are beginning resemble engineering disciplines; genetic engineering is becoming more precise, high-throughput in vitro experiments are performed by robots and measurements of many desired observables can be obtained with high spatio-temporal resolution. Advances in micro-fabrication [4] and in-vitro reconstitutive methods [5] have allowed biologists isolate pathways and mechanisms to a level of mathematical and computational tractability [6]. This section outlines the scientific paradigms in these fields, their methods and limitations, and finally what this thesis will attempt to contribute.

1.1 Bottom-up and Top-down Biology

Fortunately for biologists copies of the target of their reverse-engineering attempts are available all around us. Less fortunate is the fact that most attempts at deconstructing the cell end in loss of function and destruction of the individual components. This restriction motivates system biologists

to manipulate environmental signals *in vivo* and build mechanistic models from correlations between signals and responses [7]. Models focus on relationships between macroscopic variables where the underlying mechanisms are not known.

In vitro reconstitutive methods aim to isolate minimal mechanisms from the complexity of the whole organism in order to unpick the relative importance of microscopic details [5]. In situations where purified proteins and crystal structures are available these methods can quite accurately characterise the kinetics of proteins. Relating these parameters to the *in vivo* context however may not be relevant, as too much of the complexity may have been stripped away.

From a theoretical modelling perspective, it is important to choose a time-scale and space-scale that is relevant to the problem. If one is interested in tissue dynamics, attempting to model DNA conformations within each cell will render the problem intractable. As George Booth aptly put “*most models are wrong but some are useful*” so the role of theoretical descriptions in these settings is not necessarily to describe the way reality *is* but serve as tools to bridge the non-intuitive gap between bottom-up and top-down approaches. Where intuition fails is where the *in silico* hypothesis testing playground becomes most valuable [6].

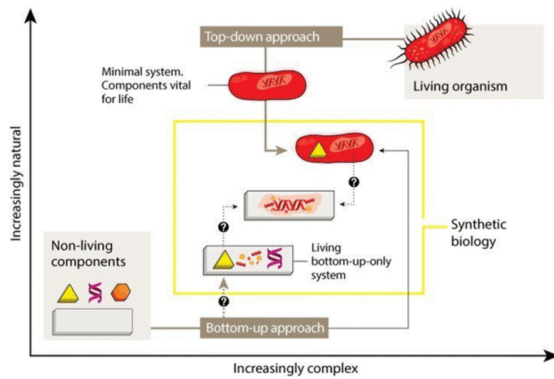


Figure 1.2: Top-down and bottom-up modelling methods

1.2 Design, Build, Test, Learn

Systems and synthetic biology have historically made progress through a process of brute force trial and error. This usually involves the interaction of many custom-made parts that are iteratively optimised by human intervention. A trend first observed in the 1980s known as *Eroom's law* reveals that discoveries in biotechnology are becoming slower and more expensive over time, despite improvements in technology [8]. This problem is compounded by the ongoing reproducibility crisis [9]. In the effort to transform methods used in academia and industry to become more systematic and predictable, a standard for the Design–Build–Test–Learn cycle has emerged – shown in figure 1.3.

This workflow has now been established as a paradigm with some aspects that have been automated by liquid handling robots, bioreactor environments and image processing pipelines. However, humans in the loop and custom moving parts still persist. The challenge in automating these processes lies in defining a programming language that has a sufficiently high level of abstraction for transparent implementation while allowing for low-level customisation [10].

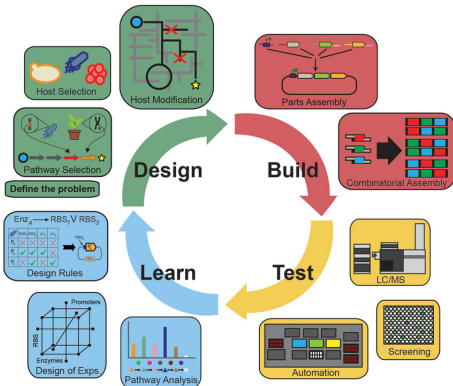


Figure 1.3: Design-Build-Test-Learn cycle from synthetic biology

This thesis will focus on modelling and inference using systems of differential and partial differential equations, which fits into the Design–Learn part of the cycle. Differential equations occupy a small subset of possible modelling tools, however they are amongst the most popular due to their ease of use formulation and simulation. This ease of access creates a zoo of models in literature making it difficult to identify the key ingredients that distinguish different models. Furthermore the relationship between multiple plausible *and* in-plausible hypotheses is rarely investigated. This motivates desire for an automated Design–Learn pipeline – outlined in Section 1.4 – which can generate and catalogue models in a transparent manner while producing insights for the Build stage. This pipeline is applied in an experiment-theory collaboration described in Chapter 3.

1.3 State of the Art

1.3.1 Inference of Differential Equations

Following the initial literature on smooth and match estimators [11] – which overcome the bottleneck having to integrate a proposed hypothesis for every parameter update – a plethora of methods for the inference of differential equations became available [12, 13]. The essence of these methods is to estimate the derivatives of the data rather than integrate the model and simultaneously estimate the qualitative and quantitative behaviours.

In most biological experiments batch-to-batch variations decrease the certainty with which it is possible to quantify a behaviour. Whether or not a parameter is identifiable, redundant or sloppy have become key questions in biology [14, 15, 16].

1.3.2 Model Reduction and Classification

Sloppiness and sensitivity analysis have been extensively used in the search for reduced models. Linear mappings between models that preserve stoichiometry and reactant structure were investigated [17, 18] and computational tools based on partition-refinement were released [19]. Structural similarity between reaction networks can be revealed by such mappings, elucidating the functional aspects of complex networks in terms of simpler networks. The aim of the Design–Learn pipeline is to extend this framework to nonlinear mappings with an emphasis on geometry rather than kinetics. Most inference techniques attempt to match geometry and kinetics simultaneously in an attempt to obtain a quantitative model. This thesis emphasises that geometry alone should be prioritised in order to obtain qualitatively equivalent models. Furthermore recent results in pattern formation theory [20] do not depend on kinetics at all, only geometry.

1.4 Design–Learn Pipeline

This section outlines the proposal for a design–learn pipeline for the purposes of model reduction and system design. Suppose experimental collaborators have provided us with time-course gene expression data \mathcal{D} , which could be taken via time-lapse microscopy of cells growing on microfluidic plates, optical density measurements from microtiter plate assays or temporal snapshots of flow cytometry measurements. On the other hand one may want to specify a behaviour \mathcal{H} which may have not yet been observed. This would be specified with top-down constraints, i.e. there exist oscillations of a fixed frequency or a region of bistability.

1.4.1 Experimental Design Loop

The experimentalists may want to know whether the data collected could result in a model of predictive power without mechanistic knowledge of the underlying biochemistry. Moreover it would be desirable gain insights in parameter regimes in the vicinity of observations, without having to wait for the theorists to produce a refined model. Such real-time insights would guide data collection protocols, optimising the amount of information gained while keeping the number of experiments performed to a minimum. Often data is noisy and at worst case contradictory; these issues must also be exposed.

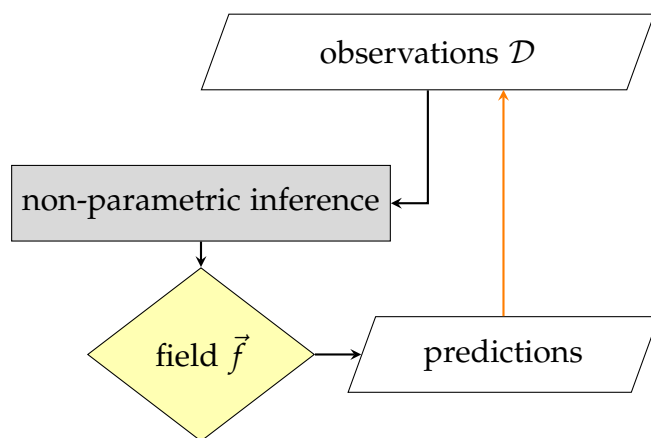


Figure 1.4: Workflow loop for optimal experimental design, without mechanistic model

Figure 1.4 outlines the workflow for optimal experimental design. The term *non-parametric* defines the procedures that have prioritised functional generality and flexibility over mechanistic insights gained from the values of the parameters and shapes of the mathematical forms. Neural networks and Gaussian process regressors are examples of non-parametric estimation procedures, which produce an estimate of the field \vec{f} that predicts gene expression rates at given expression levels. Based on these predictions, the experimentalist may proceed to collect data in the most informative parameter regions, which would in turn more accurately estimate \vec{f} .

1.4.2 Hypothesis Scoring and Model Refinement Loop

Often predictions from field \vec{f} are not enough. Models constructed with feasible biophysical assumptions $\vec{h}(\vec{\theta})$ have the potential to extrapolate predictions and give concrete biophysical meanings to each parameter $\vec{\theta}$. This way the experimentalist knows exactly which modification to the system they must make in order to achieve a desired behaviour. More often than not it is also unclear whether the model and its assumptions are reasonable, which brings us to the desire to score our hypotheses. For increased accuracy and efficiency [21] the mechanistic model $\vec{h}(\vec{\theta})$ is inferred against non-parametric estimate \vec{f} rather than the data \mathcal{D} directly. Furthermore as discussed in Section 1.3 the aim is to optimise geometry rather than kinetics. Alternatively one may construct $\vec{h}(\vec{\theta})$ to cover a whole class of models, such as those that satisfy mass-action. The expectation is that most of the parameters would be zero but some would be informative. One can obtain a distribution of optimal parameters $\rho(\vec{\theta})$ by running multiple optimisations. From this distribution one may construct alternative hypotheses and update $\vec{h}(\vec{\theta})$. By iterating this procedure one would identify the minimal model within the model class that explains the data. This process is known as model refinement or reduction.

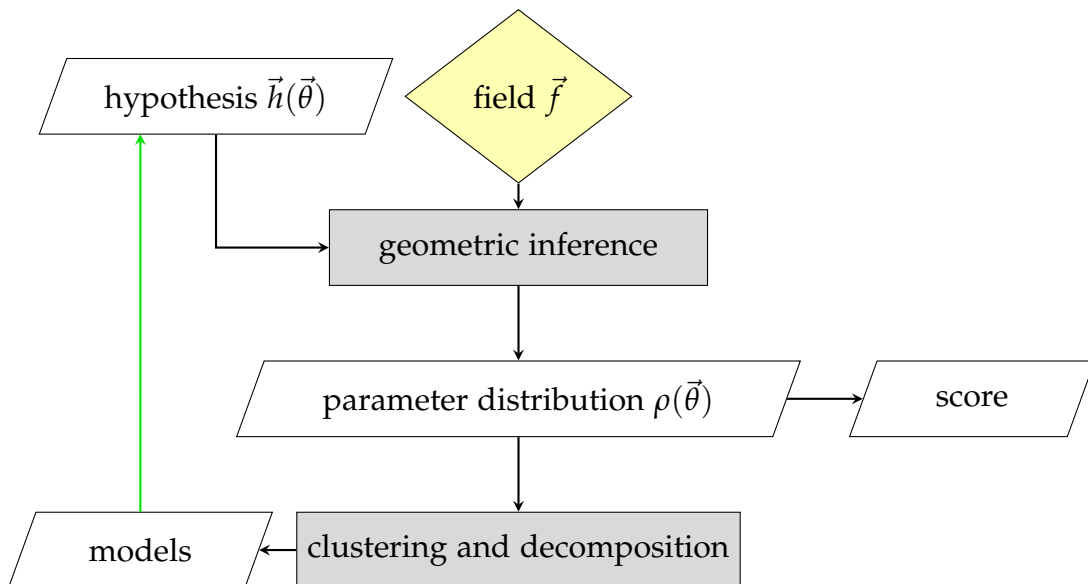


Figure 1.5: Overview of hypothesis scoring pipeline and model refinement loop

1.4.3 System Design

Suppose now that refined mechanistic models of the form $\vec{h}(\vec{\theta})$ have been obtained using the model refinement loop. These could be a library of known parts that have been individually characterised, but never combined to form a larger system. The experimentalists would like to create a system with a specified behaviour \mathcal{H} and would like to know which parts to combine and which modifications to make. The model refinement loop can be used with the design as an input.

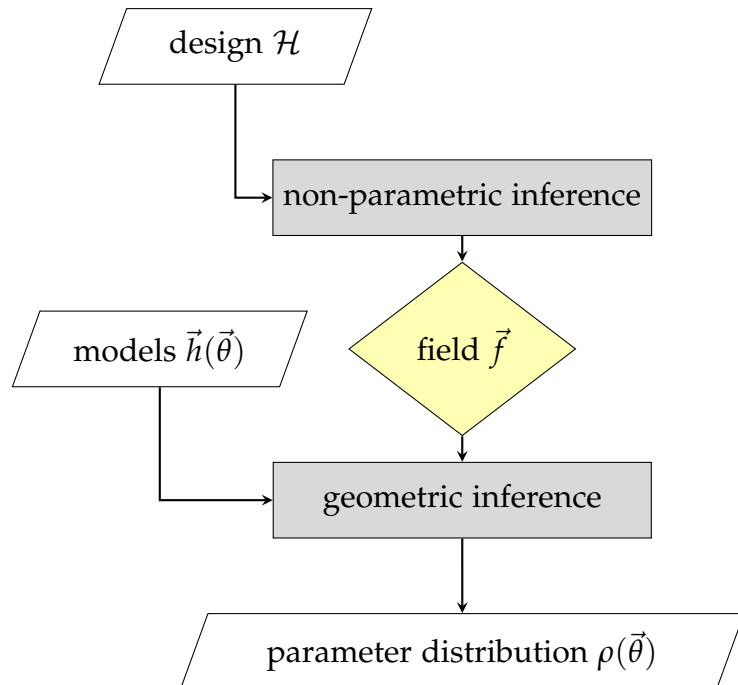


Figure 1.6: Overview of system design pipeline

Chapter 2

Theoretical Background



the passion of friendship will soon blossom into a righteous power

Bolero of Fire — Ocarina of Time

This Chapter lays out a background bifurcation theory and machine learning methods relevant to cell biology and flow cytometry. We establish the connection between the concept of phenotypes and bifurcations in Section 2.1 and lay out assumptions and definitions that are used throughout other chapters. Section 2.2 follows up with concrete applications of differential equations in cell biology and will prepare the reader for the incorporated synthetic biology publication in Chapter 3.

The problem of inferring phenotypes from data is defined in Section 2.3 with a survey relevant machine learning methods. This section discusses the pre-processing techniques to extract bifurcations from raw data, as has been done in Chapter 3, and used as a starting point in the incorporated machine learning publication in Chapter 4. Section 2.4 gives the reader a background in flow cytometry and how the machine learning methods discussed in previous sections are used by immunologists to identify immune cell phenotypes. This section lays the foundations for the interactive exploration tool presented in Chapter 5.

2.1 Describing Phenotypes with Bifurcations

A phenotype is a qualitative state or behaviour of an organism that can be described by several quantitative features. Before considering the additional complexity that comes with biology, let us first consider a simple everyday metaphor: light bulbs. Light bulbs come in various combinations of quantitative features θ which could be its shape, colour, materials and circuit design. The purpose of a light bulb is to fulfil a single function: increase in brightness as a function of voltage p , pushing the qualitative state of the bulb from *off* to *on*. Changes to bulb shape affect neither its function nor its states. Changes in color affect the quality of the *on* state but not the *off* state. Changes to circuit design and materials may change or even break the bulb's function. Fluorescent bulbs, for example, only have two possible brightness states in response to changes in voltage p , while incandescent bulbs have a continuous brightness response.

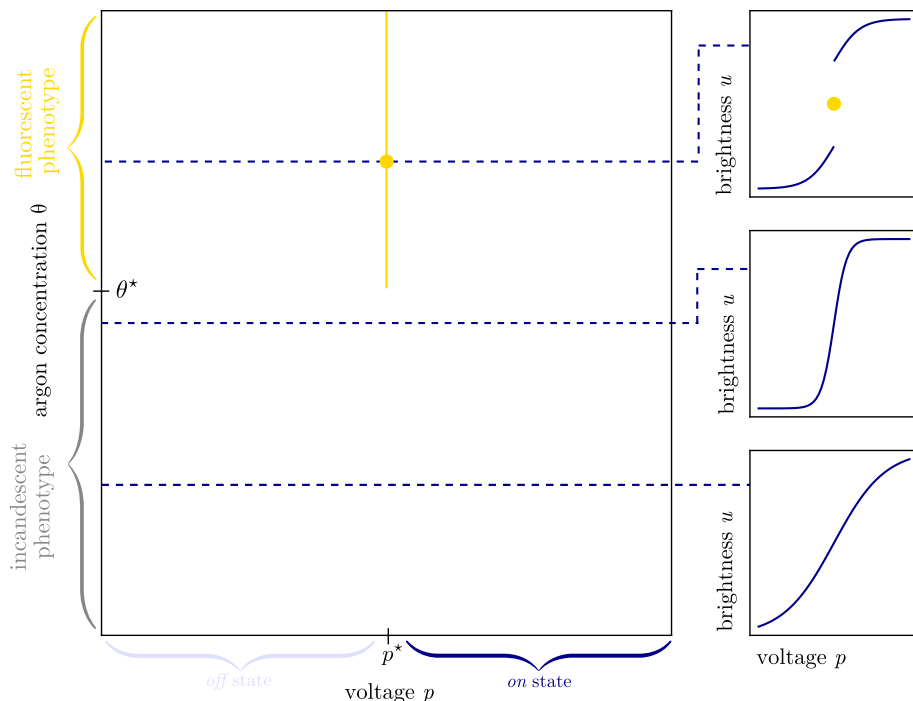


Figure 2.1: a) The bifurcations (shown in gold) at critical voltage p^* above argon concentration θ^* give rise to sudden jumps in brightness (right-hand panels). θ^* separates two bulb phenotypes and p^* separates the *on* and *off* states.

The fluorescent and incandescent bulbs can be considered as two different phenotypes distinguished by the quality of their response to voltage changes. Different colour bulbs can also be considered phenotypes, distinguished by the quality of their *on* state, rather than their response to voltage. Bifurcation theory allows us to describe the transitions between qualitative states and can be leveraged to distinguish and organise phenotypes. In this context a bifurcation becomes a punctuation that either *distinguishes between phenotypes* or *distinguishes between behaviours within a phenotype*.

Suppose we inserted a component into our light bulb that changed parameter θ in such a way so that we can change between the discrete response of the fluorescent bulb and the continuous response of the incandescent bulb. Perhaps θ could be the concentration of argon gas; the bulb would have to be wired to behave like an incandescent bulb at low concentrations. We could collect brightness u as a function of voltage p and gas concentration θ produce something similar to that shown in Figure 2.1. The bifurcations at critical voltage p^* above argon concentration θ^* give rise to sudden jumps in brightness. The bifurcations separate the *on* and *off* states of the bulb and are only present in the fluorescent phenotype. The two phenotypes lie either side of the onset of bifurcations at concentration θ^* . We can see from Figure 2.1 how knowing the locations of bifurcations allows us to organise qualitative behaviours and hence phenotypes of the bulb.

In the biological context, we can consider changes in θ as changes in the organism genotype that may or may not lead to a new phenotype. The idea of describing phenotypes in this way has been done before by Waddington []. His epigenetic landscape is a metaphor for how changes gene regulation, in our case represented by changes in θ , determines the fate of cells. He imagines the cell as a marble, rolling down a series of forking valleys representing a differentiation cascade, eventually settling

in its final phenotype. Let us adopt this metaphor for organism behaviours in response to a controlled condition (Figure 2.2). Changing the control condition places the marble at different points in the valley and each fork in the valley corresponds to different available behaviours to the organism. Changing the parameters θ changes the topology of the valleys potentially giving rise to new behaviours and therefore new phenotypes. Due to the robustness [] and fragility [] of organisms we expect most changes in θ to either kill the organism or do nothing at all. The emerging picture suggests that the route between phenotypes is a carefully created sequence of changes in θ .

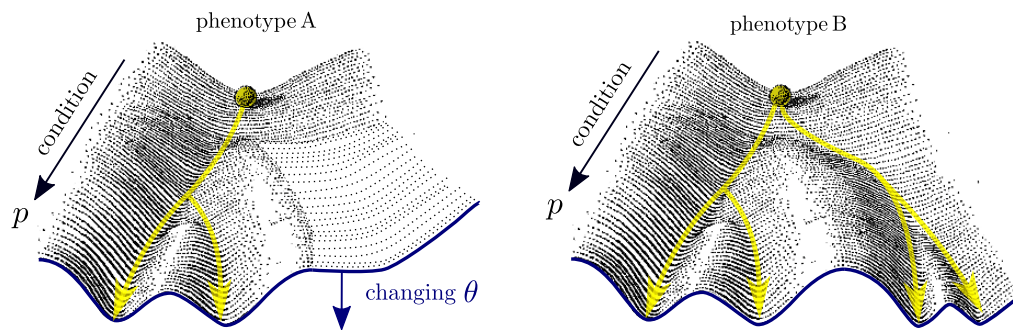


Figure 2.2: Waddington landscapes representing the set of available behaviours for two phenotypes in response to a controlled condition p . Phenotypes are related by changes in landscape topology via changes in θ

In order to enumerate the phenotype distribution in the the high-dimensional parameter space θ for a given organism we can construct a model. By parametrising such a model $F_\theta(u, p)$ by θ , we can relate the states of the organism u to experimentally controlled conditions p . Ideally a subset of u can be observed experimentally so that we may observe bifurcations in the data, as demonstrated in the right-hand panel of Figure 2.1. In the following section we shall go through a class of models that can leverage bifurcation theory.

2.1.1 Differential Equation Models

For the purposes of this thesis we will assume that the behaviour of the organism under study can be cast in terms of differential equations in N states u , M parameters θ and P control conditions p . For now we shall state the general class of models and follow up with concrete biological examples as we explore different types of bifurcations. Throughout the thesis we will consider models of the form

$$\frac{du}{dt} = F_\theta(u, p) \quad \text{where} \quad \begin{cases} F : \mathbb{R}^{N+P} \rightarrow \mathbb{R}^N \\ \theta \in \mathbb{R}^M, u \in \mathbb{R}^N, p \in \mathbb{R}^P \end{cases} \quad (2.1)$$

The total derivative $\frac{du}{dt}$ gives us the rate of change of the states with respect to time t and all variables have been vectorised with the appropriate dimension. In principle the right-hand-side F_θ can be arbitrarily complicated, containing spatial derivatives or even machine learning models such as neural networks. We shall see later when such models become relevant in biomedical modelling.

2.1.1.1 Trajectories & Field Geometry

In principle once equations (2.1) have been written down they can be integrated to obtain trajectories $u(t)$ for various initial conditions $u(t')$. We can write the solution down formally as

$$u(t) = u(t') + \int_{t'}^t F_\theta(u(s), p) ds \quad (2.2)$$

Here the integral reveals that in order to determine where the state is at time t we need to sum all the contributions of the function F_θ from the initial time t' all the way up to final time t . The function F_θ depends on the state u and must be updated with the integration variable s . This calculation can be interpreted, as shown in Figure 2.3, as choosing an initial point $u' = u(t')$ in a vector field F_θ and following the field lines until time t at which the final point $u = u(t)$ has been reached.

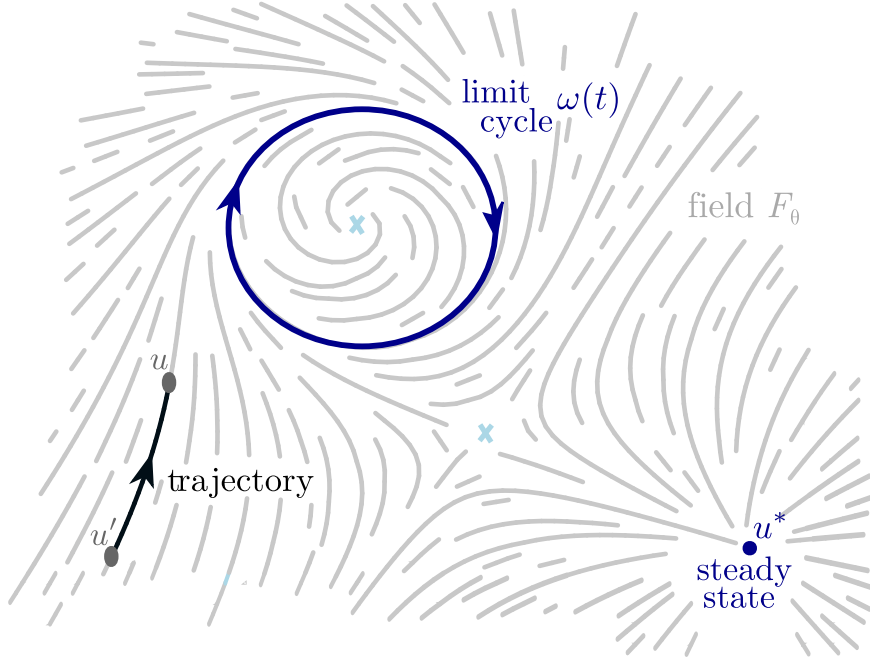


Figure 2.3: Illustration of a trajectory between $u = u(t)$ and $u' = u(t')$ over finite time $t - t'$ following the field lines of F_θ . In this example field lines either point towards steady state u^* or a limit cycle $\omega(t)$. There are two unstable fixed points marked by crosses: a saddle point separating the basins of attraction and an unstable focus enclosed by the limit cycle.

By considering the geometry of the field F_θ in state space we can determine the fate of sets of trajectories, which are ultimately pulled towards *dynamical attractors*. Such attractors can be static steady states u^* or dynamic like the limit cycle $\omega(t)$ illustrated in Figure 2.3. *Dynamical attractors* create basins of attraction defined as regions of state space in which trajectories are pulled towards the same stable structure. These basins must be separated by unstable structures, such as the saddle point marked by a cross in Figure 2.3, which define a boundary between the basins called the separatrix. Note that the direction of the field F_θ and not its magnitude $|F_\theta|$ determines the fate of a trajectories.

When equations (2.1) describe the behaviours of an organism, the attractors determine the set of qualitative behaviours available to the organism of genotype θ , whilst experiencing experimental conditions p . If changes to the genotype θ change the number, type or stability of the at-

tractors then we will observe new qualitative behaviours and hence a new phenotype. If changes to conditions p lead to changes in the state space geometry, this is interpreted as a different behavioural state available to the same phenotype. We can see therefore how casting a biomedical problem into the language of differential equations, allows us to characterise phenotypic traits with the geometry of attractors in state space.

2.1.1.2 The Jacobian Matrix

In order to quantify the geometry of a local patch of state space u we can imagine F_θ as a velocity field of water and place a tiny blob of ink surrounding the location u . The so called Jacobian matrix $\frac{\partial F_\theta}{\partial u}$ of partial derivatives at the location u transforms the basis vectors $\hat{u}(t)$ defining the blob over a short period of time Δt as depicted in Figure 2.4. The transformation is

$$\hat{u}(t + \Delta t) = \left(\mathbb{1} + \frac{\partial F_\theta}{\partial u} \Delta t \right) \hat{u}(t) \quad \text{where} \quad \hat{u} \in \mathbb{R}^N \quad \frac{\partial F_\theta}{\partial u} \in \mathbb{R}^{N \times N} \quad (2.3)$$

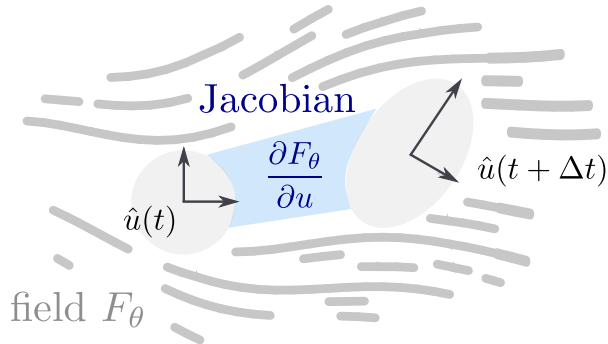


Figure 2.4: Illustration how the Jacobian matrix $\frac{\partial F_\theta}{\partial u}$ transforms the basis vectors $\hat{u}(t)$ defining a small patch of initial conditions for a short period of time Δt . The eigenvalues λ and eigenvectors \hat{v}_λ define the deformation of the patch

where $\mathbb{1}$ is the identity matrix. The eigenvalues λ and eigenvectors \hat{v}_λ of the Jacobian reveal to us the magnitudes and directions of the stretching or squeezing of the blob. We can diagonalise the Jacobian to obtain the eigenvalues and eigenvectors at any state space location u to quantify the local geometry of the field. The eigenvalue equation is written as

$$\lambda \hat{v}_\lambda = \frac{\partial F_\theta}{\partial u} \hat{v}_\lambda \quad \text{where} \quad \hat{v}_\lambda \in \mathbb{R}^N : |\hat{v}_\lambda| = 1 \quad (2.4)$$

where the eigenvectors are normalised to have unit magnitude. We can take the limit $\Delta t \rightarrow 0$ of equation (2.3) to obtain a first order matrix differential equation for the evolution of basis vectors $\hat{u}(t)$ in any patch u

$$\frac{d\hat{u}}{dt} = \frac{\partial F_\theta}{\partial u} \hat{u} \quad (2.5)$$

The coefficients given by the Jacobian matrix are time-independent and therefore the general solution can be written as a matrix exponential

$$\hat{u}(t) = e^{\frac{\partial F_\theta}{\partial u}(t-t')} \hat{u}(t') \quad (2.6)$$

where $\hat{u}(t')$ are the basis vectors that define the initial shape of the blob centred on location u . If we let the basis for the initial blob be parallel to the eigenvectors \hat{v}_λ of the Jacobian, then the evolution any vector $\sigma(t)$ within the blob expressed in its basis becomes the linear superposition

$$\sigma(t) = \sum_{\lambda} \hat{v}_{\lambda} \sigma_{\lambda}(t') e^{\lambda(t-t')} \quad (2.7)$$

where $\sigma_{\lambda}(t')$ are the initial components of the vector in the basis of the blob. This equation reveals explicitly how the sign of real parts to eigenvalues $\Re\lambda$ determine the exponential growth or shrinkage of the blob in the direction \hat{v}_λ . The imaginary parts $\Im\lambda$ determine the magnitude of rotations of the blob. Note that since the Jacobian matrix is real and eigenvalues and eigenvectors appear in conjugate pairs and therefore the overall evolution (2.7) yields real transformations of blob vectors $\sigma(t)$. The transformation (2.3) an approximation of the time-ordered exponential transformation [] and we should note that the results stated here are valid for small blobs $|\sigma(t)| \ll 1$ over short timescales $|t - t'| \ll 1$.

2.1.1.3 Time Ordered Exponentials

In this section we go a bit deeper into the origin of transformation (2.3) for those who are interested the evolution of state space blobs over arbitrary time intervals. We begin by considering the evolution of the separation between a trajectory $u(t)$ and its perturbation $u(t) + \delta u(t)$

$$\frac{d}{dt}(u + \delta u) = F_\theta(u + \delta u, p) \quad (2.8)$$

After Taylor expanding the field F_θ and recognising that equations (2.1) lead to a cancellation in the terms involving the unperturbed trajectory u we arrive at

$$\frac{d}{dt}(\delta u) = \left. \frac{\partial F_\theta}{\partial u} \right|_{u=u(t)} \delta u + \mathcal{O}(\delta u^2) \quad (2.9)$$

where $\frac{\partial F_\theta}{\partial u}$ is the Jacobian of the field and additional terms $\mathcal{O}(\delta u^2)$ involve taking higher order derivatives of the field F_θ . Choosing a perturbation sufficiently small such that we can ignore higher order terms yields a first order homogenous ordinary matrix differential equation of the form $\dot{\delta}u(t) \approx J(t)\delta u(t)$ where $J(t)$ is a time-varying Jacobian. These equations can be solved formally with time-ordered matrix exponentiation []

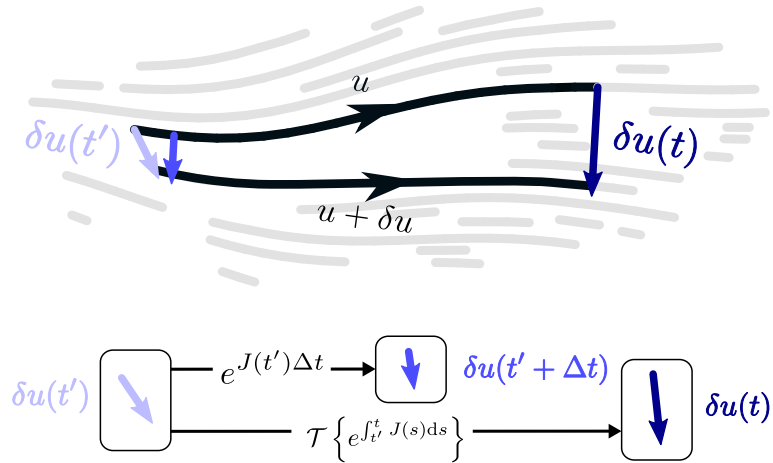


Figure 2.5: Illustration how the time ordering operator $\mathcal{T}\left\{e^{\int_{t'}^t J(s) ds}\right\}$ propagates the separation $\delta u(t)$ between adjacent trajectories u and $u + \delta u$ by repeated application of the exponentiated Jacobian $e^{J(t)\Delta t}$ evaluated along trajectory $u(t)$

$$\delta u(t) \approx \mathcal{T} \left\{ e^{\int_{t'}^t J(s) ds} \right\} \delta u(t') \quad \text{where} \quad J(t) := \frac{\partial F_\theta}{\partial u} \Big|_{u=u(t)} \quad (2.10)$$

The time-ordering defines an ordered product of matrix exponentials

$$\mathcal{T} \left\{ e^{\int_{t'}^t J(s) ds} \right\} := \lim_{\Delta t \rightarrow 0} \left(e^{J(t)\Delta t} e^{J(t-\Delta t)\Delta t} \dots e^{J(t'+\Delta t)\Delta t} e^{J(t')\Delta t} \right) \quad (2.11)$$

which can be calculated by repeated exponentiation of the Jacobian $e^{J(t)\Delta t}$ evaluated at different times along the unperturbed trajectory $u(t)$. Although this expression may look complicated it is just another matrix whose eigenvalues reveal whether the trajectories diverge $|\delta u(t \rightarrow \infty)| \rightarrow \infty$ or converge $|\delta u(t \rightarrow \infty)| \rightarrow 0$.

In situations where we want to investigate field flow over longer time intervals or where there is an explicit time dependence in the field $F_\theta(u, p, t)$ we must use the time-ordered exponential (2.11) in place of the exponentiated Jacobian.

2.1.1.4 Lyapunov Exponents

Sometimes we are only interested in the rate of change of the magnitude of deformations $|\sigma(t)|$ which can be quantified by the *finite time lyapunov exponent*

$$\Lambda(u, \Delta t) := \frac{1}{\Delta t} \log \frac{|\sigma(t + \Delta t)|}{|\sigma(t)|} \quad (2.12)$$

We remind ourselves that the blob $\sigma(t)$ is centred around state space point u , then evolved for a time Δt and therefore the exponent is a function of Δt and u . Substituting equation (2.7) we arrive at

$$\Lambda(u, \Delta t) = \frac{1}{2\Delta t} \log \left\langle e^{2\Re[\lambda]\Delta t} \right\rangle_{\sigma(t)} \geq \langle \Re[\lambda] \rangle_{\sigma(t)} \quad (2.13)$$

where $\langle \dots \rangle_{\sigma(t)}$ is a shorthand for a weighted arithmetic average over the components of the initial blob $\sigma(t)$. We have used Jensen's Inequality [] to

show that the rate of distortions is bounded by the average of real parts of eigenvalues. This bound becomes an equality for eigenvalue λ when the blob $\sigma(t)$ is initialised along only its eigenvector \hat{v}_λ . We will see later how the *Lyapunov exponents* are useful for extracting timescales around interesting structures in state space such as *fixed points* and *degeneracies*.

2.1.1.5 Fixed Points

Thus far we explored the field geometry in arbitrary patches of state space u and asked questions about local flows. It is usually not possible to set up experimental conditions to get an organism to trace out all of its available states without killing it or distorting the mechanism under study. An organisms prefers to operate within a finite set of states and would want to return to them when perturbed. In biology this is known as *homeostasis* and in the context of dynamical systems this is a stable steady state u^* which belongs to a wider class of points called *fixed points*. In the context of differential equation models, a *fixed point* is the solution of

$$\frac{du}{dt} \Big|_{u=u^*} = F_\theta(u^*, p) = 0 \quad (2.14)$$

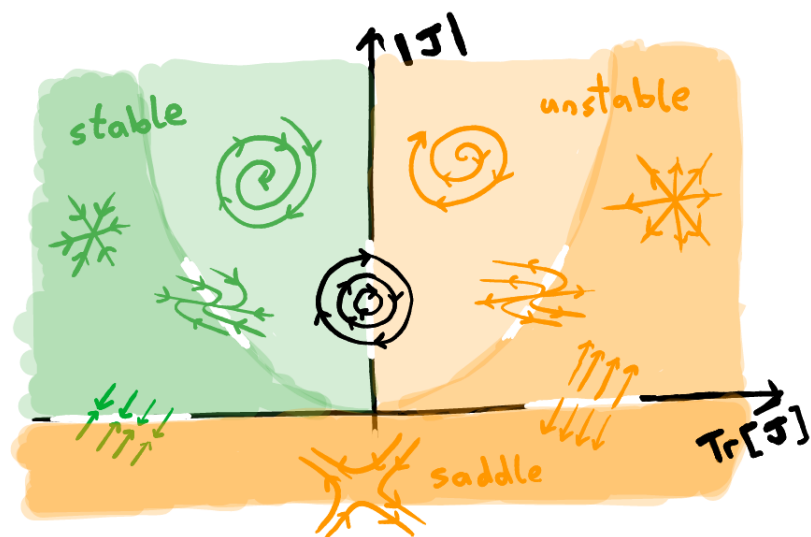


Figure 2.6: Classification of stable and unstable fixed points for a general two dimensional systems in terms of trace $\text{Tr}\left[\frac{\partial F_\theta}{\partial u}\right]$ and determinant $|\frac{\partial F_\theta}{\partial u}|$ of its Jacobian

By looking at the eigenvalues of the Jacobian, which determine local flows according to equations (2.7), we can classify the fixed point u^* . The sign of real parts $\Re\lambda$ determine whether small perturbations away from the fixed point will diverge. This defines whether the point is *stable*, *unstable* or a *saddle*. Non-zero imaginary parts $\Im\lambda \neq 0$ give rise to damped oscillation around the point; these points are called *foci*. Without real parts the flow becomes purely rotational and give rise to *cycles*.

For a two dimensional system we can express the two eigenvalues of the 2×2 Jacobian in terms of its trace $\text{Tr}[\frac{\partial F_\theta}{\partial u}]$ and determinant $|\frac{\partial F_\theta}{\partial u}|$ which allows us to conveniently reveal all the possible fixed points types, as in Figure 2.6. If at least one the eigenvalues vanishes the fixed point becomes *degenerate*. We shall see that *degenerate* field flows lead to critical slowing down in dynamics, reveal bifurcations and are useful for constructing tangent fields to implicitly defined surfaces.

2.1.1.6 Field Degeneracy

A field F_θ can be called *degenerate* where it is locally constant and hence does not cause shape changes to a blob of initial conditions in one or more directions. This means that one or more of the eigenvalues of the Jacobian vanish $\lambda = 0$ and have associated eigenvectors \hat{T}_λ tangent to the direction where the field is locally constant. Suppose the field is *degenerate* at point u^- , then the vanishing eigenvalues lead to a zero determinant $\left| \frac{\partial F_\theta}{\partial u} \right| = 0$ and the eigenvectors must be orthogonal to all the gradients

$$\left| \frac{\partial F_\theta}{\partial u} \right|_{u=u^-} = 0 \quad \frac{\partial F_\theta}{\partial u} \Big|_{u=u^-} \hat{T}_\lambda = 0 \quad \text{where} \quad \hat{T}_\lambda \in \mathbb{R}^N : |\hat{T}_\lambda| = 1 \quad (2.15)$$

The eigenvector equation yields \hat{T}_λ that span the degenerate subspace at field location u^- . The number of vectors and hence the size of the subspace is given to us by the number of vanishing eigenvalues $\lambda = 0$. In linear algebra this would be referred to as the *nullspace* or *kernel* of the Jacobian matrix. A vanishing determinant means that the Jacobian is not invertible.

2.1.1.7 Critical Slowing Down

Lets us consider the magnitude of deformations along the degenerate direction $T_\lambda(t)$ in the vicinity of the the region $u \approx u^-$ that is driven by the scalar sub-field F_λ . We expect the first-order derivatives to vanish $\frac{dF_\lambda}{dT_\lambda} \Big|_{u=u^-} = 0$ and therefore have to expand the field F_λ to an order n that will yield the first non-zero derivative. The equations expanded for $u \approx u^-$ are

$$\frac{dT_\lambda}{dt} = \frac{dF_\lambda}{dT_\lambda} \Big|_{u \approx u^-} T_\lambda(t) + \frac{1}{n!} \frac{d^n F_\lambda}{dT_\lambda^n} \Big|_{u \approx u^-} T_\lambda(t)^n + \mathcal{O}(T^{n+1}) \quad \text{where } n \geq 2 \quad (2.16)$$

Here we kept the first-order derivative because we would still like to see how the dynamics scales with time as we approach to degeneracy. This is a Bernoulli differential equation [] with constant coefficients and has a general solution

$$T_\lambda(t) = \left(\left(T_\lambda(t') e^{(t-t') \frac{dF_\lambda}{dT_\lambda} \Big|_{u \approx u^-}} \right)^{1-n} - (t-t') \frac{n-1}{n!} \frac{d^n F_\lambda}{dT_\lambda^n} \Big|_{u \approx u^-} \right)^{\frac{1}{1-n}} \quad (2.17)$$

This equation reveals two timescales for blob deformations in the vicinity of a field degeneracy: the familiar exponential timescale $e^{t-t'}$ and a new polynomial timescale $(t-t')^{\frac{1}{1-n}}$. The emergence of a polynomial timescale that dominates over the exponential is called *critical slowing down* and is a marker of degeneracy. We can see once the dynamics is confined to the degenerate subspace the eigenvalues of the Jacobian are insufficient for determining the timescales. The curvature of the field around the degenerate subspace drives the polynomial dynamics, and therefore higher-order derivatives are needed to reveal this.

This critical slowing can be observed in data when *fixed points* become *degenerate*. Degenerate fixed points are also called *critical points*. The transition between these two timescales in data is a signal that a *critical point* is nearby. We will see that *critical points* may lead to bifurcations and bifurcations are always accompanied by degeneracies in the field.

2.1.1.8 Fluctuations

Biological processes can be intrinsically noisy and the measurement apparatus can also introduce errors. Fortunately we can model such non-deterministic aspects by extending equations (2.1) to a Langevin equation

$$\frac{du}{dt} = F_\theta(u, p) + \eta(t) \quad \text{where} \quad \eta(t) \sim \mathcal{N}(\mu = 0, \Sigma = \mathbb{1}D) \quad (2.18)$$

The stochastic process $\eta(t)$ is a zero-mean white noise with equal variance D along all N dimensions resultant from a large number of independent processes such as Brownian motion and Poisson shot noise. We can apply the Kramers-Moyal expansion [] to transform this equation into an equivalent Fokker-Planck equation for the probability distribution P_θ

$$\frac{dP_\theta}{dt} + \frac{\partial}{\partial u} \cdot J_\theta = 0 \quad \text{where} \quad J_\theta := \left(F_\theta(u, p) - \frac{D}{2} \frac{\partial}{\partial u} \right) P_\theta \quad (2.19)$$

Here we cast the Fokker-Planck equation as a continuity equation with the divergence of probability current J_θ balancing the total change in probability $\frac{dP_\theta}{dt}$. In the scenario where at steady state $\frac{dP_\theta}{dt} = 0$ there are also no circulating probability currents $J_\theta = 0$ then we can solve for the distribution

$$P_\theta(u, p) = \frac{1}{Z} e^{\frac{2}{D} \int^u F_\theta(u', p) \cdot du'} \quad \text{where} \quad Z := \int_{\mathbb{R}^N} e^{\frac{2}{D} \int^u F_\theta(u', p) \cdot du'} du \quad (2.20)$$

Expanding the distribution in the vicinity of a stable fixed point gives rise to a multivariate Gaussian distribution whose covariance matrix Σ is the inverse of the Jacobian evaluated at the fixed point

$$P_\theta(u, p) \sim e^{-\frac{1}{2}(u-u^*)^\top \Sigma^{-1}(u-u^*)} \quad \text{where} \quad \Sigma^{-1} = -\frac{2}{D} \frac{\partial F_\theta}{\partial u} \Big|_{u^*} \quad (2.21)$$

We learn that accompanying the *critical slowing down* (2.17) we also have the divergence of variance along the degenerate direction. These are the two main observations that accompany bifurcations and have a deep relationship to the theory of phase transitions [].

2.1.1.9 Limit Cycle Analysis

Thus far we dealt with static state space structures like *fixed points*. We found that the eigenvalues of the Jacobian are sufficient for their characterisation, unless the field is *degenerate*, in which case higher order derivatives of the field must be investigated.

If fields lines point towards a region of state space but the region *does not* contain any fixed points, then the only other option is for the field lines to converge onto a *limit cycle*. This is actually a rough statement of the Poincaré-Bendixson theorem which allows us to define trapping regions where trajectories do not escape from and make statements about the existence or non-existence of limit cycles. A limit cycle must also enclose a finite number of *unstable foci* that push trajectories away from its center.

Newton-type methods can easily be applied to find *fixed points* because they are local structures in fields. Limit cycles are much more tricky because it is not possible to know whether a local state part of a limit cycle or not before we have seen a trajectory visit that state twice: once at $u(t)$ and then again $u(t + T)$ after some time T . This forms the basis of some optimisation methods for computing limit cycles [].

- Trapezoid method
- Collocation method
- Shooting method

2.1.2 Bifurcation Analysis

We have surveyed sufficiently many state space structures, the geometry of which determine the qualitative behaviour of the organism we are describing. An organism has many qualitative behaviours in response to conditions p and many phenotypes emerging from changes in θ .

Bifurcations are defined as qualitative changes to system behaviour in response to smooth changes to some conditions. In our setting these conditions could be either θ or p , but we will focus on changes with respect to p with the understanding that the analysis is equally valid for θ . We are ready to present the two *generic* and *robust* one parameter bifurcations: the *saddle-node* and *Hopf* bifurcation. These bifurcations are generic in the sense that they happen in N dimensional systems, but can be described as happening along one dimension. This is true because of centre manifold theory []. The bifurcations are *robust* in the sense that small changes to system parameters do not destroy the bifurcation. This is not the case for *pitchfork* and *transcritical* bifurcations which we will present in a separate section.

2.1.2.1 Generic Robust Bifurcations

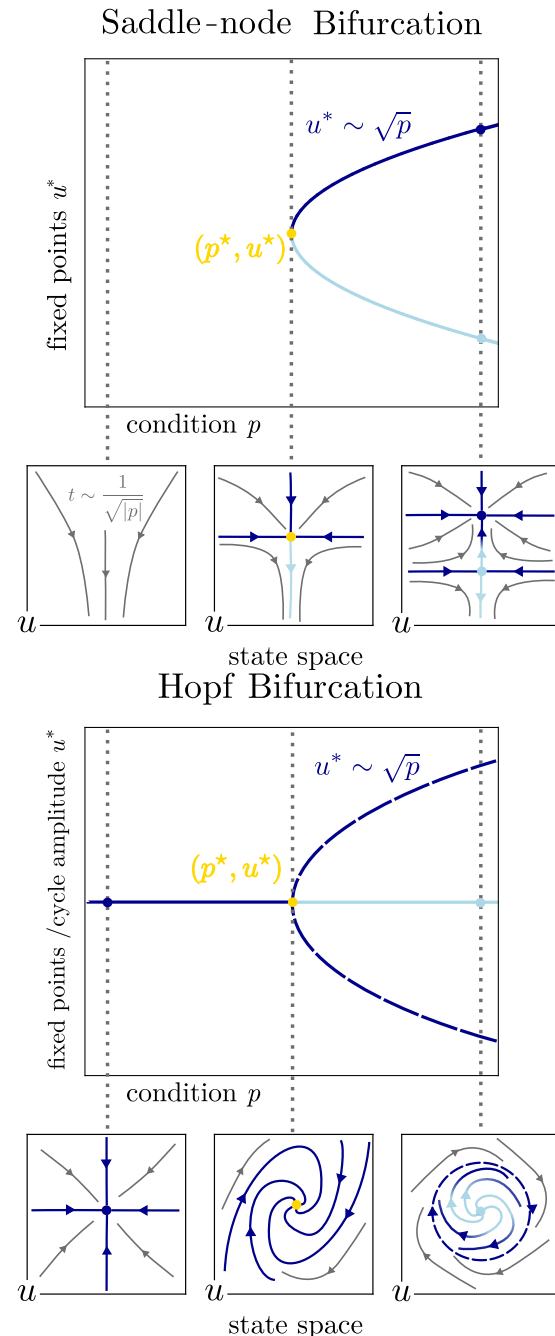


Figure 2.7: Generic and robust bifurcations. A. *Saddle-node* bifurcations create or annihilate stable and unstable pairs of fixed points. B. In *Hopf* bifurcations a stable fixed point becomes an unstable focus that pushes trajectories towards a limit cycle.

2.1.2.2 Fragile Bifurcations

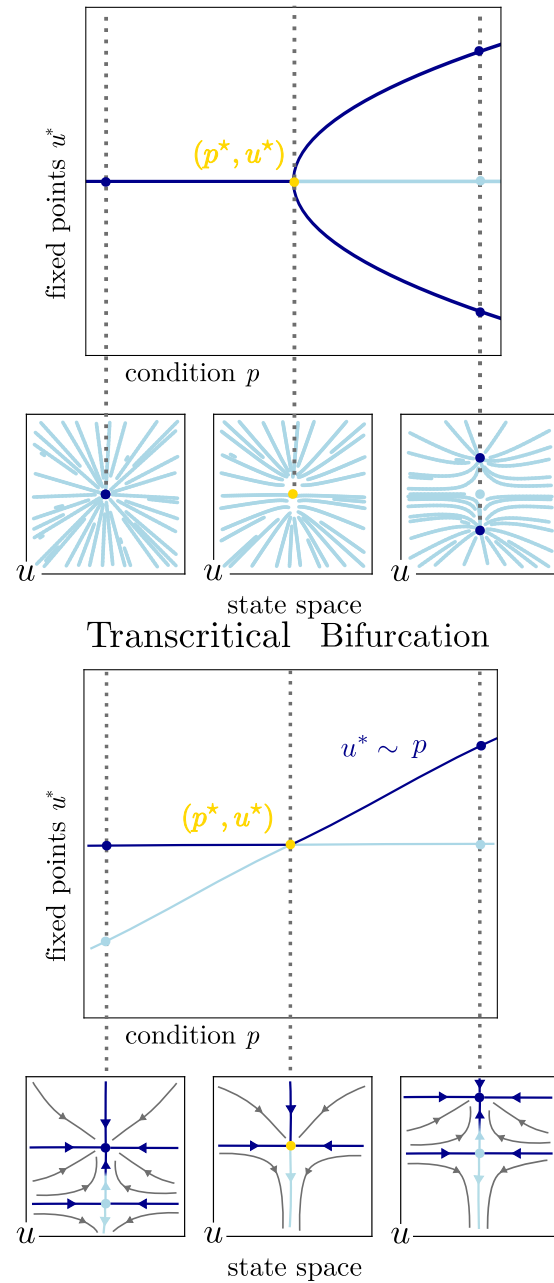


Figure 2.8: Fragile bifurcations

2.1.2.3 Global Bifurcations

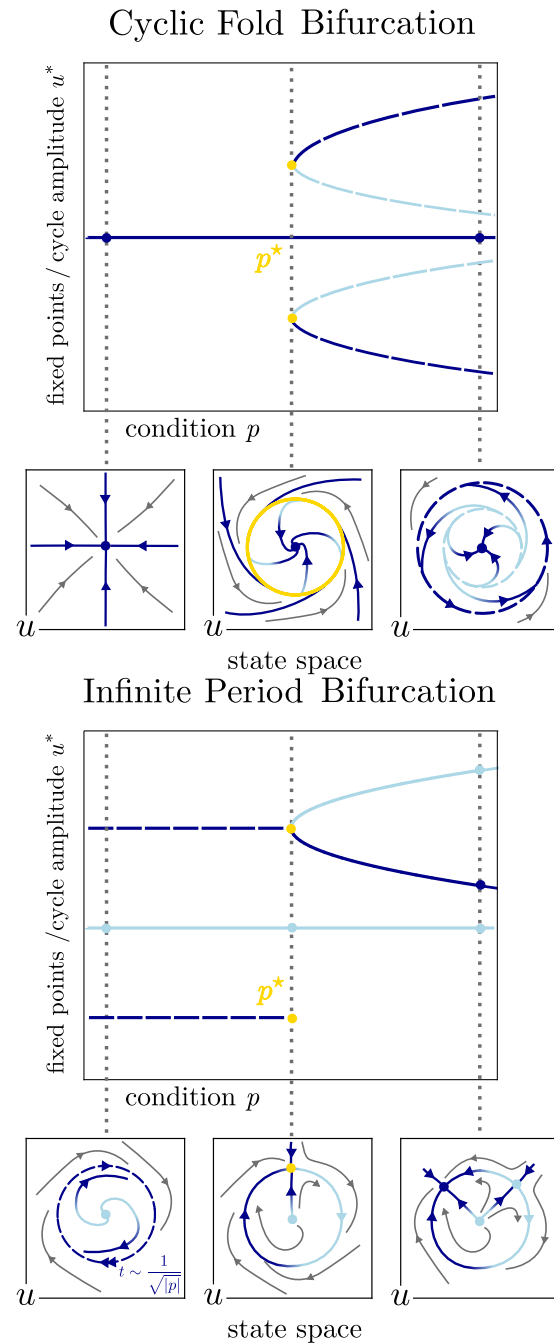


Figure 2.9: Global Bifurcations

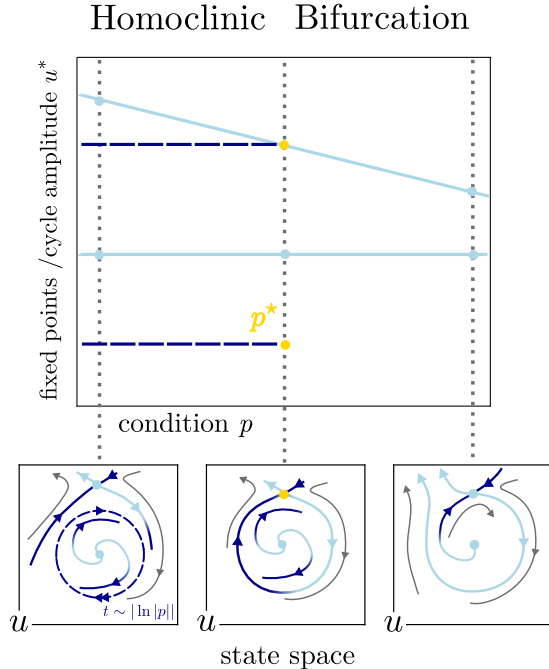


Figure 2.10: Homoclinic Bifurcation

2.1.2.4 Higher Co-dimension

- cusp and Bogdanov-Takens
- centre manifold theory

2.1.2.5 Numerical Methods

In this thesis we extensively use the library `DifferentialEquations.jl` [22] for numerically solving differential equations and `BifurcationKit.jl` [23] for calculating bifurcation diagrams.

- Parameter Continuation
- Marching cubes

2.1.3 Spatially Extended Systems

If F_θ contains spatial derivatives, additional conditions on u with respect to spatial variables $x \in \mathbb{R}^D$, where D is the dimension of the space considered, must be supplied to give a unique solution $u(x, t)$. When studying

spatio-temporal dynamics of organisms, a popular choice is to incorporate a diffusive term that models the exchange of matter between spatial locations

2.1.3.1 Turing Bifurcations

Here we first introduce diffusion macroscopically by simply adding the laplacian to mean field equation. We introduce the turning bifurcation and show how linear stability analysis is insufficient to capture pattern formation and rich inhomogeneous steady states. A promising approach may be geometrisation of the moving local equilibria [20].

2.2 Applications in Cell Biology

In this section we apply the dynamical systems theory outlined in Section 2.1 to concrete biochemical systems and provide the reader with sufficient background to understand the goals of the incorporated publication in Chapter 3.

2.2.1 Genetic Switches & Phenotype Boundaries

Every cell belonging to an organism has essentially the same genetic information inside it. In spite of this, a wide variety of cell populations such as neurons, muscle cells, immune cells and tissue specific cells interact in a highly regulated fashion. As an organism develops, how do cells which used to be identical differentiate into functionally distinct populations? How are boundaries between these populations maintained? Can these boundaries be controlled with genetic engineering?

In order to address these questions the paradigm of the *genetic switch* emerged. Genes are either expressed into proteins or not. The concentration of proteins within a cell and on its membrane determine its function and communication abilities with other cells. The genes that are turned *on* or *off* when a cell is exposed to different environments determine the cell phenotype. Genes switching between *on* and *off* in response to other genes or proteins is called *gene regulation*.

The first gene regulatory network that was discovered is the *lac operon* in the bacterium *Escherichia coli* [24]. In this network, enzymes that metabolise lactose are expressed only in the presence of lactose and absence of glucose. This regulation evolved because metabolising lactose is energetically more expensive and having the *lac* genes always turned *on* would be a waste of resources. An outline of how this network works is shown with in Figure 2.11. The main proteins involved in this mechanism are the *Lac Repressor* and β -*galactosidase* which are transcribed and translated from the *LacI* and *LacZ* genes respectively. The repressor binds to the operator which sits between the promoter and coding region *LacZ*.

When the transcription machinery binds to promoter region, it is blocked from transcribing *LacZ*. When lactose is present, binding to the repressor causes a conformational change which leads to unbinding of the complex from the DNA. Thus in the presence of lactose, *LacZ* is turned *on* and β -galactosidase is produced by the cell. In this setting lactose is referred to as the *effector*. We note that the effector of *LacZ* is actually *allolactose* which arises from the transglycosylation of lactose by β -galactosidase but for the purposes of introducing the genetic switch we need not focus in this detail. β -galactosidase hydrolyses lactose, breaking it down into glucose and galactose which decreases the overall concentration of lactose available to bind to the repressor. Eventually all the lactose is broken down and the repressors turn *off* the *LacZ* gene.

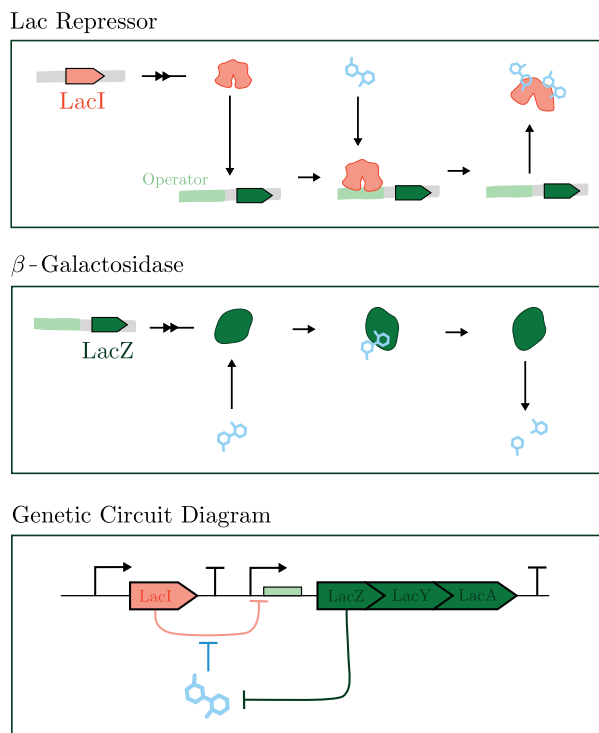
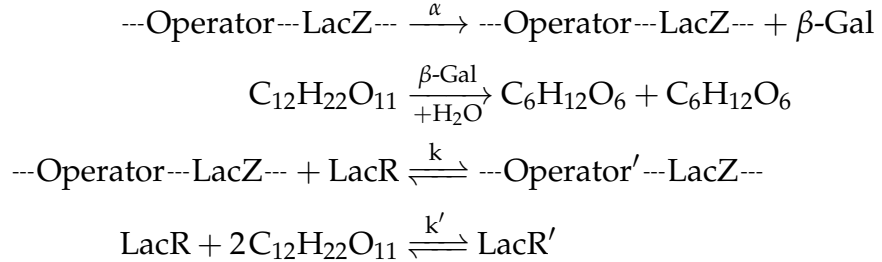
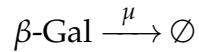


Figure 2.11: Overview of the *lac* operon

Let us first consider what happens within a single cell of constant volume. We assume the rate α of transcription and translation of *LacZ* into β -Gal is constant unless the operator region is blocked by *LacR*. The repressor is inactivated by the binding of two (allo)lactose molecules $C_{12}H_{22}O_{11}$.



Proteins degrade over some finite half-life μ we also have



The equilibrium dissociation constants k, k' define the binding affinity of $LacR$ to the operator and its effector respectively. Let rate β be the rate of hydrolysis of lactose by β -Gal. These rates are determined by molecular details, some of which can be modulated with genetic engineering. Changing the promoter sequences, for example, can modulate the rate α . Thus it makes sense to collect these rates into our model parameter $\theta = (\alpha, \beta, k, k')$. Let the concentration of the effector be the experimentally controlled condition $p = [\text{C}_{12}\text{H}_{22}\text{O}_{11}]$ and the remaining concentrations be collected in state vector $u = (\text{LacZ}, \text{LacR}, \text{Gal})$.

From this set of reactions it is possible to write down a *chemical master equation* [25, 26] whose *mean field approximation* yields a set of ordinary differential equations of the form (2.1) which are commonly referred to as *reaction rate equations*. This procedure is equivalent to the mass-action assumption used in chemistry. We note that the two major assumptions here are: a thermodynamic limit where the number of molecules is sufficiently large such that correlations due to discreteness can be ignored and a sufficiently *well mixed* cytoplasm so that we do not have to model space.

The *reaction rate equations* for the Lac operon become

$$\begin{aligned}\frac{d}{dt}\text{LacR} &= \text{LacR}' - \frac{p^2}{2}k'\text{LacR} + \text{LacZ}' - k\text{LacR}\text{LacZ} \\ \frac{d}{dt}\text{LacR}' &= -\text{LacR}' + \frac{p^2}{2}k'\text{LacR}\end{aligned}\quad (2.22)$$

$$\begin{aligned}\frac{d}{dt}\text{LacZ} &= \text{LacZ}' - k\text{LacR}\text{LacZ} \\ \frac{d}{dt}\text{LacZ}' &= -\text{LacZ}' + k\text{LacR}\text{LacZ}\end{aligned}\quad (2.23)$$

$$\begin{aligned}\frac{d}{dt}\text{Gal} &= \alpha\text{LacZ} - \mu\text{Gal} \\ \frac{dp}{dt} &= 2\text{LacR}' - p^2k'\text{LacR} - \beta p\text{Gal}\end{aligned}\quad (2.24)$$

We can see two mass conservations: the total concentration of the LacZ gene and total concentration of LacR. We can write down the conservation laws normalised such that the total concentrations add up to one

$$\text{LacR} + \text{LacR}' + \text{LacZ}' = 1 \quad (2.25)$$

$$\text{LacZ} + \text{LacZ}' = 1$$

Substituting conservation laws (2.25) into equations (2.22) and (2.23) allows us to close them and solve for the fraction of unbound LacZ available for transcription

$$\text{LacZ}(p) = \frac{1}{\frac{1}{2} + \sqrt{\frac{1}{4} + \frac{k}{1+\frac{1}{2}k'p^2}}} \quad (2.26)$$

This is a *Hill-type* term that yields a basal level of transcription $\text{LacZ}(p = 0) \sim k^{-\frac{1}{2}}$ saturates at $\text{LacZ}(p \rightarrow \infty) = 1$ with k' controlling the slope of the curve. We can now plot a vector field for equations (2.24) (Figure 2.12) revealing the dynamics between (allo)lactose and β -Gal. We can see that

for any initial concentration p and basal concentration Gal^* the presence of p stimulates more production of Gal which in turn decreases the concentration of $p \rightarrow 0$ at which point the basal expression Gal^* is reached again. This is the simplest example of *gene regulation* in response to environmental conditions but there is nothing *switch-like* about it. The *lac operon* maintains a single point of homeostasis (p^*, Gal^*) defined by

$$\frac{d}{dt}\text{Gal} \Big|_{p^*, \text{Gal}^*} = \alpha \text{LacZ}(p^*) - \mu \text{Gal}^* = 0 \quad (2.27)$$

$$\frac{dp}{dt} \Big|_{p^*, \text{Gal}^*} = -\beta p^* \text{Gal}^* = 0 \quad (2.28)$$

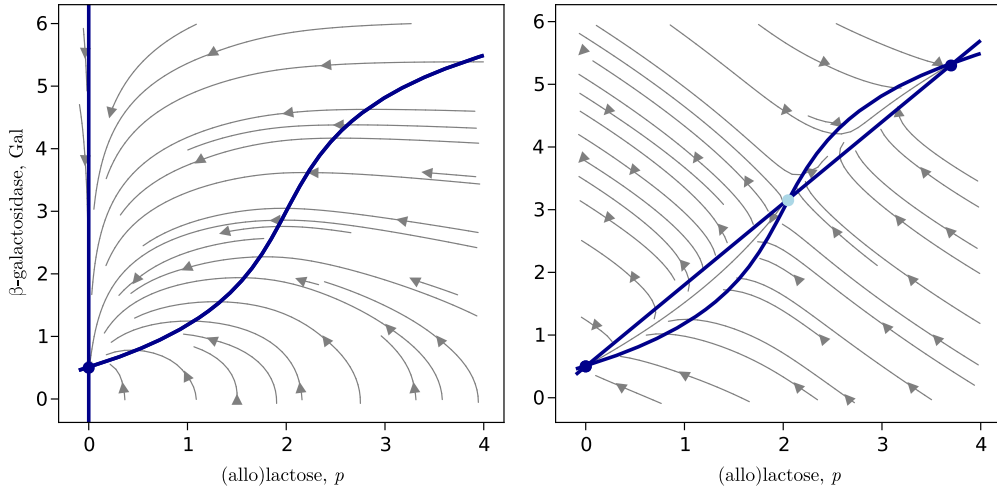


Figure 2.12: Monostable and bistable behaviour in the lac operon

In order to trigger the *switch-like* behaviour we must engineer the dynamics defining the lactose (2.28) such that it defines a curve intersecting the *Hill-type* function three times (Figure 2.12). Mathematically we suppose there exists some $f(p, \text{Gal})$ such that

$$\frac{dp}{dt} = -\beta p \text{Gal} + f(p, \text{Gal}) \quad (2.29)$$

yields three intersections with equation (2.27). In practice f can come from additional chemical reactions introduced by genetic engineering. We shall

see how this was done with non-hydrolysable synthetic analogues of the *lac operon* in Chapter 3. The main take-away from this analysis is that whenever biochemical reactions yield *Hill*-type functions with inflection points, they tend to manifest on steady-state manifolds. This means that there is a good chance there exist chemical reactions that use it for its switching behaviour. In fact when the transglycosylation of lactose into *allolactose* is taken into account, bistable behaviour is observed [].

Now that we've understood how genetic switches can manifest within a single cell, we can begin asking questions about populations of cells. We will do this again in the *mean field approximation*, where a large population of cells can be described as a continuum of spatially extended concentrations $u(x, t)$. Some of molecules can be exchanged between cells, which gives rise to non-zero *diffusion coefficients*, while others are confined within cells. As we shall see in Chapter 3, a bistable region gives rise to sharp boundaries in gene expression. Such boundaries, their velocity and stability have been studied in the context of *travelling wave solutions* of the *Kolmogorov-Petrovsky-Piskunov equation* [].

2.2.2 Self-organised Patterns & Development

During the development of any organism a hierarchy of self-organisation takes place that leads to the breaking of symmetry from a spherical cluster of undifferentiated cells to the formation of organ segments and limbs. This process is known as morphogenesis. Figure 2.13, taken from [], shows an example in which *Hox* gene expression patterns in the body segments of *Drosophila* can drastically affect its development.

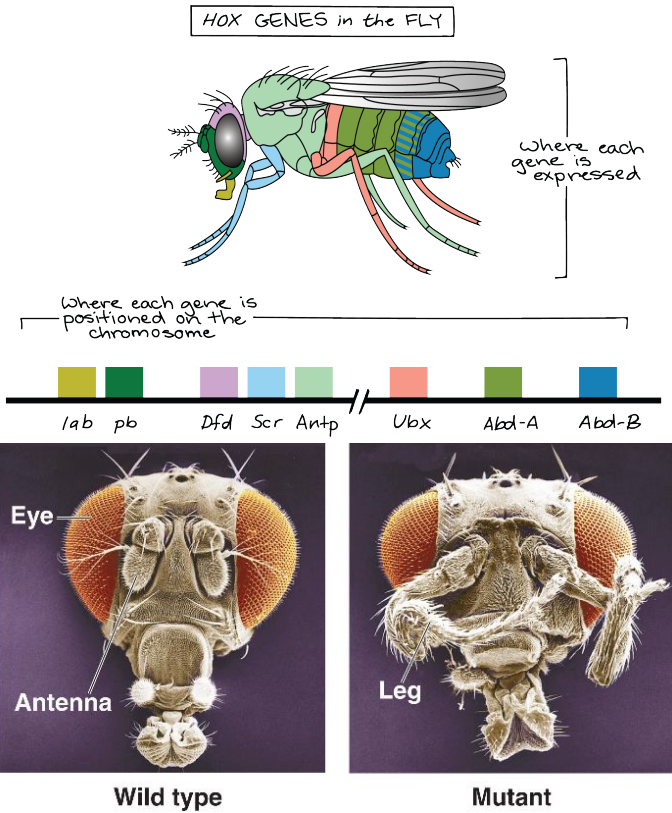


Figure 2.13: Top: *Hox* gene expression patterns in body segments of drosophila
Bottom: Mutation where legs grow in-place of antenna []

2.2.2.1 Morphogen-driven Patterns

One of the central questions in developmental biology is how positional information is sensed by a population of cells and how sharp gene expression boundaries between populations are maintained for robust organ and body segment development. The French Flag model [27] proposes that cells have a threshold response to external signalling molecules – henceforth referred to as morphogens – which pre-pattern the organism from anterior to posterior and laterally. Some examples of morphogens include Wingless, Decapentaplegic and Sonic Hedgehog. Figure 2.14 show the *Gap* expression patterns that partition the Drosophila embryo into segments which are later differentiated by *Hox* genes.

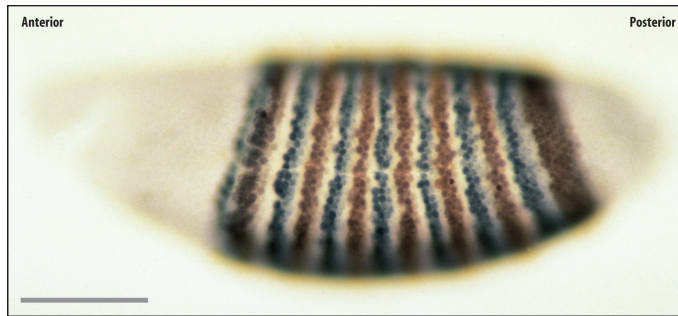


Figure 2.14: Expression patterns of pair-rule *Gap* genes in *Drosophila* embryo []

2.2.2.2 Self-organised Patterns

How are morphogen gradients set up and maintained? How can they be robust against changes in size and geometry? A canonical example of self-organisation in bacteria is the quorum sensing system [28]. Each cell secretes a signalling molecule resulting in the total concentration being proportional to the population density. This signal induces adaptive responses in metabolic and mobility in the whole colony. A long standing mathematical hypothesis that Turing patterns underlie self-organisation in cell populations. Recent literature suggests both morphogen-driven and Turing patterning mechanisms play a role in development [29]



Figure 2.15: Pigment patterns hypothesised to be generated by Turing mechanism

2.3 Phenotype Inference with Machine Learning

Thus far we have outlined how applying bifurcation analysis to a model $F_\theta(u, p)$ relating the organism state u to environmental conditions p and genotype θ can be used to distinguish its phenotypes. What do we do in circumstances where the model is partially or completely unknown? In this case, rather than deriving the functional forms relating states u from reasonable biochemical assumptions and mass-action laws, we rely on *universal function approximators* [].

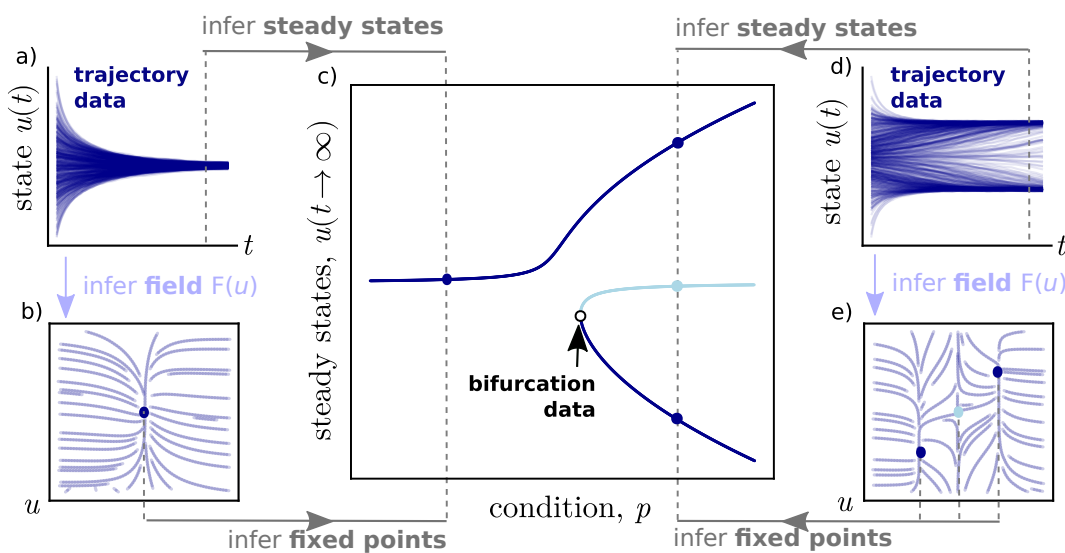


Figure 2.16: Bifurcation point extraction along the condition p via two possible routes: steady state inference (a,d→c) and fixed point inference (a,d→b,e→c). The fixed point inference route requires *universal function approximator* $F(u)$ at different values of the condition p and yields additional unstable fixed points.

When a model $F_\theta(u, p)$ is absent it becomes difficult to know which observations to collect. In the era of high-throughput biology, the solution to this is to simply collect as many observations as possible and search the high-dimensional data for mechanisms that elucidate what the organism model could be. Such data may include flow cytometry, proteomics (MS/MS), transcriptomics (scRNA-seq) metabolomics (MS) and a wide variety of next-generation sequencing data []. Thus the problem of differentiating phenotypes becomes a matter of extracting bifurcations from high dimensional *universal function approximators*.

Bifurcations along conditions p can be extracted from data via two possible routes as depicted in Figure 2.16: via a *universal function approximator* $F(u)$ which enables the location of all fixed points, including unstable ones, or via direct inference from steady state data $u(t \rightarrow \infty)$. At best we could have state trajectory data $u(t)$ like single cell trajectories extracted via segmentation and tracking in fluorescence microscopy movies (for example the data acquired using the CellASIC ONIX Microfluidic Platform in Figure 3.3c). The majority of biomedical data is sparsely sampled with respect to time (for example the flow cytometry measurements in Figure A.3 which were only collected at experiment end-points) and in such settings expecting to capture dynamical transients which would reveal the locations of unstable fixed points would be unreasonable. If we assume that the data was collected at a time where the organism is in homeostasis, then we can infer the steady states $u(t \rightarrow \infty)$ and any possible bifurcations directly from statistical measures of the data without needing a *universal function approximator* $F(u)$. The emergent picture suggests a model of the state space $F(u)$ is desirable because it fully characterises the phenotype, but requires data or prior knowledge about dynamical transients of the organism. Fortunately, as we will see, statistics on the organism in homeostasis reveal stable steady states and static bifurcations.

2.3.1 Phenotypes from Statistics in Homeostasis

Suppose we collected a high dimensional single cell omics dataset \mathcal{U} from an organism of genotype θ in various conditions p . We would like to know how many cell phenotypes there are in our dataset and how they may change in response to changes in environment p or genetic manipulation θ . Formally the data are a set of same size $|\mathcal{U}|$ as the number of cells, with an N -dimensional sample U per cell. In practice there will be missing entries as not each cell will yield the same number or quality of observations. We assume that each sample is generated by a state distribution (2.20). Not all cells share the same θ or even p and this could give rise to an unknown number of clusters around a multitude of fixed points u^* that could also depend on θ and p . We can write

$$\mathcal{U} := \{ U \mid \exists \theta, p : U \sim P_\theta(u, p) \} \quad (2.30)$$

Since we can't possibly know the distribution P_θ because that would require knowing microscopic details and deriving a reasonable model F_θ , we resort to dimensionality reduction in tandem with clustering methods to detect the phenotypes. To detect bifurcations look for regions of the data where the variance appears to diverge and we can use scaling laws from equation (2.21) to determine the type of bifurcation that is occurring and its corresponding degenerate direction.

2.3.1.1 Impute, Reduce & Cluster

While the details of particular algorithms may vary, a popular pipeline for processing high dimensional biomedical data emerged: imputation of missing values followed by a combination of clustering and dimensionality reduction []. Imputation using *nearest-neighbour methods* [], *interpolation* [] or *density sampling* [] allow merging of datasets obtained from different experimental designs. Dimensionality reduction methods such as *tSNE* [] and *UMAP* [] are used to produce two dimensional overviews of datasets

and are typically the first methods leveraged to get a feel for the global geometry of the high-dimensional point clouds. These methods also identify the highly variable feature combinations [] as well noisy features that provide any information in distinguishing cell populations []. For a suitable choice of hyperparameters these maps reveal clusters and hence the number of distinct cell sub-populations. Clustering can then be used, either in the original high-dimensional space or the reduced space to segment the clouds []. Once the dataset is clustered, in principle we've identified the modes of the steady state distribution (2.20) and differential analysis [] can be applied, together with domain knowledge, to distinguish whether any two clusters represent *different phenotypes* or *behavioural states* of the same phenotype.

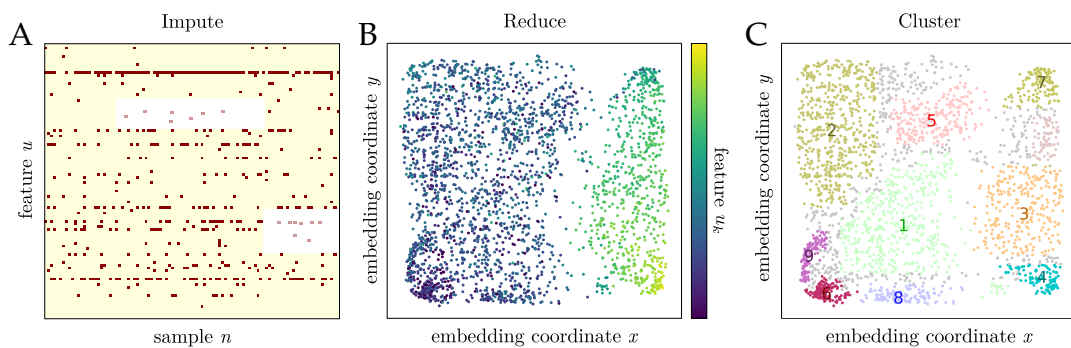


Figure 2.17: Overview of the impute, reduce & cluster methods. A. Heatmap of $N \times |\mathcal{U}|$ data matrix revealing regions of missing data that are imputed. B. Dimensionality reduction yielding an embedding which can be coloured by any feature u_k to reveal differentials between regions. C. Clustering methods yield a segmentation of the dataset into populations that share features u

By looking at the variance within each cluster as we change p we can also tell how close a population is to a bifurcation. This manifests as cluster splitting or merging with maximal variance at the splitting point. Unfortunately it would not be possible to distinguish whether a population is in a limit cycle or merely static, distributed across the states that make up the limit set. Therefore it is not possible to detect Hopf bifurcations from statistics in homeostasis.

Suppose we would like to detect saddle-node bifurcations within a bacterial cell population with respect to two experimental control conditions $p, p' \in \mathbb{R}$. We can set up a serial dilution along the columns for p and along the rows for p' in two 96-well plates. Cells allowed to grow in exponential phase in a finite concentration of either $p \ll p'$ or $p \gg p'$. Let us call this the *priming* stage of the protocol as shown in Figure 2.18a, resulting in two cell populations: p -primed cells and p' -primed cells. The priming concentrations must be chosen sufficiently high so that the resultant population states lie either side of a hypothesised cusp bifurcation. The two populations are transferred into separate 96-well plates containing the dilutions of p, p' ; we call this the *conditioning* stage in Figure 2.18a.

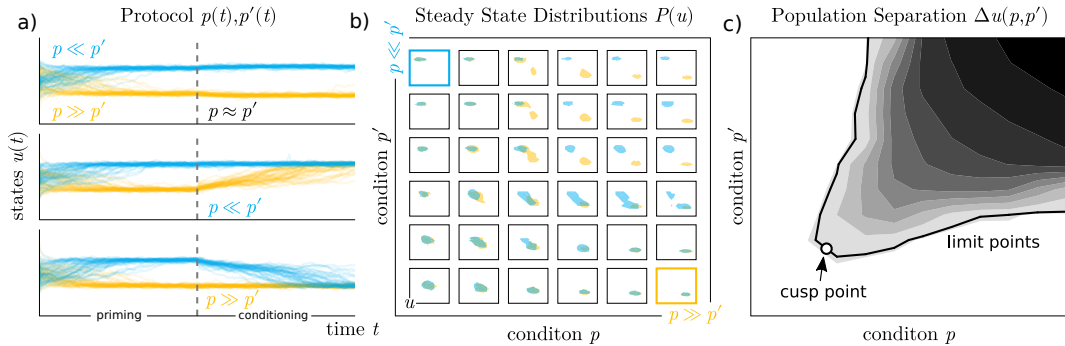


Figure 2.18: Protocols (a) for extracting limit points with respect to conditions p, p' . Steady state distributions (b). Similarity measure (c)

The cells are then transferred into a flow cytometer, gated for live singlets and processed with relevant compensation and auto-fluorescent normalisation, which would produce the population distributions $P(u)$ for the p -primed cells and $Q(u)$ for p' -primed cells in each well. By overlaying distributions $P(u), Q(u)$ for each well, a figure similar to Figure 2.18b (or Figure A.3) can be produced. Finally, the limit points can be defined by a level set of distribution similarity measure $D(P||Q)$ in the p, p' -plane as shown in Figure 2.18c. This similarity measure could be Kullback–Leibler divergence or something as simple as the distance between distribution medians. The level set must be some small positive amount ϵ above zero, picking out the onset of dissimilarity between steady state distributions

$P(u)$ and $Q(u)$, and hence the onset hysteresis. We can define the limit points as

$$\mathcal{D} = \{(p, p'): D(P||Q) = \epsilon, \epsilon > 0\} \quad (2.31)$$

This approach may break down if multi-modal distributions exist in the data. This would be the case if something happened to prevent a sub-population of cells to switch from one state another other. Reasons for this could include too much cell burden or not enough time given for cells to reach a steady state. In this case, quantifying the efficiency of switching from either side of the cusp could be a quantity of interest.

This approach would not work for extracting dynamic bifurcations such as *Hopf* since only steady state information is available. Furthermore, the accuracy of this method is subject to noise amplitude. This method works well for cases where changes in the number of stable steady states can be resolved in the measured steady state distributions.

2.3.2 Phenotypes from Machine Learning Models

Suppose we have the state as a function of time $u(t)$, sampled at sufficiently broad initial conditions $u(0)$. This would enable the estimation of field geometry $F(u)$ via *universal function approximators* such as neural networks [30] and Gaussian processes [31]. We refer the reader to a modern review of the most successful machine learning approaches for designing *universal function approximators* [32] where emphasis is made on understanding how group equivariant and group invariant transformations are stacked together. Note that we've dropped θ and p from the *universal function approximator*. We reserve θ to be a vector of biophysically meaningful parameters that make up an organism genotype. While *universal function approximators* typically have a lot of parameters, they tend not to reveal the mechanism under study and hence cannot be used to deduce which genetic design interventions can be made.

In applications where the mechanism is partially known it is possible to combine the principled microscopic derivations of reaction rate model F_θ together with some *universal function approximator* F . This is known as *grey-box modelling* [21].

2.3.2.1 Basis Functions for State Space

Suppose that rather than getting the state space geometry from trajectory data would rather specify it with high-level constraints ourselves. This may be useful in settings where we know what qualitative behaviours the model of our phenotype has but do not care about microscopic details. In this section we outline a novel basis function method for specifying state space structures, inspired by the mathematics of electromagnetism.

Suppose we would like to define a differential equation model whose trajectories approach a given limit set $\partial\Omega$, which are typically either limit cycles or fixed points. We can define a norm from any point u to the set

$$|u - \partial\Omega| := \min_{u' \in \partial\Omega} |u - u'| \quad (2.32)$$

which can be used as a scalar potential that generates a vector field $F(u)$ that drives the dynamics towards $\partial\Omega$. Additionally we would like the field to vanish on limit set $F(u \in \partial\Omega) = 0$ as well as far away from the limit set

$$F(u) = -|u - \partial\Omega| e^{-|u - \partial\Omega|} \frac{\partial}{\partial u} |u - \partial\Omega| \quad (2.33)$$

If the limit set $\partial\Omega$ is a connected surface we can additionally specify an angular momentum field $\omega(u)$ that gives rise dynamics tangent to the limit set, giving rise to limit cycles. We want the field to be tangent to the limit set $\frac{\partial}{\partial u} |u - \partial\Omega| \cdot F(u) \Big|_{u \in \partial\Omega} = 0$ and still vanish far away from the set. The field can be written in terms of tangential and normal field components to the limit set

$$F(u) = e^{-|u - \partial\Omega|} \left(\omega(u) \times \frac{\partial}{\partial u} - |u - \partial\Omega| \frac{\partial}{\partial u} \right) |u - \partial\Omega| \quad (2.34)$$

We also have an additional property that the tangential components $\omega(u) \times \frac{\partial}{\partial u}$ vanish faster than the normal components as $|u - \partial\Omega| \rightarrow \infty$. This makes any limit set $\partial\Omega$ look like a stable fixed point from a sufficient distance. We note that the cross product is only defined for three dimensions $N = 3$; the higher dimensional analogues of this operation is the wedge product \wedge defined in the language of exterior algebra [1].

Forcing the fields to vanish sufficiently far from their limit sets allows us to construct the field for multiple limit sets $\partial\Omega_k$ with their associated angular momenta $\omega_k(u)$ as a superposition

$$F(u) = \sum_k \alpha_k e^{-|u - \partial\Omega_k|} \left(\omega_k(u) \times \frac{\partial}{\partial u} - |u - \partial\Omega_k| \frac{\partial}{\partial u} \right) |u - \partial\Omega_k| \quad (2.35)$$

where the amplitudes α_k determine the relative sizes of the basins of attraction for each limit set. In addition we can let $\alpha_k < 0$ to specify unstable structures.

2.3.2.2 Comparing Fields and Models

In this early days of this thesis, we investigated whether it was possible to transform the time-domain data into state-space. This approach, and related works, are discussed in this section and can in principle be used with the microfluidic fluorescence microscopy data for parameter inference.

Consider we are given K cell trajectories $\mathcal{D}_1, \mathcal{D}_2 \dots \mathcal{D}_K$, each containing N noisy observations of the state of the cell. Let the cell state be represented by state vector $u(t) \in \mathbb{R}^N$ which is hypothesized to obey a set of ordinary differential equations of the form (2.1). Instead of integrating the equations (2.1) we would find an estimate for the derivative of the trajectories \hat{f} .

This is known as the *smoothing* step [11] should be done using unsupervised methods, for example with Gaussian Process Regressors [31] as shown in Figure 2.19. This requires the inversion of an $K' \times K'$ data matrix where $K' := \sum_k |\mathcal{D}_k|$ is the total number of trajectory data points. This has a computational complexity K'^3 which is only tractable with sparse

datasets.

Let the region $\partial\mathcal{D}$ be a boundary defined by the Delaunay tessellation of the input data. Let us define the estimate \hat{f} only within the region $\partial\mathcal{D}$ so that there are no extrapolation artefacts. For the Gaussian Process approach the estimate would be

$$\hat{f}(u) \sim \mathcal{N}(\mu(u), \Sigma(u)) \quad \text{for } u \in \partial\mathcal{D} \quad (2.36)$$

where at any given state u the field estimate \hat{f} is generated by Gaussian distributions of mean vector μ and covariance matrix Σ . Solving for these requires a choice of matrix-valued kernel function $\mathbf{K}(u, v)$ which encodes our knowledge about the local structure of the field. Sophisticated kernels for learning vector fields exist [33] for decomposing fields in conservative and solenoidal components, which aid in localising fixed points and cycles.

The simplest choice of kernel assumes the components are independent and have a finite correlation length γ , such as Gaussian radial basis functions. Here \mathbf{I} is the identity matrix and the hyperparameter γ has to be optimised.

$$\mathbf{K}(\vec{u}, \vec{v}) = \mathbf{I} e^{-\gamma |\vec{u} - \vec{v}|^2} \quad (2.37)$$

The second step is called *matching* where the estimated field \hat{f} is used as an optimisation target against some parametrised function F_θ with unknown parameters θ .

In our setting we would like to match the geometry of the field but not its magnitude; in this sense we are focusing on the qualitative aspects of the dynamics of a set of differential equations, rather than the quantitative dynamics or kinetics. This could be achieved with the following objective function

$$\mathcal{L}(\theta | \mathcal{D}) := e^{-\frac{\hat{f} \cdot F_\theta}{|\hat{f}| |F_\theta|}} \quad (2.38)$$

where the cost is minimal when the data derivative \hat{f} and the parametrised model F_θ point in the same direction and maximal when they point in

opposing directions.

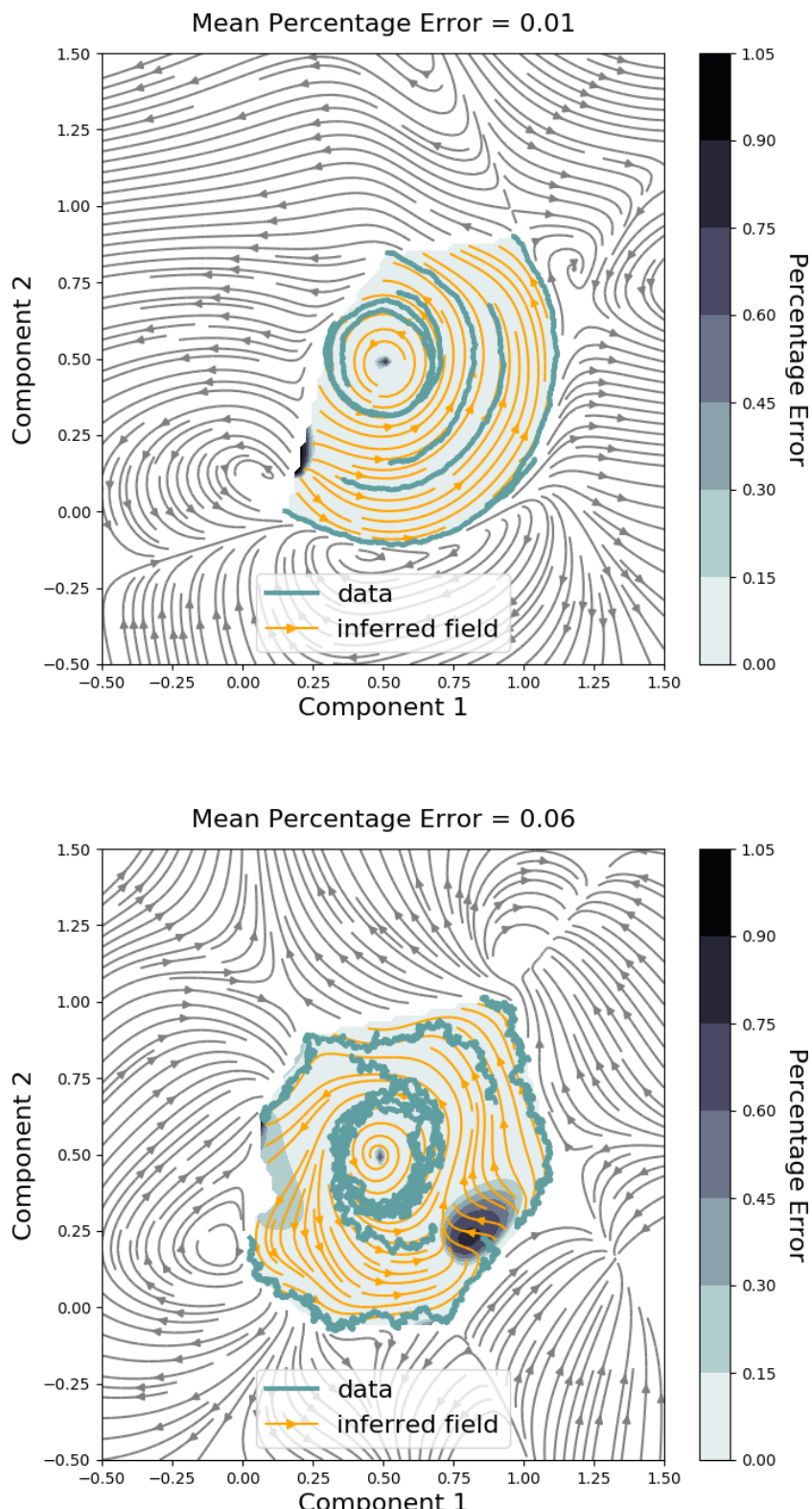


Figure 2.19: Gaussian process regressors estimating derivative of the trajectories \hat{f} from example trajectory datasets $\mathcal{D}_1 \dots \mathcal{D}_K$ with varying signal to noise ratios. Interpolation error E is shown as a heatmap; extrapolation fails

Although we are getting close to focusing on qualitative features of a model, this objective function is still sensitive to the locations and shapes of fixed point and limit cycles. What if we cared about even higher-level features such as the number of fixed points? Or perhaps whether a system oscillates or not? This is where the language of bifurcation theory described in Chapter 2 is optimally suited for this task, but first we need to discuss how to set up experiments to detect bifurcations from flow cytometry data.

- Vector field estimates too noisy to get bifurcation points?
- Divergence and the stability of fixed points
- curl and limit cycles. How does this relate to hopf example 2.19
- Do we need a bistable example?

The accuracy of the cell trajectories is limited by cell segmentation and tracking algorithms. Initial investigations into this approach also suggested that trajectories need to be of sufficient temporal resolution and sampled from a wide variety of initial conditions. Such data is not widely available and ultimately we decided to focus on a method that could be used with a well-known workhorse in biomedical research: flow cytometry.

2.4 Applications in Flow Cytometry

2.4.1 Immunophenotyping Panels

Chapter 3

Interpretation of Morphogen Gradients by a Bistable Circuit

memory of younger days

Ocarina of Time

3.1 Preface

3.1.1 Problem Statement & Context

1. Keep focus on developmental biology
2. Revised supplement as this chapter

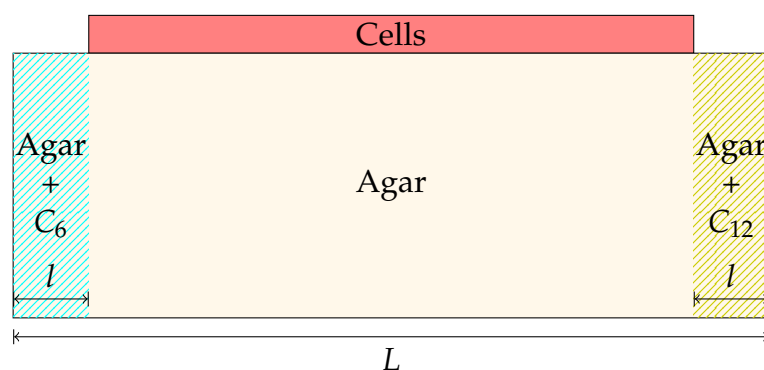


Figure 3.1: Geometry of opposing gradients experiment

This section outlines how the Design—Learn pipeline may help achieve a specific aim in a typical collaboration between theory, compu-

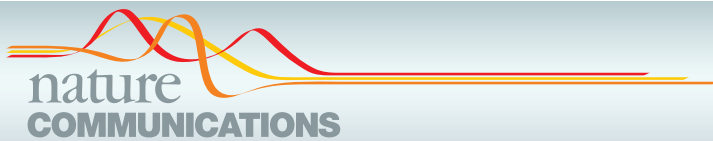
tation and experiment. The aim of this project is to reconstitute and control minimal self-organisation mechanisms which are believed play crucial roles in developmental biology. To this end *E. Coli* has been genetically engineered to produce orthogonal responses to two different input signals — henceforth this organism will be referred to as the *double exclusive reporter* circuit [34]. The colony of reporters serve as a reduced model for a multi-cellular organism during embryonic stages of development. While patterns with sharp boundaries have successfully been realised, producing Turing instabilities remains challenging as the system needs to be such that patterns develop before the colony reaches stationary phase. The role of theory and computation in this project is to help identify the parameter regimes that produce controllable and self-organised patterns.

3.1.2 Contributions

Grisha Szep is co-second author with **Om Pantage**. **Paul Grant**, **Neil Dalchau**, **Jacob Halatek** and **Andrew Philips** conceived and designed the study. **Paul Grant** designed and built the genetic circuits. **Paul Grant**, **Om Pantage** and **Valerie Coppard** performed the experiments. **Grisha Szep**, **Jacob Halatek** and **Neil Dalchau** conceived and implemented theory and modelling and wrote the supplementary information. All authors analysed and interpreted the data. **Paul Grant** and **Andrew Philips** wrote the main text. All authors provided input into the manuscript. The contributions of **Grisha Szep** the main text and supplementary include:

- **Figure 1.b** Spatial simulations of parameterized model
- **Figure 2.a-b** Calculation of region of bistability predicted by the parameterized model using arc-length continuation algorithms
- **Figure 3.b-e** Wrote bespoke inference code for quantification of boundary velocity from microscopy movies and comparison to theoretical model

- **Figure 4.d-e** Spatial simulations of the parametrized model. Novel state-space analysis of boundary formation and bistability
- **Figure S10.c** Spatial simulations analysed in state-space
- **Figure S13** A novel method for quantifying hysteresis in the flow cytometry experiments as population separation
- **Figure S25-S26** Bistability analysis of parametrized models and comparison to qualifications from flow cytometry
- **Figure S27-S33** Simulations of boundary velocity, novel way of understanding them in state space and bespoke inference methods for quantification of boundary velocity from microscopy movies
- **Figure S36** State space geometry for model with feedback loops
- **Supplementary Sections 2.2-2.4** Wrote sections outlining the methods for extracting bistability regions from data and models with and without feedback loops
- **Movies 1-5** Simulations of expression boundary formation
- **Code** Released code with documentation in GitHub Repository



ARTICLE

<https://doi.org/10.1038/s41467-020-19098-w>

OPEN

Interpretation of morphogen gradients by a synthetic bistable circuit

Paul K. Grant¹✉, Gregory Szep^{1,2,9}, Om Patange¹ , Jacob Halatek¹ , Valerie Coppard¹, Attila Csikász-Nagy¹ , Jim Haseloff¹ , James C. W. Locke^{1,3,6}, Neil Dalchau¹ & Andrew Phillips¹

During development, cells gain positional information through the interpretation of dynamic morphogen gradients. A proposed mechanism for interpreting opposing morphogen gradients is mutual inhibition of downstream transcription factors, but isolating the role of this specific motif within a natural network remains a challenge. Here, we engineer a synthetic morphogen-induced mutual inhibition circuit in *E. coli* populations and show that mutual inhibition alone is sufficient to produce stable domains of gene expression in response to dynamic morphogen gradients, provided the spatial average of the morphogens falls within the region of bistability at the single cell level. When we add sender devices, the resulting patterning circuit produces theoretically predicted self-organised gene expression domains in response to a single gradient. We develop computational models of our synthetic circuits parameterised to timecourse fluorescence data, providing both a theoretical and experimental framework for engineering morphogen-induced spatial patterning in cell populations.

¹ Microsoft Research, 21 Station Road, Cambridge CB1 2FB, UK. ² Randall Centre for Cell and Molecular Biophysics, King's College London, London WC2R 2LS, UK. ³ Sainsbury Laboratory, University of Cambridge, Cambridge CB2 1LR, UK. ⁴ Faculty of Information Technology and Bionics, Pázmány Péter Catholic University, Budapest 1083, Hungary. ⁵ Department of Plant Sciences, University of Cambridge, Cambridge CB2 3EA, UK. ⁶ Department of Biochemistry, University of Cambridge, Cambridge CB2 1QW, UK. ⁷ Present address: Department of Molecular Biology, Massachusetts General Hospital, Boston, MA 02114, USA. ⁸ Present address: Department of Genetics, Harvard Medical School, Boston, MA 02115, USA. ⁹ These authors contributed equally: Gregory Szep, Om Patange. ✉email: grant.paul@microsoft.com; andrew.phillips@microsoft.com

ARTICLE

NATURE COMMUNICATIONS | <https://doi.org/10.1038/s41467-020-19098-w>

The positional information solution to the French flag problem, in which cells compute their spatial position by responding to the concentration of a morphogen in a gradient¹, provides crucial insight into how patterns of gene expression form in a developing organism. The simplest formulation of this model – concentration thresholds leading directly to gene expression states – requires a static morphogen gradient to produce a stable pattern of gene expression^{2,3}. However, quantitative measurements in developing embryos reveal that morphogen gradients are both dynamic and transient^{4,5}, and genetic perturbations reveal that pattern formation is robust to changes in morphogen concentration^{6–8}. A gene regulatory network topology of mutual inhibition downstream of antiparallel morphogen gradients^{9–12} (Fig. 1a) has been proposed to robustly interpret dynamic gradients (Fig. 1b). However, while certain features of this topology are common to a number of developmental contexts such as the early *Drosophila* embryo and the vertebrate neural tube (reviewed in³), demonstrating how this network functions and whether it is indeed sufficient remains a challenge, due to the complexities of the different biological contexts in which it operates. Recent work in synthetic biology has proven the utility of building multicellular patterning circuits both for understanding development and for learning engineering principles^{13–18}.

Here we show that the mutual inhibition motif¹⁹ is sufficient to produce stable domains of gene expression in response to dynamic and transient morphogen gradients. By taking a synthetic biology approach^{20–23} we have built a morphogen-induced

mutual inhibition circuit from scratch that acts in isolation in *E. coli* and used it to investigate the conditions under which patterning occurs. We have also added morphogen production to the core circuit to create a reaction-diffusion patterning system that responds to a single gradient by producing two domains of gene expression with a self-organized boundary. The experimental control and precise measurement afforded by a synthetic biology framework allowed us to understand the behaviour of these patterning mechanisms at a quantitative level in the context of a mathematical model parameterized against data, and to uncover general design principles for engineering multicellular systems.

Results

Engineering mutual exclusivity. To investigate whether a simple mutual inhibition network topology can interpret dynamic gradients, we built a synthetic Exclusive Receiver circuit (Fig. 1c), based on a previous Receiver circuit design (pR33S175²⁴) that responds to two homoserine lactone (HSL) input signals, 3O-C6-HSL (C6) and 3O-C12-HSL (C12) with fluorescent protein outputs. We engineered mutual inhibition by introducing genes encoding TetR, expressed bicistronically with eYFP, and LacI, expressed bicistronically with eCFP. In addition, the C12-binding receiver protein LasR was expressed under the control of a LacI-repressible promoter, while the C6-binding receiver protein LuxR was expressed under the control of a TetR-repressible promoter. The Exclusive Receiver therefore consists of two signalling pathways that mutually repress each other, such that LasR, eYFP and TetR are expressed in the

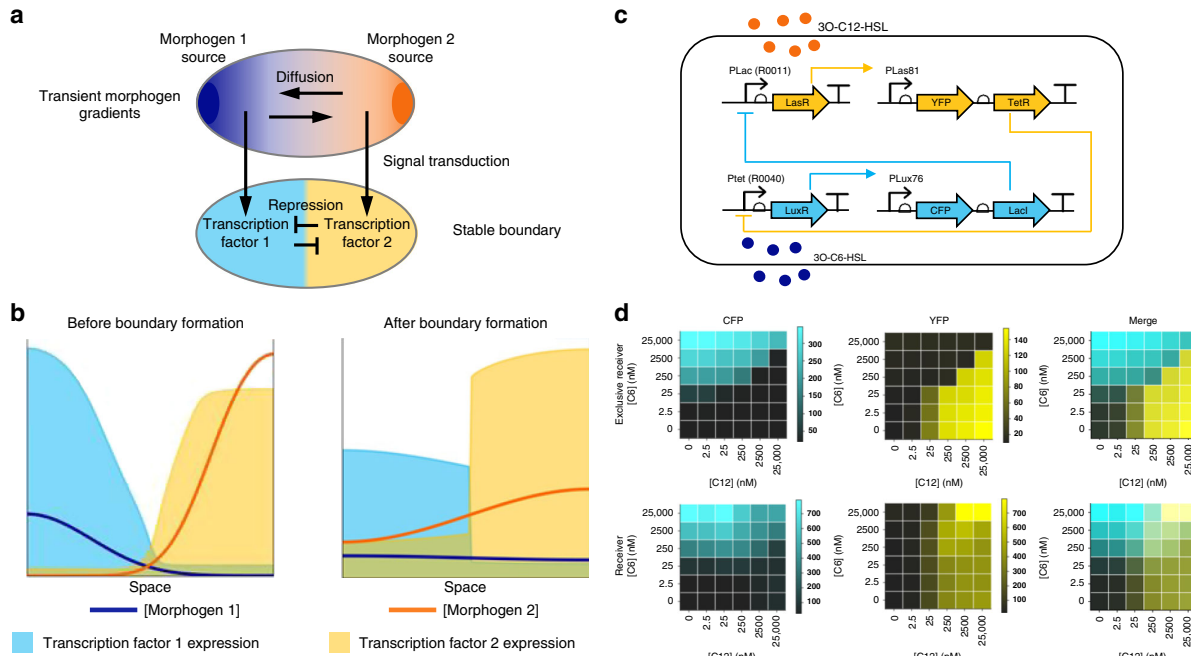


Fig. 1 A synthetic gene circuit for morphogen interpretation. **a** Schematic representation of a developing embryo. Mutual inhibition of transcription factors (cyan and yellow) downstream of antiparallel morphogen gradients (dark blue and orange) has been hypothesized to produce mutually exclusive domains of gene expression. **b** Morphogen gradients can be dynamic and transient, yet sharp, stable boundaries are observed between domains of gene expression. **c** A diagram of the Exclusive Receiver circuit. When 3O-C12-HSL (C12) levels are high, C12 binds to LasR, activating the expression of YFP and TetR, which represses the expression of LuxR, preventing expression of CFP and LacI. When 3O-C6-HSL (C6) levels are high, C6 binds to LuxR activating expression of CFP and LacI, which represses the expression of LasR, preventing expression of YFP and TetR. **d** Fluorescence output, measured in microplate fluorometer assays, of the Exclusive Receiver (top) and the Receiver (bottom) circuits represented as a ratio of CFP- (left) or YFP- (right) fluorescence to RFP fluorescence during exponential phase³⁸, cultured in the presence of the concentrations of C6 and C12 indicated. Data are representative of $n=3$ biological replicate experiments conducted on different days. See Supplementary Figs. 11 and 12 for replicates. Source data are provided as a Source Data file.

presence of the signal C12, while LuxR, eCFP and LacI are expressed in the presence of the signal C6. Unlike the Receiver circuit, which responds to the presence of both signals by producing both fluorescent proteins, the Exclusive Receiver was designed to respond exclusively to the two signals, by producing either eCFP or eYFP. Mutually exclusive reception will only occur when the repressors (TetR and LacI) are expressed such that the level of repression produced by high concentrations of one HSL is sufficient to repress detectable quantities of the other and low concentrations of HSL produce little repression. We used this mutually exclusive response as a design goal for the Exclusive Receiver circuit. We constructed a range of designs and chose a variant that exhibited a strong difference between CFP- and YFP-expressing states while maintaining a roughly equal sensitivity to the two HSLs (Supplementary Fig. 1).

To characterise the response of the Exclusive Receiver circuit to varying concentrations of C6 and C12, we performed timecourse plate fluorometry assays and calculated the promoter activity from the CFP and YFP channels using a ratiometric method²⁵. The circuit responded to high concentrations of C6 and C12 by producing CFP and YFP, respectively. As intended by the mutual inhibition design, mixtures of both signals resulted in only one fluorescent protein being produced, depending on the relative concentrations of the two signals (Fig. 1d; Supplementary Fig. 2). We confirmed these gene expression states at the single cell level using flow cytometry (Supplementary Fig. 3). In contrast, a Receiver circuit lacking mutual inhibition produced both fluorescent proteins simultaneously when both signals were present (Fig. 1d; Supplementary Figs. 2 and 3). Similar results were obtained when chemical inducers were used to suppress the repressors in the Exclusive Receiver circuit (Supplementary Fig. 4).

Mutual inhibition results in bistability. Central to the ability of mutual repression to produce a robust signal response is the

property of bistability, in which two stable steady states of gene expression are possible²⁰. We first explored this property mathematically by developing a dynamic (ordinary differential equation) model of the Exclusive Receiver circuit. The model is based on one derived for the Receiver circuit²⁴, but incorporates the repressor proteins, TetR and LacI, and their regulation of LuxR/LasR expression (see Supplementary Methods for a complete derivation). We identified parameter values that enabled the model to reproduce timecourse fluorescence data using a previously established inference methodology in which a sequence of parameter inference tasks are applied to models and data for circuits of increasing complexity²⁶ (Supplementary Methods). This enabled us to simplify the identification of parameter values of the Exclusive Receiver model by reusing values of the subset of parameters that also appear in the Receiver model. We then applied numerical continuation methods to our data-constrained model to locate saddle-node bifurcations (see Supplementary Methods), and thus the concentrations of C12 and C6 for which bistability was predicted (Fig. 2a,b, red lines).

To test whether the Exclusive Receiver circuit exhibited hysteresis, a hallmark of bistability, at the concentrations predicted by the model, we first conditioned cells in either C6 or C12 and then exposed them to varied concentrations of both signals. At concentrations that produce bistability, we expected C6-conditioned and C12-conditioned cells to remain in the CFP-expressing and YFP-expressing states, respectively. In contrast, at concentrations that produce monostability, gene expression states would be determined solely by the final concentrations. We measured CFP and YFP expression by flow cytometry (Supplementary Fig. 5). The C6-conditioned cells expressed CFP at a wider range of concentrations, while C12-conditioned cells expressed YFP at a wider range of concentrations (Fig. 1b, Fig. 2a, b). We interpret this history-dependent difference in gene expression to be due to hysteresis. Thus, the region in concentration space in which we observe this difference is the

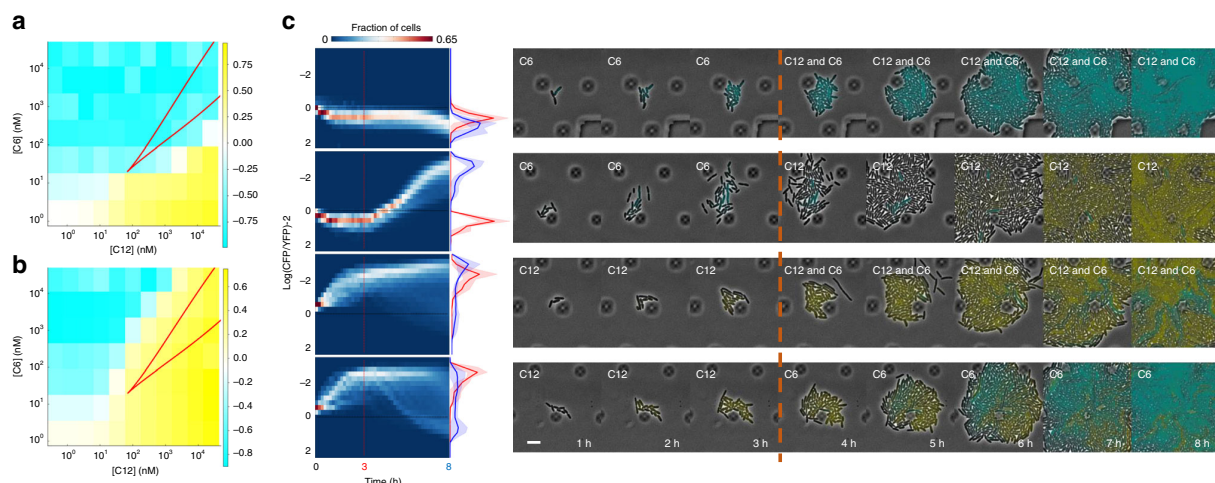


Fig. 2 Mutual inhibition produces bistability. Cells transformed with the Exclusive Receiver circuit were conditioned in either 500 nM C6 (a), or 500 nM C12 (b), and then exposed to the combinations of concentrations of C6 and C12 indicated. Cells were measured using flow cytometry and their normalized CFP minus YFP expressions were plotted. The region of bistability predicted by the parameterized model is the area within the red lines. See Supplementary Fig. 3 for gating strategy for all flow cytometry and Supplementary Fig. 13 for replicates. Source data are provided as a Source Data file. c Microfluidics cultures of cells transformed with Exclusive Receiver circuit in changing combinations of signals. Cells were grown for 3 h in the presence of either 37 nM C6 (rows 1 and 2) or 100 nM C12 (rows 3 and 4). Then media was changed to 100 nM C12 + 37 nM C6 (rows 1 and 3) or 100 nM C12 (row 2) or 37 nM C6 (row 4). Cells were imaged with a frame rate of (1 frame/10 min). Left panels are kymographs of the log-ratio of CFP expression per-cell to YFP expression per-cell, and fraction of cells as a heat map. Histograms represent the populations at 3 h (red) and 8 h (blue). Lines and shaded region represent the mean and standard deviation, respectively, over $n = 4$ biological replicates performed on 4 different days. Right panels are sample montages of cells switching state (rows 2 and 4) or exhibiting bistability (rows 1 and 3); phase contrast and fluorescence channel ranges chosen for display. Scalebar = 6 μ m.

ARTICLE

NATURE COMMUNICATIONS | <https://doi.org/10.1038/s41467-020-19098-w>

region of bistability. This region was slightly larger than that predicted by the model but was qualitatively similar, which suggested that our model captured the essential features of our circuit.

To determine whether individual cells were switching or retaining their gene expression states in response to signal combinations, as suggested by our flow cytometry data, we used microfluidic devices to observe the dynamics of single cells over time. We cultured cells with 37 nM C6 or 100 nM C12, concentrations expected to produce bistability in combination, and then switched to the opposite signal. We found that cells with high fluorescence expression could, indeed, switch to the alternative state (Fig. 2c rows 2 and 4, Supplementary Fig. 6), even when we used the much higher concentration of 1 μ M C6 (both to initially condition cells and to switch their state Supplementary Figs. 7 and 8). When cells conditioned with either C6 or C12 were exposed to both signals, the cells exhibited bistable behaviour, mostly maintaining their initial fluorescence states (Fig. 2c rows 1 and 3, Supplementary Figs. 6–8) although a comparatively small population of C12-conditioned cells do begin expressing CFP in response to mixed signals (Fig. 2c, row 3) indicating some heterogeneity in the population with respect to bistability. We hypothesize that cell to cell differences in gene expression result in differences in the HSL concentration regimes in which the cells exhibit bistability resulting in heterogeneity in switching behaviour. Together, these data indicate that, when signal concentrations gave rise to bistability, the final gene expression state was determined by the history of exposure to signals.

Hysteresis produces stable boundaries. To test how the Exclusive Receiver circuit interpreted dynamic morphogen gradients, we grew cells on filter paper printed with hydrophobic ink, such that growing colonies remained within the square in which they were inoculated but signals could diffuse through the agar beneath the filter^{24,27}. We performed these experiments in agar containing 10 μ M IPTG (1% of the standard induction concentration of 1 mM) to create a regime in which both CFP-dominating and YFP-dominating regions were observed. The addition of IPTG was required to compensate for differences in culture conditions between solid and liquid cultures (see Supplementary Fig. 34 for experiments without IPTG). While the precise mechanism is unknown, differences in culture conditions when switching to solid culture appeared to shift the bistability region such that even very low concentrations of C6 enabled bistability, preventing the appearance of a YFP-dominant regime. This was redressed through addition of IPTG, which partially derepresses LacI, shifting the region to coincide with the region in liquid culture. We cast either C6 or C12 into the agar at each end of the filter paper at varying concentrations and performed timelapse imaging of the fluorescence output of the circuit in response to the dynamic gradients produced by diffusion. When C6 and C12 were provided at concentrations that, if allowed to diffuse to homogeneity would result in 200 nM C6 and 2000 nM C12, (i.e., a 200 nM and 2000 nM spatial average, respectively), a sharp boundary was produced between mutually exclusive domains of CFP and YFP (Fig. 3a). Plotting the point in space at which CFP and YFP expression were equal (see Supplementary Methods) against time revealed that the boundary between domains did not move over time (Fig. 3b). In contrast, when spatial average concentrations of 20 nM C6 and 2000 nM C12 were used, there was an initial production of CFP near the source but it was quickly overwhelmed by YFP production and the point of equal expression moved toward the C6 source (Fig. 3a). These images measured bulk (rather than per-cell) fluorescent protein

expression so highly stable fluorescent proteins would remain detectable even after they stopped being expressed. It was therefore unsurprising that CFP remained detectable in cells close to the C6 source due to protein perdurance. Importantly, however, the CFP intensity did not increase, whereas the level of YFP did increase, indicating that the circuit had switched from CFP expression to YFP expression in these cells. At varying combinations of signal concentrations we classified boundaries (see Supplementary Methods) as static (S), moving (M), or not present (N) (Fig. 3c, Supplementary Fig. 9, Supplementary Movie 1) and observed that static boundaries occurred at signal concentrations similar to those that produced hysteresis (Fig. 2a and b).

To understand this behaviour we performed simulations and analysis of our mathematical model. We plotted the concentration of C6 and C12 experienced by physically separated cells and visualized the changes in concentration that they experienced due to diffusion (Fig. 3d, Supplementary Movie 2). We observed that cells at different points in space all converge to the spatial average concentration, but they do so by taking different paths, resulting in differences in CFP and YFP expression. Points closest to the C6 source begin in the monostable CFP region, whereas those closest to the C12 source begin in the monostable YFP region. This means that the cells are traversing the bistable region along different paths and will therefore exhibit hysteresis as they converge to the spatial average. If the spatial average concentrations lie within the bistable region, which is defined in concentration space, all cells will eventually experience concentrations within this region as the morphogens diffuse. Thus, over time, the region of cells in physical space that exhibit bistability expands to encompass the entire domain (Fig. 3e, S; Supplementary Movie 3). The result is that a cell's state will be determined by its history and cells with different histories that originated on different sides of the boundary will end up in different stable states. The cells close to the C6 source will behave like cells conditioned in C6 and express CFP while the cells close to the C12 source will behave like cells conditioned in C12 and express YFP (as in Fig. 2) and will maintain their states even after the two morphogens mix via diffusion. The result is the formation of two mutually exclusive domains of gene expression with a sharp boundary that is stable and stationary, even though the morphogen gradients that produced those domains were only present transiently. If, on the other hand, the spatial average concentrations lie outside the bistable region, a transient boundary will form and cells will switch fates as they leave the bistable region, taking on the fate determined by the morphogen of greater concentration (Fig. 3e, M; Supplementary Movies 4 and 5).

A secondary gradient creates self-organized domains. Given the ability of the mutual inhibition topology to produce stable domains of gene expression in response to antiparallel morphogen gradients, we hypothesized that it could function similarly in response to a single morphogen gradient with the addition of a secondary gradient produced by the cells themselves, which functions as a lateral inhibitor²⁸. This circuit mimics the sequential induction of organizing centres found in *C. elegans* vulval development²⁹, the rhombomeres of the vertebrate hindbrain^{30,31}, and the *Drosophila* wing disc³².

To explore this mechanism we added previously characterized Relay circuits²⁴, which produce one signal in response to the other, to the Exclusive Receiver circuit. This created an Exclusive Relay circuit that both produces and interprets morphogen gradients (Fig. 4a and Supplementary Methods). We created a transient gradient of C6 by replacing a cylinder of agar in the centre of a plate with agar containing 40 μ M C6, and plated cells

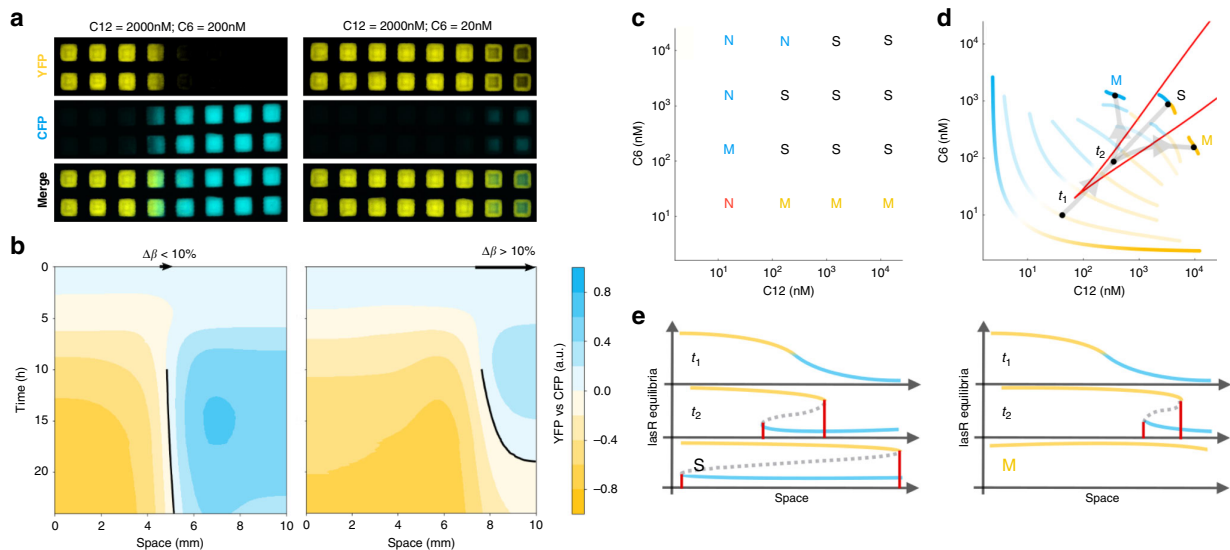


Fig. 3 Formation of stable boundaries. **a** Endpoint fluorescence microscopy of Exclusive Receiver cells grown in transient gradients of signals (C12 diffusing from the left, C6 diffusing from the right) at the spatial average concentrations indicated and in the context of 10 μ M IPTG throughout. Representative examples ($n=3$ biological replicates performed on 3 different days) of a static boundary (left) and a moving boundary (right). **b**, Corresponding kymographs of CFP and YFP fluorescence (intensity) over time (y-axes, hours) at different spatial positions (x-axes, mm). If the location of the boundary (location of equal normalized CFP and YFP fluorescences, black lines) at the end of the timelapse minus its location when it became detectable ($\Delta\beta$, arrows) was less than 10% of the domain size we considered the boundary stable. **c** Boundaries were evaluated as above at the signal concentrations indicated by letters. S indicates equilibrium concentrations at which static boundaries were observed. M indicates a moving boundary. "N" indicates no boundary. The colour of the letter indicates which FP was dominant and red indicates neither FP dominant. See supplementary Figs. 31-33 for replicates. **d** Schematic representation of the concentrations of C6 and C12 experienced by cells at different points in physical space (cyan and yellow curves) as gradients diffuse to homogeneity. Paler curves represent different timepoints. If the spatial average concentrations lie within the region of bistability, the boundary will be static (S), otherwise the boundary will move (M) and will eventually be abolished as cells adopt either CFP or YFP expression. t_1 and t_2 indicate timepoints considered in **e**. **e** Corresponding schematic representing LasR expression, coloured according to resultant fluorescent protein expression. Dashed line indicates the location of an unstable local equilibrium. Red lines indicate the spatial location in which cells are exhibiting bistability. In the case of a stationary boundary (S), the region of space containing cells exhibiting bistability expands to encompass all cells and their gene expression state is determined by their history. In the case of a moving boundary (M), the region exhibiting bistability moves rightward and disappears and the domain becomes dominated by a single monostable state.

transformed with the Exclusive Relay circuit onto gridded filters. The primary C6 gradient resulted in cells in the centre expressing CFP, LacI, and LasI (Fig. 4b and c). These cells produced C12 but were unable to sense it because they did not express LasR due to its repression by LacI. The gradients of C6 and C12 overlapped but the C12 gradient could extend further due to C12 being actively produced by a large region of cells (Fig. 4d). At a certain distance from the source of C6, the ratio of C12 to C6 favoured the C12 state such that the bistable switch 'flipped' and cells expressed YFP and TetR, repressing LuxR and the ability to sense C6. The result was two domains of mutually exclusive gene expression from a single primary morphogen gradient. As in the case of antiparallel gradients, the stability of the boundary between these domains of gene expression can be understood using the same framework: The spatial average concentration of the primary morphogen remained constant as the total density that was added at the beginning of the experiment was unchanging. The secondary morphogen, in contrast, was being produced by cells so the total density increased over time. The spatial average of both morphogens therefore moved along the axis of the secondary morphogen as cells that were sensing the primary morphogen produced the secondary (Fig. 4e, red arrows). The result is that a metastable boundary is produced that is present as long as the system remains within the region of bistability but will eventually be abolished as the secondary morphogen accumulates. Transforming the Exclusive Receiver

with a P81-LuxI Relay and creating a C12 primary gradient resulted in equivalent patterning with the physical location of the states reversed (Supplementary Fig. 10).

Discussion

By building a synthetic gene circuit composed of mutual inhibition downstream of diffusible morphogens, we have shown that this network topology in isolation is sufficient to recapitulate the behaviour, seen in multicellular developmental systems, of mutually exclusive domains of gene expression separated by a boundary that is sharp and stable despite transient and dynamic morphogen gradients. This topology also proves to be robust to differences in morphogen concentration, as variations in concentration spanning orders of magnitude result in only small changes in boundary location (Supplementary Fig. 9, Supplementary Movie 1). In addition, we have built a patterning circuit that creates a self-organised boundary between two gene expression domains in response to a primary morphogen by creating a secondary morphogen that functions as a lateral inhibitor. This circuit shares features of both a positional information model¹, in that it interprets a preexisting morphogen gradient to produce domains of gene expression, and a reaction-diffusion model^{33,34}, in that morphogen production is coincident with interpretation. These two models have previously been presented in opposition to each other, but it is likely that both mechanisms are at work in development³⁵. Our Exclusive Relay

ARTICLE

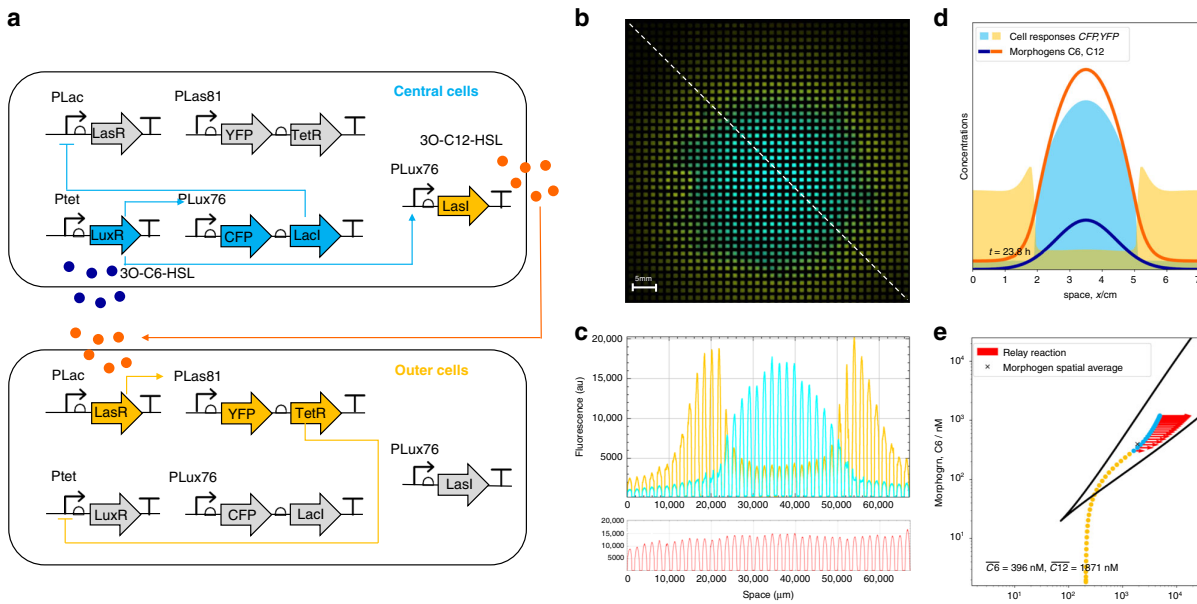


Fig. 4 Addition of a relay circuit creates self-organized domains of gene expression. **a** Circuit diagram of Exclusive Receiver cells co-transformed with a Relay circuit (P76-LasI) that responds to C6 by producing C12. **b** Isogenic cells transformed with the circuit shown in **a** and grown for 24 h in the presence of a gradient of C6 diffusing from the centre. Cells that experience high levels of C6 (central cells) will express CFP, Lacl, and LasI, causing them to produce C12 but be unable to sense it. Neighbouring cells (outer cells) that do not experience C6 will sense C12 and express YFP and TetR, resulting in mutually exclusive domains of gene expression. Cells also constitutively express mRFP1 via a genomic transgene. Image is representative of 3 biological replicates performed on 3 different days. **c** Quantitation of fluorescence along the dotted line in **b**. Cyan, yellow, and red indicate CFP, YFP, and RFP expression, respectively. **d** Final timepoint of simulation shows a secondary gradient of C12 (orange) produced in response to the primary C6 gradient (dark blue). Cyan and yellow indicate simulated CFP and YFP expression, respectively. **e** Final time point of simulation in C6-C12 space labelling points in physical space by their CFP and YFP expression (cyan and yellow points), and showing the production of C12 as vectors (red arrows) that move the spatial average (x) toward increasing C12 (see supplementary video 6).

circuit forms patterns by using two in-phase morphogen gradients to produce a primary response whose spread is limited by the gradient of the secondary morphogen, due to its larger magnitude and diffusive radius. The result is concentration-dependent domains of gene expression produced in response to a morphogen gradient, just as in the French flag model. However, due to the hysteresis of the bistable core of the circuit, these domains of gene expression are metastable even though the primary morphogen gradient diffuses to homogeneity. It is worth noting that the boundary between the eYFP-expressing domain and the domain that expresses neither fluorescent protein is determined simply by the threshold of response to C12 and is therefore not a stable boundary. This boundary could be stabilised by recapitulating the mechanism we have described via the addition of a third morphogen (and mutual inhibition with C12) either diffusing from the opposite direction to the primary gradient (as in Fig. 3) or as a second relay mechanism (as in Fig. 4). The fact that genetic circuits optimized in different contexts can be directly composed to produce more complex patterns suggests that the synthesis of reaction-diffusion and positional information mechanisms may be readily obtainable through evolution, and therefore common in development. This also provides a blueprint for designing synthetic gene circuits that produce spatiotemporal patterns in cell populations, which could lay the groundwork for rationally designing self-organizing, self-repairing materials and tissues.

Methods

Plasmid construction. The exclusive receiver circuit and variants described in Supplementary Fig. 1 were cloned using Gibson Assembly³⁶ using pRS3S175²⁴ as a

starting point. Primers used for Gibson assembly can be found in Supplementary Table 1.

Plate fluorometer assays. The exclusive reporter construct was transformed into EC10G *E. coli* cells with a chromosomally integrated mRFP1 construct²⁴. Overnight cultures were grown from glycerol stocks in M9 media supplemented with 0.4% glucose, 0.2% casamino acids, and 50 µg/ml kanamycin (supplemented M9) then diluted back 1:100, allowed to grow to an OD of 0.3 then diluted 1:1000. Cultures were aliquoted into black-walled, clear-bottom 96-well plates (Greiner µClear) in a volume of 200 µl per well and measurements taken every 10 min for ~1000 min in a BMG FLUOstar Omega plate fluorometer using BMG FluoStar Omega Reader Control Software 5.10R2. 3-oxohexanoyl-homoserine lactone, C6, (Cayman Chemicals) and 3-oxododecanoyl-homoserine lactone C12, Cayman Chemicals were dissolved to a concentration of 200 nM in DMSO then C6 was diluted in supplemented M9 to the concentrations described, while C12, due to its limited solubility in aqueous media, was first diluted 1:50 in ethanol then diluted in supplemented M9 medium to the concentrations described.

Flow-cytometric analysis of hysteresis. EC10G cells transformed with the exclusive receiver construct were grown overnight from glycerol stocks as described for plate fluorometer assays. Overnight culture was diluted 1:100 and incubated until OD 0.2. Cells were then resuspended 1:100 in supplemented M9 supplemented with either C6 or C12 at 500 nM each and conditioned for 2 h. Following conditioning, cells were washed three times in supplemented M9 by centrifugation at 3200 × g for 4 min. and seeded at 1:1000 into wells of a 96-well plate containing combinations of varying concentrations of C6 and C12 as indicated in Supplementary Fig. 5. The plate was incubated for 5 h with continuous OD monitoring. OD measurements at 5 h were consistently within the exponential growth range (0.3–0.8). Following 5 h incubation, cells were diluted 1:6 in PBS and analysed by flow cytometry on a BD FACSCelesta (BD Biosciences, San Jose, CA, USA) equipped with HTS and a standard optical setup. Data was collected using FACSDiva 8.01. CFP was excited with violet laser 405 nm and detected with 525/50 BP filter - 505 LP mirror combination. YFP was excited with blue laser 488 nm and detected with 530/30 BP filter - 505 LP mirror combination. RFP was excited with yellow-green laser 561 nm and detected with 610/20 BP filter - 600 LP mirror combination. Instrument quality control was performed prior to each experiment

using BD CS&T beads. Fluorescence compensation parameters were determined using induced and untreated exclusive reporter cells and 30,000 events were counted within RFP gate for each sample. Data analysis was performed with FCS Express v.7 software (DeNovo Software, Glendale, CA, USA). The gating strategy for all flow cytometry was the same and is shown in Supplementary Figs. 3c and 5c.

Microfluidics. Glycerol stocks of EC10G transformed with the Exclusive Receiver were streaked on LB agar plates. Colonies were picked into M9 and grown at 37 °C overnight, then diluted 1:1000 into M9 and grown for 4 h 45 min at 37 °C into exponential phase. The culture was typically diluted 1:100 in M9 before being loaded into the CellASIC ONIX B04A-03 microfluidic device using the manufacturer's protocol (EMD Millipore Corporation). Cells were supplied with media using a pressure of 5 psi in the device. The entire device, along with most of the microscope, was incubated at 37 °C during movie acquisition. Cell segmentation was done on the RFP channel using the published Schnitzcells software (release 1.1, 2005)³⁷. The mean YFP and CFP fluorescence normalized to cell area was then calculated by averaging the corresponding pixels in the respective channels. Movies with no cells or non-growing cells were excluded by keeping only those movies with greater than 20 and 50 cells at 3 and 6 h, respectively. Non-cell segmentation artefacts were excluded by area (<200 pixels) and Euler number (<1) computed with the regionprops function of MATLAB 2014a.

Microfluidics microscopy. Microfluidics devices were imaged using a widefield microscope with epifluorescence and phase contrast imaging modes (Nikon Ti-eclipse, Nikon, UK) equipped with the Nikon Perfect Focus (PFS) Unit. Illumination for the epifluorescence was provided by a white light LED source (SOLA SE Light Engine or Spectra X Light Engine, Lumencor, USA), transmitted by a liquid light guide (Lumencor, USA), through a fluorescence filter cube (YFP Channel: 49003; ET/Sputtered series ET-EYFP, exciter: ET500/20x, dichroic: T515LP, emitter: ET535/30m; CFP Channel: 49001; ET/Sputtered series ET-CFP, exciter: ET436/20x, dichroic: T455LP, emitter: ET480/40m; RFP Channel: 41027-Calculm Crimson, excitation: HQ580/20x, dichroic: Q595LP, emitter: HQ630 /60m, Chroma, USA), and a CFI Plan Apochromat 100x oil immersion objective (NA 1.45, Nikon). Phase contrast illumination was provided by a 100 W lamp via a condenser unit (Nikon). Images were acquired on CoolSNAP HQ2 camera (Photometrics, USA). The sample was held in motorized stages (Nikon). The sample was incubated along with much of the microscope body using a temperature controlled, heated chamber (Solent Scientific, UK). The microscope was controlled with MetaMorph software (version 7.8.10.0, Molecular Devices, USA). Fluorescent beads (TetraSpeck microspheres, 0.5 μm, Molecular Probes, USA) were imaged as a calibration standard.

Solid culture assays. Exponential phase cultures were grown to an OD of 0.3 and plated onto Iso-Grid membranes (Neogen) on supplemented M9 with 1.5% agar at a volume of 0.5 μl per square. Gradients were created by cutting holes in supplemented M9-agar (1.5%) plates (cast in OmniTray [Nunc]) containing 10 μM IPTG. Holes were cut on both ends of a domain to be inoculated at a size of 25% of the domain, each. Holes were then filled with liquid M9-agar to which either 3O-C6- or 3O-C12-HSL had been added at 4X concentration. After hardening, excess agar was cut away leaving each domain isolated. For relay circuit assays, circular holes were punched in the centre of plates using the back of a pipette tip and the holes were filled with ~200 μl of liquid agar containing 40 μM of the appropriate HSL. Plates were sealed with parafilm and imaged using a motorized Leica M205 FA fluorescence stereo microscope controlled using Leica LAS X software. Plates were incubated at 37 °C using a DigiTherm microscope temperature control air bath (Tritech Research). Illumination was an LED white light source (Lumencor) with excitation filters of 426–446 nm, 490–510 nm, and 555–589 nm, and emission filters of 460–500 nm, 520–550 nm, and 608–682 nm. Tiled images were taken every 10 min and were stitched using Leica LAS X software.

Reporting summary. Further information on research design is available in the Nature Research Reporting Summary linked to this article.

Data availability

Source data are provided with this paper. Plate fluorometer and flow cytometry datasets can be found in supplementary file sourcedata.zip. Raw microscopy images (Figures 2c, 3a, 4b) are available on request to the authors. The exclusiver receiver plasmid is available from Addgene (Addgene ID 160376). All other relevant data are available from the authors upon reasonable request. Source data are provided with this paper.

Code availability

Code is available at GitHub repository <https://github.com/gszep/double-exclusive-reporter>. Source data are provided with this paper.

Received: 15 July 2020; Accepted: 23 September 2020;

Published online: 02 November 2020

References

- Wolpert, L. Positional information and the spatial pattern of cellular differentiation. *J. Theor. Biol.* **25**, 1–47 (1969).
- Jaeger, J. & Reinitz, J. On the dynamic nature of positional information. *BioEssays* **28**, 1102–1111 (2006).
- Briscoe, J. & Small, S. Morphogen rules: design principles of gradient-mediated embryo patterning. *Development* **142**, 3996–4009 (2015).
- Kicheva, A. et al. Kinetics of morphogen gradient formation. *Science* **315**, 521–5 (2007).
- Durrieu, L. et al. Bicoid gradient formation mechanism and dynamics revealed by protein lifetime analysis. *Mol. Syst. Biol.* **14**, e8355 (2018).
- Driever, W. & Nüsslein-Volhard, C. A gradient of bicoid protein in *Drosophila* embryos. *Cell* **54**, 83–93 (1988).
- Balaskas, N. et al. Gene regulatory logic for reading the sonic hedgehog signaling gradient in the vertebrate neural tube. *Cell* **148**, 273–284 (2012).
- Fried, P. & Iber, D. Read-out of dynamic morphogen gradients on growing domains. *PLOS ONE* **10**, e0143226 (2015).
- Clyde, D. E. et al. A self-organizing system of repressor gradients establishes segmental complexity in *Drosophila*. *Nature* **426**, 849–853 (2003).
- Sokolowski, T. R., Erdmann, T. & TenWolde, P. R. Mutual repression enhances the steepness and precision of gene expression boundaries. *PLoS Comput. Biol.* **8**, e1002654 (2012).
- Zagorski, M. et al. Decoding of position in the developing neural tube from antiparallel morphogen gradients. *Science* **356**, 1379–1383 (2017).
- Srinivasan, S. et al. A BMP-FGF morphogen toggle switch drives the ultrasensitive expression of multiple genes in the developing forebrain. *PLoS Comput. Biol.* **10**, 1–16 (2014).
- Toda, S., Blauch, L. R., Tang, S. K. Y., Morsut, L. & Lim, W. A. Programming self-organizing multicellular structures with synthetic cell-cell signaling. *Science* **361**, 156–162 (2018).
- Kong, W., Blanchard, A. E., Liao, C. & Lu, T. Engineering robust and tunable spatial structures with synthetic gene circuits. *Nucleic acids Res.* **45**, 1005–1014 (2017).
- Sekine, R., Shibata, T. & Ebisuya, M. Synthetic mammalian pattern formation driven by differential diffusivity of Nodal and Lefty. *Nat. Commun.* **9**, 5456 (2018).
- Schaerli, Y. et al. A unified design space of synthetic stripe-forming networks. *Nat. Commun.* **5**, 4905 (2014).
- Payne, S. et al. Temporal control of self-organized pattern formation without morphogen gradients in bacteria. *Mol. Syst. Biol.* **9**, 697 (2013).
- Cao, Y. et al. Programmable assembly of pressure sensors using pattern-forming bacteria. *Nat. Biotechnol.* **35**, 1087–1093 (2017).
- Shen-Orr, S. S., Milo, R., Mangan, S. & Alon, U. Network motifs in the transcriptional regulation network of *Escherichia coli*. *Nat. Genet.* **31**, 64–68 (2002).
- Gardner, T. S., Cantor, C. R. & Collins, J. J. Construction of a genetic toggle switch in *Escherichia coli*. *Nature* **403**, 339–342 (2000).
- Basu, S., Gerchman, Y., Collins, C. H., Arnold, F. H. & Weiss, R. A synthetic multicellular system for programmed pattern formation. *Nature* **434**, 1130–1134 (2005).
- Youk, H. & Lim, W.A. Secreting and sensing the same molecule allows cells to achieve versatile social behaviors. *Science* (New York, N.Y.) **343**, 1242782 (2014).
- Cao, Y. et al. Collective space-sensing coordinates pattern scaling in engineered bacteria. *Cell* **165**, 620–630 (2016).
- Grant, P. K. et al. Orthogonal intercellular signaling for programmed spatial behavior. *Mol. Syst. Biol.* **12**, 849 (2016).
- Rudge, T. J. et al. Characterization of Intrinsic Properties of Promoters. *ACS Synth. Biol.* **5**, 89–98 (2016).
- Dalchau, N. et al. Scalable dynamic characterization of synthetic gene circuits. Preprint at <https://www.biorxiv.org/content/10.1101/635672v1> (2019).
- Boehm, C. R., Grant, P. K. & Haseloff, J. Programmed hierarchical patterning of bacterial populations. *Nat. Commun.* **9**, 776 (2018).
- Meinhardt, H. & Gierer, A. Pattern formation by local self-activation and lateral inhibition. *BioEssays* **22**, 753–760 (2000).
- Simske, J. S. & Kirn, S. K. Sequential signalling during *caenorhabditis elegans* vulval induction. *Nature* **375**, 142–146 (1995).
- Hernandez, R. E., Rikhof, H. A., Bachmann, R. & Moens, C. B. vhnfl integrates global RA patterning and local FGF signals to direct posterior hindbrain development in zebrafish. *Development* **131**, 4511–4520 (2004).
- Schilling, T. F., Nie, Q. & Lander, A. D. Dynamics and precision in retinoic acid morphogen gradients. *Curr. Opin. Genet. Dev.* **6**, 562–569 (2012).
- Piddini, E. & Vincent, J. P. Interpretation of the Wingless Gradient Requires Signaling-Induced Self-Inhibition. *Cell* **136**, 296–307 (2009).
- Turing, A. M. The chemical basis of morphogenesis. *Philos. Trans. R. Soc. Lond. Ser. B, Biol. Sci.* **237**, 37–72 (1952).
- Gierer, A. & Meinhardt, H. A theory of biological pattern formation. *Kybernetik* **12**, 30–9 (1972).
- Green, J. B. A. & Sharpe, J. Positional information and reaction-diffusion: two big ideas in developmental biology combine. *Development* **142**, 1203–1211 (2015).

ARTICLE

NATURE COMMUNICATIONS | <https://doi.org/10.1038/s41467-020-19098-w>

36. Gibson, D. G. et al. Enzymatic assembly of DNA molecules up to several hundred kilobases. *Nat. Methods* **6**, 343–345 (2009).
37. Young, J. W. et al. Measuring single-cell gene expression dynamics in bacteria using fluorescence time-lapse microscopy. *Nat. Protoc.* **7**, 80–88 (2012).
38. Yordanov, B. et al. A Computational Method for Automated Characterization of Genetic Components. *ACS Synth. Biol.* **3**, 578–588 (2014).

Acknowledgements

We would like to thank Jeremy Green for helpful comments on the manuscript.

Author contributions

P.K.G., N.D., J.H., and A.P. conceived and designed the study. P.K.G. designed and built the genetic circuits. P.K.G., O.P., and V.C. performed the experiments. G.S., J.H., and N.D. conceived and implemented theory and modelling and wrote the supplementary information. All authors analysed and interpreted the data. P.K.G. and A.P. wrote the main text. All authors provided input into the manuscript.

Competing interests

The authors declare no competing interests.

Additional information

Supplementary information is available for this paper at <https://doi.org/10.1038/s41467-020-19098-w>.

Correspondence and requests for materials should be addressed to P.K.G. or A.P.

Peer review information *Nature Communications* thanks the anonymous reviewer(s) for their contribution to the peer review of this work. Peer reviewer reports are available.

Reprints and permission information is available at <http://www.nature.com/reprints>

Publisher's note Springer Nature remains neutral with regard to jurisdictional claims in published maps and institutional affiliations.



Open Access This article is licensed under a Creative Commons Attribution 4.0 International License, which permits use, sharing, adaptation, distribution and reproduction in any medium or format, as long as you give appropriate credit to the original author(s) and the source, provide a link to the Creative Commons license, and indicate if changes were made. The images or other third party material in this article are included in the article's Creative Commons license, unless indicated otherwise in a credit line to the material. If material is not included in the article's Creative Commons license and your intended use is not permitted by statutory regulation or exceeds the permitted use, you will need to obtain permission directly from the copyright holder. To view a copy of this license, visit <http://creativecommons.org/licenses/by/4.0/>.

© The Author(s) 2020

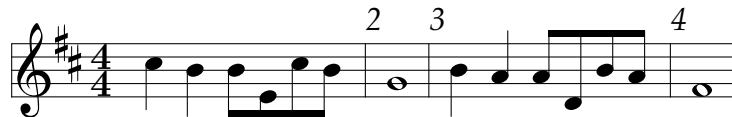
3.7 Afterword

The decision to focus on single cell trajectories and flow cytometry came from the limitations of using microplate data in Chapter 3. The model parameters θ were estimated using a hierarchical monte-carlo approach and time-course fluorescence microplate measurements (details of which can be found in Appendix A.2.1). The time-courses include information about dynamical transients and colony growth in liquid culture. The desired cusp bifurcation, however, lives in state-space rather than the time-domain. The disconnect between the domain that the data lives in and the domain of the design goals poses the risk of over-fitting the model on undesired information that exists in the data domain.

It is not possible to observe the cusp bifurcation in microplate data, due to the averaging of signals originating from heterogeneous cell populations. Instead, the cusp bifurcation can be observed in flow cytometry measurements of colonies in exponential phase (Supplementary Figure A.3) and microfluidic fluorescence microscopy data (Figure 3.3c) where computations on single-cell trajectories reveal the hysteresis loop which must necessarily accompany the cusp.

Chapter 4

Parameter Inference with Bifurcation Diagrams



the melody that will draw you into the infinite darkness

Nocturne of Shadow — Ocarina of Time

4.1 Preface

4.1.1 Problem Statement & Context

This chapter focuses on the problem of looking for parameter regimes for dynamical systems that result in bifurcations. This has been coined as *inverse bifurcation analysis* [35]. Formally we are looking for parameters θ for which the equation (2.1) has at least one fixed point for which bifurcation criteria (see Section 2.1.2) are satisfied. These bifurcations are to be placed along control condition $p \in \mathbb{R}$.

Inverse bifurcation analysis becomes relevant to biomedical researchers in settings where there is a design goal to engineer an organism with a distinct phenotype (as discussed in Chapter 1). Such a phenotype can be a the *double exclusive reporter* investigated in the interdisciplinary collaboration in synthetic developmental biology presented in Chapter 3.

This *E. Coli* phenotype exhibits a cusp bifurcation leading to a bistable response with respect to two input signals as shown in Figure 3.3. The engineering goal could be a phenotype with a specific cell cycle [36, 37] which involves the positioning of *Hopf bifurcations* that mark the onset of oscillations in protein concentrations from stable equilibria. Finally the design of self-organised patterns such as stripes and spots in mammalian coat patterns could be another engineering goal. According to a long standing mathematical hypotheses [38] that underpins developmental mechanisms this may involve the search for *Turing bifurcations*.

Before we get carried away and think that with the right tooling we could genetically control the length scale of spots or stripes on cats, we must remind ourselves that *in vivo* gene regulatory networks mostly consist of unknown and experimentally inaccessible parameters. Furthermore, we find that usually there exist multiple equally valid models that describe the observed behaviour, and so turn to *model selection* methods. Even if we had an accurate and unique model to describe an organism, generic tools for *inverse bifurcation analysis* are limited as we've explored in Chapter 2 and experienced in practice in Chapter 3. In an attempt to address these limitations, the incorporated publication (sections 4.2 – 4.6) focuses on the design of systems of ordinary differential equations with *pitchfork* and *saddle-node* bifurcation diagrams. Although the publication focuses on parameter synthesis for a subset of bifurcations, steps towards *Hopf* bifurcations are made (see Appendix B.5), and the approach lays foundations for differentiable optimisation methods that leverage bifurcation theory. A view towards how this approach can be used for the design of *Turing patterns* and model selection is discussed in concluding Chapter 6.

4.1.2 Contributions

Grisha Szep prepared the manuscript, designed the cost function, derived mathematical results, wrote and released the Julia package under the supervision of **Neil Dalchau** and **Attila Czikasz-Nagy**.

Parameter Inference with Bifurcation Diagrams

Gregory Szep

King's College London
London, WC2R 2LS, UK
gregory.szep@kcl.ac.uk

Attila Csikász-Nagy

Pázmány Péter Catholic University
Budapest, 1083, Hungary
csikasnagy@gmail.com

Neil Dalchau

Microsoft Research Cambridge
Cambridge, CB1 2FB, UK
ndalchau@gmail.com

Abstract

Estimation of parameters in differential equation models can be achieved by applying learning algorithms to quantitative time-series data. However, sometimes it is only possible to measure qualitative changes of a system in response to a controlled condition. In dynamical systems theory, such change points are known as *bifurcations* and lie on a function of the controlled condition called the *bifurcation diagram*. In this work, we propose a gradient-based approach for inferring the parameters of differential equations that produce a user-specified bifurcation diagram. The cost function contains an error term that is minimal when the model bifurcations match the specified targets and a bifurcation measure which has gradients that push optimisers towards bifurcating parameter regimes. The gradients can be computed without the need to differentiate through the operations of the solver that was used to compute the diagram. We demonstrate parameter inference with minimal models which explore the space of saddle-node and pitchfork diagrams and the genetic toggle switch from synthetic biology. Furthermore, the cost landscape allows us to organise models in terms of topological and geometric equivalence.

1 Introduction

Inverse problems [1] arise in biology and engineering in settings when the model is not fully known and the desire is to match model behaviour to a given set of observations. This helps systematically guide both model and experimental design. While we would like to understand the quantitative details of a system, often only qualitative changes in response to varying experimental conditions can be robustly measured across independent studies [2, 3]. For example, several studies are likely to agree that the human immune system activates above a threshold concentration of a pathogen and deactivates at a lower threshold concentration, but may disagree on the exact quantities of the thresholds or the magnitudes of the immune response. Bifurcation theory provides us a framework for studying these transitions in a manner that is independent of quantitative details [4]. The emerging picture suggests that identification of the qualitative behaviour – the bifurcation diagram – should precede any attempt at inferring other properties of a system [5].

Inferring the parameters of a model directly from a bifurcation diagram is difficult because it is not obvious how multiple parameters in concert control the existence and position of a bifurcation. It could even be impossible for the model to bifurcate in the manner desired. For models with a sufficiently small number of parameters, finding specific bifurcation diagrams is typically done by

hand [6]. Several approaches exist to place bifurcations to desired locations once a manifold is present [7–9] yet typically resort to sampling techniques to search for them in the first place [10, 11]. It is always possible to design bespoke goodness of fit measures to find specific model behaviours, for example using the period and phase of limit cycle oscillations [12]. However, this approach does not generalise across a wider set of qualitative behaviours. Progress has been made in cases where model structure and stability conditions are used to refine the search space [13, 14] yet the resulting objectives are still not explicit in the bifurcation targets and also not differentiable. In the emerging field of scientific machine learning [15–17], parameters of structured mechanistic models are favoured over flexible models in larger parameter spaces. A scalable method for navigating the space of bifurcation diagrams would enable design of differential equations with high-level qualitative constraints. Furthermore one could begin organising models according to qualitatively distinct behaviours.

Back-propagation through differential equation solvers has been a breakthrough over the past couple of years [18, 19] that enabled scalable parameter inference for differential equations from trajectory data. Although one could use trajectory data to create the aforementioned qualitative constraints [20, 21] this would entail over-constraining information originating from the kinetics and dynamical transients of the model. Furthermore, such data usually does not contain sufficient information about dynamical transients in order to identify kinetic parameters. Techniques for back-propagating through implicit equation solvers have also been developed [22, 23] although to the best of the authors' knowledge have not been applied to bifurcation diagrams at the time of writing this paper.

The problem of inferring differential equation parameters against a user-specified bifurcation diagram decomposes into two parts: searching for bifurcating regimes and matching the locations of bifurcation points to desired values. Matching bifurcation locations is a supervised problem where the data are expressed as bifurcations points [8, 11]. Searching for bifurcations is an unsupervised problem because when bifurcations are not present, there is no distance defined between data and prediction [10]. Therefore only properties of the model can be used to start the search. We propose an approach for performing both tasks in an end-to-end fashion. The bifurcation diagram encodes high-level qualitative information defined by state space structures, rather than kinetics. We apply the strategy of implicit layers [22, 23] to calculate gradients. To compute the diagram we use a predictor-corrector method called deflated continuation [24, 25] developed for partial differential equations.

We find that the cost function landscape contains basins that not only allow us to synthesise models with a desired bifurcation diagram but also allow us to organise models in terms of topological and geometric equivalence. We discuss the relevance of this in model selection. In summary, our paper has the following main contributions:

- An end-to-end differentiable method for locating bifurcations in parameter space and then matching their dependency on a control condition to user-specified locations
- Implementation of the method as a Julia package `BifurcationInference.jl`
- Leveraging the cost landscape for a novel way of organising differential equation models in terms of geometric and topological equivalence

1.1 Preliminaries

Suppose we collected observations along a scalar control condition $p \in \mathbb{R}$ and conclude that there are specific values of p for which there are qualitative changes in system behaviour. Let \mathcal{D} be the set of those values and let us hypothesise that these transitions occur due to bifurcations in the dynamics that drive the underlying mechanism. Let us model the mechanism with a parametrised set of differential equations for states $u \in \mathbb{R}^N$ with a vector function F_θ in a parameter space $\theta \in \mathbb{R}^M$.

For the purposes of introducing this work, we will consider the simplest class of bifurcations known as *co-dimension one* bifurcations not including limit cycles. Therefore \mathcal{D} should contain conditions for which we hypothesise changes in multi-stable behaviour. Let the equations be

$$\frac{\partial u}{\partial t} = F_\theta(u, p) \quad \text{where} \quad F_\theta : \mathbb{R}^{N+1} \rightarrow \mathbb{R}^N \quad (1)$$

In the context of the differential equations, and not considering limit cycles for now, we show that a static non-degenerate bifurcation can be defined by a set of conditions on the determinant of the Jacobian $|\frac{\partial F_\theta}{\partial u}|$. The determinant of the Jacobian quantifies the rate at which trajectories in a local

patch of state-space $u \in \mathbb{R}^N$ converge or diverge. Let $s \in \mathbb{R}$ parametrise the curves that trace out the bifurcation diagram. Any location on the curve $u(s)$ and $p(s)$ must satisfy the steady-state of equations (1). Directional derivatives $\frac{d}{ds}$ along the diagram require the calculation of a vector that is tangent to the diagram (see Supplementary A). The determinant approaching zero along the diagram means that the dynamics of the system are slowing down, which is an important indicator for the onset of a transition between qualitative behaviours. Furthermore, the slowing down must necessarily be followed by a breakdown of stability; for this to be true it is sufficient *but not necessary* to require that the determinant cross zero with a finite slope, meaning that its directional derivative along the diagram $\frac{d}{ds} \left| \frac{\partial F_\theta}{\partial u} \right|$ is not zero. This is the non-degeneracy condition. The set of predicted values for the control condition $\mathcal{P}(\theta) \subset \mathbb{R}$ at which bifurcations occur are defined as

$$\mathcal{P}(\theta) := \left\{ p \mid \exists u : F_\theta(u, p) = 0, \left| \frac{\partial F_\theta}{\partial u} \right| = 0, \frac{d}{ds} \left| \frac{\partial F_\theta}{\partial u} \right| \neq 0 \right\} \quad (2)$$

A proof of how the conditions (2) are necessary and sufficient for static non-degenerate bifurcations is detailed in Supplementary B. The most common bifurcations between steady states, not including limit cycles, are saddle-nodes and pitchforks [26]. Saddle-node bifurcations, which often appear in pairs (Figure 1A) are defined by stable and unstable fixed points meeting and disappearing. Pitchfork bifurcations occur where a single steady state splits into two stable and one unstable steady state (Figure 1B shows an *imperfect* pitchfork; a *perfect* pitchfork arises when $\theta_1 = 0$). To illustrate these bifurcations, we define minimal models (Figure 1) that span the space of saddle-node and pitchforks, where indeed zero crossings in the determinant with a finite slope define the set of prediction $\mathcal{P}(\theta)$. The location of these crossings in general may not match the targets \mathcal{D} .

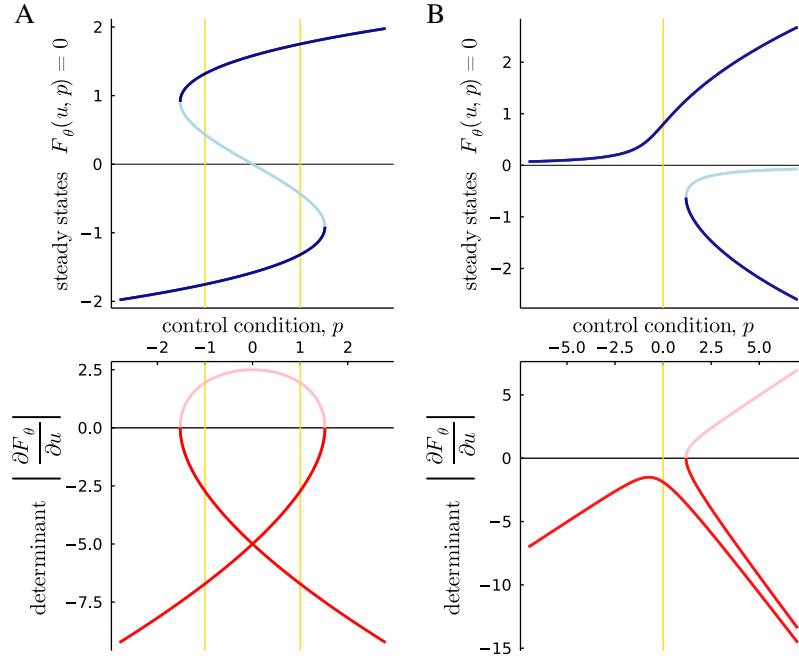


Figure 1: Illustration of bifurcation diagrams for minimal models of bifurcations. A. Saddle-node bifurcations arise for $F_\theta(u, p) = p + \theta_1 u + \theta_2 u^3$ when $\theta = (\frac{5}{2}, -1)$. B. Pitchfork bifurcations arise for $F_\theta(u, p) = \theta_1 + pu + \theta_2 u^3$ when $\theta = (\frac{1}{2}, -1)$. Targets are illustrated by light yellow vertical lines. Bifurcation curves are shown as solid blue and red lines, with lighter shades indicating the determinant crossing zero at locations $\mathcal{P}(\theta)$ giving rise to unstable solutions.

For a given set of parameters θ one could compute the set of predicted bifurcations $\mathcal{P}(\theta)$ using parameter continuation methods [25, 24]. Our goal is to find optimal parameters θ^* that match predictions $\mathcal{P}(\theta^*)$ to specified targets \mathcal{D} . We must design a suitable cost function L so that

$$\theta^* := \operatorname{argmin}_\theta L(\theta|\mathcal{D}) \quad (3)$$

The optimal θ^* is not expected to always be unique, but is in general a manifold representing the space of qualitatively equivalent models. Ideally, the cost function L should reward θ for which the number of predicted bifurcations is equal to the number of targets, $|\mathcal{P}(\theta)| = |\mathcal{D}|$. This is especially important in the case where there are no predictions $|\mathcal{P}(\theta)| = 0$.

2 Proposed Method

2.1 Cost Function

To identify parameter sets that give rise to bifurcation diagrams with specified bifurcation points, we propose a cost function that comprises two terms. The role of the error term is simply to reward predicted bifurcations to coincide with the specified target locations. This of course relies on such bifurcations existing. The role of the eigenvalue term is to encourage an optimiser to move towards parameter regimes that do exhibit bifurcations.

2.1.1 Error term: matching bifurcations to target locations

In order for predicted bifurcations $p(\theta) \in \mathcal{P}(\theta)$ to match targets $p' \in \mathcal{D}$ we need to evaluate an error term $|p(\theta) - p'|$. A naive approach might take an average over the norms for all prediction-target pairs. However this gives rise to unwanted cross-terms and the possibility of multiple predictions matching the same target without any penalty for unmatched targets. Therefore, we choose a geometric mean over the predictions and an arithmetic mean over targets:

$$E(\theta, \mathcal{D}) = \frac{1}{|\mathcal{D}|} \sum_{p' \in \mathcal{D}} \prod_{p(\theta) \in \mathcal{P}(\theta)} |p(\theta) - p'|^{\frac{1}{|\mathcal{P}|}} \quad (4)$$

The error term is only zero when each target is matched by at least one prediction and allows for cases where the number of predictions is greater than or equal to the number of targets $|\mathcal{P}| \geq |\mathcal{D}|$. An alternative approach, which undesirably introduces more hyper-parameters, would be to let each prediction $\mathcal{P}(\theta)$ represent the centroid of a mixture distribution and use expectation-maximisation to match the centroids to targets \mathcal{D} .

2.1.2 Eigenvalue term: encouraging bifurcations

We can see from Figure 1 and definition (2) that predictions $p(\theta)$ can be identified by looking for points along the curve where the determinant crosses zero $|\frac{\partial F_\theta}{\partial u}| = 0$ with a finite slope $\frac{d}{ds} |\frac{\partial F_\theta}{\partial u}| \neq 0$. Using these quantities we can define a positive semi-definite measure $\varphi_\theta(s)$ of zero crossings in the determinant along a curve parametrised by s which we define as

$$\varphi_\theta(s) := \left(1 + \left| \frac{\frac{d}{ds} |\frac{\partial F_\theta}{\partial u}|}{\frac{d}{ds} |\frac{\partial F_\theta}{\partial u}|} \right| \right)^{-1} \quad (5)$$

The bifurcation measure $\varphi_\theta(s)$ is maximal at bifurcations and has finite gradients in non-bifurcating regimes (Figure 2). More specifically, the measure $\varphi_\theta(s)$ is one at bifurcation points and goes to zero an odd number of times between bifurcations. This is because $|\frac{\partial F_\theta}{\partial u}|$ must eventually turn around in order to return back to zero, resulting in the directional derivative $\frac{d}{ds} |\frac{\partial F_\theta}{\partial u}|$ going to zero. Hence the measure $\varphi_\theta(s)$ goes to zero for each turning point (see Figure 2).

On the other hand, as the determinant $|\frac{\partial F_\theta}{\partial u}|$ diverges, we approach regimes far away from any bifurcations and hence $\varphi_\theta(s) \rightarrow 0$. Since we would still like to have non-zero gradients with respect to θ in these regimes we designed the measure to go to zero sufficiently slowly.

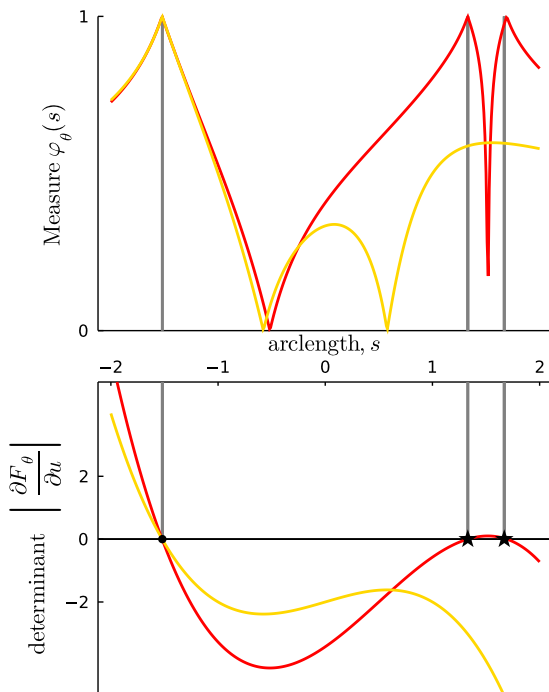


Figure 2: Bifurcation measure $\varphi_\theta(s)$ and determinant $|\frac{\partial F_\theta}{\partial u}|$ along the arclength s of two different bifurcation curves demonstrating how maximising the measure along the curve maintains the existing bifurcation marked by a circle, while encouraging new bifurcations marked by stars.

While the calculation of the determinant is straightforward, its directional derivative requires a tangent vector to the bifurcation curve. Fortunately the tangent vector $T_\theta(s)$ at the solution $u(s), p(s)$ anywhere along the curve s can be calculated as the nullspace of the rectangular $N \times (N + 1)$ Jacobian

$$\frac{\partial F_\theta}{\partial(u, p)} \Big|_{F_\theta(u(s), p(s))=0} \cdot T_\theta(s) = 0 \quad (6)$$

This equation guarantees that the tangent vector $T_\theta(s)$ is orthogonal to all hyper-planes defined by the components of F_θ . In this setting the dimension of the nullspace is always known, and therefore can reliably be calculated using QR factorisation methods [27].

Equipped with a measure that quantifies the appearance of bifurcations along a bifurcation arc we can define the total measure for a bifurcation diagram as

$$\Psi(\theta) := \frac{\int_{F_\theta(u, p)=0} \varphi_\theta(s) ds}{\int_{F_\theta(u, p)=0} ds}. \quad (7)$$

Here we denote $\int_{F_\theta(u, p)=0} ds$ as the sum of the line integrals in $(u, p) \in \mathbb{R}^{N+1}$ defined by the level set $F_\theta(u, p) = 0$ with s being an arbitrary parametrisation of the curves. The total measure $\Psi(\theta)$ is normalised such that $\Psi(\theta) \rightarrow 1$ in the regimes where the controlled condition region p is densely packed with bifurcations. The total measure $\Psi(\theta)$ is added to the error term as if it were a likelihood. This defines the cost function as

$$L(\theta|\mathcal{D}) := (|\mathcal{P}| - |\mathcal{D}|) \log \Psi(\theta) + E(\theta, \mathcal{D}), \quad (8)$$

The pre-factor $|\mathcal{D}| - |\mathcal{P}|$ in the eigenvalue term ensures that the gradients are always pushing optimisers towards a state where $|\mathcal{D}| = |\mathcal{P}|$. This can be seen as a step-wise annealing of the eigenvalue term until the desired state is reached.

2.2 Differentiating the cost function

To make use of gradient-based optimisers to locate desired bifurcation diagrams, we show here how to differentiate the cost function. First, we note that while individual bifurcations $p(\theta)$ depend smoothly on θ , the total number of predictions $|\mathcal{P}|$ does not have gradient contributions with respect to θ . Therefore, we can safely drop the dependency in the prediction counter and now proceed in taking gradients with respect to θ knowing that the only dependencies we need to track are for individual bifurcations $p(\theta)$ within the definition the error term (4) and the total measure (7). Therefore,

$$\frac{\partial L}{\partial \theta} = (|\mathcal{P}| - |\mathcal{D}|) \lambda \frac{\partial \Psi}{\partial \theta} \Psi(\theta)^{-1} + \frac{1}{|\mathcal{D}||\mathcal{P}|} \sum_{p'} \prod_{p(\theta)} |p(\theta) - p'|^{\frac{1}{|\mathcal{P}|}} \sum_{p(\theta)} \frac{\partial p}{\partial \theta} (p(\theta) - p')^{-1} \quad (9)$$

In a similar vein to back-propagation through neural differential equations [18] we would like to be able to calculate the gradient $\frac{\partial L}{\partial \theta}$ without having to differentiate through the operations of the solver that finds the bifurcation diagram $F_\theta(u, p) = 0$ and the bifurcation locations $p(\theta)$. To calculate the gradient of the measure $\frac{\partial \Psi}{\partial \theta}$ we need to differentiate line integrals that depend on θ . Fortunately this can be done by the application of the generalised Leibniz integral rule, details of which can be found in Supplementary C.

The gradient of the bifurcation points $\frac{\partial p}{\partial \theta}$ is found by application of the implicit function theorem to a vector function $G_\theta : \mathbb{R}^{N+1} \rightarrow \mathbb{R}^{N+1}$ whose components represent the two constraints $F_\theta(u, p) = 0$ and $|\frac{\partial F_\theta}{\partial u}| = 0$. By following a similar strategy to that used by implicit layers [22] we yield an $(N + 1) \times M$ Jacobian representing a deformation field [28] for each θ direction. The gradient we are looking for becomes

$$\frac{\partial p}{\partial \theta} = -\hat{p} \cdot \frac{\partial G_\theta}{\partial(u, p)}^{-1} \frac{\partial G_\theta}{\partial \theta} \Big|_{G_\theta(u, p)=0} \quad \text{where} \quad G_\theta(u, p) := \begin{bmatrix} F_\theta(u, p) \\ |\frac{\partial F_\theta}{\partial u}| \end{bmatrix} \quad (10)$$

Here \hat{p} is a unit vector in $(u, p) \in \mathbb{R}^{N+1}$ that picks out the deformations along the p -direction. If we wanted to place the bifurcation at target steady state u' as well as target control condition p' we would use the full $(N + 1) \times M$ deformation matrix. Calculation of this matrix involves inverting an

$(N + 1) \times (N + 1)$ Jacobian $\frac{\partial G_\theta}{\partial(u,p)}$. Instead of explicitly inverting the Jacobian the corresponding system of linear equations is solved. The determinant of this Jacobian goes to zero in the degenerate case where $\frac{d}{ds} |\frac{\partial F_\theta}{\partial u}| = 0$, further justifying our choice of measure $\Psi(\theta)$ which discourages the degenerate case.

The cost function is piece-wise smooth and differentiable with undefined gradients only in parameter contours where the number of predictions $|\mathcal{P}|$ changes; this is when $\Psi(\theta)$ is undefined and the inverse of $\frac{\partial G_\theta}{\partial(u,p)}$ does not exist. Given a set of solutions to $F_\theta(u, p) = 0$ and locations $p(\theta)$ the gradient $\frac{\partial L}{\partial \theta}$ can be evaluated using automatic differentiation methods [29–31] without needing to back-propagate through the solver that obtained the level set $F_\theta(u, p) = 0$ in the forward pass.

3 Experiments & Results

In this section, we apply the method first to minimal examples that can produce saddle-node and pitchfork bifurcations (both $N = 1, M = 2$), and then a slightly more complex model ($N = 2, M = 5$) that has multiple parametric regimes producing saddle-node bifurcations. We also demonstrate our method on a model of greater complexity, to convince the reader that the method can be used on more realistic examples with practical significance. In Supplementary D we demonstrate the identification of saddle-node bifurcations and damped oscillations in a model ($N = 4, M = 21$) of a synthetic gene circuit in *E. coli* [3].

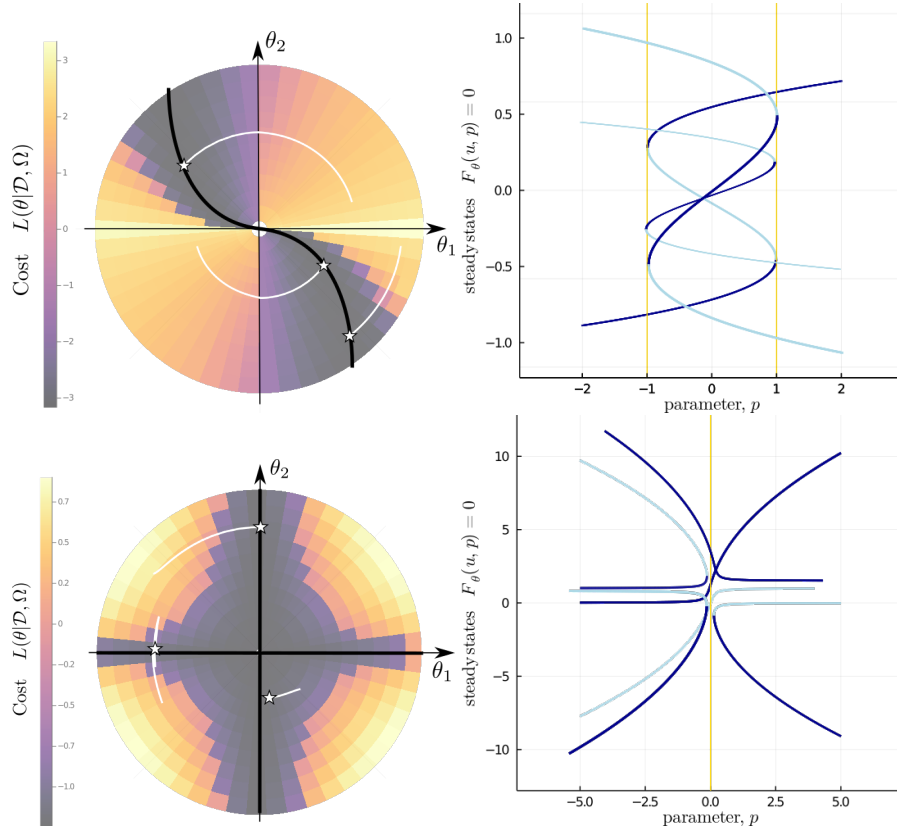


Figure 3: Saddle-node $F_\theta(u, p) = p + \theta_1 u + \theta_2 u^3$ and pitchfork $F_\theta(u, p) = \theta_1 + up + \theta_2 u^3$ optimised with respect to θ so that predicted bifurcations $\mathcal{P}(\theta)$ match targets \mathcal{D} in control condition p . The right panel shows bifurcation diagrams for the three optimal θ^* marked by stars on the left panel. The optimisation trajectories in white follow the gradient of the cost, approaching the black lines of global minima in the left panel

3.1 Minimal Models

Optimisations of two parameters (θ_1, θ_2) using simple gradient descent from Flux.jl with learning rate $\eta = 0.01$ for the minimal saddle-node and pitchfork models (Figure 1) yield trajectories approach-

ing lines of global minima in the cost function (Figures 3) which represent a set of geometrically equivalent models. Two bifurcation diagrams are geometrically equivalent if the number, type and locations of bifurcations match the specified targets \mathcal{D} .

We can see that the geometrically equivalent lines are contained within larger basins where the correct number and type of bifurcations are present but do not match the locations of targets \mathcal{D} . All models within this basin are in some sense topologically equivalent. This hierarchical classification allows us to identify the set of models that satisfy observed qualitative behaviour [5] before any attempt at inferring kinetic parameters, which is done by choosing a model along the line of geometrically equivalent models.

Optimisation trajectories for the two minimal models appear mostly circumferential. This is because the models were set up such that the radial direction from the origin in θ space mostly scale kinetics whereas the circumferential direction changes the bifurcation topology. This suggests that the gradients of our cost function seek to change model geometry over kinetics.

3.2 Genetic Toggle Switch

In this section we optimise a model where the states share a Hill function relationship with co-operatively $n = 2$; these models often emerge from mass action kinetics with quasi-steady state approximations and are used to model species concentrations. After re-scaling the equations governing the dynamics of concentrations, the simplified equations for state u_1 and u_2 become

$$\partial_t u_1 = \frac{a_1 + (pu_2)^2}{1 + (pu_2)^2} - \mu_1 u_1 \quad \partial_t u_2 = \frac{a_2 + (ku_1)^2}{1 + (ku_1)^2} - \mu_2 u_2 \quad (11)$$

where a_k is the baseline production rate for species k in the absence of the other species. Each species has a finite degradation rate μ_k . Finally we have two sensitivity constants p and k , one of which is chosen as our control condition. A baseline production rate $a_k > 1$ recovers an inhibitor type hill function for species k and is an activator otherwise. The sensitivities are proportional to the slope of the hill productions. Solving for the steady states, substituting the equation for u_1 into u_2 and rearranging gives rise to the relationship

$$\frac{k}{\mu_1} = \frac{(1 + (\frac{p}{\mu_2}u')^2)\sqrt{a_2 - u'}}{(a_1 + (\frac{p}{\mu_2}u')^2)\sqrt{u' - 1}} \quad \text{where} \quad u' := u_2\mu_2 \quad (12)$$

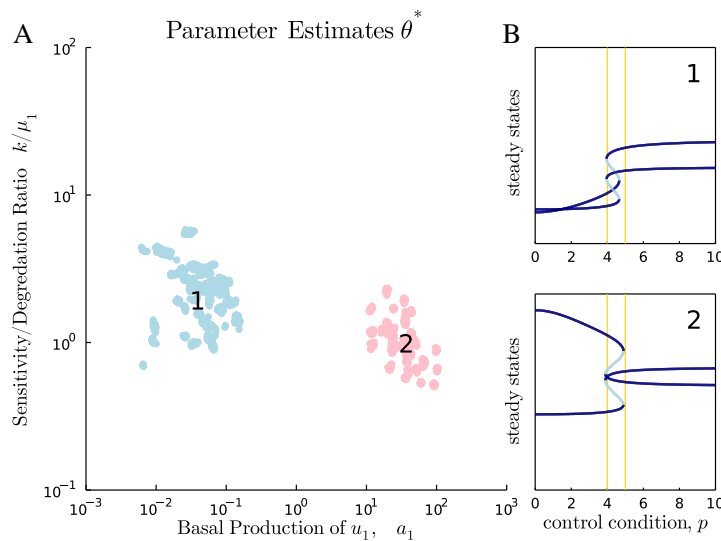


Figure 4: Bifurcation inference for the two-state model (11). A. Optimal parameter estimates θ^* for the targets $\mathcal{D} = \{4, 5\}$ reveal two clusters of qualitatively different regimes: mutual activation ($a_1 < 1$; cluster 1) and mutual inhibition ($a_1 > 1$; cluster 2). B. Example bifurcation diagrams indicate positively and negatively correlated dependencies between the two model states, as a function of the control condition.

which reveals that only a_1, a_2 and the ratio between the sensitivity and degradation parameters, $\frac{k}{\mu_1}$, affect the solutions to this equation, and hence the locations of the bifurcations (Figure 4A). In 98% of 800 runs, optimisation using the ADAM optimiser [32] from Flux.jl with learning rate $\eta = 0.1$ converged to one of two clusters: mutual activation ($a_1 < 1, a_2 < 1$; cluster 1) and mutual inhibition ($a_1 > 1, a_2 > 1$; cluster 2) regimes. Example bifurcation diagrams illustrate how the bifurcation curves of each species are positively correlated in mutual activation and negatively correlated for mutual inhibition (Figure 4B).

In order to maintain biological interpretability, optimisation was restricted to the positive parameter regime by transforming the parameters to log-space $\theta \rightarrow 10^\theta$. At the beginning of each optimisation run an initial θ was chosen in the log-space by sampling from a multivariate normal distribution with mean zero and standard deviation one.

3.3 Complexity

Performing one iteration of the optimisation requires the computation of the gradient of the cost (9), requiring a computation of the bifurcation diagram with parameter continuation methods, which includes the evaluation of matrix inversions (10). Instead of evaluating the inversions directly, we solve a system of linear equations, applying the same strategy as implicit layers [22, 23]. This leaves us with the computational bottleneck of calculating the determinant of the state space Jacobian, required in both the bifurcation measure (5) and gradient (10). This calculation scales like N^2 where N is the number of state space variables (Figure 5A).

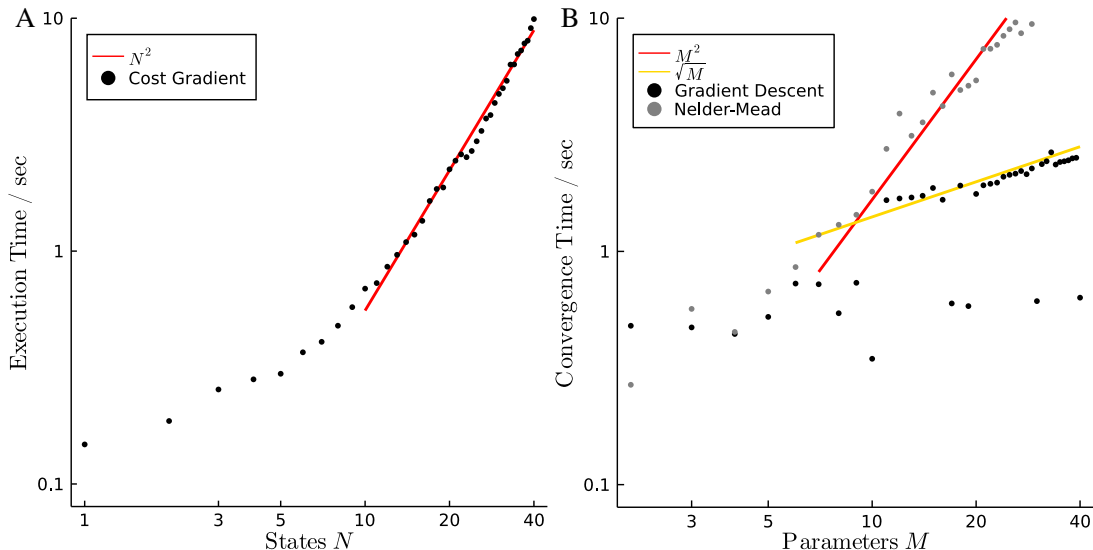


Figure 5: A. Execution time (time to calculate cost gradient) with respect to states N . B. Convergence times (the time it takes to find and match a bifurcation to within 1% of a specified target) with respect to the number of parameters M , comparing against a gradient-free approach: Nelder-Mead. Calculations were performed on an Intel Core i7-6700HQ CPU @ 2.60GHz x 8 without GPU acceleration.

For the complexity study, a model was designed so that it is extensible both in the number of parameters M and the number of states N . There are many choices for this; we opted for a model of the form

$$\begin{cases} \partial_t u_1 = \sin^2 p - (\theta_1 \sin^2 p + 1)u_1 \\ \partial_t u_n = u_{n-1} - (\mu_n^2 + 1)u_n \end{cases} \quad 2 \leq n \leq N \quad (13)$$

In this model only the first state u_1 defines the shape of the bifurcation diagram, while the remaining states are merely linearly proportional to the first. The parameters μ_n contain sums of θ_m allowing us a flexible choice on the number of parameters while maintaining stable solutions for the bifurcation diagram.

While still tractable on laptop computers for states $N < 100$ our implementation currently does not scale well for partial differential equations where a large the number of states N arises from discretisation of the spatial variables. The only reason we need this determinant is because it

is an indicator of bifurcations. We can address the computational bottleneck by finding a more computationally efficient way of calculating this indicator. One approach would be to take the product of a finite subset of eigenvalues of the system. Note that any more efficient calculation must still permit back-propagation through it.

To demonstrate the benefits of the gradient-based aspect of our method we compare convergence times of gradient descent against a gradient-free approach. We use the Nelder-Mead method from `Optim.jl` [33] and obtain convergence times as the number of parameters M is increased (Figure 5B). We observe that for our method convergence times scale like \sqrt{M} compared to M^2 for the gradient-free approach.

4 Conclusion & Broader Impact

We proposed a gradient-based approach for inferring the parameters of differential equations that produce a user-specified bifurcation diagram. By applying implicit layers [22, 23] and the generalised Leibniz rule [34] to the geometry of the implicitly defined steady states [35] it is possible to use automatic differentiation methods to efficiently calculate gradients. We defined a bifurcation measure that uses the determinant of the state-space Jacobian as an indicator for bifurcating parameter regimes in the eigenvalue term of the cost function. The gradients of the cost can be efficiently computed using automatic differentiation methods. The computational bottleneck is the evaluation of the state-space Jacobian determinant which limits the implementation to ordinary differential equations.

We demonstrated our approach on models with one bifurcation parameter that can give rise to pitchforks and saddle-nodes. The estimated parameters form distinct clusters, allowing us to organise models in terms of topological and geometric equivalence (Figure 3). In the case of the genetic toggle switch (Figure 4) and a more complex model [3] (Figure D.1) we recovered mutual activation and inhibition regimes. In the more complex model we found a damped oscillatory regime that was not known about in the original paper.

Although we did not consider limit cycles, the bifurcation measure can be extended to detect Poincaré-Andronov-Hopf bifurcations alongside changes in stability of fixed points (see Supplementary E for details). This measure enables detection of the onset of damped oscillations and/or the emergence of limit cycles (Figure E.1). Used together with a steady state solver that detects periodic solutions and gradient-based optimisation, we can specify regions of damped oscillation and limit cycles. Our approach generalises naturally to bifurcation manifolds such as limit point curves or surfaces. This is because the normal components of implicit derivatives can still be calculated for under-determined systems of equations [28, 36, 37]. In the case of manifolds it would be more appropriate to use isosurface extraction algorithms rather than continuation to obtain the steady-state manifold. Our approach does not depend on the details of the steady-state solver and therefore can still be applied.

In dynamical systems theory the geometry of state-space determines all of the qualitative behaviours of a system. Our work makes progress towards designing models directly in state-space, rather than the spatial or temporal domain. This is valuable to experimentalists who only have qualitative observations available to them and wish to navigate the space of qualitative behaviours of their system. Our work lies within a trend of progress in the scientific machine learning community, where structured domain-informed models are favoured over flexible models that live in large parameter spaces.

5 Acknowledgements

We would like to acknowledge Kieran Cooney for the fruitful conversations that helped guide the derivations and computational approach. A special thanks go to Romain Veltz and the Julia community for helpful pointers on package development and discussions over Slack. This work was supported by Microsoft Research through its PhD Scholarship Programme and the EPSRC Centre for Doctoral Training in Cross-Disciplinary Approaches to Non-Equilibrium Systems (CANES, EP/L015854/1).

References

- [1] U. G. Abdulla, R. Poteau, A. Binder, H. W. Engl, C. Flamm, P. K. Å. Ugler, J. Lu, S. M. Å. Uller, and P. Schuster, “Inverse problems in systems biology,” *Inverse Problems*, vol. 25, p. 51, 2009.
- [2] J. J. Tyson, K. Chen, and B. Novak, “Network dynamics and cell physiology,” *Nature reviews Molecular cell biology*, vol. 2, no. 12, pp. 908–916, 2001.
- [3] P. Grant, G. Szep, O. Patange, J. Halatek, V. Coppard, A. Csikász-Nagy, J. Haseloff, J. Locke, N. Dalchau, and A. Phillips, “Interpretation of morphogen gradients by a synthetic bistable circuit,” *Nature Communications*, vol. 11, no. 1, 2020.
- [4] Y. A. Kuznetsov, “Topological Equivalence, Bifurcations, and Structural Stability of Dynamical Systems,” in *Elements of Applied Bifurcation Theory*, pp. 39–76, Springer New York, 2004.
- [5] M. P. H. Stumpf and E. Roesch, “Parameter inference in dynamical systems with co-dimension 1 bifurcations,” *Royal Society*, vol. 6, no. 10, 2019.
- [6] A. Csikász-Nagy, D. Battogtokh, K. C. Chen, B. Novák, and J. J. Tyson, “Analysis of a Generic Model of Eukaryotic Cell-Cycle Regulation,” *Biophysical Journal*, vol. 90, pp. 4361–4379, 6 2006.
- [7] K. Iwasaki and Y. Kamimura, “An inverse bifurcation problem and an integral equation of the Abel type,” *Inverse Problems*, vol. 13, pp. 1015–1031, 1997.
- [8] J. Lu, H. W. Engl, and P. Schuster, “Inverse bifurcation analysis: Application to simple gene systems,” *Algorithms for Molecular Biology*, vol. 1, pp. 1–16, 7 2006.
- [9] I. Dobson, “Distance to Bifurcation in Multidimensional Parameter Space: Margin Sensitivity and Closest Bifurcations,” in *Bifurcation Control: Theory and Applications*, pp. 49–66, Springer, Berlin, Heidelberg, 4 2004.
- [10] V. Chickarmane, S. R. Paladugu, F. Bergmann, and H. M. Sauro, “Bifurcation discovery tool,” *BIOINFORMATICS APPLICATIONS NOTE*, vol. 21, no. 18, pp. 3688–3690, 2005.
- [11] E. D. Conrad, J. Tyson, R. Laubenbacher, J. Phillips, and M. Renardy, “Bifurcation Analysis and Qualitative Optimization of Models in Molecular Cell Biology with Applications to the Circadian Clock,” *Virginia Tech*, 4 2006.
- [12] J. C. W. Locke, A. J. Millar, and M. S. Turner, “Modelling genetic networks with noisy and varied experimental data: the circadian clock in *Arabidopsis thaliana*,” *Journal of theoretical biology*, vol. 234, no. 3, pp. 383–393, 2005.
- [13] I. Otero-Muras and J. R. Banga, “Optimization-based prediction of fold bifurcations in nonlinear ODE models,” *IFAC-PapersOnLine*, vol. 51, pp. 485–490, 1 2018.
- [14] I. Otero-Muras, P. Yordanov, and J. Stelling, “A method for inverse bifurcation of biochemical switches: inferring parameters from dose response curves,” *BMC Systems Biology*, vol. 8, p. 114, 2014.
- [15] C. Rackauckas and Q. Nie, “Differentialequations.jl - a performant and feature-rich ecosystem for solving differential equations in julia,” *Journal of Open Research Software*, vol. 5, no. 1, 2017.
- [16] C. Rackauckas, Y. Ma, V. Dixit, X. Guo, M. Innes, J. Revels, J. Nyberg, and V. Ivaturi, “A comparison of automatic differentiation and continuous sensitivity analysis for derivatives of differential equation solutions,” *arXiv preprint arXiv:1812.01892*, 2018.
- [17] C. Rackauckas, Y. Ma, J. Martensen, C. Warner, K. Zubov, R. Supekar, D. Skinner, and A. Ramadhan, “Universal Differential Equations for Scientific Machine Learning,” *arXiv*, 2020.
- [18] R. T. Q. Chen, Y. Rubanova, J. Bettencourt, and D. Duvenaud, “Neural Ordinary Differential Equations,” *NIPS*, vol. 109, pp. 31–60, 6 2018.

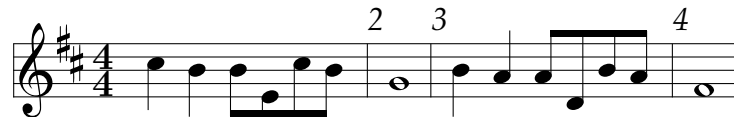
- [19] C. Rackauckas, M. Innes, Y. Ma, J. Bettencourt, L. White, and V. Dixit, “DiffEqFlux.jl - A Julia Library for Neural Differential Equations,” *ArXiv*, 2019.
- [20] S. Ranciati, C. Viroli, and E. Wit, “Bayesian Smooth-and-Match strategy for ordinary differential equations models that are linear in the parameters,” *ArXiv*, 2017.
- [21] F. Khadivar, I. Lauzana, and A. Billard, “Learning dynamical systems with bifurcations,” *Robotics and Autonomous Systems*, vol. 136, p. 103700, 2 2021.
- [22] A. Look, S. Doneva, M. Kandemir, R. Gemulla, and J. Peters, “Differentiable Implicit Layers,” *ArXiv*, 10 2020.
- [23] S. Bai, J. Z. Kolter, and V. Koltun, “Deep Equilibrium Models,” *arXiv*, 9 2019.
- [24] P. E. Farrell, C. H. L. Beentjes, and Å. Birkisson, “The computation of disconnected bifurcation diagrams,” *arXiv*, 3 2016.
- [25] R. Veltz, “BifurcationKit.jl,” tech. rep., Inria Sophia-Antipolis, 7 2020.
- [26] M. Haragus and G. Iooss, *Local Bifurcations, Center Manifolds, and Normal Forms in Infinite-Dimensional Dynamical Systems*. London: Springer London, 2011.
- [27] Z. Drmač and Z. Bujanović, “On the Failure of Rank-Revealing QR Factorization Software – A Case Study,” *ACM Transactions on Mathematical Software*, vol. 35, 7 2008.
- [28] S. Jos and R. Schmidt, “On the velocity of an implicit surface,” *ACM Transactions on Graphics*, vol. 30, pp. 1–7, 5 2011.
- [29] J. Revels, M. Lubin, and T. Papamarkou, “Forward-Mode Automatic Differentiation in Julia,” *ArXiv*, 2016.
- [30] M. Innes, E. Saba, K. Fischer, D. Gandhi, M. C. Rudilosso, N. M. Joy, T. Karmali, A. Pal, and V. Shah, “Fashionable Modelling with Flux,” *CoRR*, vol. abs/1811.01457, 2018.
- [31] M. Innes, “Flux: Elegant Machine Learning with Julia,” *Journal of Open Source Software*, 2018.
- [32] D. P. Kingma and J. Ba, “Adam: A Method for Stochastic Optimization,” *arXiv*, 12 2014.
- [33] P. K. Mogensen and A. N. Riseth, “Optim: A mathematical optimization package for Julia,” *Journal of Open Source Software*, vol. 3, p. 615, 4 2018.
- [34] H. Flanders, “Differentiation Under the Integral Sign,” *The American Mathematical Monthly*, vol. 80, p. 615, 6 1973.
- [35] R. Goldman, “Curvature formulas for implicit curves and surfaces,” in *Computer Aided Geometric Design*, vol. 22, pp. 632–658, Elsevier, 10 2005.
- [36] M. Tao, J. Solomon, and A. Butscher, “Near-Isometric Level Set Tracking,” *Computer Graphics Forum*, vol. 35, pp. 65–77, 8 2016.
- [37] M. Fujisawa, Y. Mandachi, and K. T. Miura, “Calculation of Velocity on an Implicit Surface by Curvature Invariance,” *Information and Media Technologies*, vol. 8, no. 4, pp. 674–680, 2013.
- [38] M. Kratochvíl, O. Hunewald, L. Heirendt, V. Veríssimo, J. Vondrášek, V. P. Satagopam, R. Schneider, C. Trefois, and M. Ollert, “GigaSOM.jl: High-performance clustering and visualization of huge cytometry datasets,” *GigaScience*, vol. 9, pp. 1–8, 11 2020.

4.8 Afterword

- extension to cusp bifurcation
- extension to spatial system and turing
- designing limit cycles

Chapter 5

Exploring Bifurcations between Phenotypes



Who knows what might happen to those who are consumed by greed

Ocarina of Time

5.1 Preface

5.1.1 Problem Statement & Context

The studies in chapters 3-4 were carried out under the assumption that the underlying microscopic mechanisms that give rise to different phenotypes of an organism are known, and therefore can be modelled with differential equations that have interpretable parameters θ . In section 2.3 we outlined some popular machine learning approaches that can be used in settings where the underlying mechanism is partially or completely unknown. This chapter presents a study in immunology. While detailed models of the immune system exist [], in the advent of high-throughput biology new mechanisms and exceptions are continuously being discovered []. This is done by identifying immune cell populations, their function and mechanism of action from tissue and blood samples taken from an organ-

ism in homeostasis. *Immunophenotyping* methods use antibodies to identify cells based on the types of antigens or markers on their surface. As we shall see, such datasets are typically high-dimensional data clouds that can be reduced with the help of *universal function approximators* and clustered to identify different immune cell phenotypes. Such high-dimensional data clouds also appear in chapter 4 when optimal parameters θ reveal clusters of topologically or geometrically equivalent models.

In this chapter we argue the importance of interactive tools that allow immunologists to navigate high-dimensional data clouds from heterogeneous experimental setups. Such tools enable crowd-sourced consensus phenotyping of cell populations, discovery of rare populations and iterative refinement of a model of the immune system. An interactive tool *FlowAtlas.jl* is presented in an adaptation of a manuscript prepared for *Nature Methods: Brief Communications* at the time of writing the thesis. While the focus of this chapter remained grounded in immunology, we note these methods can be adapted to multi-omics data []. We conclude this chapter with a vision of how approaches in chapters 4 and 5 can be combined to realise a high-throughput *Design-Learn* pipeline.

5.1.2 Contributions

Grisha Szep is co-first author with **Valerie Coppard**. **Joanne Jones**, **Daniel Rainbow**, **Sarah Howlett** and **Lorna Jarvis** conceived and designed the study. [missing name] processed donor tissue samples. **Valerie Coppard** designed the flow cytometry panels and performed the experiments. **Grisha Szep** conceived and implemented computational pipeline and interactive software. All authors analysed and interpreted the data. **Grisha Szep** and **Valerie Coppard** wrote the main text. All authors provided input into the manuscript.

5.2 Abstract

As the dimensionality, throughput and complexity of cytometry data increases, so does the demand for user-friendly, interactive analysis tools that leverage high-performance machine learning frameworks. We introduce FlowAtlas.jl: an interactive web application that bridges the familiar user-friendly environment of FlowJo and computational tools in Julia developed by the rapidly growing scientific machine learning community. We demonstrate the workflow on a novel human multi-tissue, multi-donor dataset, addressing relevant biological questions with examples.

5.3 Introduction

Rapid advancements in the capabilities of flow and mass cytometry have brought about a new era of high-dimensional cell phenotyping. Modern cytometers allow unprecedented ability to measure over 40 parameters [39] and the pace of multi-parametric analyses as well as the development of new dyes, with improved spectral performance, has been accelerating in recent years. However, these technological advancements have not been accompanied by equally impressive developments in user-friendly data analysis tools necessary to deliver a powerful, intuitive and unbiased approach to the analysis of high-dimensional data. At present, exploratory analysis of multi-parametric data presents researchers with a considerable challenge. The widely used commercial platforms such as FlowJo rely on manual sequential cell population gating, best suited for targeted analyses of well-defined cell subsets, rather than exploratory discovery of novel populations in high-complexity datasets. Although an attempt has been made to integrate dimensionality reduction and automated cell population clustering algorithms into these platforms, the algorithm implementations lack flexibility and interactivity and require substantial data down-sampling, ultimately reducing their utility.

To address the need for computational tools designed specifically for

data discovery, exploration and visualisation, a number of stand-alone computational pipelines written in R, Matlab and Python programming languages have been developed. However, despite their advanced capabilities, uptake amongst biomedical researchers remains low - most likely due to the lack of inter-operability with familiar tools such as FlowJo, as well as high entry requirements for computational literacy.

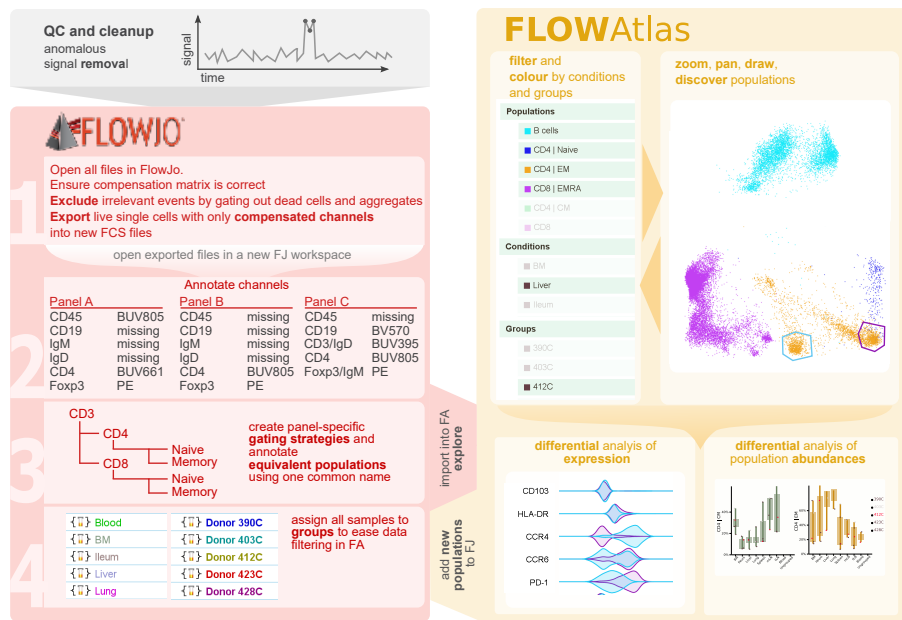


Figure 5.1: Overview of FlowAtlas.jl workflow in tandem with FlowJo

Here, we present FlowAtlas.jl — our effort to address the growing need for high-performance, flexible and interactive analysis tools that enable the visual, exploration and profiling of hundreds of millions of cells in high-dimensional flow cytometry datasets with no data downsampling or command line input. FlowAtlas.jl is fully inter-operable with FlowJo, allows concomitant analysis of datasets created with non-identical panel designs and empowers researchers to explore data in a fully interactive, graphical environment using a new analysis concept. We showcase the capabilities of FlowAtlas.jl using a novel, human flow cytometric dataset, consisting of immune cells extracted from the tissues of five deceased organ donors, collected over a 5-month period and stained using three slightly different

antibody panels.

This work is presented in an effort to strengthen the open-source collaborations between researchers using flow cytometry and the rapidly growing scientific machine learning community in Julia programming language.

5.4 Proposed Method

FlowAtlas.jl is designed to be used in an iterative discovery loop with FlowJo, where traditional gating strategies created in FlowJo provide initial annotation of main populations, conditions, and sample filtering options to guide the discovery of new sub-populations in FlowAtlas.jl, inside and outside of the specified gates. To prevent the need for downsampling, we implemented *EmbedSOM* [40] a powerful dimensionality reduction method. State-of-the-art missing value handling methods and novel features within FlowAtlas.jl also allow users to merge flow cytometry datasets acquired using different antibody panels enabling their concomitant analysis. For example, in our dataset three panel designs were used (see Table C.3), where CD4 was assigned to BUV661 in Panel A and to BUV805 in Panels B and C. In addition, Panel C had three B cell makers not present in Panels A or B, whereas Panel A had CD45 which was not present in Panels B and C. Consequently, three panel-specific gating strategies were created in FlowJo (see Extended Figure 5.2) to define common cell populations. FlowAtlas.jl was then able to seamlessly merge these datasets using channel marker annotations provided by the user in FlowJo, and combine equivalent cell populations based on their annotations irrespective of panel-specific gating strategy. Analysis steps are outlined in Figure 5.1.

5.4.1 Pre-processing

Prior to commencing data analysis, we strongly recommend performing raw data QC and clean up. This is necessary to ensure that acquisition anomalies which often result from sudden flow rate or signal acquisition

instability are detected and removed (Figure 5.1, top grey box). We performed data clean-up using the interactive implementation of FlowAI [41]. This will ensure more accurate and reproducible embedding and analysis results. High quality files were saved and imported into FlowJo for next steps of data pre-processing described below.

Next, the cleaned-up files of all datasets to be analysed are imported into FlowJo. Ensure that compensation matrices of every dataset are correct and create simple gating to exclude dead cells and aggregates (Figure 5.1 FlowJo box, step 1). Following this, we exported terminal live lymphocyte gate in all samples as new FCS files with only compensated fluorescence channels (leaving our scatter channels). Since data embedding is the most computationally intensive step, removal of irrelevant events reduces file size by approximately 40% and results in a substantially shortened embedding times without compromising relevant data. From now on, all analysis is performed with these newly exported files.

5.4.2 Annotation in FlowJo

standard hierarchical gating of high-level cell subsets. Samples acquired with different panel designs should be imported into the same FlowJo workspace but separated into different groups and gated with group-specific gating strategy. The goal is to implement panel-appropriate gating, while defining common cell subsets across all sample groups. It is critical to label equivalent populations across all datasets with a common name irrespective of gating strategy that defines them as they are automatically imported into FlowAtlas.jl and used for all further analysis. For example, CD4 effector memory (CD4EM) T cells can be gated differently depending on panel design as illustrated in our dataset see Extended Figure 5.2 but they should be labelled as CD4EM in every panel. In order to ensure successful panel merging by FlowAtlas.jl, all fluorescent channels must also be annotated with their respective markers in FlowJo. Although panel merging precludes differential analysis of expression densities using MFI values

for non-identical panels, it still allows qualitative and cell frequency comparisons of common populations across such datasets.

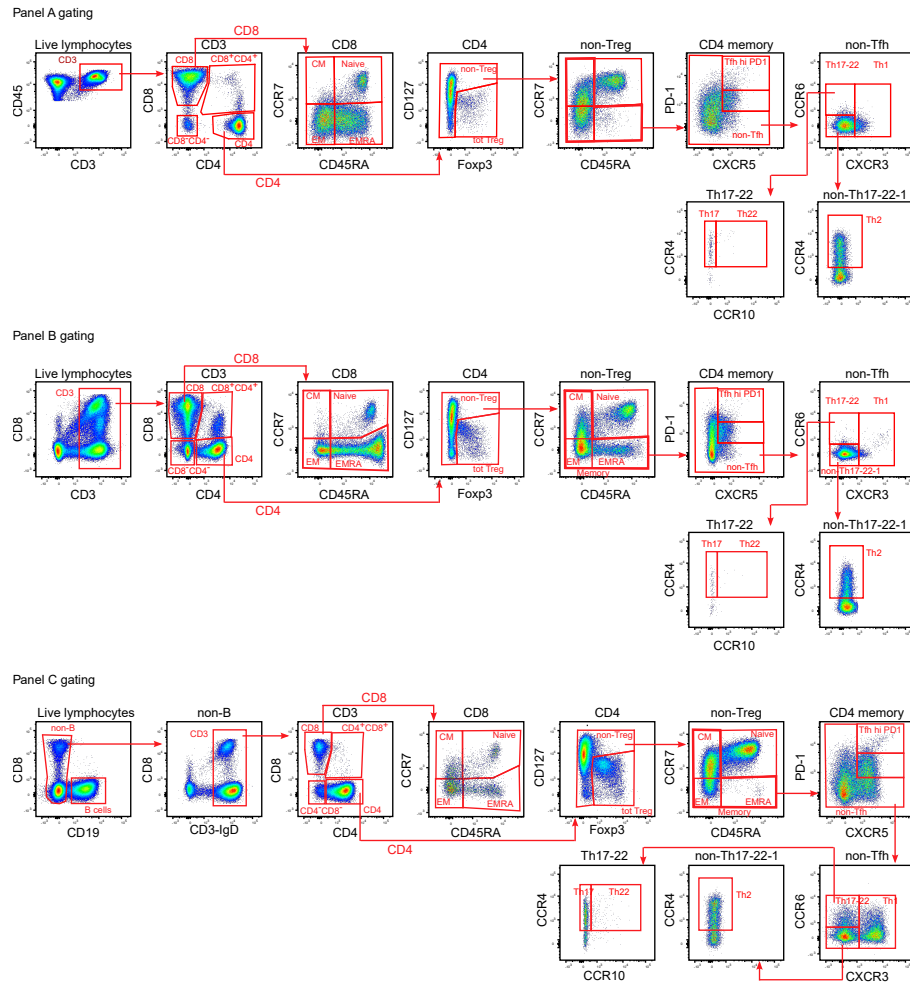


Figure 5.2: Panel-specific gating strategies created in FlowJo.

Next, to enable a flexible and intuitive data exploration, group all samples into as many groups as would be informative for exploratory analysis (for example group samples by donor, tissue, treatment, panel, etc). FlowAtlas.jl imports these gate names to population labels without requiring the gating strategies to be the same across different samples and allowing comparative analysis of these populations across datasets. Cells that fall outside of FlowJo-defined gates will be automatically placed into the "Unlabelled" population by FlowAtlas and can be fully explored.

5.4.3 Exploration in FlowAtlas.jl

Next, import FlowJo analysis workspace file (.wsp extension) into FlowAtlas.jl, which will trigger automatic dataset merging and calculation of embedding (Figure 5.1, FlowAtlas box). The embedding computation is performed only once and the embedding file with .som extension is stored in the FlowAtlas.jl folder. This file stores the topology of computed clusters and allows users to quickly return to their analysis. Sharing a .som file together with .wsp and .FCS files with colleagues will allow everyone to work on the same embedding topology and easily confirm findings and analysis reproducibility. Once the computation is complete, FlowAtlas.jl will open a graphical analysis environment in your default browser (Figure 5.1, FlowAtlas box). We leverage high-performance library GigaSOM.jl [42] and interactive visualisation libraries D3.js [43] and OpenLayers [44] to make the embedding fully interactive, with zooming, panning, event filtering and colouring by marker expression densities or any custom condition (such as sample group) provided by the researcher in FlowJo and where unlimited number of areas of interest (AOI) can be drawn directly in the data embedding for comparative analysis of marker expression with violin plots or comparative frequency analysis of selected cell populations and conditions using box plots. For example, Figure 5.1 (FlowAtlas box) shows how selecting B cells and CD4 T cell subsets in Liver of donor 412C will display embedding of only cells defined and colour-coded by these filters and allow users to easily identify fine differences in the underlying sub-cluster structures. Any number of such sub-clusters can be interactively compared to each other by drawing colour-coded AOI directly in the embedding and displaying overlayed violin plots of sub-cluster-specific marker expression. Once unique sub-populations are identified, they can be validated in FlowJo where new population gates defining these cells can be created. The new populations will then be read by FlowAtlas.jl and statistics output can be created or further exploration performed. The gating strategy in FlowJo

can thus be iteratively updated with new Cell populations discovered in FlowAtlas.jl. The iterative discovery process simplifies the identification of rare or novel cell populations that would otherwise be missed due to data down-sampling or under-fitting in unsupervised clustering approaches.

5.5 Results

5.5.1 T-regulatory Sub-populations

We used total CD4 Treg population (defined in Figure 5.2) to illustrate how new sub-populations can be easily and intuitively identified in FlowAtlas.jl (Figure 5.3). First, relative population frequency boxplot statistics can be generated for total Treg population across all tissues and panels (Figure 5.3a). The statistics is calculated relative to the top-level parental population selected in the FlowAtlas.jl or relative to a sum of all selected populations. In our dataset, total Treg represented over 20% of CD4 T cells in mesenteric lymph nodes in all donors. Displaying the embedding of total Treg cells for all donors and tissues of Panel C and colouring cells by density of Helios expression (Figure 5.3b) shows that total Treg population is comprised of Helios⁺ and Helios⁻ sub-populations. Zooming into the embedding reveals additional sub-cluster structures that warrant exploration. Before any further analysis, batch effects that arise due to inter-experimental or inter-panel variability can be easily detected by colouring a cell population by its panel or experiment of origin and observing differences in cluster position, geometry and marker MFI as we did for tot Treg in Figure 5.3c. Note how CD4 MFI creates a bimodal distribution due to different fluorochrome used in Panel A. Although some differences in cluster locations are notable between panels, overall Treg population embedding looks consistent. Next, we used Panel C as a reference for further exploration of sub-cluster characteristics. Once they are defined, same results can be obtained for Panels A and B (Extended Figure is coming). For this, we re-coloured tot Treg embedding shown in b, by tissue

origin, drew AOI around individual sub-clusters and inspected the differences in marker expression using auto-generated violin plots (Figure 5.3d). This showed a clear difference in the expression of CD45RA, CCR7, CCR4 and CD69 between individual AOI, with red having a naive phenotype $CD45RA^+CCR7^+CCR4^-CD69^-$, while yellow, grey and violet showing characteristics of memory subset. Yellow $CD45RA^-CCR7^-CCR4^+CD69^-$ Grey $CD45RA^{-/lo}CCR7^-CCR4^-CD69^+$ and violet $CD45RA^-CCR7^-CCR4^+CD69^+$. Grey and yellow memory subsets are $D69^+$ - a sign of tissue homing. Dividing the embedding by tissue reveals differences in tissue specific enrichment of individual Treg subsets. With blood lacking the grey and violet subsets, which is in line with their tissue homing phenotype. Next, we validated the presence of these subsets in FlowJo (Figure 5.3e). Plotting CD69 vs CCR4 for tot Treg subset in thoracic lymph nodes (tLN) clearly shows the presence of the four sub-populations identified in FlowAtlas.jl. We created new FlowJo gates corresponding to the four subsets and returned to FlowAtlas.jl where we re-coloured Treg embedding by these subsets. This revealed that each individual subset includes both Helios $^+$ and Helios $^-$ sub-populations (refer to the density of Helios expression shown in b). Since FJ gates for the four new Treg subsets have been gated and read by FA, population frequency statistics can be automatically generated (box plots).

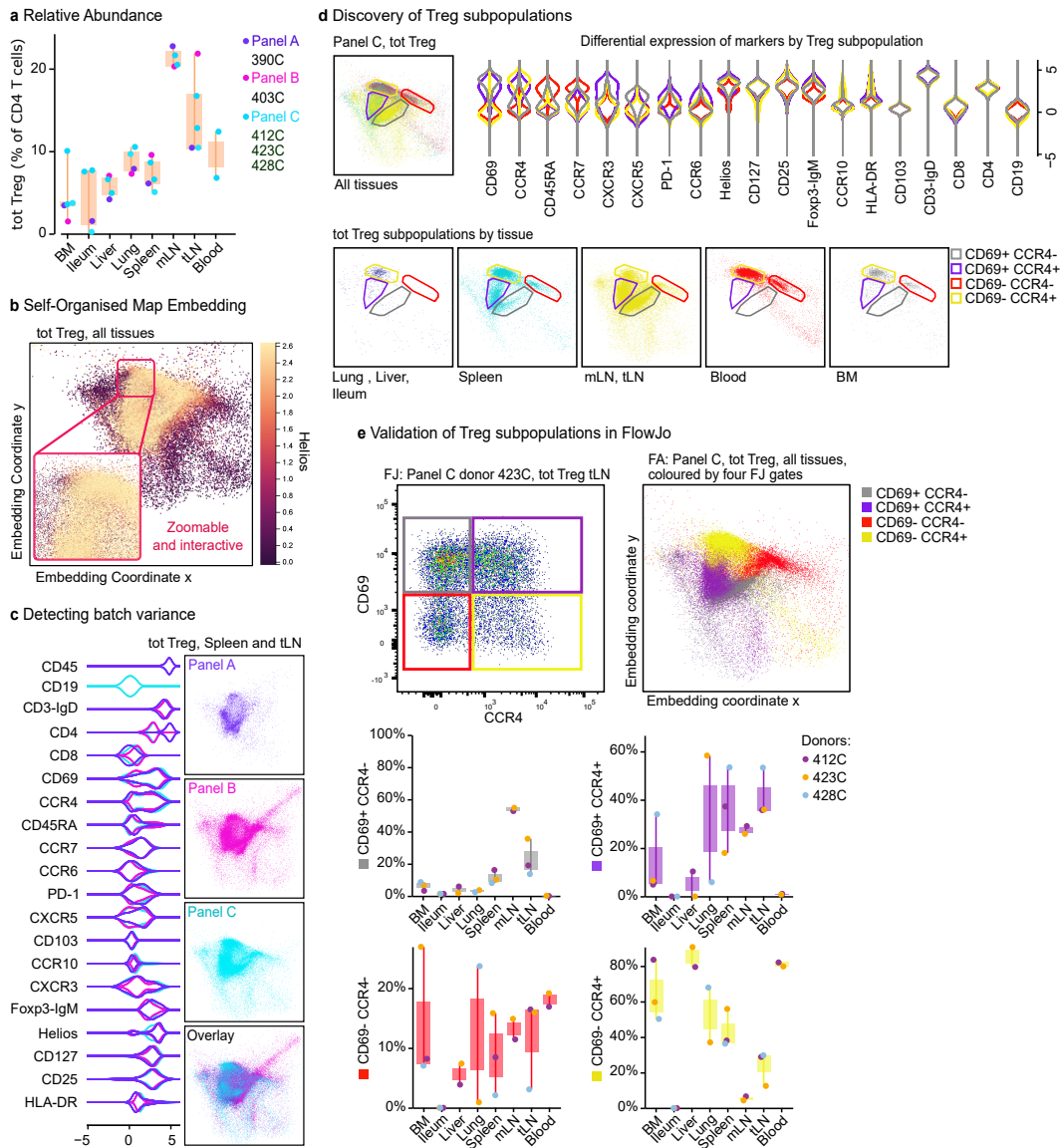


Figure 5.3: Treg sub-population discovery with FlowAtlas.jl and verification with FlowJo

5.5.2 T-helper cell populations

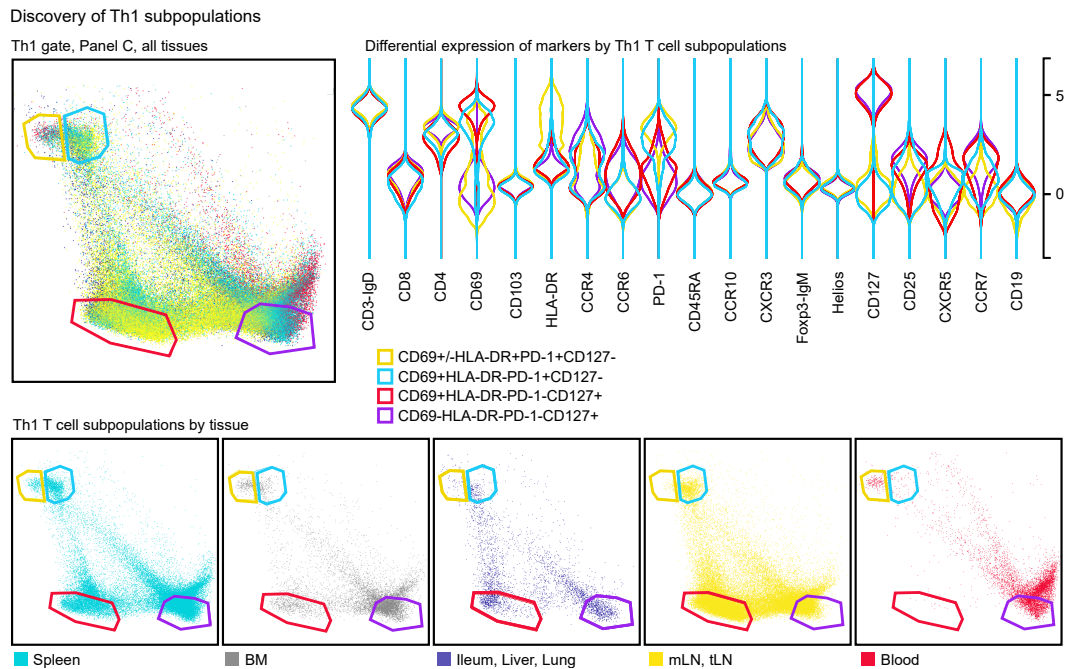


Figure 5.4: Exploration of Th1 T cell subpopulations.

5.6 Discussion

FlowAtlas.jl brings new analysis concept to biomedical scientist by linking the familiar FlowJo workflow with high-performance machine learning framework in a fully graphical, interactive environment. FlowAtlas.jl allows an embedding of millions of high-dimensional events to be rapidly computed without downsampling on an average laptop. Moreover, we utilise state-of-the-art missing data handling methods that allow users to perform concomitant cross-study analysis of datasets with non-identical panel designs or marker numbers. The resulting embedding is highly interactive offering zooming to explore deeper cluster structures, colouring events by custom conditions, selectively filtering embedded events by samples or population subsets, generating frequency statistics and drawing AOI directly in the embedding for comparative analysis of marker expression in sub-cluster structures. Findings can be immediately validated in FlowJo in an iterative discovery loop with FlowAtlas.jl simplifying the

identification and validation of rare or novel cell populations that would otherwise be missed due to data down-sampling or under-fitting in unsupervised clustering approaches.

5.7 Methods

5.7.1 Tissue Acquisition & Dissociation

All samples were collected via the Cambridge Biorepository for Translational Medicine under Research Ethics Committee approval 15/EE/0152. Tissue was obtained from five deceased organ donors following circulatory death. Donor metadata is given in Extended Data Table C.1. Briefly, following cessation of circulatory function donors proceeded to organ donation. Organs were perfused *in situ* with cold organ preservation solution and cooled with topical application of ice. Samples for the study were obtained within 60 minutes of cessation of circulation and placed in University of Wisconsin organ preservation solution for transport at 4°C to the laboratory. Lung and liver samples were obtained from the left lower lobe of the lung and the right lobe of the liver. In addition, two donor-matched blood samples were collected prior to withdrawal of life support, under approval 97/290.

To minimise the possibility of processing-depended differences in cell surface marker expression, all samples, including blood, were processed using enzymatic digestion protocol. Briefly, solid tissues were weighed, transferred into 10cm tissue culture dishes and cut into small pieces. Up to 5g of tissue was then transferred to each of eight GentleMACS C tubes (Miltenyi Biotec) containing 5mL of dissociation media composed of X-vivo15 supplemented with 0.13U/mL Liberase TL (Roche), 10U/mL Benzonase nuclease (Millipore/Merck), 2% (v/v) heat-inactivated fetal bovine serum (FBS, Gibco), penicillin (100 U/ml, Sigma-Aldrich), streptomycin (0.1 mg/ml, Sigma-Aldrich), and 10mM HEPES (Sigma Aldrich). The samples were then dissociated on a GentleMACS Octo dissociator (Miltenyi

Biotec) running a protocol that provided gradual ramping up of homogenisation speed and two 15 minute heating/mixing steps at 37°C. Digested tissue was passed through a 70 μ m MACS Smartstrainer (Miltenyi Biotec) and the flow-through was first washed with media supplemented with 2 mM EDTA and then with PBS. Mononuclear cells were enriched by Ficoll-Paque (GE Healthcare) density centrifugation according to manufacturer's instructions. Following, density centrifugation, mononuclear layer was collected, washed once with PBS and cell pellet was resuspended in FACS buffer (PBS, 2.5% FBS).

Bone marrow aspirates and peripheral blood samples were first subjected to Ficoll-Paque density centrifugation, according to manufacturer's instructions, the mononuclear layer was then collected, washed with PBS and cells were treated with the same dissociation media as solid tissues for 30 min at 37°C prior to washing and resuspension in FACS buffer.

5.7.2 Flow Cytometry

Depending on the cell yield, up to 1x10⁶ mononuclear cells/tissue were stained with antibodies shown in Extended Data Table C.2. Not all donors were stained with the same panel. To expand total number of markers, sentinel panel design was implemented where CD3 and IgD were detected with antibodies conjugated to BUV395 and Foxp3 and IgM were detected with antibodies conjugated to PE in some donors. Refer to Extended Data Table C.3 for details.

Single cell suspensions were washed once in PBS, transferred into 96 v-bottom plate and stained with Zombie UV viability dye for 30 min at 4°C following by a wash with FACS buffer. Cell pellets were resuspended in 50 μ l FACS buffer with Human FcR block (BD Biosciences) and incubated for 10 min at 4°C. Next, cells were pelleted, excess buffer removed and 100 μ l of antibody master mix composed of cell-surface antibody cocktail (see Table Extended Data C.3), BV buffer (BD) and True-Stain Monocyte Blocker (Biolegend) and incubated for 1h at 4°C. Following incubation, cells

were washed three times in PBS and prepared for intracellular staining using transcription factor fixation/permeabilisation kit (eBioscience) according to the manufacturer’s instructions. Following IC staining, cell were resuspended in PBS and analysed on BD FACSymphony A3 cell analyser within 10 hours.

5.7.3 Imputation & Embedding

When some markers are not present in every dataset, cells for which a marker is missing are not displayed in the embedding when the embedding is coloured by the expression of the missing marker in FlowAtlas.jl. To compute the initial embedding, however, missing values are sampled from non-missing values.

or re-use embedding transformations on new datasets. Note that the number of channels and names of the new dataset must match those used to calculate the embedding. With this approach it is possible to calculate an embedding for a sub-sampled dataset to save time and use the resultant transformation on the whole dataset to retain the embedding coordinates of rare populations. Enables novel population discovery

5.7.4 Data & Code Availability

All data is made available in FlowRepository; code and installation instructions can be found in our GitHub Repository

5.8 Afterword

Chapter 6

Conclusions

*A childish mind will turn
to noble ambition*

Ocarina of Time

6.1 Limitations

6.2 Future work

1. How can thesis results be applied to biological computing [45]

Appendix A

Interpretation of Morphogen Gradients by a Bistable Circuit

Supplementary Information

Interpretation of morphogen gradients by a synthetic bistable circuit

Paul K. Grant¹, Gregory Szep^{1,2,9}, Om Patange^{3,7,8,9}, Jacob Halatek¹, Valerie Coppard¹, Attila Csikász-Nagy^{2,4}, Jim Haseloff⁵, James C. W. Locke^{1,3,6}, Neil Dalchau¹, and Andrew Phillips¹

¹Microsoft Research, 21 Station Road, Cambridge CB1 2FB, UK

²Randall Centre for Cell and Molecular Biophysics, King's College London WC2R 2LS, London, UK

³Sainsbury Laboratory, University of Cambridge, Cambridge CB2 1LR, UK

⁴Faculty of Information Technology and Bionics, Pázmány Péter Catholic University, 1083 Budapest, Hungary

⁵Department of Plant Sciences, University of Cambridge, Cambridge CB2 3EA, UK

⁶Department of Biochemistry, University of Cambridge, Cambridge CB2 1QW, UK

⁷Present address: Department of Molecular Biology, Massachusetts General Hospital, Boston, MA 02114, USA

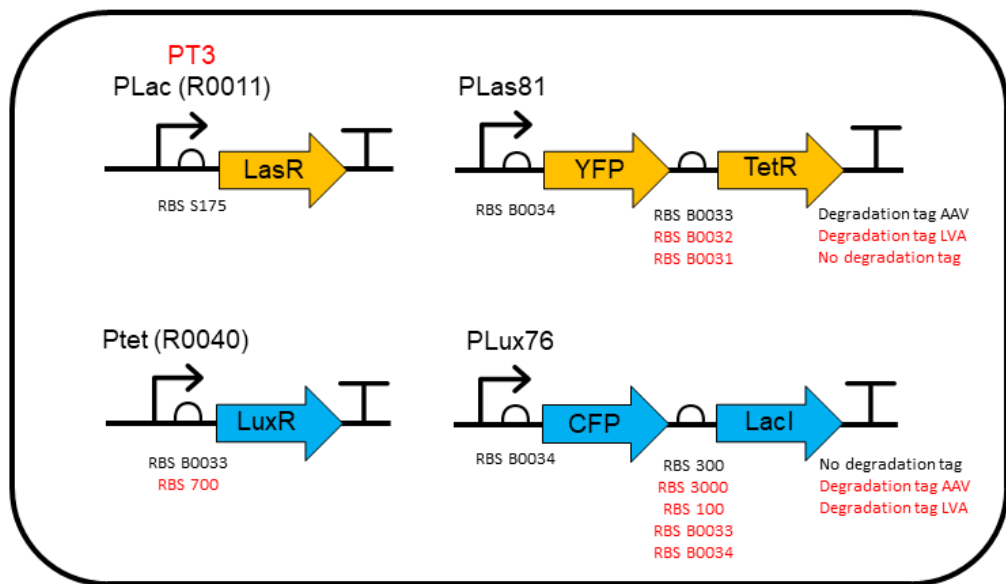
⁸Present address: Department of Genetics, Harvard Medical School, Boston, MA 02115, USA

⁹These authors contributed equally: Gregory Szep, Om Patange

Contents

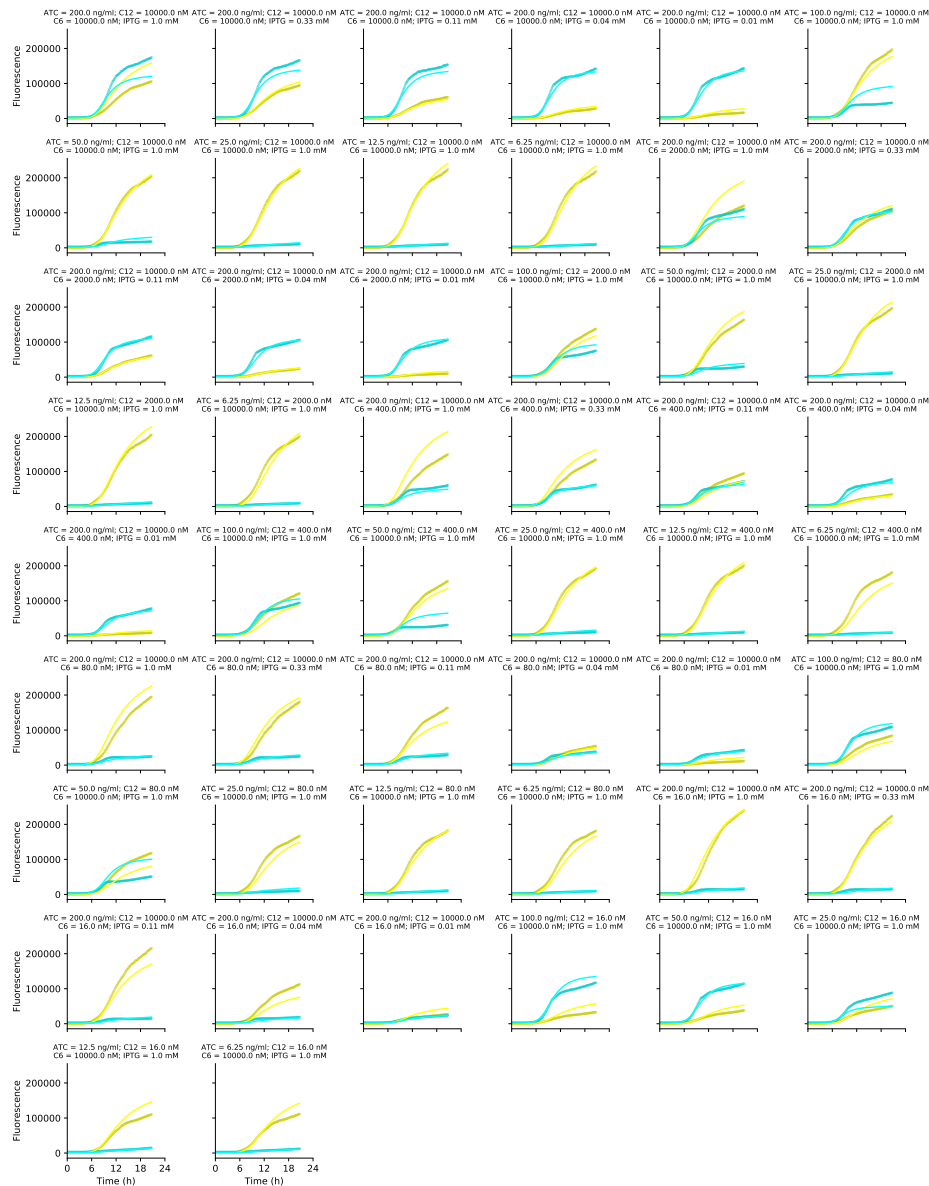
1 Supplementary Figures	2
2 Supplementary Methods	18
2.1 Differential Equation Models and Parameter Inference	19
2.2 Bistability Analysis	40
2.3 Boundary Experiments	42
2.4 Models of the Exclusive Receiver Relay Circuits	50

1 Supplementary Figures

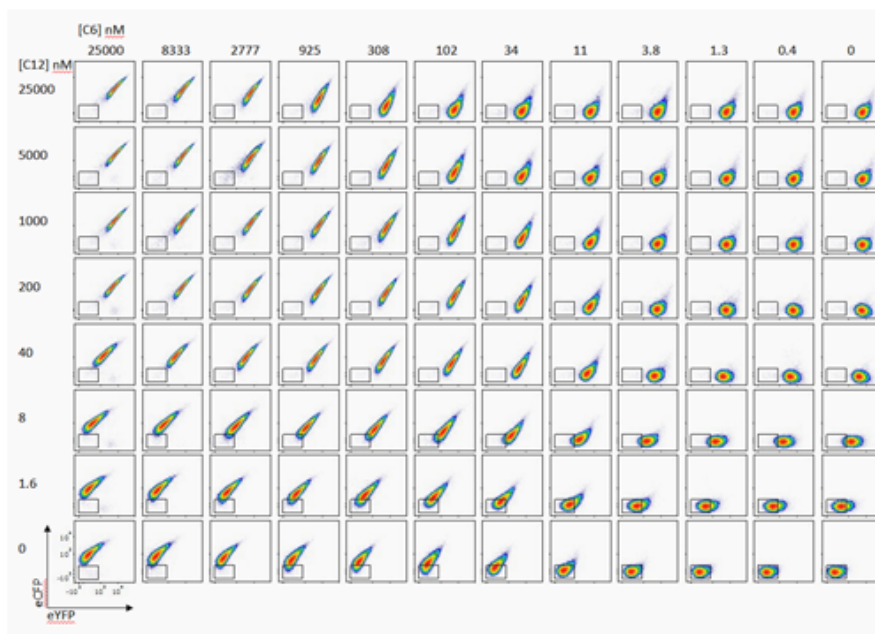
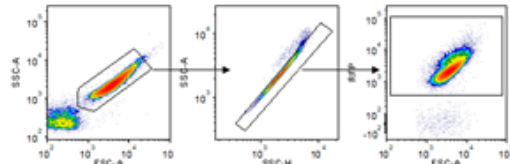


Supplementary Figure 1: Circuit variants. A circuit diagram of the exclusive receiver circuit with genetic parts labelled in black that were included in the final circuit and in red that were evaluated but discarded. Not all combinations of parts were tested.

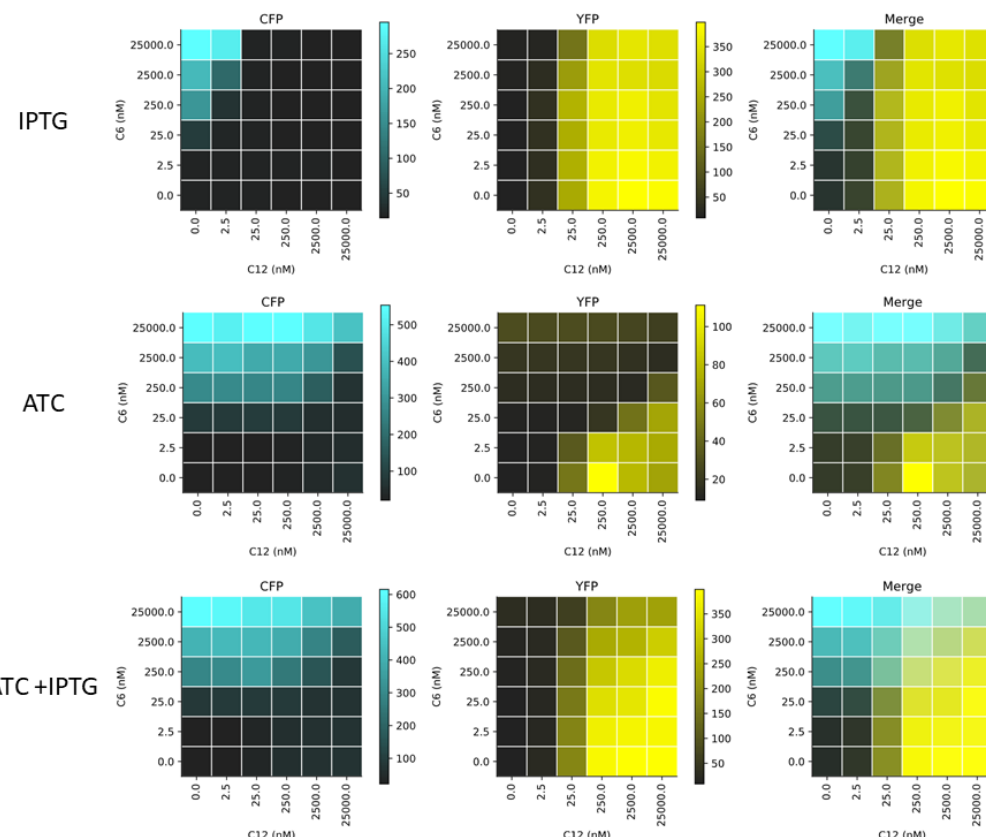




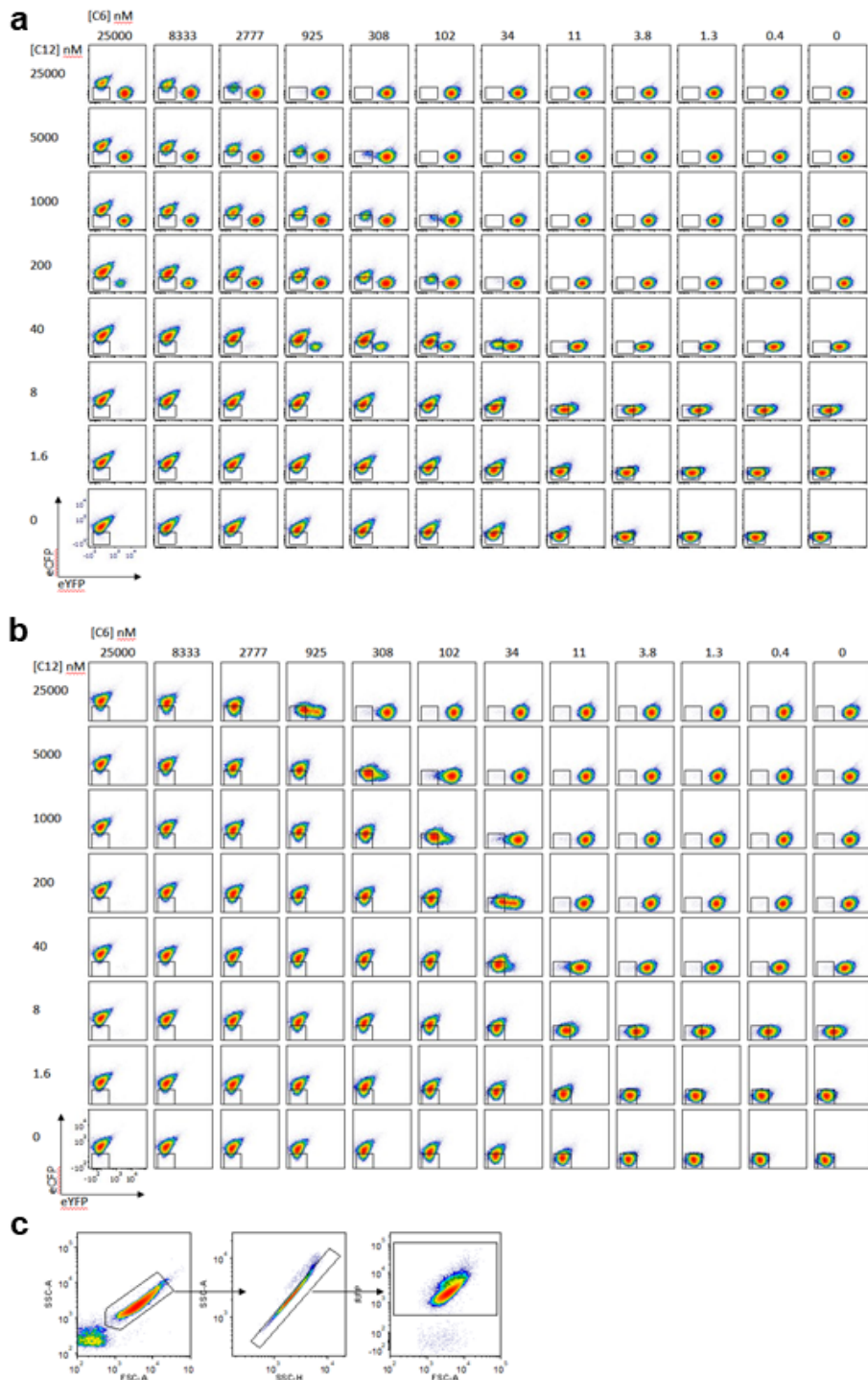
Supplementary Figure 2: Raw timecourse fluorescence traces. Fluorescence output, measured in microplate fluorometer assays, of the Exclusive Receiver circuit, plotted as CFP (dark cyan) and YFP (dark yellow) fluorescence against time, at the concentrations of C6, ATC, and IPTG indicated. Model simulations (cyan and yellow) of the maximum likelihood parameters are overlaid. Source data are provided as a Source Data file.

a**b****c**

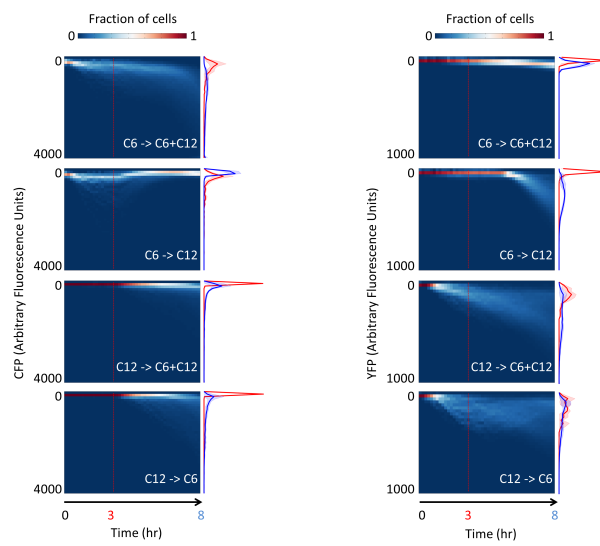
Supplementary Figure 3: Flow cytometry measurements of naive cells a, Exclusive Receiver cells cultured in the indicated concentrations of C6 and C12. YFP fluorescence is plotted on the X-axis while CFP fluorescence is plotted on the Y-axis. b, Receiver cells cultured in the indicated concentrations of C6 and C12. Square indicates the position of untreated cells. c, Gating strategy. Cells also constitutively express mRFP1 via a genomic transgene. Only RFP⁺ cells were used for analysis and electronic noise, cell debris and cell clusters were excluded sequentially. Source data are provided as a Source Data file.



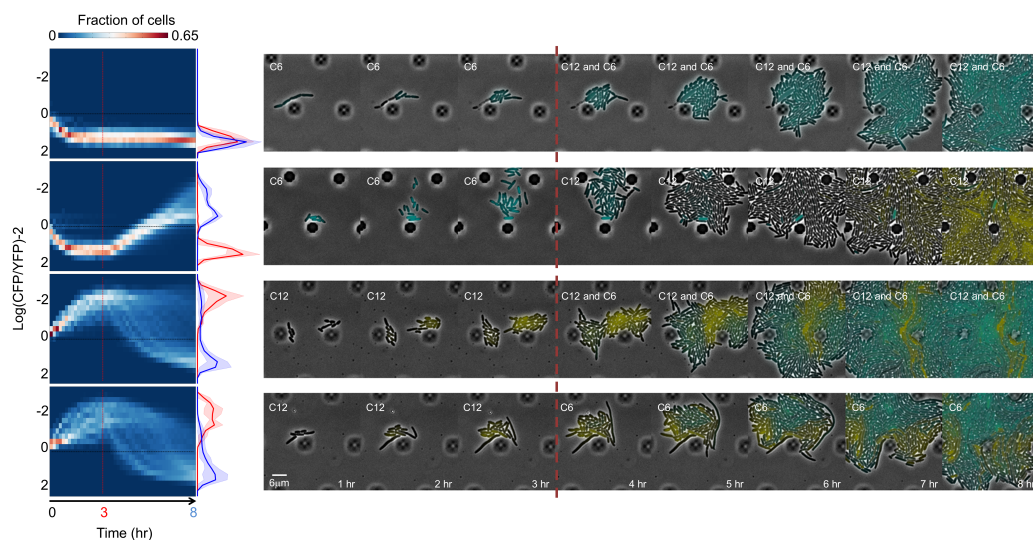
Supplementary Figure 4: ATC and IPTG derepress mutual inhibition. Fluorescence output, measured in microplate fluorometer assays, of the Exclusive Receiver circuit represented as a ratio of CFP- (left) or YFP- (right) fluorescence to RFP fluorescence during exponential phase cultured in the presence of 1 mM IPTG (top), 100 ng/ml ATC (middle) or 1 mM IPTG + 100 ng/ml ATC and the concentrations of 3O-C6-HSL (C6) and 3O-C12-HSL (C12) indicated (see methods for a description of analysis). Source data are provided as a Source Data file.



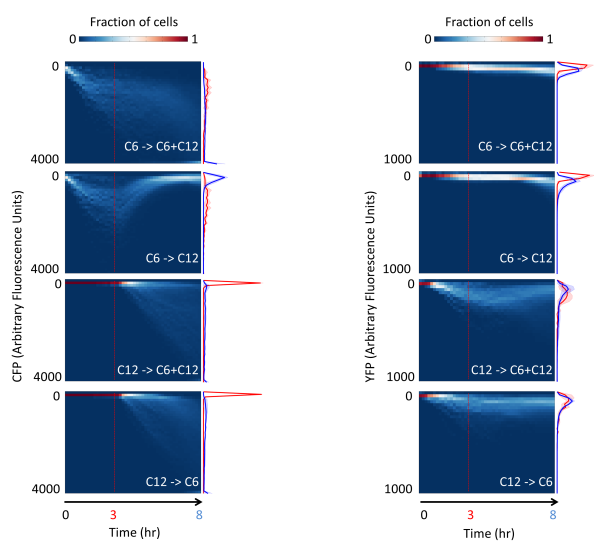
Supplementary Figure 5: Flow cytometry measurements of conditioned cells a, Cells conditioned in 500 nM C12 then exposed to the indicated concentrations of C6 and C12. YFP fluorescence is plotted on the X-axis while CFP fluorescence is plotted on the Y-axis. b, Cells conditioned in 500 nM C6 then exposed to the indicated concentrations of C6 and C12. Square indicates the position of untreated cells. c, Gating strategy. Cells also constitutively express mRFP1 via a genomic transgene. Only RFP⁺ cells were used for analysis and electronic noise, cell debris and cell clusters were excluded sequentially. Source data are provided as a Source Data file.



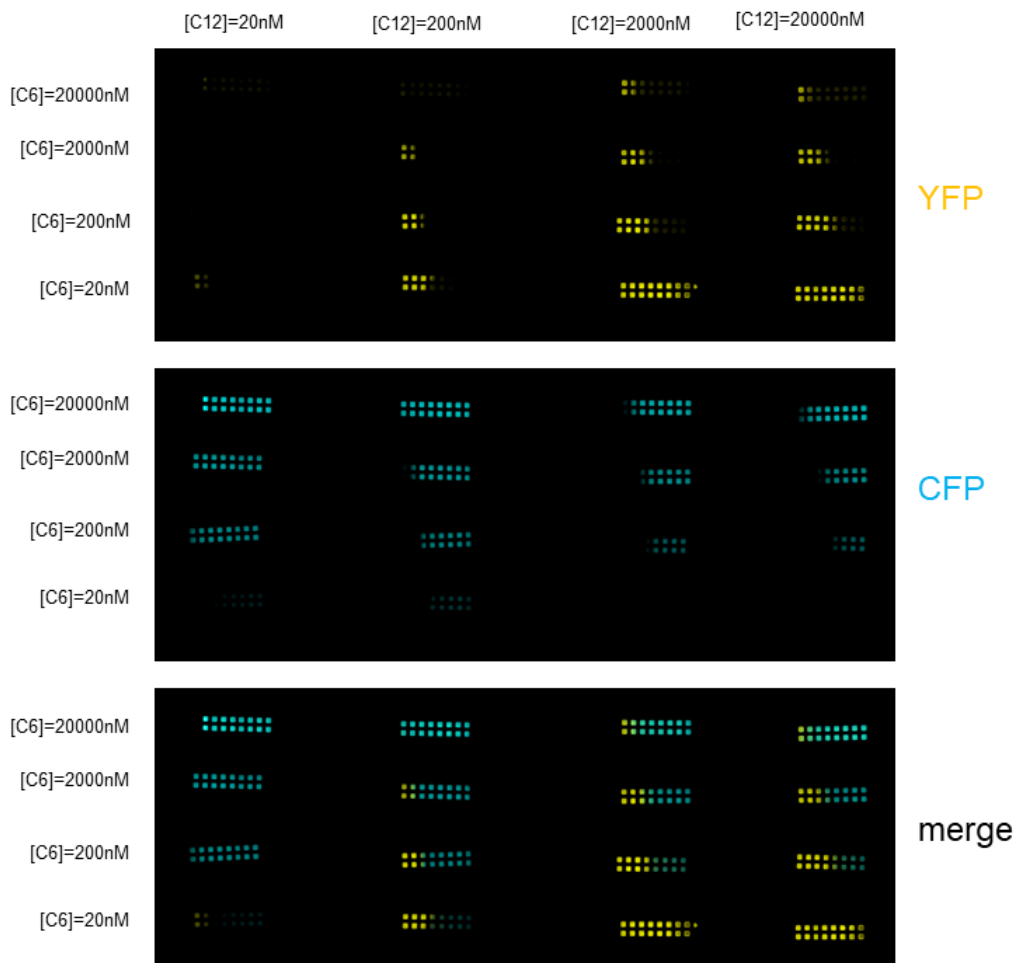
Supplementary Figure 6: Microfluidics measurements of bistability. Single-cell data used to compute ratios in Figure 2c. Cells were grown in microfluidic chips for 3 hours in the presence of either 37 nM C6 (rows 1 and 2) or 100 nM C12 (rows 3 and 4). Then media was changed to 100 nM C12 + 37 nM C6 (rows 1 and 3) or 100 nM C12 (row 2) or 37 nM C6 (row 4). Cells were imaged with a frame rate of (1 frame/10 minutes). Left panels in each column are kymographs of the CFP (left column) or YFP (right column) expression per-cell, and fraction of cells as a heat map. Histograms represent the populations at 3 hours (red) and 8 hours (blue). Lines and shaded region represent the mean and standard deviation, respectively, over $n = 4$ biological replicates performed over 4 different days.



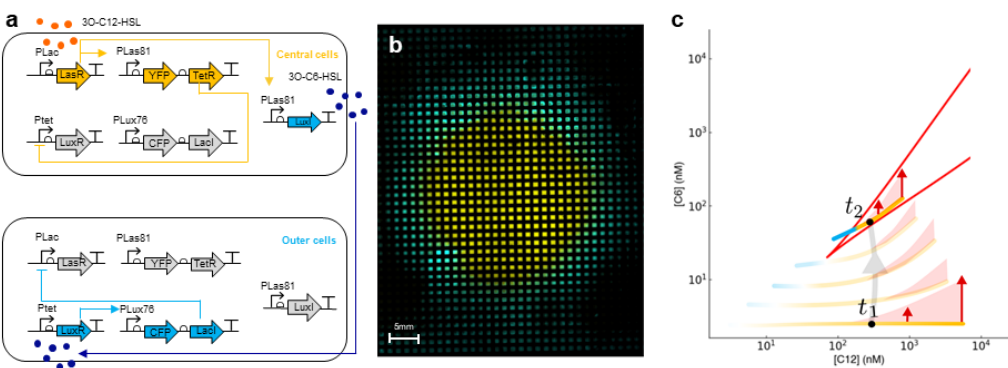
Supplementary Figure 7: Bistability and switching of single cells is robust to high C6 signal concentration. Cells were grown in microfluidic chips for 3 hours in the presence of either 1 μM C6 (rows 1 and 2) or 100 nM C12 (rows 3 and 4). Then media was changed to 100 nM C12 + 1 μM C6 (rows 1 and 3) or 100 nM C12 (row 2) or 1 μM C6 (row 4). Cells were imaged with a frame rate of (1 frame/10 minutes). Left panels are kymographs of the log-ratio of CFP expression per-cell to YFP expression per-cell, and fraction of cells as a heat map. Histograms represent the populations at 3 hours (red) and 8 hours (blue). Lines and shaded region represent the mean and standard deviation, respectively, $n = 4$ biological replicates performed over 4 different days. Right panels are sample montages of cells switching state (rows 3 and 4) or exhibiting bistability (rows 1 and 2); phase contrast and fluorescence channel ranges chosen for display.



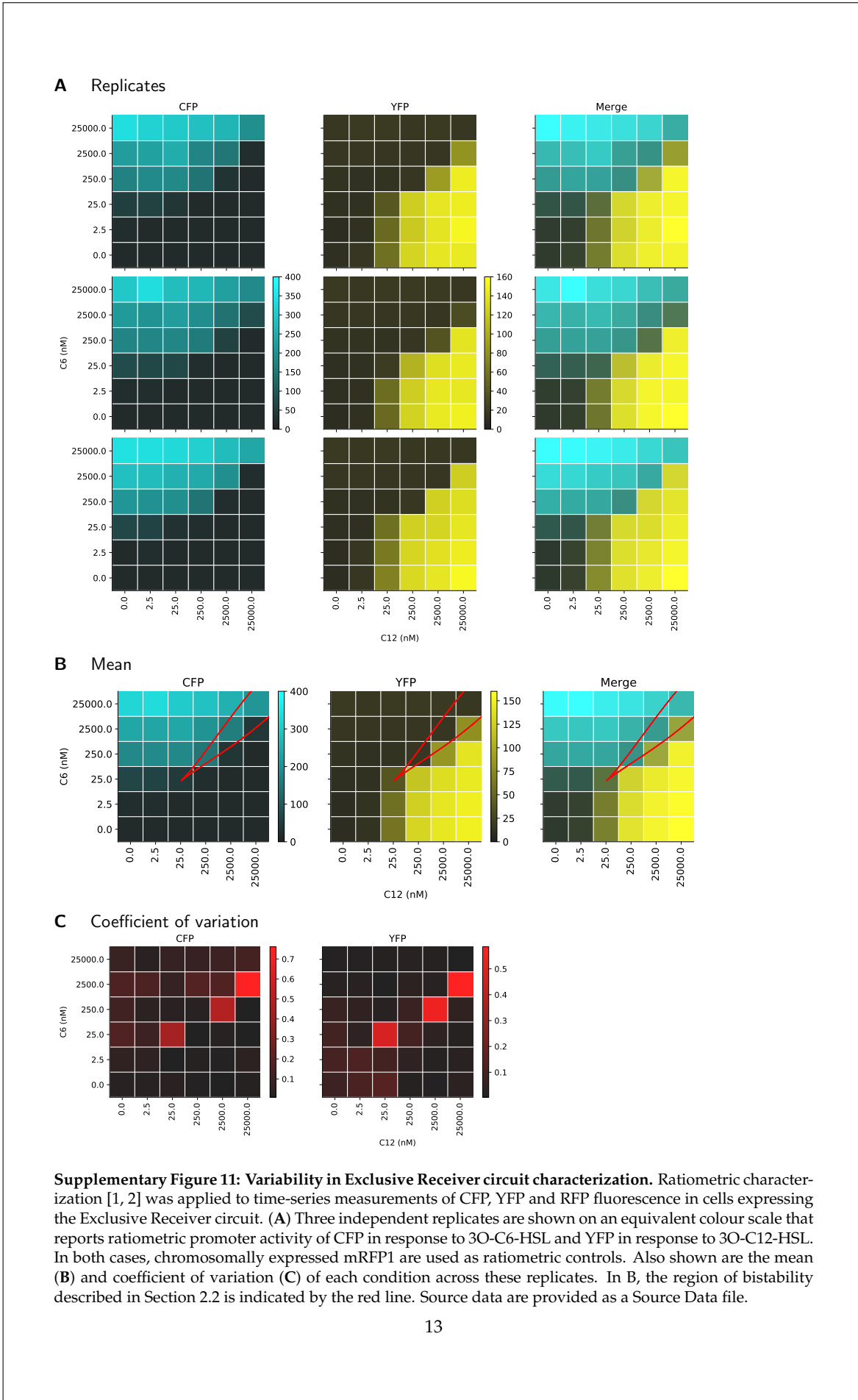
Supplementary Figure 8: Microfluidics measurements of bistability with high C6 signal concentration. Single-cell data used to compute ratios in 7. Cells were grown in microfluidic chips for 3 hours in the presence of either 1 μ M C6 (rows 1 and 2) or 100 nM C12 (rows 3 and 4). Then media was changed to 100 nM C12 + 1 μ M C6 (rows 1 and 3) or 100 nM C12 (row 2) or 1 μ M C6 (row 4). Cells were imaged with a frame rate of (1 frame/10 minutes). Left panels in each column are kymographs of the CFP (left column) or YFP (right column) expression per-cell, and fraction of cells as a heat map. Histograms represent the populations at 3 hours (red) and 8 hours (blue). Lines and shaded region represent the mean and standard deviation, respectively, over $n = 4$ biological replicates performed over 4 different days.

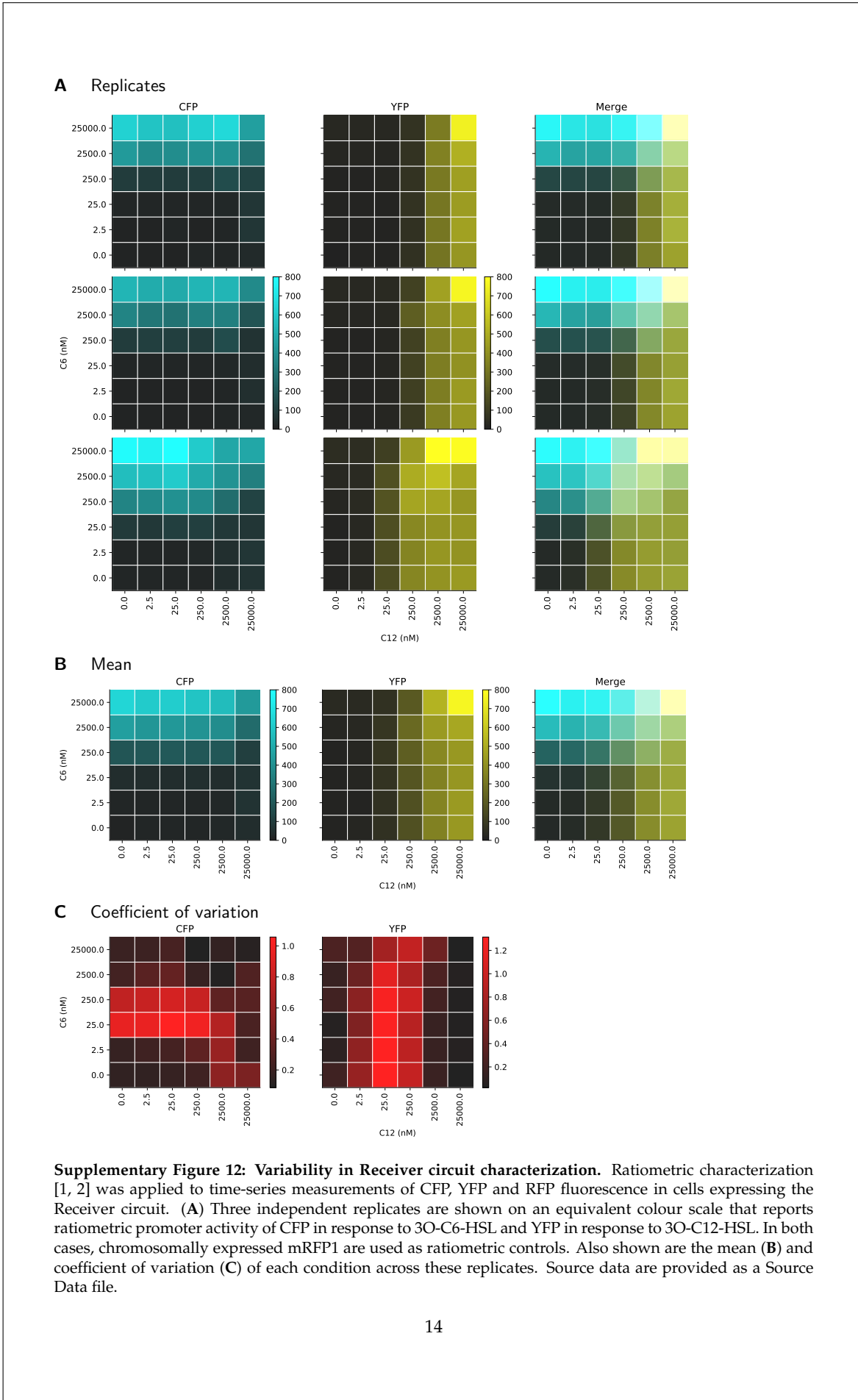


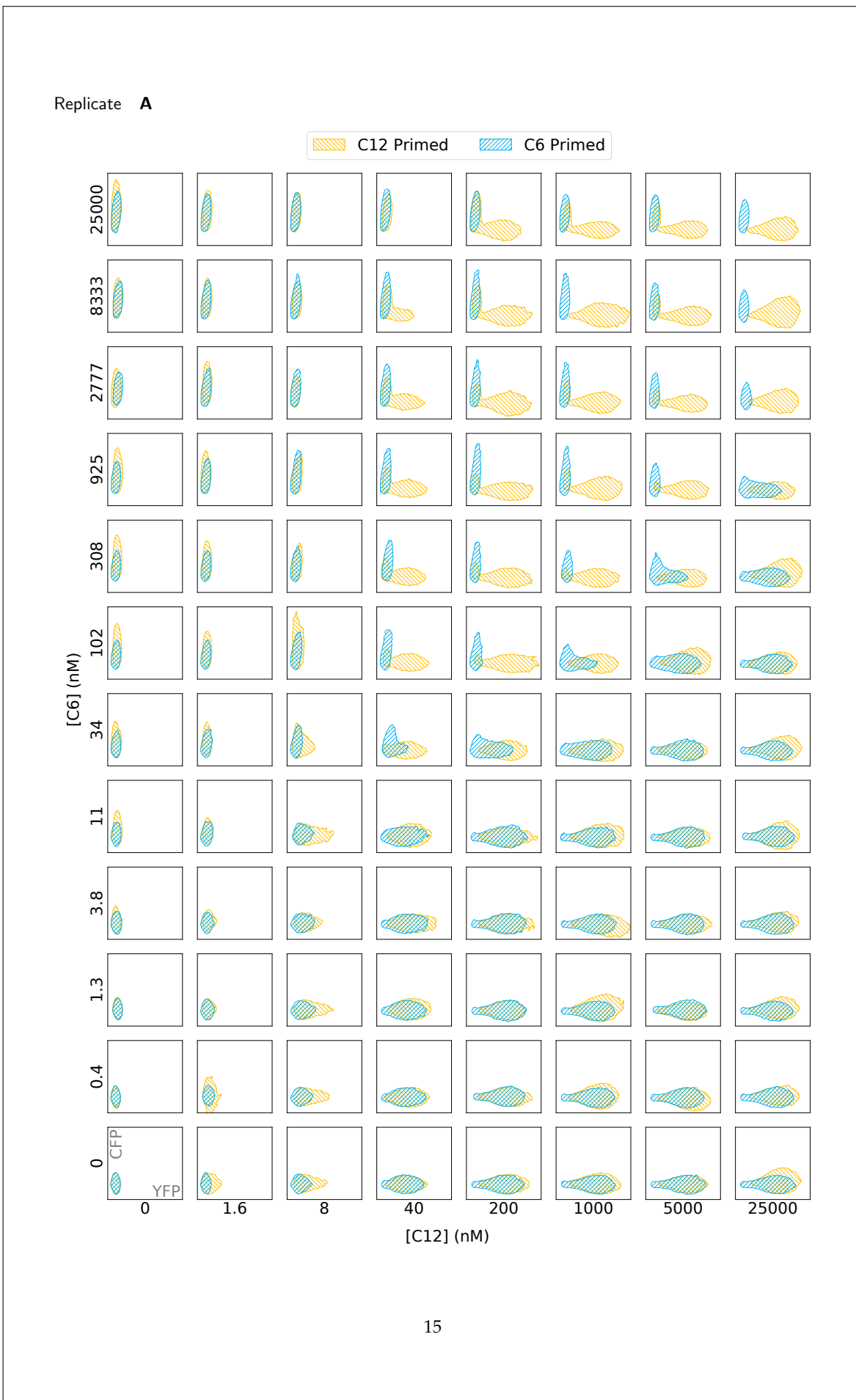
Supplementary Figure 9: Boundaries summarized in Figure 3c Endpoint fluorescence microscopy of Exclusive Receiver cells grown in transient gradients of signals (C12 diffusing from the left, C6 diffusing from the right) at the spatial average concentrations indicated and in the context of 10 μ M IPTG throughout.

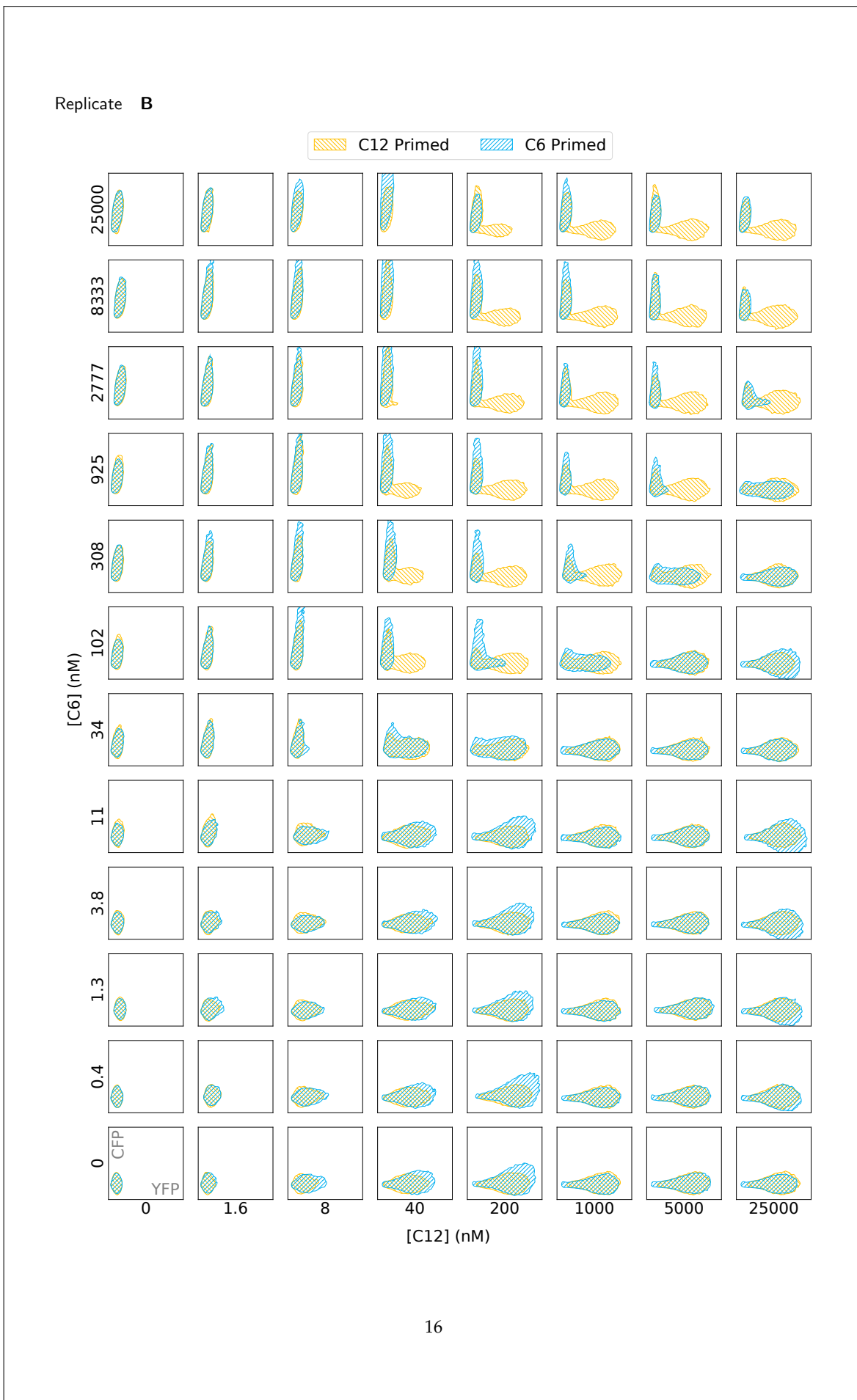


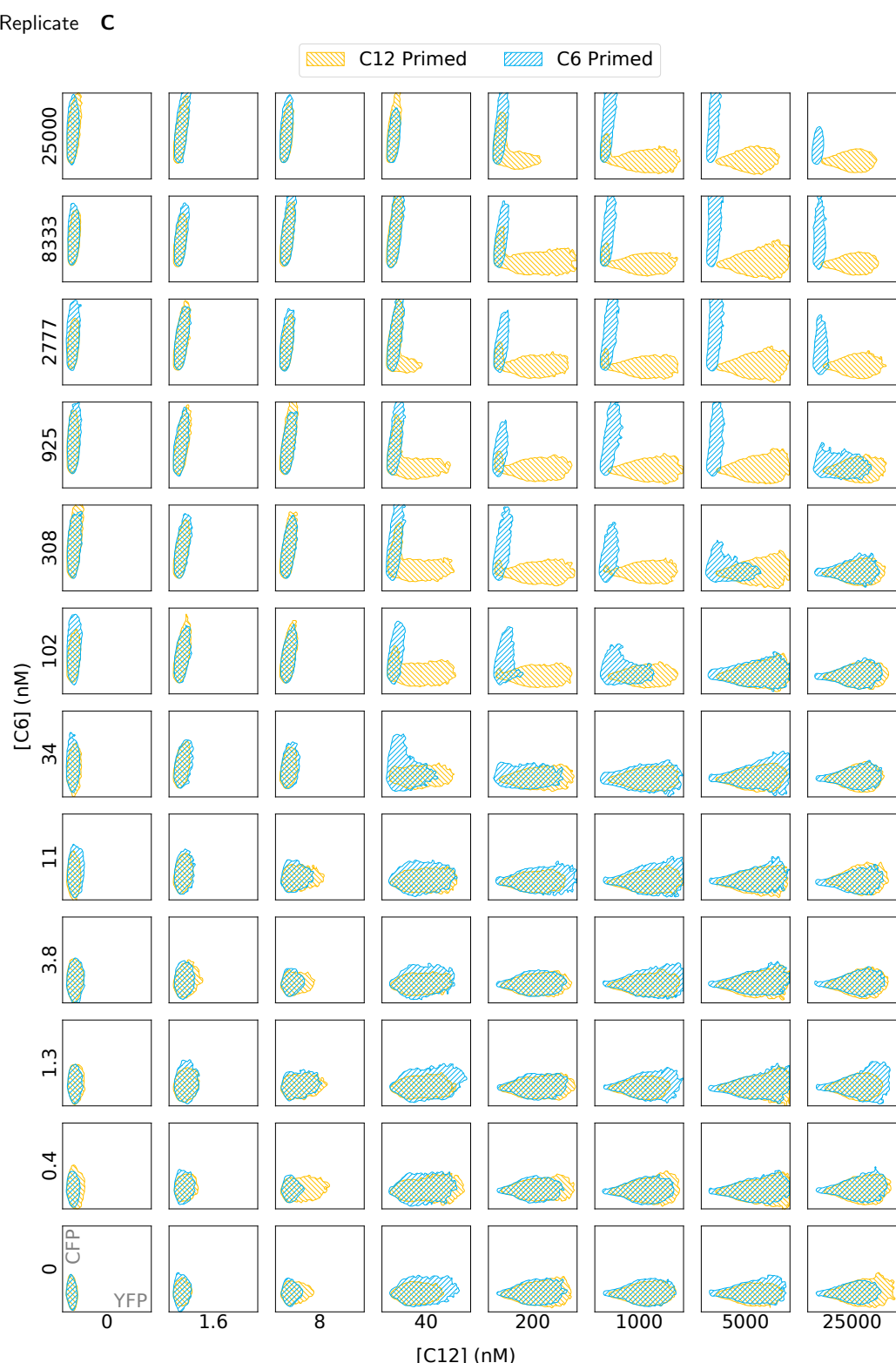
Supplementary Figure 10: Swapping primary and secondary morphogens also produces patterning. **a**, A circuit diagram of exclusive reporter cells co-transformed with the P81-LuxI relay device that responds to C12 by producing C6. Cells that experience high levels of C12 (central cells) will express YFP, TetR, and LuxI, causing them to produce C6 but be unable to sense it. Neighbouring cells (outer cells) that do not experience C12 will sense C6 and express CFP and LacI. **b**, Isogenic cells transformed with the circuit shown in (a) grown for 24 hours in the presence of a gradient of C12 diffusing from the centre express CFP and YFP in mutually exclusive domains of gene expression. **c**, A simulation in C6-C12 space over time (t_1 - t_2) labelling points in physical space by their CFP and YFP expression (cyan and yellow points), and showing the production of C6 as vectors (red arrows) that move the spatial average (black point) toward increasing C6. The bistable region is outlined in red.











Supplementary Figure 13: Hysteresis flow cytometry experiments. Each replicate (A-C) is the overlay of two independent experiments with cells initialised in either 500 nM 3O-C6-HSL or 500 nM 3O-C12-HSL and transferred into varying concentrations of morphogens as indicated on the major axes. Regions of concentrations where the final population state depends on its initial state are visible along the diagonal. CFP and YFP fluorescence on the minor axes are normalised by RFP and centred such that auto-fluorescence of the 0 nM dilution is fixed in the bottom left. Source data are provided as a Source Data file.

2 Supplementary Methods

Supplementary Table 1: Primers used for Gibson assembly of the exclusive receiver circuit

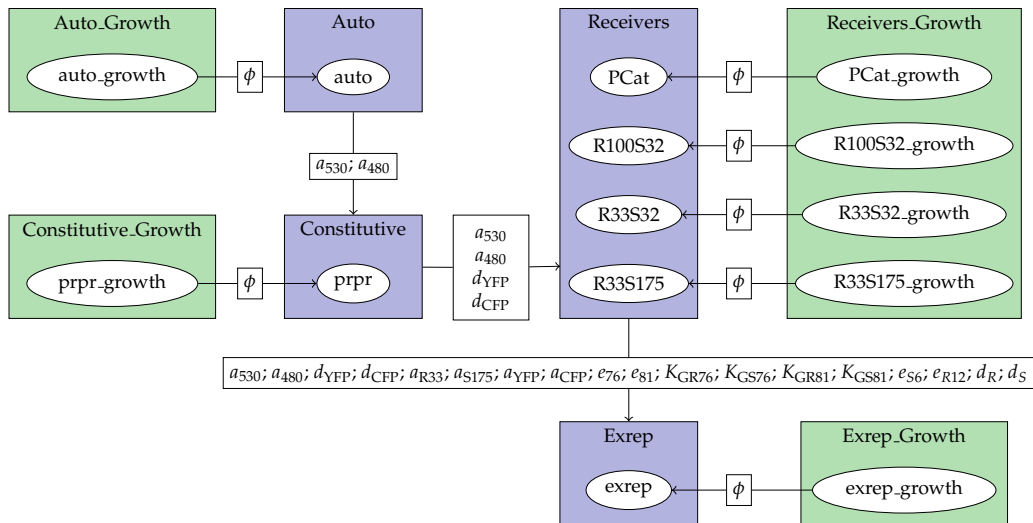
Primer name	Sequence
PGMSR014 LacIND F	TTTATTGATGCCTGGCTTATTACTGCCCGCTTCCAGTCGG
PGMSR015 LacIND R	GCGGGCAGTAATAAAGCCAGGCATCAAATAAAACGAAAGG
PGMSR038 LacI300 F	TTTAGGACTGGACGGCGAAGGCCTGATGGAGTTCTAGTAT-
	TATTACTGTACAGCTCGTCCATGCC
PGMSR039 LacI300 R	AGAACTCCCATCAGGCCCTCGCCGTCCAGTCCTAAAATGGT-
	GAATGTGAAACCAGTAACGTTAT
PG081 Kan F	GGAATCGAACATGCAACCGGGC
PG082 Kan R	TGATGCGCTGGCAGTGTTC
PG342 Tet33 F	TCACACAGGACTACTAGATGTCCAGATTAGATAAAAG-
	TAAAGTGATTAACAGCGC
PG343 Tet33 R	ATCTAACATGGACATCTAGTAGTCCTGTGTGATTATTACTG-
	TACAGCTCGTCCATGCCG
PG373 TetAAV F	CGAAAAACTACGCTGCTGCTGTTAATAACCAGGCAT-
	CAAATAAAACGAAAGGC
PG374 TetAAV R	TGGTTATTAAACAGCAGCAGCGTAGTTTCGTCGTTGCTGCG-
	GACCCAC
JS3F Ori	GAGTGTATACTGGCTACTATGTTGGCACTG
JS3R Ori	CAGTGCCAACATAGTAAGCCAGTACACTC

2.1 Differential Equation Models and Parameter Inference

In this section, we derive ordinary differential equation (ODE) models for the reaction kinetics underlying the Exclusive Receiver circuit. These derivations broadly follow the derivations of the Receiver circuit in [3] and [4]. Importantly, we introduce differences in that original derivation that lead to changes in the location of bifurcations in (C12,C6) space, when those derivations are extended to incorporate dynamics of the repressor proteins LacI and TetR, and their chemical inhibitors IPTG and ATC.

Dynamic characterization with inference graphs

In order to infer the parameters of the Exclusive Receiver circuit, we adopt the strategy described in [4], evaluating parameters of sub-circuits first, and propagating their inferred values to larger circuits that embed those same parameters. This results in an inference graph, where we infer parameters over a sequence of models and corresponding datasets.



Supplementary Figure 14: Inference graph for characterizing the Exclusive Receiver circuit. Blue rectangular nodes are inference problems for collections of synthetic gene circuit models, compared with CFP and YFP measurements, while green rectangular nodes are inference problems for the growth models of the circuits in the downstream blue nodes, compared with OD₆₀₀ measurements. Internal to the coloured nodes are white elliptical nodes, which correspond to individual synthetic gene circuits and one or more associated dataset(s). White rectangular nodes are the sets of inferred parameters that are propagated between nodes. To simplify the notation, ϕ has been used to denote the set of growth model parameters, which are culture-specific (local) values for r , K and t_{lag} , and are propagated as maximum likelihood estimates. All other parameters are global (non-culture-specific) values and propagated as marginal posterior estimates.

The simplest possible cell line to characterize is one in which there is no synthetic gene circuit at all. Applying dynamic characterization in this context enables us to quantify autofluorescence, and so we name this circuit *auto*. Therefore, we measured cells under a range of conditions to explore how gene expression capacity influenced time-series measurements at fluorescence wavelengths corresponding to CFP and YFP. Subsequently, we characterize a circuit (*prpr*) in which CFP and YFP are driven by constitutive promoters (PR), enabling us to characterize the rates of degradation of the fluorescent proteins. Next, we use four variants of simple HSL receiver (PCat, R100S32, R33S32 and R33S175) to characterize the genetic parts associated with LuxR and LasR receiver proteins and their interactions with HSL molecules 3OC6HSL (C6) and 3OC12HSL (C12). Finally, having obtained parameter estimates for parts associated with CFP, YFP, LuxR and LasR, we characterize the Exclusive Receiver circuit (*exrep*) itself, establishing quantitative estimates for the parts associated with TetR and LacI repressor proteins.

In the following, we introduce the models for each of the circuits just mentioned, define their parameters and present results of the inference.

Autofluorescence model

The model we used for autofluorescence assumes that the rate of autofluorescence is constant, and that the fluorescent material dilutes with cell growth. As such, the equations for intracellular autofluorescence corresponding to CFP and YFP are

$$\frac{d\rho}{dt} = \gamma(\rho) \cdot \rho \quad (1a)$$

$$\frac{dc_{480}}{dt} = a_{480} - \gamma(\rho) \cdot c_{480} \quad (1b)$$

$$\frac{dc_{530}}{dt} = a_{530} - \gamma(\rho) \cdot c_{530} \quad (1c)$$

where $\gamma(\rho) = r(1 - \frac{\rho}{K})$ is the specific growth rate of the cell culture with density ρ .

To compare with experimental measurements, we consider the bulk fluorescence given by

$$B_{480} = \rho \cdot c_{480} + b_{480} \quad (2a)$$

$$B_{530} = \rho \cdot c_{530} + b_{530} \quad (2b)$$

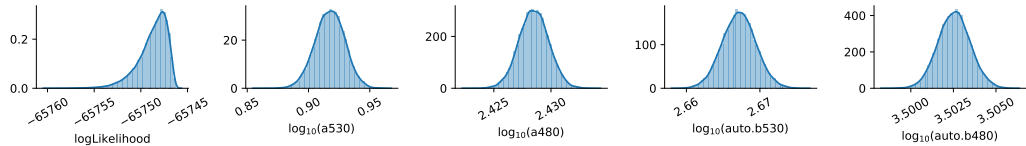
where c_{480} and c_{530} are modelled as in (1). Here, the quantities b_{480} and b_{530} represent background fluorescence at 480 nm and 530 nm, corresponding to CFP and YFP respectively.

Inference. We use the data in [4] to infer the parameters of the auto circuit. Cells were treated with EtOH to perturb cell growth, enabling us to determine how autofluorescence changes with different cellular growth rates. The priors used are detailed in the following table.

Supplementary Table 2: Priors for the auto circuit characterization. In the unit column, Fl denotes fluorescence units. The scaling column refers to the proposal distribution used to generate new parameters during MCMC.

Parameter	Description	Unit	Distribution	Scaling
a_{480}	Autofluorescence (CFP)	Fl.cell ⁻¹ .h ⁻¹	$U(10^{-3}, 10^3)$	Log
a_{530}	Autofluorescence (YFP)	Fl.cell ⁻¹ .h ⁻¹	$U(10^{-3}, 10^3)$	Log
b_{480}	Background fluor. (CFP)	Fl	$U(0, 10^4)$	Real
b_{530}	Background fluor. (YFP)	Fl	$U(0, 5 \times 10^3)$	Real

The marginal posterior estimates are shown in Figure 15. Simulation of the maximum likelihood estimate is shown in Figure 16.



Supplementary Figure 15: Marginal parameter posterior estimates of the auto model parameters. The marginal distributions are computed from 20 independent MCMC chains.



Supplementary Figure 16: Comparison of auto model with fluorescence measurements. Simulations are for B_{480} (cyan lines) and B_{530} (yellow lines), evaluated with the maximum likelihood parameter set. Measurements of bulk culture fluorescence are shown for the emission wavelengths corresponding to CFP (cyan circles) and YFP (yellow circles). EtOH treatment concentrations are indicated atop each panel.

Constitutive (prpr) model

The prpr circuit described above uses the constitutive PR promoter to drive CFP and YFP expression, in two separate operons. Following the derivation in [4], we arrive at a system of equations that describe the time-evolution of the intracellular concentrations of CFP and YFP as

$$\frac{dc}{dt} = \gamma(\rho).c \quad (3a)$$

$$\frac{dc_{\text{CFP}}}{dt} = a_{\text{CFP}} - (d_{\text{CFP}} + \gamma(\rho))c_{\text{CFP}} \quad (3b)$$

$$\frac{dc_{\text{YFP}}}{dt} = a_{\text{YFP}} - (d_{\text{YFP}} + \gamma(\rho))c_{\text{YFP}} \quad (3c)$$

where a_{CFP} and a_{YFP} are aggregated parameters that incorporate the rate of transcription and translation of CFP and YFP respectively. To compare with bulk culture fluorescence data, we use the observer model

$$B_{480} = \rho.(c_{\text{CFP}} + c_{480}) + b_{480} \quad (4a)$$

$$B_{530} = \rho.(c_{\text{YFP}} + c_{530}) + b_{530} \quad (4b)$$

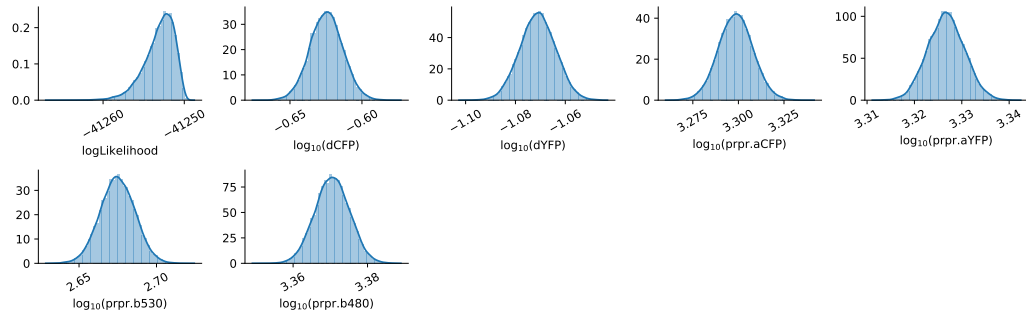
where the dynamics of c_{480} and c_{530} are governed by equations (1) above.

Inference. We use the data in [4] to infer the parameters of the prpr circuit. Cells were treated with chloramphenicol to perturb cell growth, enabling us to establish how constitutively expressed proteins are altered with different cellular growth rates. While the model above does not explicitly describe any explicit functional response to chloramphenicol, our general strategy of allowing the cell growth parameters to vary across different measurements enables the effect of chloramphenicol on growth rates to be implicitly captured. The quantification of autofluorescence was reused from the auto circuit (upstream in the inference graph), but the background fluorescence parameters were re-inferred. The priors used are detailed in Table 3. The marginal posterior estimates are shown in Figure 17.

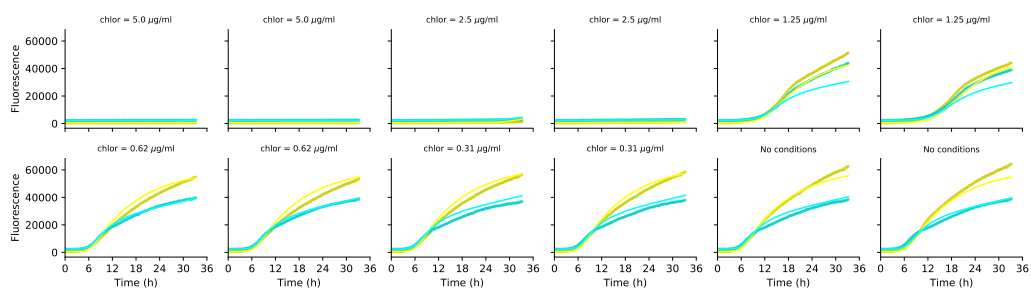
Supplementary Table 3: Priors for the prpr circuit characterization. In the unit column, Fl denotes fluorescence units. The scaling column refers to the proposal distribution used to generate new parameters during MCMC.

Parameter	Description	Unit	Distribution	Scaling
d_{CFP}	CFP degradation	h^{-1}	$U(10^{-3}, 10^0)$	Log
d_{YFP}	YFP degradation	h^{-1}	$U(10^{-3}, 10^0)$	Log
a_{CFP}	CFP synthesis	$\text{Fl.cell}^{-1}.\text{h}^{-1}$	$U(10^0, 10^5)$	Log
a_{YFP}	YFP synthesis	$\text{Fl.cell}^{-1}.\text{h}^{-1}$	$U(10^0, 10^5)$	Log
b_{480}	Background fluor. (CFP)	Fl	$U(0, 10^4)$	Real
b_{530}	Background fluor. (YFP)	Fl	$U(0, 5 \times 10^3)$	Real

Simulation of the maximum likelihood estimate is shown in Figure 18. The simulated CFP and YFP largely agree with the measured fluorescence at the culture level. As the effect of chloramphenicol is not explicitly modelled here, this comparison indicates that the majority of the effect of chloramphenicol can be described via its effect on cell growth. Any additional direct effect on CFP and YFP expression directly, is relatively minor.



Supplementary Figure 17: Marginal parameter posterior estimates of the prpr model parameters. The marginal distributions are computed from 20 independent MCMC chains.



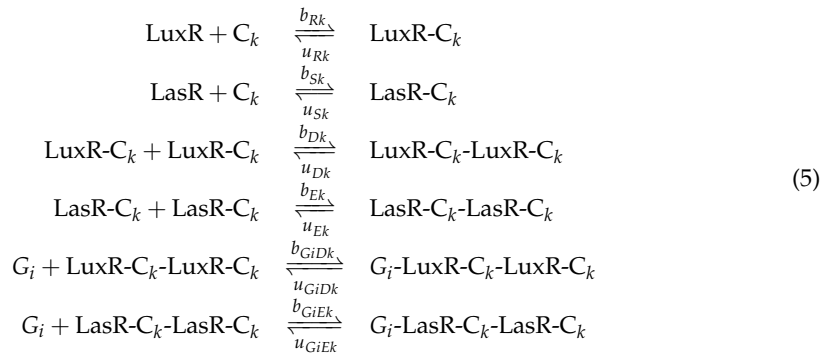
Supplementary Figure 18: Comparison of prpr model with fluorescence measurements. Simulations are of bulk CFP (cyan lines) and YFP (yellow lines) fluorescence, evaluated with the maximum likelihood parameter set. Measurements of bulk culture fluorescence are shown for CFP (cyan circles) and YFP (yellow circles). Chloramphenicol treatment concentrations are indicated atop each panel.

Receiver model

We consider the dynamic characterization of the HSL Receiver circuit introduced in [3] and modelled dynamically in [4, 5]. In this circuit, which we refer to in the main text as the Receiver, two variations of the wild-type PLux promoter, PLux76 and PLas81, were engineered to bind preferentially to activated LuxR and LasR complexes respectively. As LuxR favours binding of C6 and LasR favours binding of C12, optimized expression of LuxR and LasR can lead to near-orthogonal intracellular detection of C6 and C12. The Receiver device was originally measured with PLux76 upstream of the coding sequence for CFP, and PLas81 upstream of the coding sequence for YFP.

Version 1 - Uniform degradation. The first version of the model we introduce is derived in [4]. It is based on the assumption that all degradation processes are of the same order, e.g. LuxR monomers are degraded at a similar rate as LuxR Dimers bound to HSLs. Subsequently, we will introduce an alternative derivation where we assume that complexes are protected from degradation, i.e. that degradation mainly occurs on the monomer level. We start by repeating some of the derivation from [4].

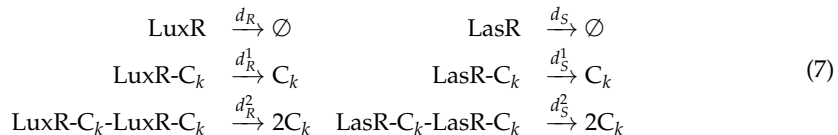
We denote by C_k the HSL molecule with length k carbon chain, and by G_i the PLux76 and PLas81 promoters. Then similar to the derivation in [3], we can specify all of the reactions between the HSLs, LuxR and LasR, and eventual binding of transcriptional regulators to PLux76/PLas81.



Constitutive expression of LuxR and LasR is described by

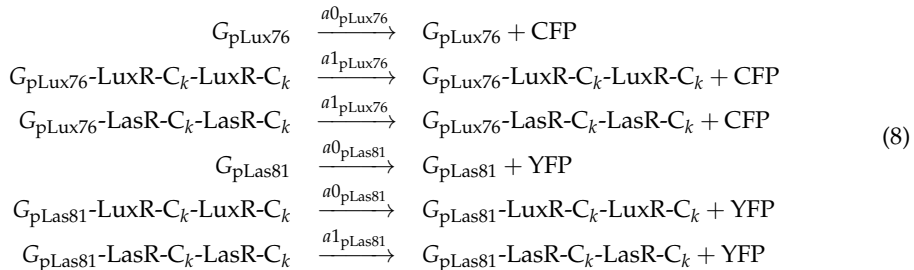


Degradation of LuxR and LasR is described by



where d_R^1 and d_R^2 are distinguishable from d_R to describe the effect of HSL molecules protecting receiver proteins from degradation.

Inducible expression of CFP and YFP by P_{OLux} and P_{OLas} respectively is described by



To produce a simplified ODE model amenable to parameter inference, we start with the equations describing LuxR and LasR protein, their complexes involving C₆ and C₁₂, and the bound/unbound promoters. Crucially, in this first derivation, we make a *rapid equilibrium* assumption for the binding reactions (5), and obtain the following relationships

$$[G_i\text{-LuxR-C}_k\text{-LuxR-C}_k]^* = K_{GDk}[G_i][\text{LuxR-C}_k\text{-LuxR-C}_k] \quad (9a)$$

$$[\text{LuxR-C}_k\text{-LuxR-C}_k]^* = K_{Dk}[\text{LuxR-C}_k]^2 \quad (9b)$$

$$[\text{LuxR-C}_k]^* = K_{Rk}[c_R][C_k] \quad (9c)$$

where $K_{Rk} = \frac{b_{Rk}}{\gamma + u_{Rk}}$, $K_{Dk} = \frac{b_{Dk}}{u_{Dk}}$ and $K_{GiDk} = \frac{b_{GiDk}}{u_{GiDk}}$. Therefore (also symmetry of LuxR and LasR),

$$[G_i\text{-LuxR-C}_k\text{-LuxR-C}_k]^* = K_{GiDk}K_{Dk}(K_{Rk}[C_k][c_R])^2 \quad (10a)$$

$$[G_i\text{-LasR-C}_k\text{-LasR-C}_k]^* = K_{GiEk}K_{Ek}(K_{Sk}[C_k][c_S])^2 \quad (10b)$$

where the new K's are defined as above.

To reduce the system to fewer variables, we consider the evolution of total LuxR, and seek to co-ordinate this with the rapid equilibrium relationships above. By denoting the total concentration of LuxR as c_R, we can write down its time-evolution as

$$\frac{d[R]_T}{dt} = \frac{d[c_R]}{dt} + \sum_k \left(\frac{d[\text{LuxR-C}_k]}{dt} + 2 \frac{d[\text{LuxR-C}_k\text{-LuxR-C}_k]}{dt} + 2 \sum_i \frac{d[G_i\text{-LuxR-C}_k\text{-LuxR-C}_k]}{dt} \right) \quad (11a)$$

$$= a_R - \gamma[c_R] - d_R[c_R] \dots \\ - \sum_k \left((\gamma + d_R^1)[\text{LuxR-C}_k] + (\gamma + d_R^2)[\text{LuxR-C}_k\text{-LuxR-C}_k] + \gamma \sum_i [G_i\text{-LuxR-C}_k\text{-LuxR-C}_k] \right) \quad (11b)$$

If there are differences between d_R, d_R¹ and d_R², then further reduction is complicated. However, by assuming that HSL is not protective of receiver protein (d_R¹ = d_R² = d_R), we obtain the simplification

$$\frac{dc_R}{dt} = a_R - (\gamma + d_R)c_R \quad (12)$$

Now using a conservation relationship for LuxR, we can obtain

$$c_R = [\text{LuxR}] + \sum_k \left([\text{LuxR-C}_k] + 2[\text{LuxR-C}_k\text{-LuxR-C}_k] + 2 \sum_i [G_i\text{-LuxR-C}_k\text{-LuxR-C}_k] \right) \\ = [\text{LuxR}] + \sum_k \left(K_{Rk}[\text{LuxR}][C_k] + 2K_{Dk}K_{Rk}^2[\text{LuxR}]^2[C_k]^2 + \sum_i 2K_{GiDk}[G_i]K_{Dk}K_{Rk}^2[\text{LuxR}]^2[C_k]^2 \right)$$

When C_k is low, total LuxR is closely approximated by free LuxR, c_R ≈ [LuxR]. But when C_k is high, c_R should be partitioned between the [LuxR-C_k-LuxR-C_k] and [G_i-LuxR-C_k-LuxR-C_k] species. Therefore, to simplify the analysis, we propose modelling this by using the assumption

$$c_R \approx [\text{LuxR}] + \sum_k [\text{LuxR-C}_k] = [\text{LuxR}] \left(1 + \sum_k K_{Rk}[C_k] \right) \quad (13)$$

which still captures the saturation of LuxR by C_k , using the approximations

$$[\text{LuxR}] \approx c_R \cdot \frac{1}{1 + \sum_k K_{Rk}[C_k]} \quad (14\text{a})$$

$$[\text{LuxR-C}_k] \approx c_R \cdot \frac{K_{Rk}[C_k]}{1 + \sum_k K_{Rk}[C_k]} \quad (14\text{b})$$

$$[\text{LuxR-C}_k\text{-LuxR-C}_k] \approx K_{Dk}c_R^2 \left(\frac{K_{Rk}[C_k]}{1 + \sum_k K_{Rk}[C_k]} \right)^2 \quad (14\text{c})$$

$$[G_i\text{-LuxR-C}_k\text{-LuxR-C}_k] \approx K_{GR}^{(i)}[G_i]c_R^2 \left(\frac{K_{Rk}[C_k]}{1 + \sum_k K_{Rk}[C_k]} \right)^2 \quad (14\text{d})$$

where $K_{GR}^{(i)} = K_{GiDk}K_{Dk}$ is assumed to be independent of which signal is bound (k), equivalent to the derivation in [3]. By symmetry, we immediately obtain equivalent expressions for interactions between LasR, HSL and PLux promoters. We denote the total concentration of LasR as c_S .

In addition to the saturation of LuxR and LasR, our reduced model also allows for saturation of G_i . By taking advantage of the conservation law

$$\begin{aligned} N_i &= [G_i] + [G_i\text{-LuxR-C}_6\text{-LuxR-C}_6] + [G_i\text{-LuxR-C}_{12}\text{-LuxR-C}_{12}] + \dots \\ &\quad [G_i\text{-LasR-C}_6\text{-LasR-C}_6] + [G_i\text{-LasR-C}_{12}\text{-LasR-C}_{12}], \end{aligned}$$

we can derive the rate of production of mRNA as a function of c_R , c_S [C_6] and [C_{12}]. For notational convenience we write $c_6 := [C_6]$ and $c_{12} := [C_{12}]$. Then,

$$P_i(c_6, c_{12}, c_R, c_S) = \frac{\epsilon^{(i)} + K_{GR}^{(i)}B_R + K_{GS}^{(i)}B_S}{1 + K_{GR}^{(i)}B_R + K_{GS}^{(i)}B_S} \quad (15)$$

where the fractions of bound LuxR and LasR are defined by

$$B_R := c_R^2 \left(\frac{K_{Rk}c_k}{1 + \sum_k K_{Rk}c_k} \right)^{n_R}, \quad B_S := c_S^2 \left(\frac{K_{Sk}c_k}{1 + \sum_k K_{Sk}c_k} \right)^{n_S} \quad (16)$$

Here, we have introduce alternative exponents n_R and n_S , analogous to the usage of n in [3]. Accordingly, we obtain the following system of equations

$$\frac{d\rho}{dt} = \gamma(\rho) \cdot \rho \quad (17\text{a})$$

$$\frac{dc_R}{dt} = a_R - (d_R + \gamma(\rho)) \cdot c_R \quad (17\text{b})$$

$$\frac{dc_S}{dt} = a_S - (d_S + \gamma(\rho)) \cdot c_S \quad (17\text{c})$$

$$\frac{dc_{\text{CFP}}}{dt} = a_{\text{CFP}} \cdot P_{76}(c_6, c_{12}, c_R, c_S) - (d_{\text{CFP}} + \gamma(\rho)) \cdot c_{\text{CFP}} \quad (17\text{d})$$

$$\frac{dc_{\text{YFP}}}{dt} = a_{\text{YFP}} \cdot P_{81}(c_6, c_{12}, c_R, c_S) - (d_{\text{YFP}} + \gamma(\rho)) \cdot c_{\text{YFP}} \quad (17\text{e})$$

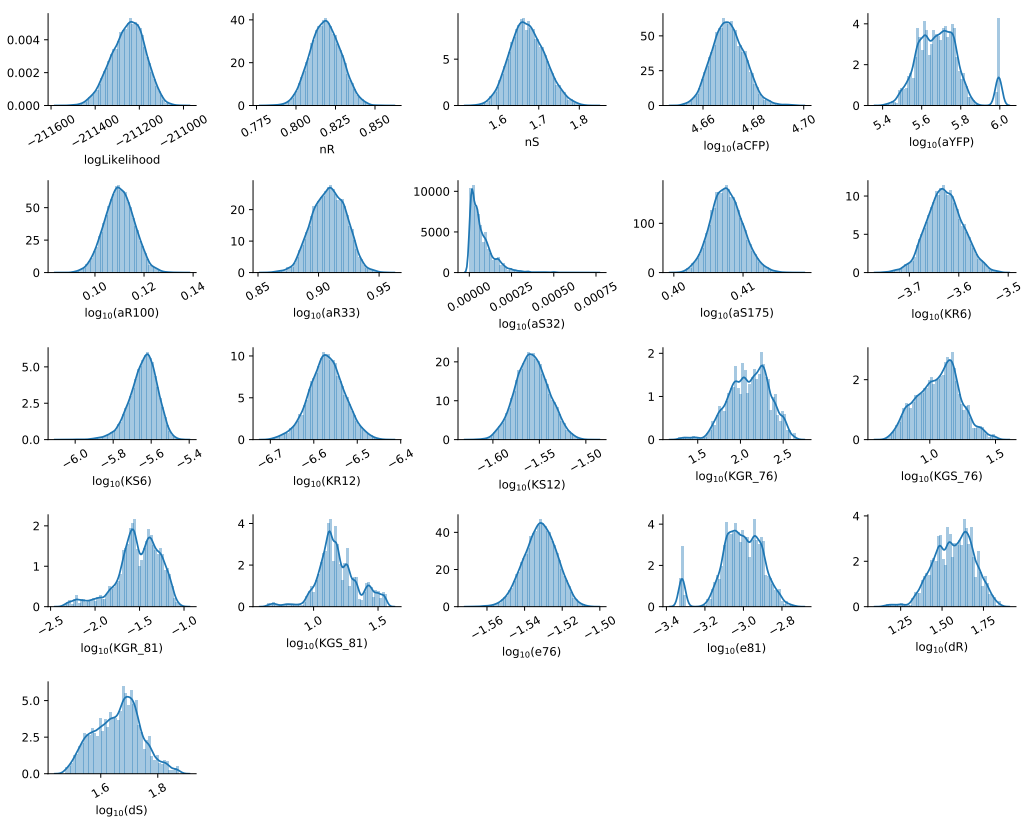
Inference for version 1 (uniform degradation). To characterize the LuxR and LasR signalling components, we used measurements of the response of four Receiver circuits from [3] to treatment with C6 and C12 over 3-fold dilutions. The maximum LuxR and LasR production rates were normalized to the values corresponding to the Pcat promoters, as done previously [3], thus setting the scale for unobserved concentrations of LuxR and LasR.

We used (uninformative) uniform priors on the previously uncharacterized parameters, and (informative) truncated Gaussian priors on f_{480} , f_{530} , d_{CFP} and d_{YFP} with mean and standard deviation taken from the marginal posteriors of the prpr circuit characterization. We did not propagate the marginal posteriors of a_{CFP} and a_{YFP} as the promoter involved differed between the prpr circuit and Receiver circuits. The priors used are detailed in the following table.

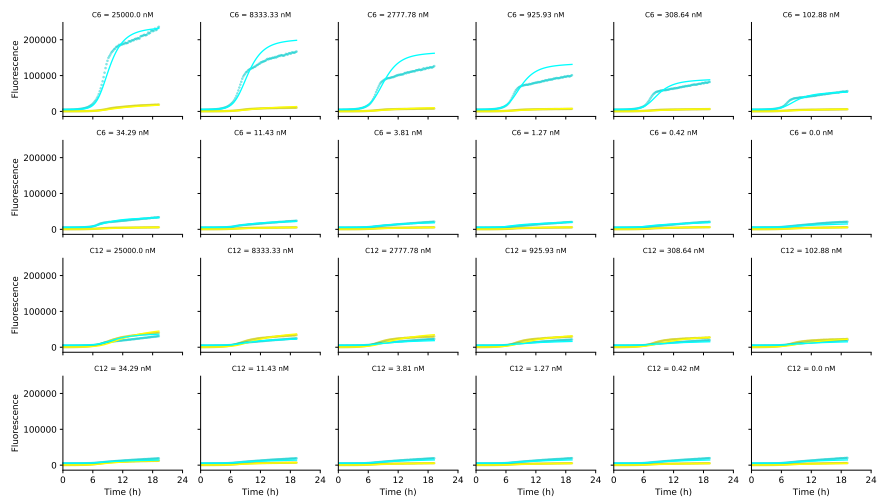
The marginal posterior estimates are shown in Figure 19. Simulation of the maximum likelihood estimate is shown in Figure 20.

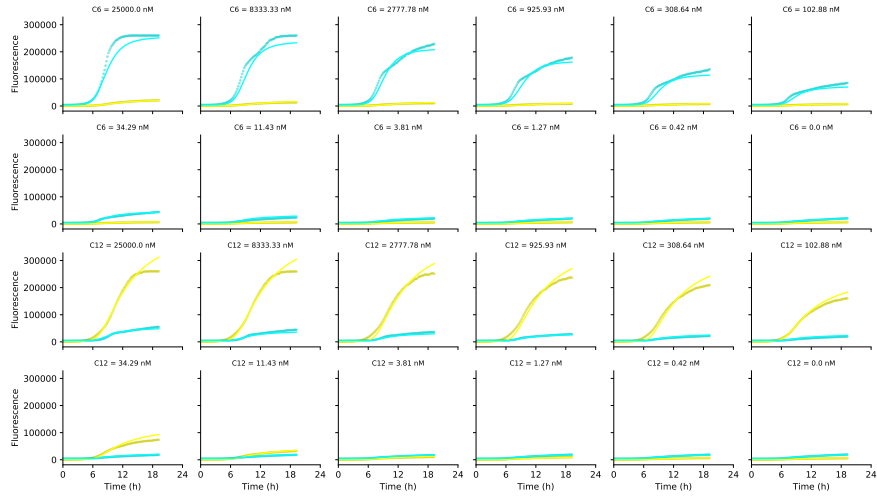
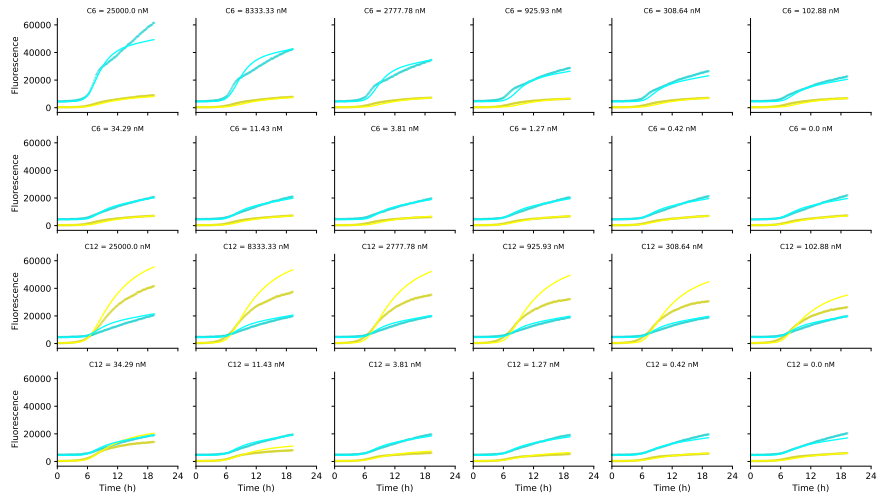
Supplementary Table 4: Priors for version 1 of the Receiver circuit characterization. In the unit column, M_R and M_S denote the normalised mass units for LuxR and LasR, and Fl denotes fluorescence units. The scaling column refers to the proposal distribution used to generate new parameters during MCMC.

Parameter	Description	Unit	Distribution	Scaling
a_{R100}	LuxR synthesis	$M_R \cdot h^{-1}$	$U(1, 10^2)$	Log
a_{R33}	LuxR synthesis	$M_R \cdot h^{-1}$	$U(1, 10^2)$	Log
a_{S32}	LasR synthesis	$M_S \cdot h^{-1}$	$U(1, 10^2)$	Log
a_{S175}	LasR synthesis	$M_S \cdot h^{-1}$	$U(1, 10^2)$	Log
d_R	LuxR degradation	h^{-1}	$U(10^{-2}, 10^2)$	Log
d_S	LasR degradation	h^{-1}	$U(10^{-2}, 10^2)$	Log
K_{R6}	Dissociation (LuxR-C6)	nM^{-1}	$U(10^{-8}, 1)$	Log
K_{S6}	Dissociation (LasR-C6)	nM^{-1}	$U(10^{-8}, 1)$	Log
K_{R12}	Dissociation (LuxR-C12)	nM^{-1}	$U(10^{-8}, 1)$	Log
K_{S12}	Dissociation (LasR-C12)	nM^{-1}	$U(10^{-8}, 1)$	Log
$K_{GR}^{(76)}$	Dissociation (P76-LuxR)	M_R^{-2}	$U(10^{-4}, 10^3)$	Log
$K_{GS}^{(76)}$	Dissociation (P76-LasR)	M_S^{-2}	$U(10^{-8}, 10^3)$	Log
$K_{GR}^{(81)}$	Dissociation (P81-LuxR)	M_R^{-2}	$U(10^{-8}, 10^3)$	Log
$K_{GS}^{(81)}$	Dissociation (P81-LasR)	M_S^{-2}	$U(10^{-4}, 10^3)$	Log
n_R	Hill constant (LuxR-HSL)	-	$U(0.5, 2)$	Real
n_S	Hill constant (LasR-HSL)	-	$U(0.5, 2)$	Real
$e^{(76)}$	Leak production (P76)	-	$U(10^{-4}, 1)$	Log
$e^{(81)}$	Leak production (P81)	-	$U(10^{-4}, 1)$	Log
a_{CFP}	CFP synthesis	$Fl \cdot cell^{-1} \cdot h^{-1}$	$U(10^2, 10^6)$	Log
a_{YFP}	YFP synthesis	$Fl \cdot cell^{-1} \cdot h^{-1}$	$U(10^2, 10^6)$	Log
b_{480}	Background fluor. (CFP)	Fl	$U(0, 10^4)$	Real
b_{530}	Background fluor. (YFP)	Fl	$U(0, 5 \times 10^3)$	Real



Supplementary Figure 19: Marginal parameter posterior estimates of the Receiver model (version 1) parameters. The marginal distributions are computed from 20 independent MCMC chains.

A Pcat circuit**B R100S32 circuit**

C R33S32 circuit**D R33S175 circuit**

Supplementary Figure 20: Comparison of Receiver models with fluorescence measurements. Simulations are of bulk CFP (cyan lines) and YFP (yellow lines) fluorescence, evaluated with the maximum likelihood parameter set. Measurements of bulk culture fluorescence are shown in for CFP (cyan circles) and YFP (yellow circles). C6 and C12 treatment concentrations are indicated atop each panel.

Version 2 - Protected degradation. Here we provide an alternative derivation for the model reduction based on the assumption that HSL complexes and dimers are protected from degradation, i.e. that degradation predominantly occurs on the level of LuxR/LasR monomers. This is supported by in vitro analysis of purified LuxR suggesting that LuxR protein is unstable in the absence of 3OC6-HSL [6]. Furthermore, we assume that all dilution effects occur on a slow time scale as compared to the kinetic. With this derivation, we obtain the same functional structure of the promoter activities of PLux76 and PLas81 from equation (15), but with the definitions of the bound fraction of LuxR and LasR given instead by

$$B_R := c_R^2 (c_6^{n_R} + (e_{R12} c_{12})^{n_R}), \quad B_S := c_S^2 ((e_{S6} c_6)^{n_S} + c_{12}^{n_S}) \quad (18)$$

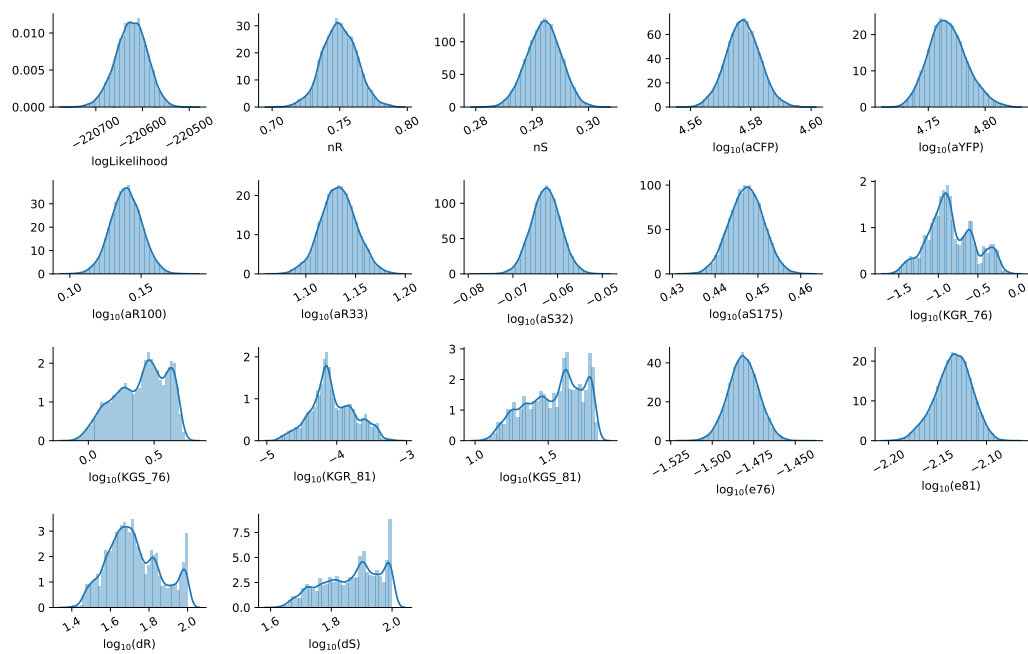
where $e_{R12} = \frac{K_{R12}}{K_{R6}}$ and $e_{S6} = \frac{K_{S6}}{K_{S12}}$ result from dividing by K_{R6} and K_{S12} . Consequently, the parameters $K_{GR}^{(i)}$ and $K_{GS}^{(i)}$ in equation (15) are rescaled by K_{R6} and K_{S12} respectively.

Inference for version 2 (Protected degradation). We carried out parameter inference for version 2 of the model directly equivalent to that done for version 1. The complete list of prior distributions for the parameters is as follows.

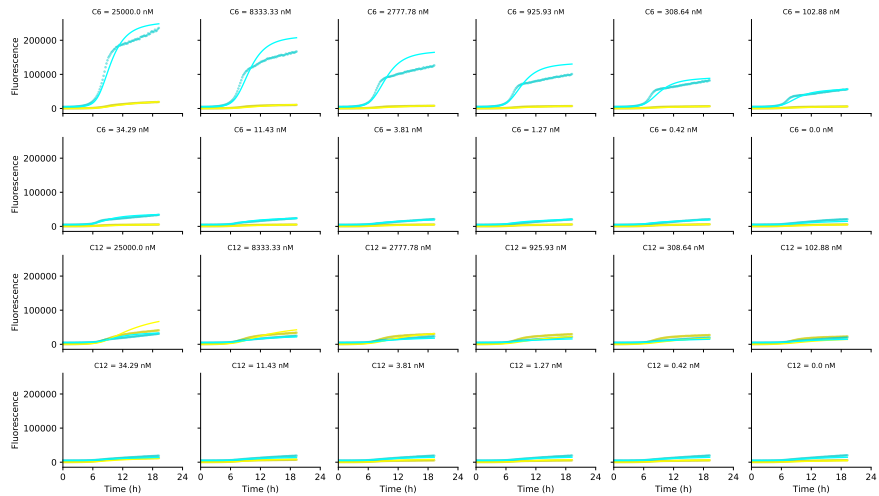
Supplementary Table 5: Priors for version 2 of the Receiver circuit characterization. In the unit column, M_R and M_S denote the normalised mass units for LuxR and LasR, and Fl denotes fluorescence units. The scaling column refers to the proposal distribution used to generate new parameters during MCMC.

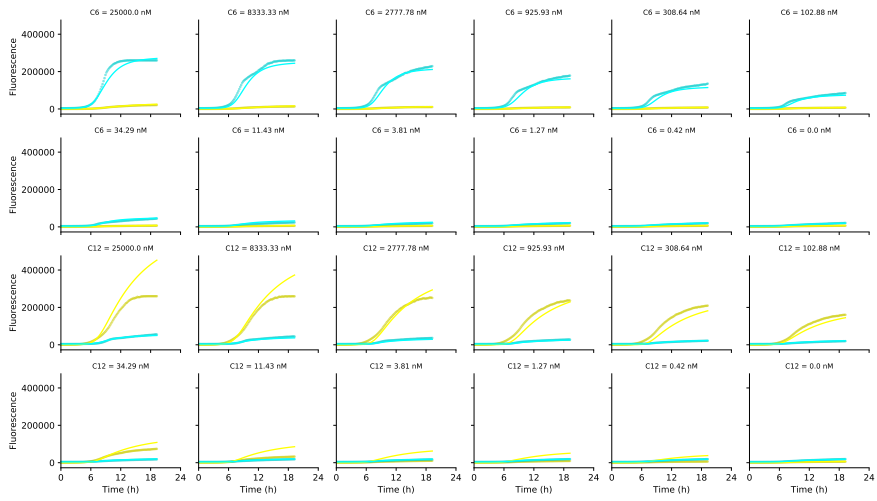
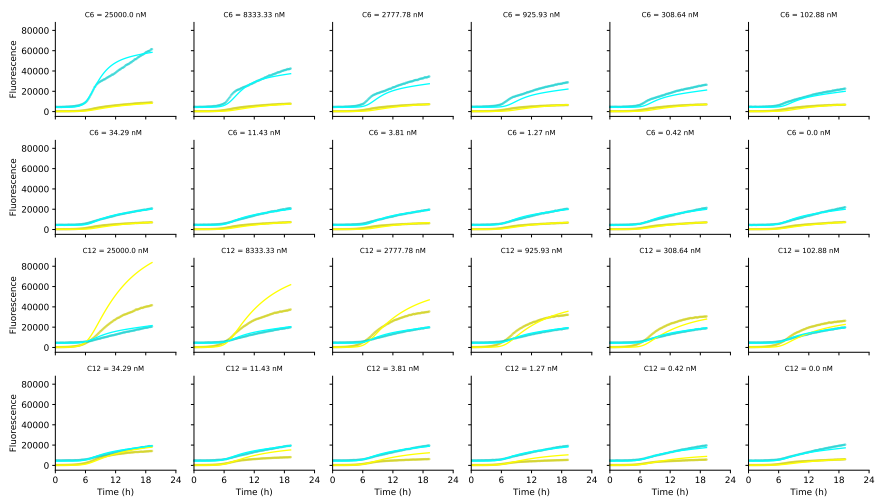
Parameter	Description	Unit	Distribution	Scaling
a_{R100}	LuxR synthesis	$M_R \cdot h^{-1}$	$U(1, 10^2)$	Log
a_{R33}	LuxR synthesis	$M_R \cdot h^{-1}$	$U(1, 10^2)$	Log
a_{S32}	LasR synthesis	$M_S \cdot h^{-1}$	$U(1, 10^2)$	Log
a_{S175}	LasR synthesis	$M_S \cdot h^{-1}$	$U(1, 10^2)$	Log
d_R	LuxR degradation	h^{-1}	$U(10^{-2}, 10^2)$	Log
d_S	LasR degradation	h^{-1}	$U(10^{-2}, 10^2)$	Log
e_{R12}	Chemical crosstalk (LuxR)	-	$U(10^{-8}, 1)$	Log
e_{S6}	Chemical crosstalk (LasR)	-	$U(10^{-8}, 1)$	Log
$K_{GR}^{(76)}$	Dissociation (P76-LuxR)	$M_R^{-(2+n_R)}$	$U(10^{-4}, 10^3)$	Log
$K_{GS}^{(76)}$	Dissociation (P76-LasR)	$M_S^{-(2+n_S)}$	$U(10^{-8}, 10^3)$	Log
$K_{GR}^{(81)}$	Dissociation (P81-LuxR)	$M_R^{-(2+n_R)}$	$U(10^{-8}, 10^3)$	Log
$K_{GS}^{(81)}$	Dissociation (P81-LasR)	$M_S^{-(2+n_S)}$	$U(10^{-4}, 10^3)$	Log
n_R	Hill constant (LuxR-HSL)	-	$U(0.2, 2)$	Real
n_S	Hill constant (LasR-HSL)	-	$U(0.2, 2)$	Real
$e^{(76)}$	Leak production (P76)	-	$U(10^{-4}, 1)$	Log
$e^{(81)}$	Leak production (P81)	-	$U(10^{-4}, 1)$	Log
a_{CFP}	CFP synthesis	$Fl \cdot cell^{-1} \cdot h^{-1}$	$U(10^2, 10^6)$	Log
a_{YFP}	YFP synthesis	$Fl \cdot cell^{-1} \cdot h^{-1}$	$U(10^2, 10^6)$	Log
B_{480}	Background fluorescence (CFP)	Fl	$U(0, 10^4)$	Real
B_{530}	Background fluorescence (YFP)	Fl	$U(0, 5 \times 10^3)$	Real

The marginal posterior estimates are shown in Figure 21. Simulation of the maximum likelihood estimate is shown in Figure 22.



Supplementary Figure 21: Marginal parameter posterior estimates of the Receiver model (version 2) parameters. The marginal distributions are computed from 20 independent MCMC chains.

A Pcat circuit**B R100S32 circuit**

C R33S32 circuit**D R33S175 circuit**

Supplementary Figure 22: Comparison of Receiver models with fluorescence measurements. Simulations are of bulk CFP (cyan lines) and YFP (yellow lines) fluorescence, evaluated with the maximum likelihood parameter set. Measurements of bulk culture fluorescence are shown in for CFP (cyan circles) and YFP (yellow circles). C6 and C12 treatment concentrations are indicated atop each panel.

Exclusive Receiver model

To model the Exclusive Receiver, we consider the inhibition of PTet by TetR and PLac by LacI, and the mechanism of chemical inhibition by IPTG and ATC. For promoter regulation, we use the inhibition Hill function

$$H_I(x, n) := \frac{1}{1 + x^n} \quad (19)$$

Typically, these functions would include a parameter for the half-saturation concentration, but we omit that here because, without loss of generality, [LacI] and [TetR] can be arbitrarily scaled by those half-saturation concentrations. In such a rescaling, the half-saturation constants get embedded within the maximal production rates, a_L and a_T . For the chemical inhibitors, we assume a reaction of the form



Correspondingly, the action of IPTG and ATC is proportional to the product of its concentration and its target repressor protein concentration.

$$\frac{d\rho}{dt} = \gamma(\rho).\rho \quad (21a)$$

$$\frac{dc_{YFP}}{dt} = a_{YFP}.f_{81}(c_6, c_{12}, c_R, c_S) - (\gamma(\rho) + d_{YFP})c_{YFP} \quad (21b)$$

$$\frac{dc_{CFP}}{dt} = a_{CFP}.f_{76}(c_6, c_{12}, c_R, c_S) - (\gamma(\rho) + d_{CFP})c_{CFP} \quad (21c)$$

$$\frac{dc_{530}}{dt} = b_Y - \gamma(\rho).c_{530} \quad (21d)$$

$$\frac{dc_{480}}{dt} = b_C - \gamma(\rho).c_{480} \quad (21e)$$

$$\frac{dc_R}{dt} = a_R.H_I(c_T, n_T) - (\gamma(\rho) + d_R).c_R \quad (21f)$$

$$\frac{dc_S}{dt} = a_S.H_I(c_L, n_L) - (\gamma(\rho) + d_S).c_S \quad (21g)$$

$$\frac{dc_L}{dt} = a_L.P_{76}(c_6, c_{12}, c_R, c_S) - (\gamma(\rho) + d_L + i_I.c_I).c_L \quad (21h)$$

$$\frac{dc_T}{dt} = a_T.P_{81}(c_6, c_{12}, c_R, c_S) - (\gamma(\rho) + d_T + i_A.c_A).c_T \quad (21i)$$

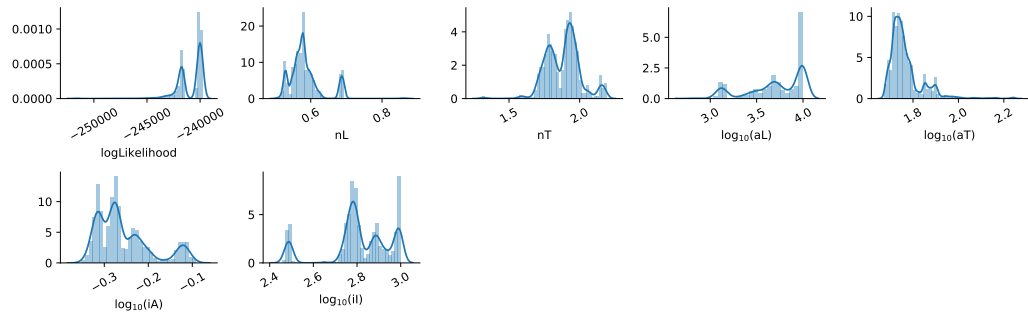
where P_{76} and P_{81} are defined in (15).

Inference for version 1 (uniform degradation). The inference procedure was less robust for the Exclusive Receiver, as compared with upstream circuits in the inference graph. In particular, we found it was not possible to identify a unique mode within the parameter space when all parameters were allowed to be flexible. Specifically, there was strong interdependency within the triplet $\{a_L, d_L, i_I\}$ and the triplet $\{a_T, d_T, i_A\}$. Our interpretation is that we are unable to fully recover the time-scales of variations in c_L and c_T , as they are likely to not vary much during the experiments we used for characterization. It's likely that c_L and c_T quickly stabilise to equilibria when the cells are transferred to the media containing the treatments (specific concentrations of C6, C12, IPTG and ATC). In which case, only those equilibrium values will be identifiable, and not the production and degradation rates separately. Therefore, in the final version of the inference results presented here, we have fixed the degradation rates of LacI and TetR to 1 h^{-1} .

Even when running the inference with d_L and d_T fixed, we found that chain convergence was not perfect, and some chains got stuck in local optima. Therefore, in our marginal posterior estimates, we have only included chains that converged to relatively good likelihood scores Figure 23. The marginals clearly indicate some additional flexibility in the inferred parameter values, possibly resulting from the larger parameter space being navigated, which includes uninformative priors for the parameters listed in Table 6, but also some flexibility in all of the parameters associated with the Receiver module, despite them having a strong prior.

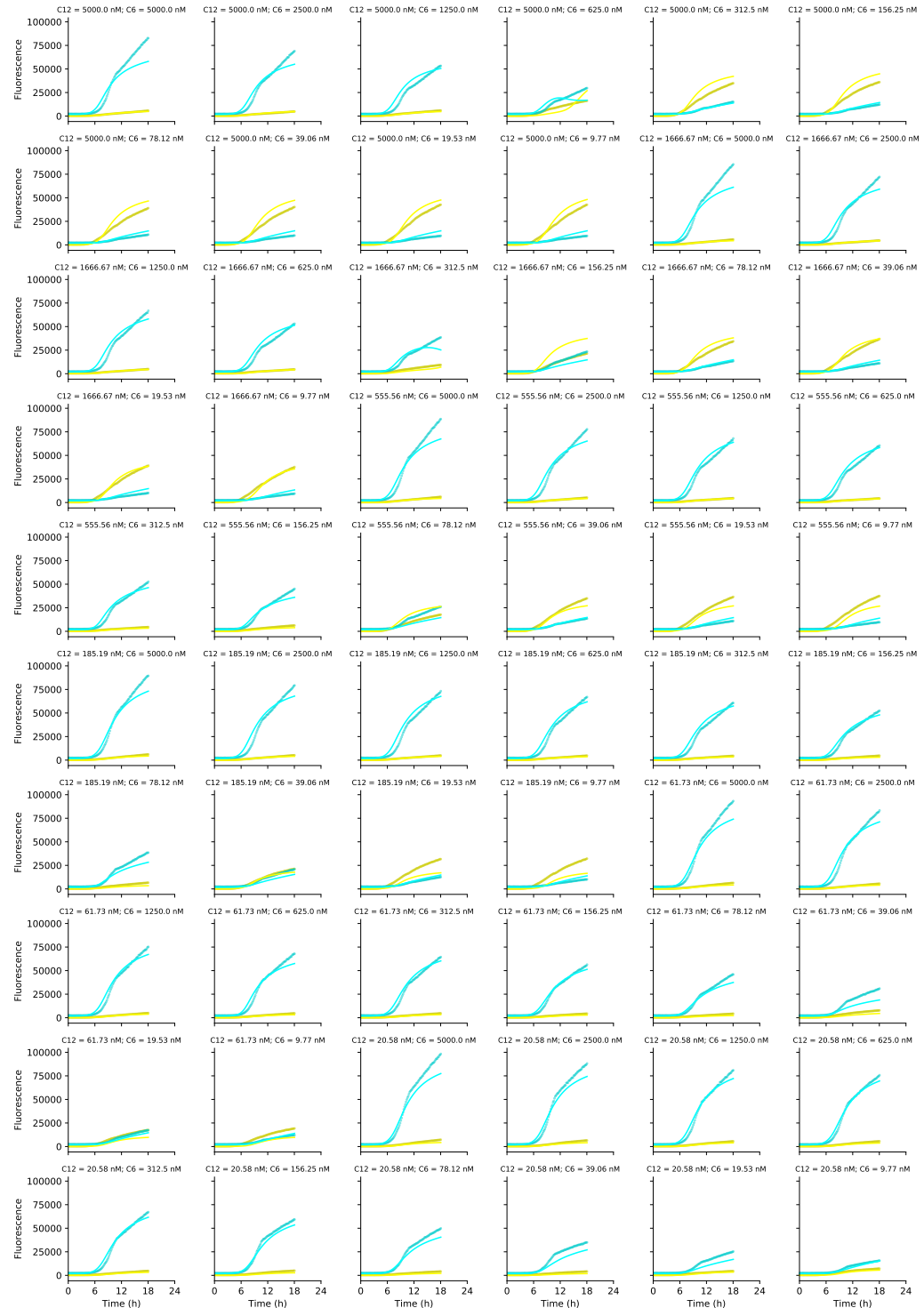
Supplementary Table 6: Priors for the Exclusive Receiver circuit characterization. In the unit column, M_L and M_T denote the normalised mass units for LacI and TetR, and Fl denotes fluorescence units. The scaling column refers to the proposal distribution used to generate new parameters during MCMC.

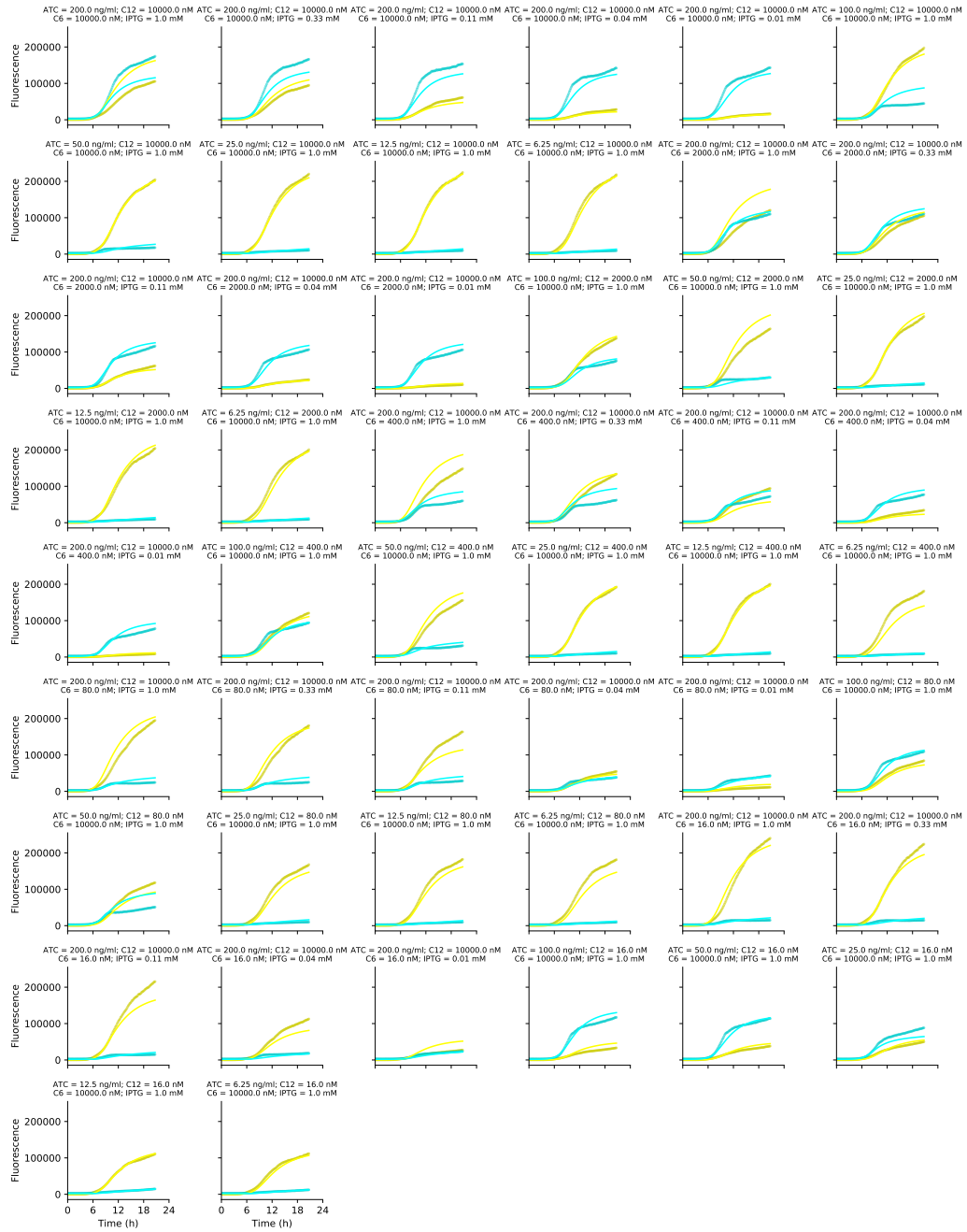
Parameter	Description	Unit	Distribution	Scaling
a_L	LacI synthesis	$M_L \cdot h^{-1}$	$U(1, 10^4)$	Log
a_T	TetR synthesis	$M_T \cdot h^{-1}$	$U(1, 10^4)$	Log
d_L	LacI degradation	h^{-1}	1 (Fixed)	N/A
d_T	TetR degradation	h^{-1}	1 (Fixed)	N/A
n_L	Hill constant (Laci)	-	$U(0.5, 4.0)$	Real
n_T	Hill constant (TetR)	-	$U(0.5, 4.0)$	Real
i_A	ATC inhibition of TetR	$M_T^{-1} \cdot (\text{ng/ml ATC})^{-1} \cdot h^{-1}$	$U(10^{-2}, 10^3)$	Log
i_I	IPTG inhibition of LacI	$M_L^{-1} \cdot (\text{mM IPTG})^{-1} \cdot h^{-1}$	$U(10^{-2}, 10^3)$	Log
B_{480}	Background fluor. (CFP)	Fl	$U(0, 10^4)$	Real
B_{530}	Background fluor. (YFP)	Fl	$U(0, 5 \times 10^3)$	Real



Supplementary Figure 23: Marginal parameter posterior estimates of the Exclusive Receiver model (version 1) parameters. The marginal distributions are computed from 9 of 20 independent MCMC chains. Chains were discarded that did not converge to high log-likelihood regions.

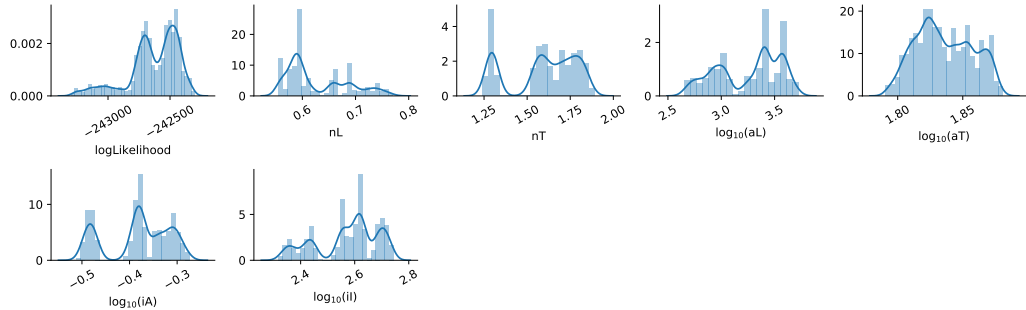
Simulation of the maximum likelihood estimate is shown in Figure 23.

A 2d dilution of C₆ and C₁₂

B Characterization of IPTG and ATC

Supplementary Figure 23: Comparison of Exclusive Receiver model (version 1) with fluorescence measurements. Simulations are of bulk CFP (cyan lines) and YFP (yellow lines) fluorescence, evaluated with the maximum likelihood parameter set. Measurements of bulk culture fluorescence are shown in for CFP (cyan circles) and YFP (yellow circles). C6, C12, ATC and IPTG treatment concentrations are indicated atop each panel.

Inference for version 2 (Protected degradation). The inference procedure was also not completely robust for version 2 of the Exclusive Receiver model. We used the same uninformative priors for the parameters specific to the Exclusive Receiver model as in version 1, including fixing d_L and d_T . Again, in our marginal posterior estimates, we have only included chains that converged to relatively good likelihood scores Figure 24.



Supplementary Figure 24: Marginal parameter posterior estimates of the Exclusive Receiver model (version 2) parameters. The marginal distributions are computed from 8 of 20 independent MCMC chains. Chains were discarded that did not converge to high log-likelihood regions.

Simulation of the maximum likelihood estimate is shown in Extended Data Figure 2.

2.2 Bistability Analysis

In this section we outline computations used to create Figure 2b in the main text which compares regions of bistability indicated by hysteresis experiments in flow cytometry to that given by the differential equation model for the exclusive receiver circuit.

To characterize the region in the (c_{12}, c_6) plane where bistability occurs, we used numerical continuation to calculate a co-dimension two limit curve. The code in `get_bifurcations.jl` in our repository takes advantage of the Julia package `PseudoArcLengthContinuation.jl` [7]. To calculate the bifurcations, we only need consider the steady states of the model. The auto-fluorescence equations are independent of the others and CFP and YFP are simply readouts of c_L and c_T respectively, leaving only four coupled equations to solve, defined by state vector $\mathbf{c} = (c_R, c_S, c_L, c_T)$. For simplicity of analysis, we assume that cell density ρ is constant, and consequently the specific growth rate $\gamma(\rho) =: \gamma_0$ is constant. Later, we check this assumption in Figure 26. With this simplification, the model given by (21) can be represented compactly as

$$\frac{d\mathbf{c}}{dt} = \mathbf{F}_\theta(\mathbf{c}, \mathbf{u}) \quad (22)$$

where $\mathbf{u} = (c_6, c_{12}, c_I, c_A)$ are the experimental control parameters, θ is the vector containing the inferred parameters from Section S1 and γ_0 .

To improve the numerical stability of numerical continuation, we transform the model into \log_{10} coordinates via the element-wise transformations $\mathbf{c} \rightarrow 10^\mathbf{c}$ and $\mathbf{u} \rightarrow 10^\mathbf{u}$ yielding

$$\frac{d\mathbf{c}}{dt} = \frac{\mathbf{F}_\theta(10^\mathbf{c}, 10^\mathbf{u}) 10^{-\mathbf{c}}}{\ln(10)} \quad (23)$$

The steady states are defined by zeros of the numerator of the right-hand side. We can immediately see that this transformation induced a zero at $\mathbf{c} \rightarrow \infty$ which we are not interested in and thus simply seek to solve

$$\mathbf{F}_\theta(10^\mathbf{c}, 10^\mathbf{u}) = 0 \quad (24)$$

To further increase numerical stability of finding 24 we explicitly calculate the Jacobian in the log coordinate system. Luckily the Jacobian in the new coordinates can be expressed in terms of the matrix product between the Jacobian in the original coordinates and the Jacobian of the coordinate transformation

$$\frac{\partial \mathbf{F}_\theta}{\partial \mathbf{c}} \rightarrow \ln(10) \frac{\partial \mathbf{F}_\theta}{\partial \mathbf{c}} \Big|_{\mathbf{c} \rightarrow 10^\mathbf{c}} \text{Diag}[10^\mathbf{c}] \quad (25)$$

where $\text{Diag}[\mathbf{v}]$ is a diagonal matrix with the vector components of \mathbf{v} along the diagonal. The Jacobian in the original coordinates is

$$\frac{\partial \mathbf{F}_\theta}{\partial \mathbf{c}} = \begin{pmatrix} 0 & 0 & 0 & a_{R33} \frac{\partial H_T}{\partial T} \\ 0 & 0 & a_{S175} \frac{\partial H_L}{\partial L} & 0 \\ a_L \frac{\partial P_{76}}{\partial R} & a_L \frac{\partial P_{76}}{\partial S} & 0 & 0 \\ a_T \frac{\partial P_{81}}{\partial R} & a_T \frac{\partial P_{81}}{\partial S} & 0 & 0 \end{pmatrix} - \text{Diag} \left[\gamma_0 + \begin{pmatrix} d_R \\ d_S \\ d_L \\ d_T \end{pmatrix} + \begin{pmatrix} 0 \\ 0 \\ i_I c_I \\ i_A c_A \end{pmatrix} \right] \quad (26)$$

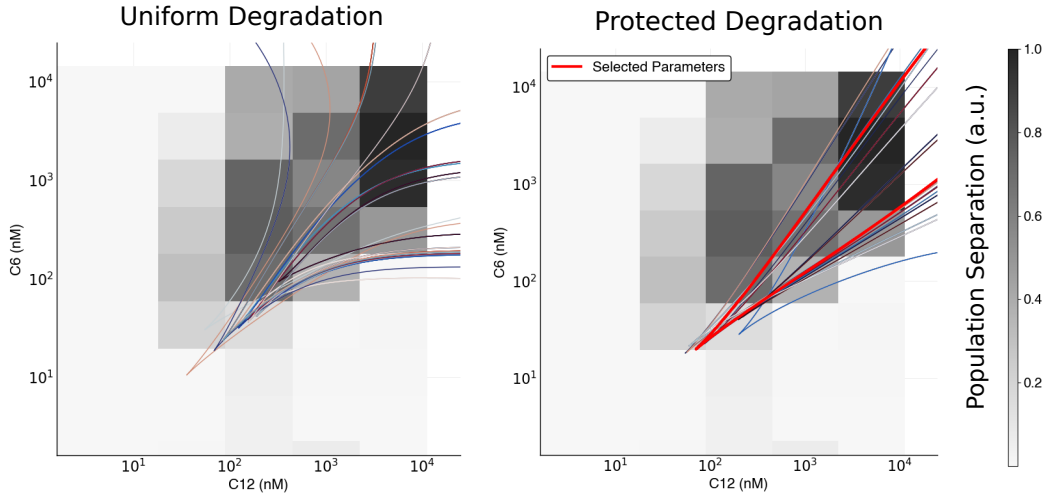
where partials of inhibitory hill functions and promoter activities are

$$\frac{\partial H_X}{\partial X} = \frac{-n_X c_X^{(n_X-1)}}{(1+c_X^{n_X})^2} \quad \frac{\partial P_N}{\partial X} = \frac{K_{GX}^N (1-e_N)}{[1+K_{GR}^N B_R(c_R) + K_{GS}^N B_S(c_S)]^2} \frac{\partial B_X}{\partial X} \quad (27)$$

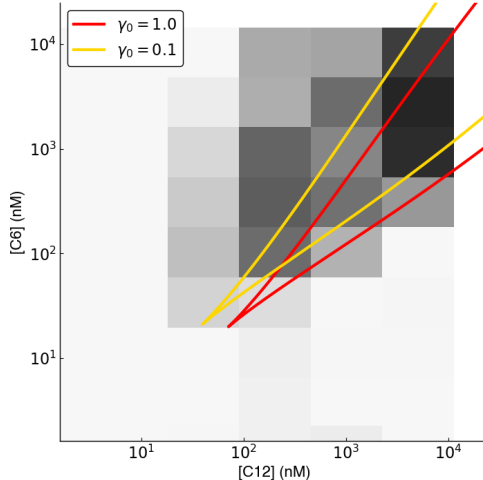
and partial bound molecules for uniform and protected degradation models are respectively

$$\frac{\partial B_X}{\partial X} = 2c_X \frac{(K_{X6}c_6)^{n_X} + (K_{X12}c_{12})^{n_X}}{(1+K_{X6}c_6+K_{X12}c_{12})^{n_X}} \quad \frac{\partial B_X}{\partial X} = 2c_X \begin{cases} c_6^{n_X} + (E_{R12}c_{12})^{n_X} & X = R \\ c_{12}^{n_X} + (E_{S6}c_6)^{n_X} & X = S \end{cases}$$

Given the rate function \mathbf{F}_θ and its Jacobian $\frac{\partial \mathbf{F}_\theta}{\partial c}$ in log coordinates we can perform a co-dimension one parameter continuation for a fixed value of c_{12} along the c_6 direction to find a limit point. Then the solution can be continued along a limit curve in the (c_6, c_{12}) plane along both directions until the limits of the observation region are met. Figure 25 reveals these curves for different models and inferred maximum likelihood parameter sets θ and Figure 26 reveals that the chosen model for the main text is insensitive to changes in growth γ_0 and therefore we can safely assume that the qualitative behaviour of the model will not change if the cell density is constant. For simplicity, this is what is done in the spatial simulations in Sections 2.3 and 2.4.



Supplementary Figure 25: Bifurcation curves for uniform and protected degradation models. Curves are plotted on top of bimodal population separation heatmaps generated from flow cytometry data. The selected maximum likelihood parameters are used in the main text.



Supplementary Figure 26: Bifurcation curve insensitivity specific growth rate γ_0 . The cell density is a monotonically increasing function of time that saturates at the carrying capacity. Concomitantly, the specific growth rate declines towards 0. By evaluating the bifurcation diagram at different values of γ_0 , we can see how the cusp would move over time. Here the maximum likelihood parameters from the main text reveal that the cusp does not move much as the cell density increases over time.

2.3 Boundary Experiments

Simulation and local equilibria

For spatial simulations a simple forward-Euler method is implemented in `get_movie.py`. The bacterial colonies for the spatial experiments were placed on top of agar with no signalling molecules inside it. Then additional volumes of agar were attached either side of the width of the experiment with different concentrations of c_6 and c_{12} . The signalling molecules then diffuse in the agar and established a cross-gradient felt by the bacterial colonies. These are governed by diffusion

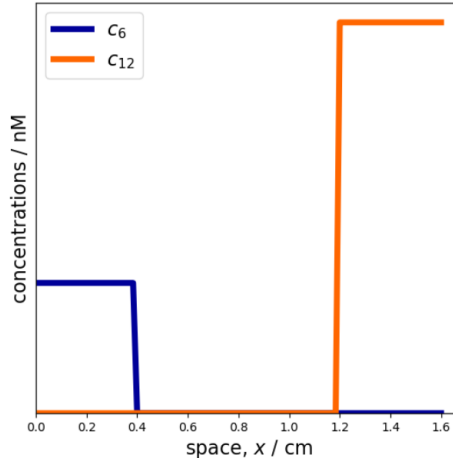
$$\frac{\partial c_X(x, t)}{\partial t} = D_X \frac{\partial^2 c_X(x, t)}{\partial x^2} \quad (28)$$

where $D_6 = 1.8 \cdot 10^{-6} \text{ m}^2 \cdot \text{h}^{-1}$ and $D_{12} = 0.9 \cdot 10^{-6} \text{ m}^2 \cdot \text{h}^{-1}$.

The initial conditions for spatial simulations are zero everywhere except for $c_6(x, t)|_{t=0}$ and $c_{12}(x, t)|_{t=0}$ initialised in small regions widths w on opposite sides of the experiment of width W at concentrations such that the homogeneous equilibrium after diffusion would be $c_6(x, t)|_{t \rightarrow \infty} = \bar{C}_6$ and $c_{12}(x, t)|_{t \rightarrow \infty} = \bar{C}_{12}$ with zero-flux boundary conditions. Therefore

$$c_6(x, t)|_{t=0} = \frac{W\bar{C}_6}{w} H(w - x) \quad c_{12}(x, t)|_{t=0} = \frac{W\bar{C}_{12}}{w} H(x - W + w) \quad (29)$$

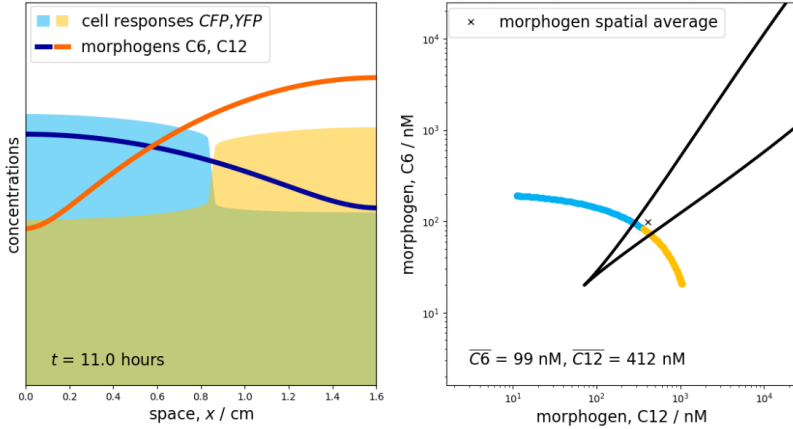
where $H(x)$ is a unit step function.



Supplementary Figure 27: Initial conditions $c_6(x, t)|_{t=0}$ and $c_{12}(x, t)|_{t=0}$ with $W = 1.6 \text{ cm}$ and $w = 0.4 \text{ cm}$

Each location x experiences concentrations c_6, c_{12} which define a local equilibrium for the remaining state variables. These local equilibria evolve over time and are chased by the actual concentrations of protein in the cells at that location. As shown by Figure 25, at some concentrations c_6, c_{12} there may two stable equilibria rather than one. Therefore it becomes useful to not only display the dynamics in the one dimensional spatial domain but also in the (c_6, c_{12}) plane. How and when local equilibria bifurcate reveals the eventual fate of the spatial pattern.

Figure 28 shows a snapshot of the dynamics in the spatial domain x and the (c_6, c_{12}) plane. A sharp boundary in space forms when the state density in (c_6, c_{12}) moves into the bistable region enclosed by the limit point curve. This means that, given the cross-gradient initial conditions 29, if the homogeneous equilibrium \bar{C}_6, \bar{C}_{12} lies within the bistable region, a sharp stationary boundary will form. If \bar{C}_6, \bar{C}_{12} lies below the cusp of the limit point curve, only soft boundaries will form. In other regions outside the bistable cone the sharp boundary has a finite velocity and will eventually leave the experimental region. See supplementary movies 2-5 for examples of the above. This motivated the experimental exploration of the space of \bar{C}_6, \bar{C}_{12} and measurements of boundary velocity, which are described in the following section.



Supplementary Figure 28: Dynamics in the spatial domain x on the left and (c_6, c_{12}) plane on the right. Spatial averages of morphogens \bar{C}_6, \bar{C}_{12} are 99 nM and 412 nM respectively for both panels

Computation of the boundary velocity

The velocity of the boundary is determined using `get_movement.py` from the TIFF image stack $M[t, x, y, s]$ obtained by the fluorescence microscope from one experiment, set up with a chosen \bar{C}_6, \bar{C}_{12} combination. Here t indexes the time point, x and y index the width and height and s indexes the three channels: CFP, YFP and RFP.

First the data are normalised by the RFP channel. This way the location of the boundary can be defined by comparing the pixel values of one channel against the other. The pixels are masked for the colony grid squares $(x, y) \in \Omega$ which are otherwise surrounded by hydrophobic ink filter paper, on which no colonies grow. The grid squares are detected by thresholding the constituent RFP channel at the `end` time point.

$$X[t, x, y, s] := \frac{M[t, x, y, s]}{M[t, x, y, \bullet]} \quad \text{where } (x, y) \in \Omega \quad (30)$$

$$\text{where } \Omega := \left\{ (x, y) : M[\text{end}, x, y, \bullet] > \frac{1}{2} \right\} \quad (31)$$

Next, a sigmoidal basis function Bayesian Ridge regressor is applied to each channel and time point along the width x of the preprocessed data $X[t, x, y, s]$. Sigmoidal basis functions are used because they satisfy the zero-flux boundary conditions as well as our expectations that the fluorescence profile across the width of the experiment will mostly be flat with a transient step due to the cross-gradient. The unknown weights ϕ of the basis functions are obtained by minimising the objective

$$J_\phi[t, s] := \sum_{(x, y) \in \Omega} ||X[t, x, y, s] - f_\phi(x)[t, s]||^2 \quad (32)$$

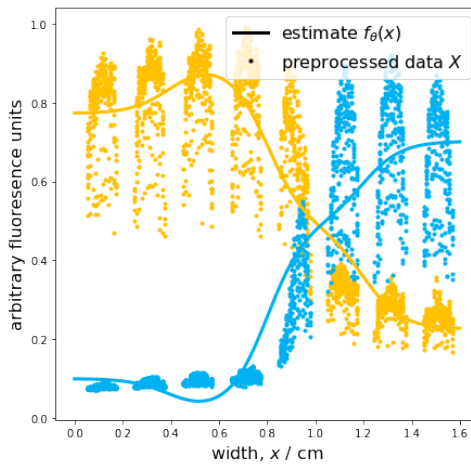
$$\text{where } f_\phi(x) := \sum_{(\alpha, \mu, \sigma) \in \phi} \frac{\alpha}{1 + e^{-\frac{x-\mu}{\sigma}}} \quad (33)$$

With the continuous estimate $f_{\phi^*}(x)$ for each $[t, s]$, the location of the boundary can be obtained even if it was estimated to lie between two colonies as seen in Figure 29. Since this continuous estimate is obtained for each point in time, the position of the boundary can be tracked in a smooth kymograph as shown in Figure 30. We define the boundary location $\beta[t]$ to be where the estimate of the CFP channel \bullet is equal to that of the YFP channel \circ ,

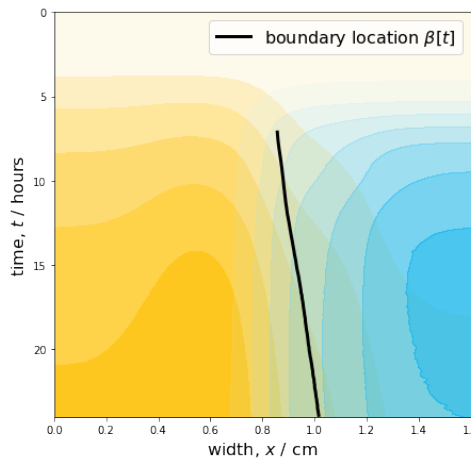
$$f_{\phi^*}(\beta)[t, \bullet] = f_{\phi^*}(\beta)[t, \bullet] \quad (34)$$

The distance travelled by the boundary $\Delta\beta$ from its formation time t^* to the end as a fraction of the size of the experiment W can now be computed. The formation time t^* was judged by eye and seems to lie between 3 – 5 h, at which fluorescence values are sufficiently steep to form a sharp boundary. The boundary should have travelled at least 10% along the width - which is the approximate size of one colony grid square - in order to be classified as moving.

$$\Delta\beta = \frac{\beta[t^*] - \beta[\text{end}]}{W} \quad (35)$$

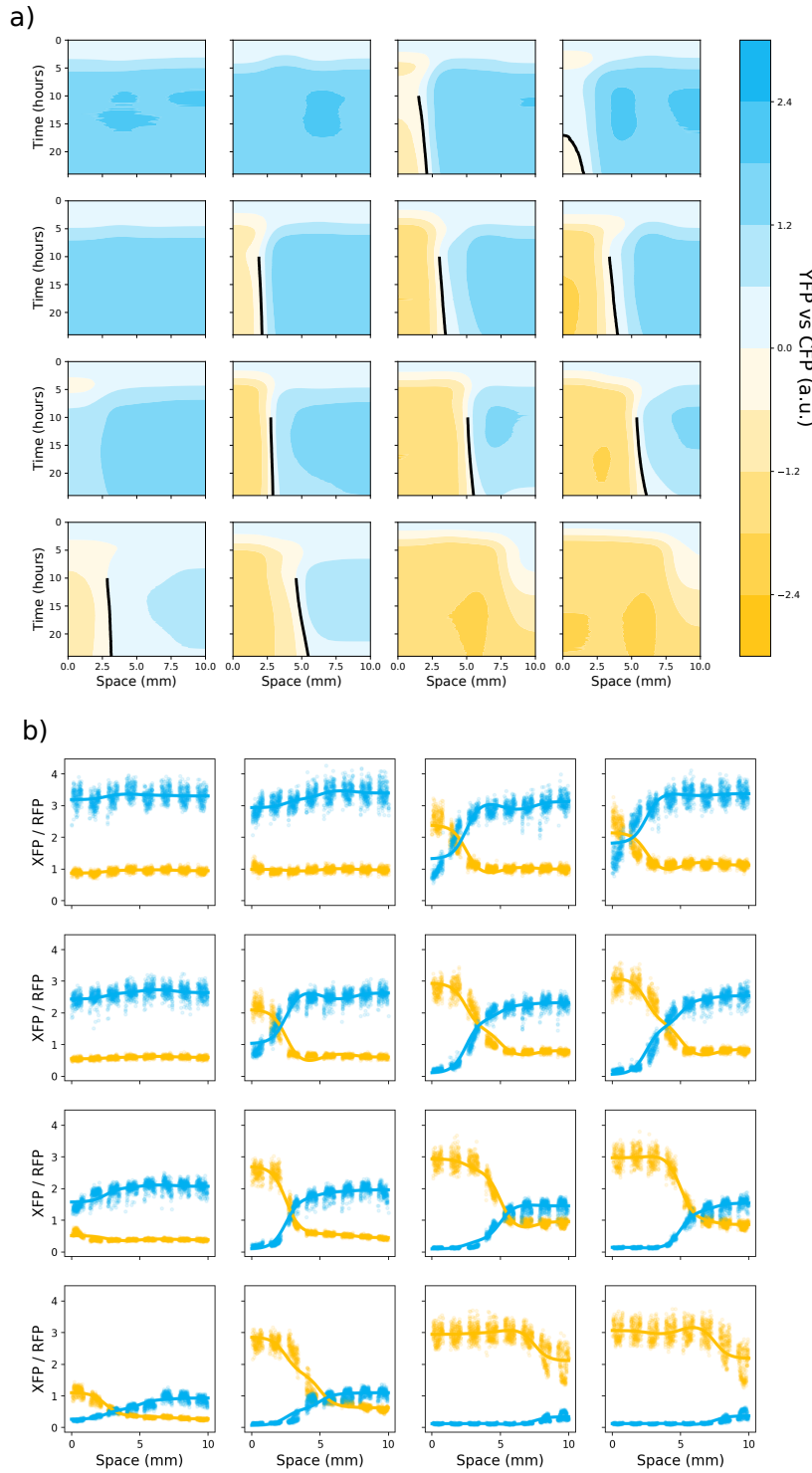


Supplementary Figure 29: Bayesian Ridge regression estimate $f_{\phi}(x)$ from preprocessed data X

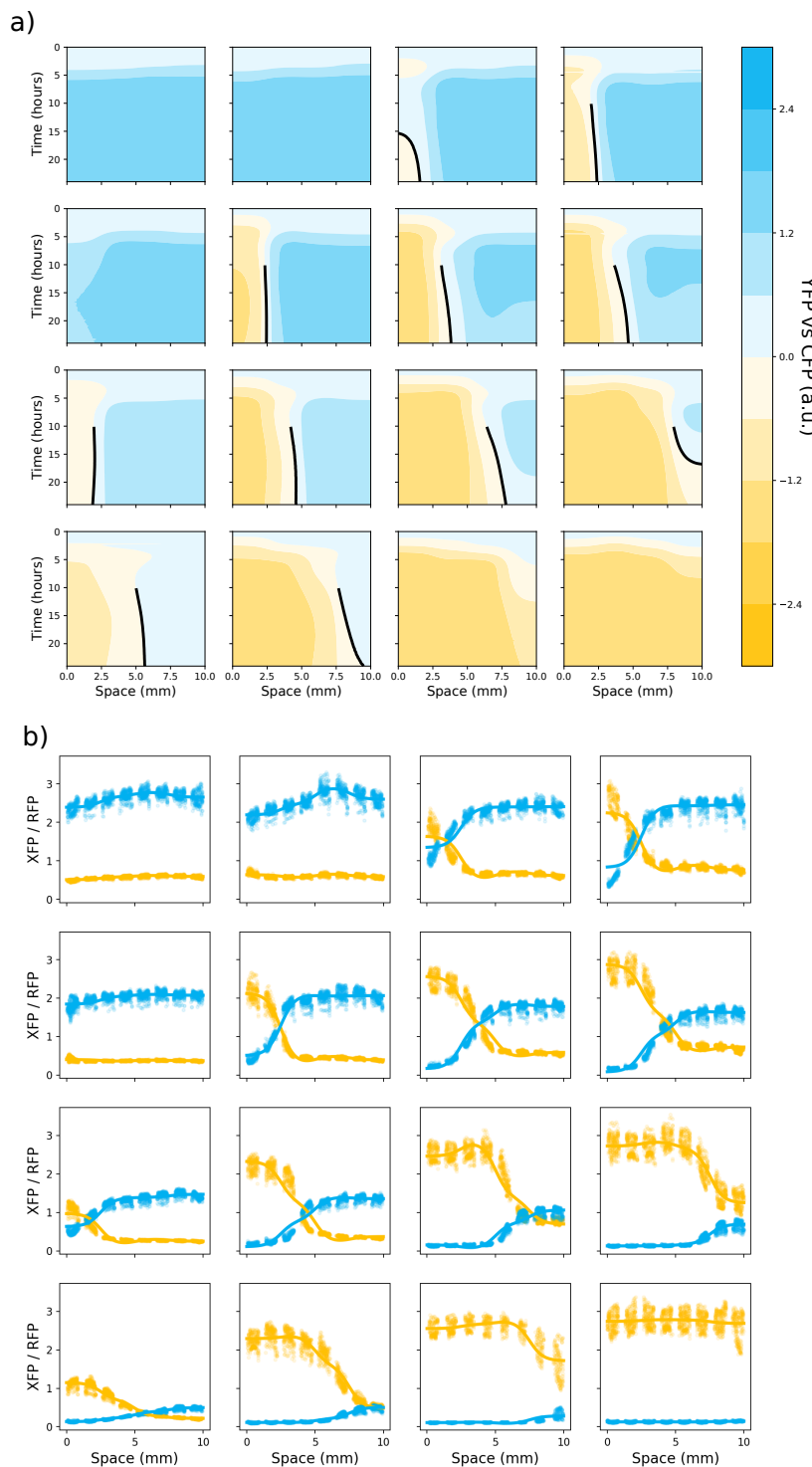


Supplementary Figure 30: Boundary location $\beta[t]$ by equating estimates from two channels

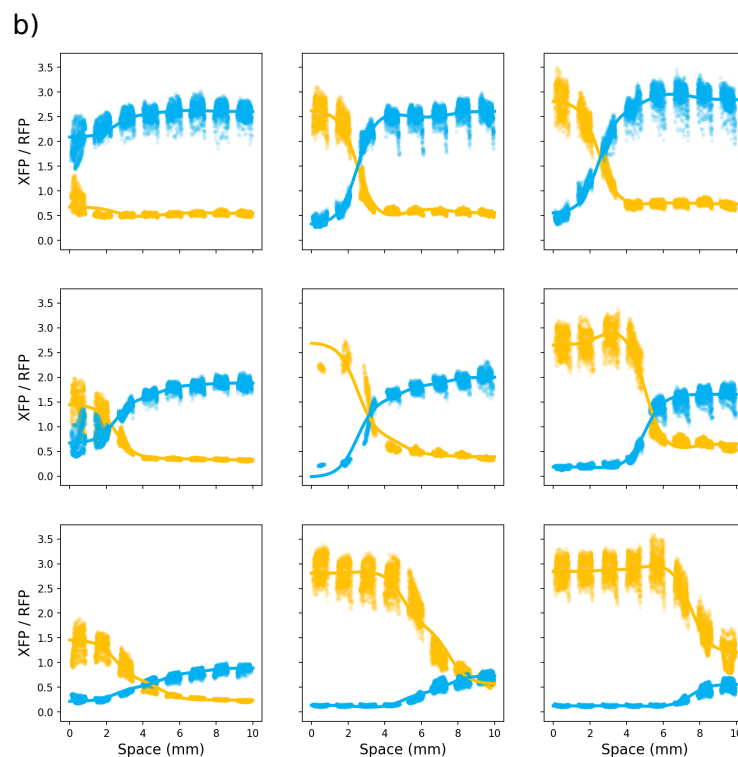
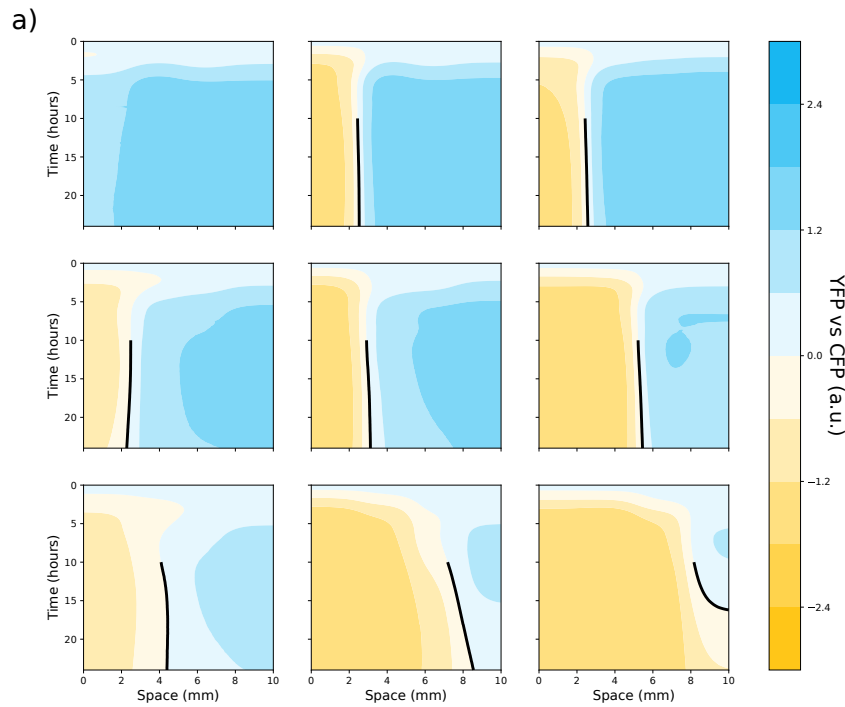
The distance travelled $\Delta\beta$ can be investigated for different equilibrium concentrations $\overline{C6}$ and $\overline{C12}$. Figure 31 shows results for a two dimensional dilution between 5 nM and 25000 nM and fixed 10 μ M IPTG. The subsequent classification using $\Delta\beta$ is shown as Figure 3c in the main text.



Supplementary Figure 31: a) Boundary movements $\beta[t]$ for a grid of equilibrium concentrations $\overline{C}_6, \overline{C}_{12}$ and fixed 10 μM IPTG. This is an expanded version of Figure 3c in the main text, showing the kymographs that were used for classification. b) Bayesian Ridge regression estimates for final time points of preprocessed data X



Supplementary Figure 32: a) Replicate of Figure 31 for a two dimensional dilution of $\overline{C}_6, \overline{C}_{12}$ between 5 nM and 25000 nM and fixed 10 μ M IPTG. b) Bayesian Ridge estimates for final time points of preprocessed data X

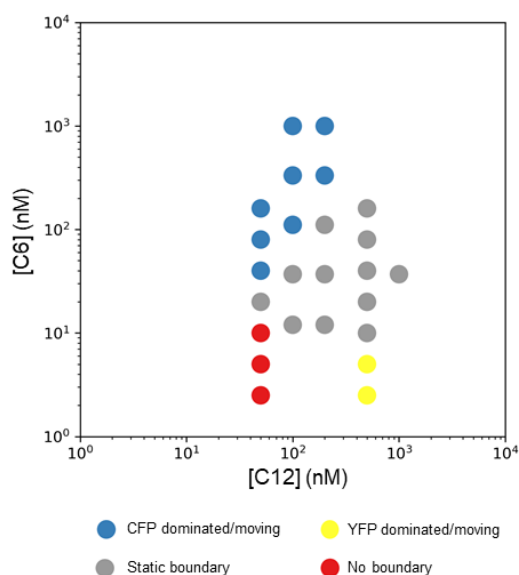


Supplementary Figure 33: a) Replicate of Figure 31 for a two dimensional dilution of $\overline{C6}, \overline{C12}$ between 20 nM and 2000 nM and fixed 10 μ M IPTG. b) Bayesian Ridge estimates for final time points of preprocessed data X

Use of IPTG to influence bifurcation curve

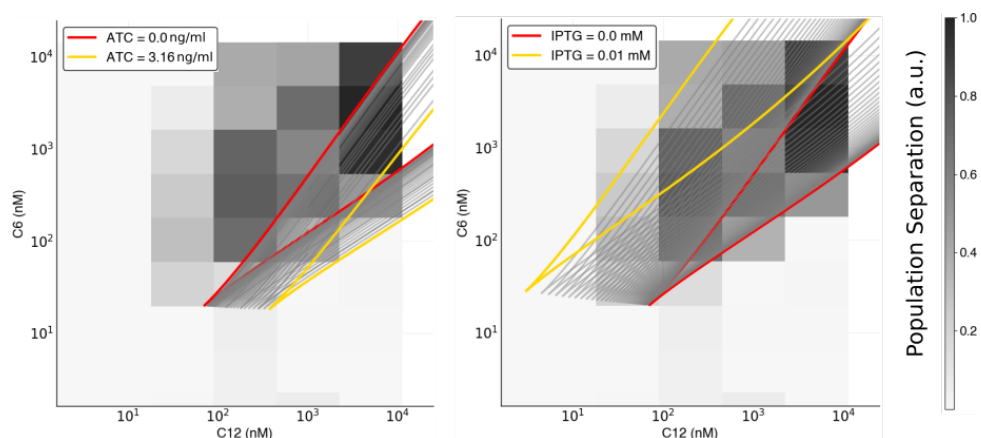
Solid culture experiments on boundary movement were initially performed in the absence of IPTG. We observed stationary boundaries at the concentrations labelled as grey points (Figure S24). The shape of the region encompassing the grey points was qualitatively similar to the conical bistability region we observed in previous experiments and in our models, but was quantitatively shifted such that even very low concentrations of C6 enabled bistability. We hypothesized that this was due to minor differences in culture conditions between solid and liquid cultures. We hypothesized that the addition of a low concentration of IPTG would partially derepress LacI, thereby making the YFP-dominant region larger and more like that seen in liquid culture. We used IPTG to shift the bistability region back (Figure S25) to coincide with the region in liquid culture. This allowed us to perform the solid culture experiments in a regime in which we could observe the transition from stable boundary to moving boundary with YFP dominance, by using higher concentrations of C12 while keeping C6 constant.

Experiments with the relay circuit (Fig. 4b) performed as expected without the need for addition of IPTG or ATC.



Supplementary Figure 34: Boundary movement in the absence of IPTG Boundaries were classified by eye at the spatial average concentrations indicated.

Experiments with the relay circuit (4a) performed as expected without the addition of IPTG or ATC.



Supplementary Figure 35: Bifurcation curve dependence on ATC and IPTG. Increasing the concentrations c_A or c_I shifts the cusp point keeping the general shape of the bistable region. Here the maximum likelihood parameters from the main text are used as the reference cusp.

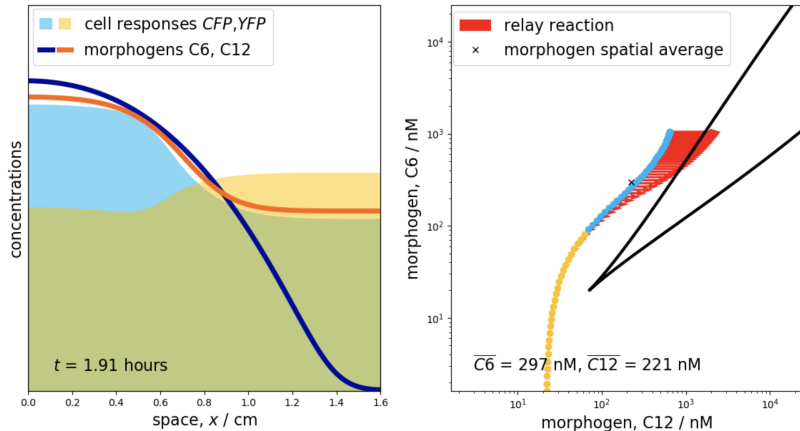
2.4 Models of the Exclusive Receiver Relay Circuits

The Exclusive Receiver Relay circuits were described in Figure 4 of the main text. The models for these circuits are simple extensions of the constant density model of the Exclusive Receiver circuit (22) with $\rho = \rho_0$, $\gamma = \gamma_0$ and production terms in the signal diffusion equations

$$\frac{\partial c_6(x, t)}{\partial t} = D_6 \frac{\partial^2 c_6(x, t)}{\partial x^2} + k_{C6}\rho_0 c_{\text{luxI}} \quad \frac{\partial c_{12}(x, t)}{\partial t} = D_{12} \frac{\partial^2 c_{12}(x, t)}{\partial x^2} + k_{C12}\rho_0 c_{\text{lasI}} \quad (36)$$

$$\frac{dc_{\text{luxI}}}{dt} = P_{81} - (\gamma_0 + d_{\text{luxI}})c_{\text{luxI}} \quad \frac{dc_{\text{lasI}}}{dt} = P_{76} - (\gamma_0 + d_{\text{lasI}})c_{\text{lasI}} \quad (37)$$

Here, the additional production terms $k_{C6}\rho_0 c_{\text{luxI}}$ and $k_{C12}\rho_0 c_{\text{lasI}}$ break mass conservation of the signalling molecules and thus may increase the spatial averages \bar{C}_6 , \bar{C}_{12} . These terms can be visualised as vertical and horizontal vector fields components in the (c_6, c_{12}) plane respectively, which induce a drift on the local equilibria and the spatial average \bar{C}_6 , \bar{C}_{12} . Since there is no saturation of signal production, the spatial average \bar{C}_6 , \bar{C}_{12} will eventually always move outside of the bistable region, giving rise to a uniform dominant CFP or YFP profile. Within the finite observation time $t < 24$ h however, we may observe sharp boundaries forming, as the spatial average \bar{C}_6 , \bar{C}_{12} passes through the bistable region. Figure 36 shows how even monotonic gradients can facilitate boundary formation.



Supplementary Figure 36: Dynamics of the relay circuit for $k_{C12} > 0$, $k_{C6} = 0$ in the spatial domain x on the left and (c_6, c_{12}) plane on the right, showing additional reaction terms as red vectors driving the dynamics. This way even monotonic gradients can facilitate boundary formation

The additional parameters $k_{C6}, k_{C12}, d_{\text{luxI}}, d_{\text{lasI}}$ are tuned by hand. Simulations in Section 2.3 suggest that local cellular responses approach local equilibria faster than the diffusion timescales of signalling molecules. This means we can reasonably assume that our system is diffusion-limited and so reactive dynamics (37) are much faster than diffusive dynamics (36) and we can apply the quasi-steady state assumption to (36) yielding

$$\frac{\partial c_6(x, t)}{\partial t} = D_6 \frac{\partial^2 c_6(x, t)}{\partial x^2} + \frac{k_{C6}\rho_0 P_{81}}{\gamma_0 + d_{\text{luxI}}}, \quad \frac{\partial c_{12}(x, t)}{\partial t} = D_{12} \frac{\partial^2 c_{12}(x, t)}{\partial x^2} + \frac{k_{C12}\rho_0 P_{76}}{\gamma_0 + d_{\text{lasI}}}, \quad (38)$$

and therefore in effect only two ratio parameter ratios need to be tuned. These ratios determine the magnitude of the relay reactions in the (c_6, c_{12}) plane, which determine whether diffusion had contracted the local equilibria to the spatial average \bar{C}_6 , \bar{C}_{12} before or after having crossed into bistable region. Boundaries only form if contraction to \bar{C}_6 , \bar{C}_{12} occurred after entering the bistable region. See supplementary movies 6-7 for examples of these cases.

References

- [1] Boyan Yordanov, Neil Dalchau, Paul K Grant, Michael Pedersen, Stephen Emmott, Jim Haseloff, and Andrew Phillips. A computational method for automated characterization of genetic components. *ACS synthetic biology*, 3(8):578–588, 2014.
- [2] Timothy J. Rudge, James R. Brown, Fernan Federici, Neil Dalchau, Andrew Phillips, James W. Ajioka, and Jim Haseloff. Characterization of Intrinsic Properties of Promoters. *ACS Synthetic Biology*, 5(1):89–98, jan 2016.
- [3] Paul K Grant, Neil Dalchau, James R Brown, Fernan Federici, Timothy J Rudge, Boyan Yordanov, Om Patange, Andrew Phillips, and Jim Haseloff. Orthogonal intercellular signaling for programmed spatial behavior. *Molecular Systems Biology*, 12(1):849, 2016.
- [4] Neil Dalchau, Paul K. Grant, Prashant Vaidyanathan, Carlo Spaccasassi, Colin Gravill, and Andrew Phillips. Scalable dynamic characterization of synthetic gene circuits. *bioRxiv*, page 635672, aug 2019.
- [5] Geoffrey Roeder, Paul K Grant, Andrew Phillips, Neil Dalchau, and Edwards Meeds. Efficient amortised bayesian inference for hierarchical and nonlinear dynamical systems. In *International Conference on Machine Learning (ICML 2019)*, 2019.
- [6] ML Urbanowski, CP Lostroh, and EP Greenberg. Reversible acyl-homoserine lactone binding to purified vibrio fischeri luxr protein. *Journal of Bacteriology*, 186(3):631–637, 2004.
- [7] Romain Veltz. PseudoArcLengthContinuation.jl, March 2019.

Appendix B

Parameter Inference with Bifurcation Diagrams

Supplementary Material

A Bifurcation Diagrams as Tangent Fields

Let each component of the vector function F_θ in the model (1) implicitly define a surface embedded in \mathbb{R}^{N+1} . Let's assume that the intersection of these N surfaces exists and is not null or degenerate, then the steady states of (1) must be a set of one dimensional space curves in $z \in \mathbb{R}^{N+1}$ defined by

$$F_\theta(z) = 0 \quad (\text{A.1})$$

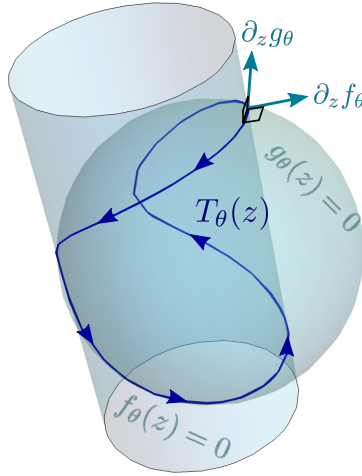


Figure A.1: Two implicit surfaces $f_\theta(z) = 0$ and $g_\theta(z) = 0$ in \mathbb{R}^3 intersecting to form a space curve which is tangent to field $T_\theta(z)$ and perpendicular to gradients $\partial_z f_\theta$ and $\partial_z g_\theta$

An expression for the field $T_\theta(z)$ tangent to the set of curves would allow us to take derivatives and integrals along the bifurcation curve. This is exactly what we need to do to evaluate our cost function 8. Fortunately the tangent field can be constructed by ensuring it is perpendicular to the gradient ∂_z of each component of F_θ as illustrated by an example two component system in Figure A.1. The tangent field $T_\theta(z)$ can be constructed perpendicular to all gradient vectors using the properties of the determinant [35]

$$T_\theta(z) := \begin{vmatrix} \hat{z} \\ \partial_z F_\theta \end{vmatrix} \quad T_\theta : \mathbb{R}^{N+1} \rightarrow \mathbb{R}^{N+1} \quad (\text{A.2})$$

$$= \sum_{i=1}^{N+1} \hat{z}_i (-1)^{i+1} \left| \frac{\partial F_\theta}{\partial (z \setminus z_i)} \right| \quad (\text{A.3})$$

where \hat{z} is a collection of unit basis vectors in the \mathbb{R}^{N+1} space and $\partial_z F_\theta$ is an $N \times (N+1)$ rectangular Jacobian matrix of partial derivatives and $z \setminus z_i$ denotes the N dimensional vector z with component z_i removed. This construction ensures perpendicularity to any gradients of F_θ

$$T_\theta(z) \cdot \partial_z f_\theta = \left| \frac{\partial_z f_\theta}{\partial_z F_\theta} \right| = 0 \quad \forall f_\theta \in F_\theta \quad (\text{A.4})$$

since the determinant of any matrix with two identical rows or columns is zero. Note that the tangent field $T_\theta(z)$ is actually defined for all values of z where adjacent field lines trace out other level sets where $F_\theta(z) \neq 0$. Furthermore deformations with respect to θ are always orthogonal to the tangent

$$T_\theta(z) \cdot \frac{dT_\theta}{d\theta} = 0 \quad (\text{A.5})$$

Figure A.2 shows how the bifurcation curve defined by $F_\theta(z) = 0$ picks out one of many level sets or traces in tangent field $T_\theta(z)$ for the saddle and pitchfork. The tangent field $T_\theta(z)$ can always be

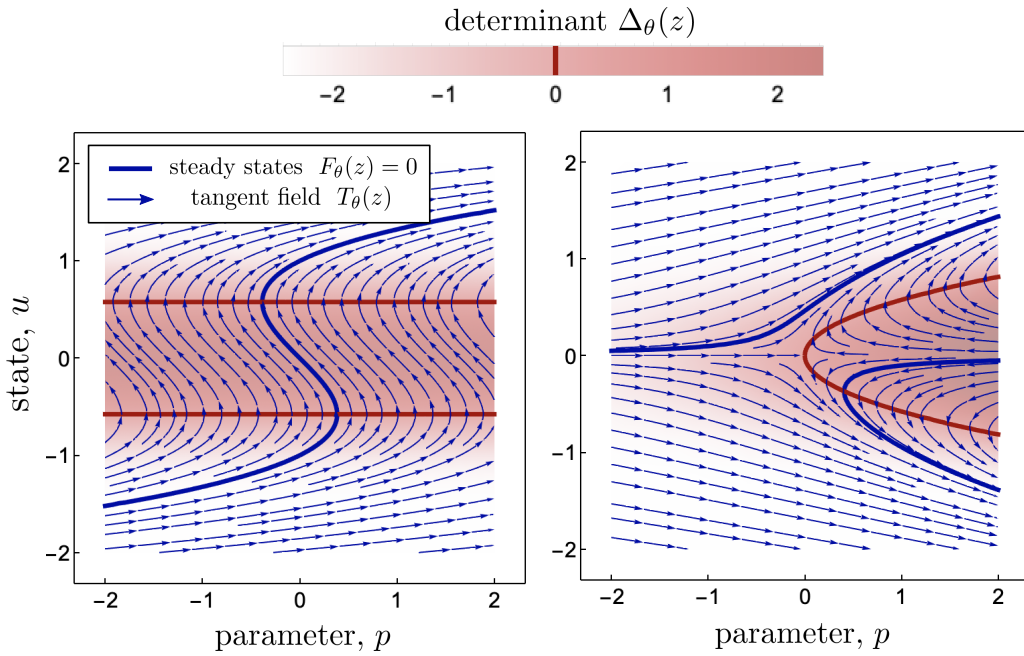


Figure A.2: Left/Right : Determinant $|\frac{\partial F_\theta}{\partial u}|$ and tangent field $T_\theta(z)$ for the saddle-node/pitchfork models for some set values of θ revealing that $|\frac{\partial F_\theta}{\partial u}| = 0$ defines bifurcations

analytically evaluated by taking the determinant in (A.2). We will proceed with calculations on $T_\theta(z)$ in the whole space z and pick out a single trace by solving $F_\theta(z) = 0$ later. For our two models

$$\begin{aligned} T_\theta(z) &= \hat{u} - (3\theta_2 u^2 + \theta_1) \hat{p} & T_\theta(z) &= u \hat{u} - (3\theta_2 u^2 + p) \hat{p} \\ &\text{saddle-node model} & &\text{pitchfork model} \end{aligned} \quad (\text{A.6})$$

Figure A.2 reveals that $|\frac{\partial F_\theta}{\partial u}| = 0$ is also a level set and that the intersection with level set $F_\theta(z) = 0$ defines the bifurcations at specific parameter θ . In this particular setting we can see that the tangent field $T_\theta(z)$ only folds when $|\frac{\partial F_\theta}{\partial u}| = 0$. Plotting the value of the determinant along $F_\theta(z) = 0$ from Figure A.2 would give rise to Figures 1. The directional derivative of the determinant $|\frac{\partial F_\theta}{\partial u}|$ along the tangent field $T_\theta(z)$ is defined as

$$\frac{d}{ds} \left| \frac{\partial F_\theta}{\partial u} \right| := \hat{T}_\theta(z) \cdot \frac{\partial}{\partial z} \left| \frac{\partial F_\theta}{\partial u} \right| \quad (\text{A.7})$$

where $\hat{T}_\theta(z)$ is the unit tangent field.

B Bifurcation Measure Properties

Consider a vector $v(s) \in \mathbb{R}^N$ parametrised by $s \in \mathbb{R}$ that is tangent to an equilibrium manifold defined by $F_\theta(u) = 0$. The conditions for a non-degenerate static bifurcation at s^* along such a tangent can be expressed in terms of an eigenvalue $\lambda(s)$ of the state-space Jacobian crossing zero with a finite slope. A bifurcation exists at s^* if

$$\frac{\partial F_\theta}{\partial u} v(s) = \lambda(s) v(s) \quad \exists \lambda : \quad \lambda(s)|_{s=s^*} = 0 \quad \frac{d\lambda}{ds} \Big|_{s=s^*} \neq 0 \quad (\text{B.1})$$

These conditions are necessary and sufficient for a non-degenerate static local breakdown of stability. For now we do not consider dynamic bifurcations involving limit cycles or imaginary parts of eigenvalues and restrict $\lambda \in \mathbb{R}$. Cases where both $\lambda(s)|_{s=s^*} = 0$ and $\frac{d\lambda}{ds}|_{s=s^*} = 0$ require investigation into higher order derivatives $\frac{d^n \lambda}{ds^n}|_{s=s^*}$. These are the cases we refer to as *degenerate* and are not considered here.

Instead of considering conditions on each eigenvalue individually it is possible to use the determinant of the state-space Jacobian to detect whether the conditions (B.1) are satisfied. The determinant can

be expressed as the product of eigenvalues

$$\left| \frac{\partial F_\theta}{\partial u} \right| = \prod_{n=1}^N \lambda_n(s) \quad (\text{B.2})$$

Applying the product rule when differentiating yields

$$\frac{d}{ds} \left| \frac{\partial F_\theta}{\partial u} \right| = \sum_{n=1}^N \frac{d\lambda_n}{ds} \prod_{n' \neq n} \lambda_{n'}(s) \quad (\text{B.3})$$

$$= \left| \frac{\partial F_\theta}{\partial u} \right| \sum_{n=1}^N \frac{d\lambda_n}{ds} \lambda_n(s)^{-1} \quad (\text{B.4})$$

Substituting this expression into measure (5)

$$\varphi_\theta(s) = \left(1 + \left| \sum_{n=1}^N \frac{d\lambda_n}{ds} \lambda_n(s)^{-1} \right|^{-1} \right)^{-1} \quad (\text{B.5})$$

Which implies the following

$$\exists \lambda : \begin{cases} \lambda(s) = 0 & \frac{d\lambda}{ds} \neq 0 \\ \lambda(s) \neq 0 & \frac{d\lambda}{ds} \rightarrow \pm\infty \end{cases} \implies \varphi_\theta(s) = 1 \quad (\text{B.6})$$

If there exists an eigenvalue that satisfies conditions (B.1) then the measure is equal to one. The measure also approaches one in cases where the rate of change of an eigenvalue with respect to a manifold s location diverges while not crossing zero. This gives rise to finite gradients in the eigenvalue term in regimes far away from any bifurcation.

C Leibniz Rule for Space Curves

Suppose there exists a one dimensional space curve $\mathcal{C}(\theta)$ embedded in $z \in \mathbb{R}^{N+1}$ whose geometry changes depending on input parameters $\theta \in \mathbb{R}^M$. This curve could be open or closed and changes in θ could change the curve topology as well. Let the function $\gamma_\theta : \mathbb{R} \rightarrow \mathbb{R}^{N+1}$ be a parametrisation of the position vector along the curve within a fixed domain $s \in \mathcal{S}$. Note that the choice of parametrisation is arbitrary and our results should not depend on this choice. Furthermore, if we parametrise the curve $\mathcal{C}(\theta)$ with respect to a fixed domain \mathcal{S} the dependence on θ is picked up by the parametrisation $\gamma_\theta(s)$. We can write a line integral of any scalar function $L_\theta : \mathbb{R}^{N+1} \rightarrow \mathbb{R}$ on the curve as

$$L(\theta) := \int_{\mathcal{C}(\theta)} L_\theta(z) dz = \int_{\mathcal{S}} L_\theta(z) \left| \frac{d\gamma_\theta}{ds} \right| ds \Big|_{z=\gamma_\theta(s)} \quad (\text{C.1})$$

where $\left| \frac{d\gamma_\theta}{ds} \right|$ is the magnitude of tangent vectors to the space curve and we remind ourselves that the integrand is evaluated at $z = \gamma_\theta(s)$. We would like to track how this integral changes with respect to θ . The total derivative with respect to θ can be propagated into the integrand [34] as long as we keep track of implicit dependencies

$$\frac{dL}{d\theta} = \int_{\mathcal{S}} \left| \frac{d\gamma_\theta}{ds} \right| \left(\frac{\partial L}{\partial \theta} + \frac{\partial L}{\partial z} \cdot \frac{dz}{d\theta} \right) + L_\theta(z) \frac{d}{d\theta} \left| \frac{d\gamma_\theta}{ds} \right| ds \Big|_{z=\gamma_\theta(s)} \quad (\text{C.2})$$

Here we applied the total derivative rule in the first term due to the implicit dependence of z on θ through $z = \gamma_\theta(s)$. Applying the chain rule to the second term

$$\frac{d}{d\theta} \left| \frac{d\gamma_\theta}{ds} \right| = \left| \frac{d\gamma_\theta}{ds} \right|^{-1} \frac{d\gamma_\theta}{ds} \cdot \frac{d}{d\theta} \left(\frac{d\gamma_\theta}{ds} \right) \quad (\text{C.3})$$

By choosing an s that has no implicit θ dependence we can commute derivatives

$$\frac{d}{d\theta} \left(\frac{d\gamma_\theta}{ds} \right) = \frac{d}{ds} \left(\frac{d\gamma_\theta}{d\theta} \right) \implies \frac{d}{d\theta} \left| \frac{d\gamma_\theta}{ds} \right| = \left| \frac{d\gamma_\theta}{ds} \right|^{-1} \frac{d\gamma_\theta}{ds} \cdot \frac{d}{ds} \left(\frac{d\gamma_\theta}{d\theta} \right) \quad (\text{C.4})$$

To proceed we note that the unit tangent vector can be written as an evaluation of a tangent field $\hat{T}_\theta(z)$ defined in the whole domain $z \in \mathbb{R}^{N+1}$ along the parametric curve $z = \gamma_\theta(s)$. The unit tangent field may disagree with the tangent given by $\frac{d\gamma_\theta}{ds}$ up to a sign

$$\hat{T}_\theta(z) \Big|_{z=\gamma_\theta(s)} = \pm \left| \frac{d\gamma_\theta}{ds} \right|^{-1} \frac{d\gamma_\theta}{ds} \quad (\text{C.5})$$

this leads to

$$\frac{d}{d\theta} \left| \frac{d\gamma_\theta}{ds} \right| = \left| \frac{d\gamma_\theta}{ds} \right| \left(\hat{T}_\theta(z) \cdot \frac{\partial}{\partial z} \left(\frac{d\Gamma_\theta}{d\theta} \right) \cdot \hat{T}_\theta(z) \right)_{z=\gamma_\theta(s)} \quad (\text{C.6})$$

It is possible to find the normal deformation of the implicit space curves due to changes in θ . This can be done by taking the total derivative of the implicit equation defining the level set

$$\frac{dF_\theta(z)}{d\theta} = \frac{\partial F}{\partial \theta} + \frac{\partial F}{\partial z} \cdot \frac{dz}{d\theta} \quad (\text{C.7})$$

We can rearrange for $\frac{dz}{d\theta}$ using the Moore-Penrose inverse of the rectangular Jacobian matrix $\frac{\partial F}{\partial z}$ which appeared in equation (A.2). Since the level set is defined by $F_\theta(z) = 0$ the total derivative along the level set $dF_\theta(z) = 0$ and we arrive at an expression for the deformation field [28]

$$\frac{dz}{d\theta} = -\frac{\partial F^\top}{\partial z} \left(\frac{\partial F}{\partial z} \frac{\partial F^\top}{\partial z} \right)^{-1} \frac{\partial F}{\partial \theta} \quad (\text{C.8})$$

The tangential component of the deformation field is not uniquely determined because there is no unique way of parametrising a surface. This is the subject of many computer graphics papers [28, 36, 37]. We are however not interested in the continuous propagation of a mesh - as is the subject of those papers. In fact we are looking for a deformation field that is orthogonal to the tangent vector $\hat{T}_\theta(z) \cdot \frac{dz}{d\theta} = 0$ for the space curve, and therefore letting the tangential component of the deformation equal zero is a valid choice and we can it instead of the parametrised deformation

$$\frac{d\gamma_\theta}{d\theta} \rightarrow \frac{dz}{d\theta} \quad (\text{C.9})$$

To summarise we now have the gradient of our line integral only in terms of the implicit function defining the integration region.

$$\frac{dL}{d\theta} = \int_{F_\theta(z)=0} \frac{\partial L}{\partial \theta} + \frac{\partial L}{\partial z} \cdot \varphi_\theta(z) + L_\theta(z) \hat{T}_\theta(z) \cdot \frac{\partial \varphi}{\partial z} \cdot \hat{T}_\theta(z) dz \quad (\text{C.10})$$

$$\text{where } \hat{T}_\theta(z) := \frac{T_\theta(z)}{|T_\theta(z)|} \quad T_\theta(z) := \begin{vmatrix} \hat{z} \\ \partial_z F_\theta \end{vmatrix} \quad \varphi_\theta(z) := -\frac{\partial F^\top}{\partial z} \left(\frac{\partial F}{\partial z} \frac{\partial F^\top}{\partial z} \right)^{-1} \frac{\partial F}{\partial \theta} \quad (\text{C.11})$$

We have settled on choosing normal deformations which we will call $\varphi_\theta(z)$. The above result can be seen as the generalised Leibniz rule [34] for the case of line integration regions. The last integrand term can be seen as the divergence the vector field $\varphi_\theta(z)$ projected onto the one dimensional space curve.

D Application of Bifurcation Inference to a Complex Model

To demonstrate the wider reaching applicability of our method we optimise the *double exclusive reporter* [3], a synthetic gene circuit in *E. coli* that was designed to exhibit a cusp bifurcation. The circuit behaviour is observed by measuring a fluorescent protein whose expression is controlled by transcription factors (regulatory proteins) LacI (L) and TetR (T), whose expression is in turn controlled by externally controllable *input* signals c_6 and c_{12} . To apply the method, we consider one of the input signals be the control condition $c_6 = p$, with the other packed together with the remaining 20 parameters into vector θ . Once the optima θ^* have been obtained, we perform dimensionality reduction using GigaSOM.jl [38] so that the results can be visualised in a two dimensional embedding (Figure D.1A).

The embedding reveals four optimal parameter regions. We find that, as with the two-state model in the main text (11), there are two qualitatively distinct regimes: mutual activation (region 1) and inhibition (regions 2-4). The mutual inhibition region can be further subdivided into three regions that are geometrically equivalent, but kinetically distinct: region 3 has swapped kinetic roles for regulatory proteins LacI and TetR compared to region 2, and region 4 has additional damped oscillations in the dynamics across the whole range of *input* c_6 (Figure D.1B). The two dimensional embedding of sampled optima θ^* enables navigation the space of qualitative behaviours of the *double exclusive reporter* and organisation in terms of geometric and kinetic equivalence.

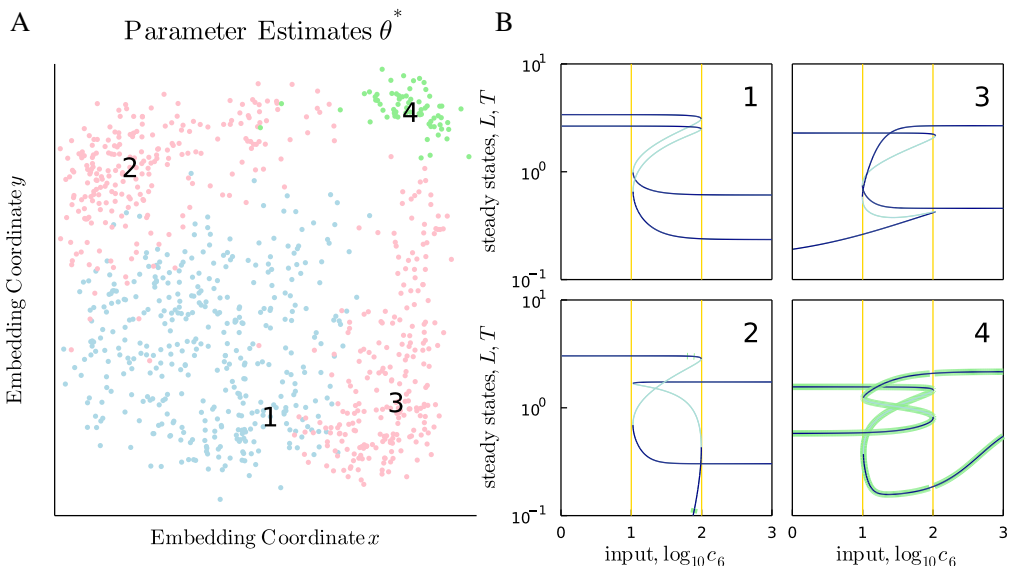


Figure D.1: Bifurcation inference for the *double exclusive reporter*. A. Optimal parameter estimates θ^* for the targets $\mathcal{D} = \{1, 2\}$ (indicated by yellow lines in panel B) reveal four regions with two geometrically different regimes: mutual activation (region 1) and mutual inhibition (regions 2-4). B. Example bifurcation diagrams indicate that region 2 has swapped kinetics between L and T to region 3. Region 4 has models with non-zero imaginary parts to eigenvalues indicating damped oscillations (shown in light green).

These results were obtained with a modification of the bifurcation measure (5) to improve convergence rates. In parameter regimes where bifurcations are not present, according to conditions (B.6), maximising the measure $\varphi_\theta(s)$ can lead to a divergence in directional derivative $\frac{d\lambda}{ds} \rightarrow \pm\infty$ rather than a creation of a bifurcation. To discourage this from happening we can flatten out the gradients in that regime by applying the tanh non-linearity to the determinant. This leads to

$$\varphi_\theta(s) := \left(1 + \left| \frac{\tanh \left| \frac{\partial F_\theta}{\partial u} \right|}{\frac{d}{ds} \tanh \left| \frac{\partial F_\theta}{\partial u} \right|} \right| \right)^{-1} \quad (\text{D.1})$$

E Extension for Hopf Bifurcations

In order to detect bifurcations involving limit cycles, the measure must be extended to detect changes in the real part $\Re[\lambda(s)]$ for any eigenvalue of the Jacobian. These conditions can no longer be compactly written in terms of the determinant. Instead, the measure can be defined as the sum of eigenvalue terms

$$\varphi_\theta(s) := \sum_{\lambda(s) \in \frac{\partial F_\theta}{\partial u}} \left(\left| \frac{d}{ds} \log \Re[\lambda(s)] \right|^{-1} + 1 \right)^{-1} \quad (\text{E.1})$$

The directional derivative of the logarithm diverges under two conditions: when eigenvalues vanish $\lambda(s) = 0$ and when the directional derivative $\frac{d}{ds} \Re[\lambda(s)]$ diverges. These properties are sufficient for detecting the onset of damped oscillations and emergence of limit cycles via Hopf bifurcation as shown in Figure E.1. Eigenvalues with negative real part which gain a finite imaginary part give rise to damped oscillations. At this onset we observe a discontinuity in the derivative $\frac{d}{ds} \Re[\lambda(s)]$ which is detected by equation (E.1). Once damped oscillations exist, flipping the stability of the stable fixed point gives rise to a limit cycle, which can be detected by inspecting $\Re[\lambda(s)]$.

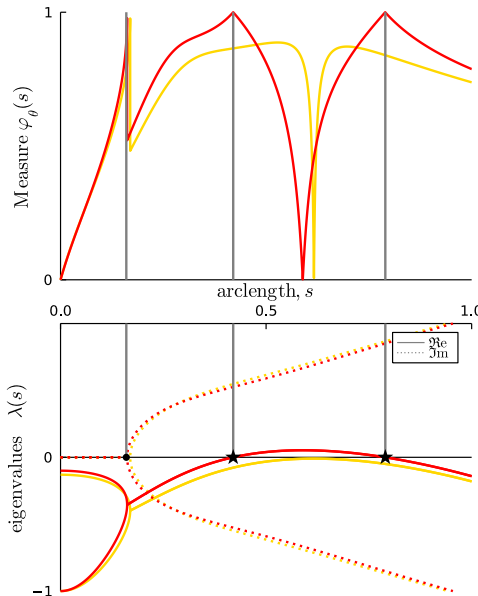


Figure E.1: Bifurcation measure $\varphi_\theta(s)$ and eigenvalues $\lambda(s)$ along the arclength s for two different bifurcation curves demonstrating how the measure detects non-zero imaginary parts $\Im[\lambda]$ (onset of damped oscillations marked by circle) and sign changes in real parts $\Re[\lambda]$ (Hopf bifurcations marked by stars)

In principle it is possible to construct measures to detect a variety of bifurcations as long as the conditions can be expressed in terms of derivatives with respect to fixed-point manifold direction s . Measures can be used sequentially or in parallel to encourage optimisers to run through a sequence of bifurcations or place specific bifurcation types next to each other.

Appendix C

Exploring Bifurcations between Phenotypes

C.1 Supplementary Tables

DonorSex	Age ID	Primary Multi-cause of death	Days in hospital	BMI	CMV / EBV / TOXO	Smoking (u/- day)	Alcohol (u/- day)	Antibiotics within 2 weeks of death	Steroids
390C F	65-70	ICH	✓	2	30-35	+/-	?	<1	✗
403C M	50-55	ICH	✓	8	30-35	+/-	✓	<1	Co, T
423C M	60-65	ICH	✗	2	20-25	-/+/-	✓	>9	G, F
412C M	70-75	ICH	✗	5	26-30	-/+/+	✓	<2	A*, F, G, C, Co
428C F	55-60	ICH	✗	3	20-25	-/+/-	✓	>9	Co

F = Female; M = Male; ICH = intracranial haemorrhage; CMV = Cytomegalovirus; EBV = Epstein-Barr virus; TOXO = Toxoplasmosis; Co = Co-amoxiclav; A = Amoxicillin; T = Tazocin; F = Flucloxacillin; G = Gentamicin; D = Dexamethasone; C = Clarithromycin; ? = Not known; P = Prednisolone; *pre-admission, †pre-treatment

Table C.1: Donor Metadata

Specificity	Fluorochrome	Clone	Source
CD3	BUV395	SK7	BD
CD8	BUV563	RPA-T8	BD
CD69	BUV737	FN50	BD
CD4	BUV805	SK3	BD
CD4	BUV661	SK3	BD
CD45	BUV805	HI30	BD
CD103	BV421	Ber-ACT8	BD
HLA-DR	BV510	G46-6	BD
CD127	PE-Cy7	HIL-7R-M21	BD
CCR4	BV605	L291H4	Biolegend
CCR6	BV650	11A9	BD
PD-1	BV711	EH12.1	BD
CD45RA	BV786	HI100	BD
CCR10	BB515	1B5	BD
CXCR3	BB700	1C6/CXCR3	BD
CXCR5	APC-R700	RF8B2	BD
CCR7	APC-Fire750	G043H7	Biolegend
CD25	APC	M-A251	BD
CD25	APC	2A3	BD
CD19	BV570	HIB19	Biolegend
IgM	PE	G20-127	BD
IgD	BUV395	IA6-2	BD
Foxp3	PE	269D/C7	BD
Foxp3	PE	PCH101	eBioscience
Helios	PE-Dazzle	22F6	Biolegend
Zombie UV	-	-	Biologend

Table C.2: Details of antibodies used in this study

Specificity	Panels: Donor:	Fluorochromes		
		A 390C	B 403C	C 412C, 423C, 428C
CD45	BUV805	-	-	
CD19	-	-	BV570	
IgM	-	-	PE	
IgD	-	-	BUV395	
CD4	BUV661	BV805	BV805	
CD3	BUV395	BUV395	BUV395	
CD8	BUV563	BUV563	BUV563	
CD69	BUV737	BUV737	BUV737	
CD103	BV421	BV421	BV421	
HLA-DR	BV510	BV510	BV510	
CD127	PE-Cy7	PE-Cy7	PE-Cy7	
CCR4	BV605	BV605	BV605	
CCR6	BV650	BV650	BV650	
PD-1	BV711	BV711	BV711	
CD45RA	BV786	BV786	BV786	
CCR10	BB515	BB515	BB515	
CXCR3	BB700	BB700	BB700	
CXCR5	APC-R700	APC-R700	APC-R700	
CCR7	APC-Fire750	APC-Fire750	APC-Fire750	
CD25	APC	APC	APC	
Foxp3	PE	PE	PE	
Helios	PE-Dazzle	PE-Dazzle	PE-Dazzle	
Zombie UV	Zombie UV	Zombie UV	Zombie UV	

Table C.3: Immunophenotyping panel designs used in the dataset

Bibliography

- [1] A M Turing. On Computable Numbers, with an Application to the Entscheidungsproblem. *Proceedings of the London Mathematical Society*, s2-42(1):230–265, 1 1937.
- [2] Nicholas Metropolis. The beginning of the Monte Carlo method. *Los Alamos Science*, 15(584):125–130, 1987.
- [3] Dermot Turing. *X, Y and Z : The Real Story of How Enigma Was Broken*. The History Press, 2018.
- [4] Ashkan Shafiee and Anthony Atala. Tissue Engineering: Toward a New Era of Medicine. *Annual Reviews Medicine*, 68:29–40, 2017.
- [5] Kerstin Göpfrich, Ilia Platzman, and Joachim P. Spatz. Mastering Complexity: Towards Bottom-up Construction of Multifunctional Eukaryotic Synthetic Cells. *Trends in Biotechnology*, 36(9):938–951, 9 2018.
- [6] James Sharpe. Computer modeling in developmental biology: growing today, essential tomorrow. *Development (Cambridge, England)*, 144(23):4214–4225, 12 2017.
- [7] Sofia Triantafillou, Vincenzo Lagani, Christina Heinze-Deml, Angelika Schmidt, Jesper Tegner, and Ioannis Tsamardinos. Predicting Causal Relationships from Biological Data: Applying Automated Causal Discovery on Mass Cytometry Data of Human Immune Cells. *Scientific Reports*, 7(1):12724, 12 2017.

- [8] Jack W. Scannell, Alex Blanckley, Helen Boldon, and Brian Warrington. Diagnosing the decline in pharmaceutical R&D efficiency. *Nature Reviews Drug Discovery*, 11(3):191–200, 3 2012.
- [9] John P A Ioannidis. Why most published research findings are false. *PLoS medicine*, 2(8):e124, 2005.
- [10] Alessandro Abate, Luca Cardelli, Marta Kwiatkowska, Luca Laurenti, and Boyan Yordanov. Experimental Biological Protocols with Formal Semantics. In *Lecture Notes in Computer Science*, volume 11095 LNBI, pages 165–182. Springer, Cham, 9 2018.
- [11] Shota Gugushvili and Chris A.J. Klaassen. root n-consistent parameter estimation for systems of ordinary differential equations: bypassing numerical integration via smoothing. *Bernoulli*, 18(3):1061–1098, 8 2012.
- [12] Steven L. Brunton, Joshua L. Proctor, and J. Nathan Kutz. Sparse Identification of Nonlinear Dynamics with Control (SINDYc). *IFAC-PapersOnLine*, 49(18):710–715, 5 2016.
- [13] Nico S Gorbach, Stefan Bauer, and Joachim M Buhmann. Scalable Variational Inference for Dynamical Systems. *ArXiv*, 2017.
- [14] Oana-Teodora Chis, Alejandro F. Villaverde, Julio R. Banga, and Eva Balsa-Canto. On the relationship between sloppiness and identifiability. *Mathematical Biosciences*, 282:147–161, 12 2016.
- [15] Attila Gábor, Alejandro F. Villaverde, and Julio R. Banga. Parameter identifiability analysis and visualization in large-scale kinetic models of biosystems. *BMC Systems Biology*, 11(1):54, 12 2017.
- [16] Alejandro F. Villaverde, Antonio Barreiro, and Antonis Papachristodoulou. Structural Identifiability of Dynamic Systems Biology Models. *PLOS Computational Biology*, 12(10):e1005153, 10 2016.

- [17] Luca Cardelli. Morphisms of reaction networks that couple structure to function. *BMC Systems Biology*, 8(1):84, 2014.
- [18] Luca Cardelli, Mirco Tribastone, Max Tschaikowski, and Andrea Vandin. Maximal aggregation of polynomial dynamical systems. *Proceedings of the National Academy of Sciences*, 114(38):10029–10034, 9 2017.
- [19] Luca Cardelli, Mirco Tribastone, Max Tschaikowski, and Andrea Vandin. ERODE: A Tool for the Evaluation and Reduction of Ordinary Differential Equations. In *Lecture Notes in Computer Science*, volume 10206 LNCS, pages 310–328. Springer, Berlin, Heidelberg, 2017.
- [20] J. Halatek and E. Frey. Rethinking pattern formation in reaction–diffusion systems. *Nature Physics*, page 1, 2 2018.
- [21] Geoffrey Roeder, Paul K Grant, Andrew Phillips, Neil Dalchau, and Edward Meeds. Efficient Amortised Bayesian Inference for Hierarchical and Nonlinear Dynamical Systems. *ICML*, pages 4445–4455, 5 2019.
- [22] Christopher Rackauckas and Qing Nie. Differentialequations.jl - a performant and feature-rich ecosystem for solving differential equations in julia. *Journal of Open Research Software*, 5(1), 2017.
- [23] Romain Veltz. BifurcationKit.jl. Technical report, Inria Sophia-Antipolis, 7 2020.
- [24] François Jacob and Jacques Monod. Genetic regulatory mechanisms in the synthesis of proteins. *Journal of Molecular Biology*, 3(3):318–356, 6 1961.
- [25] Daniel T. Gillespie. A rigorous derivation of the chemical master equation. *Physica A: Statistical Mechanics and its Applications*, 188(1-3):404–425, 9 1992.

- [26] Daniel T Gillespie. Stochastic Simulation of Chemical Kinetics. *Annu. Rev. Phys. Chem.*, 58:35–55, 2007.
- [27] L Wolpert. Positional information and the spatial pattern of cellular differentiation. *Journal of theoretical biology*, 25(1):1–47, 10 1969.
- [28] Melissa B. Miller and Bonnie L. Bassler. Quorum Sensing in Bacteria. *Annual Review of Microbiology*, 55(1):165–199, 10 2002.
- [29] J. B. A. Green and J. Sharpe. Positional information and reaction-diffusion: two big ideas in developmental biology combine. *Development*, 142(7):1203–1211, 4 2015.
- [30] Ricky T. Q. Chen, Yulia Rubanova, Jesse Bettencourt, and David Duvenaud. Neural Ordinary Differential Equations. *NIPS*, 109(NeurIPS):31–60, 6 2018.
- [31] Matthias Seeger. Gaussian processes for machine learning. *International journal of neural systems*, 14(2):69–106, 2004.
- [32] Michael M. Bronstein, Joan Bruna, Taco Cohen, and Petar Veličković. Geometric Deep Learning: Grids, Groups, Graphs, Geodesics, and Gauges. *ArXiv*, 4 2021.
- [33] Edward J Fuselier and Grady B Wright. A radial basis function method for computing Helmholtz-Hodge decompositions. *IMA Journal of Numerical Analysis*, 37(2):774–797, 2017.
- [34] P. K. Grant, N. Dalchau, J. R. Brown, F. Federici, T. J. Rudge, B. Yordanov, O. Patange, A. Phillips, and J. Haseloff. Orthogonal intercellular signaling for programmed spatial behavior. *Molecular Systems Biology*, 12(1):849–849, 1 2016.
- [35] James Lu, Heinz W. Engl, and Peter Schuster. Inverse bifurcation analysis: Application to simple gene systems. *Algorithms for Molecular Biology*, 1(1):1–16, 7 2006.

- [36] Attila Csikász-Nagy, Bela Novák, and John Tyson. Reverse engineering models of cell cycle regulation. *Advances in experimental medicine and biology*, 641:88–97, 2008.
- [37] Emery D Conrad, John Tyson, Reinhard Laubenbacher, John Phillips, and Michael Renardy. Bifurcation Analysis and Qualitative Optimization of Models in Molecular Cell Biology with Applications to the Circadian Clock. *Virginia Tech*, 4 2006.
- [38] A. M. Turing. The Chemical Basis of Morphogenesis. *Philosophical Transactions of the Royal Society B: Biological Sciences*, 237(641):37–72, 8 1952.
- [39] Lily M Park, Joanne Lannigan, and Maria C Jaimes. OMIP-069: Forty-Color Full Spectrum Flow Cytometry Panel for Deep Immunophenotyping of Major Cell Subsets in Human Peripheral Blood. *Cytometry Part A*, 97(10):1044–1051, 2020.
- [40] Miroslav Kratochvíl, Abhishek Koladiya, Jana Balounova, Vendula Novosadova, Karel Fišer, Radislav Sedlacek, Jiří Vondrášek, and Karel Drbal. Rapid single-cell cytometry data visualization with Embed-SOM. *bioRxiv*, page 496869, 12 2018.
- [41] Chen Hao Gianni Monaco. flowAI, 2017.
- [42] Miroslav Kratochvíl, Oliver Hunewald, Laurent Heirendt, Vasco Verissimo, Jiří Vondrášek, Venkata P Satagopam, Reinhard Schneider, Christophe Trefois, and Markus Ollert. GigaSOM.jl: High-performance clustering and visualization of huge cytometry datasets. *GigaScience*, 9(11):1–8, 11 2020.
- [43] D3.js, 2011.
- [44] OpenLayers, 2006.

- [45] Neil Dalchau, Gregory Sz  p, Rosa Hernansaiz-Ballesteros, Chris P. Barnes, Luca Cardelli, Andrew Phillips, and Attila Csik  sz-Nagy. Computing with biological switches and clocks. *Natural Computing*, page 1–19, 6 2018.